

# Novel phases and phase transitions in open quantum systems: Condensates, Many-body localization and entanglement

Inaugural-Dissertation  
zur  
Erlangung des Doktorgrades  
der Mathematisch-Naturwissenschaftlichen Fakultät  
der Universität zu Köln

vorgelegt von  
**Ori Alberton**  
aus Tel-Aviv, Israel

Köln, 2021

Berichtersteller: Prof. Dr. Sebastian Diehl  
Dr. Michael Scherer  
Tag der mündlichen Prüfung: 17.11.2020

# ABSTRACT

In this thesis we explore different phenomena occurring in open quantum many-body systems. This is a research field which is becoming increasingly more important due to the experimental progress towards realization of quantum-simulators and quantum computers using a variety of platforms, from ultracold atoms to superconducting qubit arrays. These systems are inherently driven and open, and it is an ongoing effort to develop theoretical tools and approaches to study their non-equilibrium physics.

In the first part of this thesis we explore the different non-equilibrium condensate phases of resonantly interacting bosons in the presence of coherent pump and incoherent losses. This study might be of relevance to existing Rydberg-polariton setups. We derive an effective non-equilibrium field-theory of this model and study its resulting phase diagram. We find a rich phase diagram including a phase where particles form a condensate of tightly bound molecules. By changing the detuning from the scattering resonance it is possible to drive an Ising phase transition from the molecule condensate phase to a more standard atom condensate phase.

In the second part of this thesis we explore the many-body localization (MBL) transition in an open-driven system. Typically, coupling to a bath is expected to destroy localization and transform the sharp MBL transition to a crossover. Here we show how one can use the couplings to non-equilibrium baths in order to detect sharp signatures of the transition, including the divergence of the dynamical exponent in the Griffith regime of the ergodic phase. This is done by solving for the steady-state of the Lindblad quantum-master equation using matrix-product operator techniques. Our work here suggests a new scalable numerical approach to study the MBL transition.

In the third part of this thesis we study the entanglement properties of measurement trajectories in a free-fermion system subject to dephasing noise. These trajectories describe the evolution of an open system when photons exiting the system are continuously monitored. We are inspired by recent works which studied the entanglement dynamics in hybrid quantum circuits consisting of random-unitary gates and projective measurements. There it was found that a phase transition between a phase with volume-law scaling of entanglement and an area-law phase occurs at a critical value of the measurement rate. In our case we find a new regime, where at weak noise rate the system exhibits logarithmic entanglement scaling, similar to that of  $(1 + 1)d$  conformal field-theories. For some measurement protocols, we find a transition to an area-law phase at a critical noise strength.





# ACKNOWLEDGEMENTS

The writing of this PhD thesis is the the end of a long journey, and it is a pleasure to thank all the people who made this journey possible. First and foremost I would like to thank my advisor Prof. Sebastian Diehl, for giving me the opportunity to pursue physics research in his group, for many interesting discussions, and for providing advice and support. I would also like to thank Dr. Michael Scherer for serving as the second examiner in my thesis committee and Prof. Markus Grüninger for serving as the head of the thesis committee.

During my time in the institute of theoretical physics in Cologne, I had the pleasure to interact and collaborate with several people. Thanks goes to Alessio Chiocchetta for our collaboration on the work described in chapter 3 and for teaching me how to be more pragmatic and more positive. To Michael Buchhold for the fun collaboration that led to the work described in chapter 5. To Zala Lenarčič for the collaboration on our MBL project described in chapter 4, and for being a great friend in general. In addition I would like to thank Achim Rosch and Ehud Altman, who were also part of that collaboration.

Thanks to Henry Legg, Roi Holtzman, Michael Buchhold, Alessio Chiocchetta and Zala Lenarčič for proofreading parts of this thesis. Thanks to Mariela Boevska for administrative support and help. Thanks also goes to all the other memebers of the Diehl group and the THP for all the nice conversations during lunch and coffee breaks. In addition to all those already mentioned, I would like to mention: Emilio Torres, Jan Gelhausen, Henry Legg, Jamir Marino, Björn Ladewig and Yuval Vinkler.

I would also like to thank my climbing friends here in Cologne: Johannes, Sarina, Toni, Aaron, Etienne, Alon, Sarah and Felix. Nothing helps more than a scary climb on the basalt walls of Ettringen, when one is frustrated with the hardships of research. Thanks goes also to my friends and family in Israel, and above all to my mother, who raised me on her own, and always provided support and love , even when I was far away in a foreign country. Finally, my deepest thanks goes to Linda, for the love and support in bad and good times, for making me a better person and for all the happy moments.



# CONTENTS

1	INTRODUCTION	1
2	BACKGROUND: QUANTUM OPEN SYSTEMS	5
2.1	The quantum master equation . . . . .	5
2.2	Keldysh path-integral description of open quantum systems . . . . .	9
2.3	Experimental platforms . . . . .	19
3	CONDENSATE PHASES OF COHERENTLY DRIVEN BOSONS CLOSE TO A SCATTERING RESONANCE	27
3.1	Introduction . . . . .	27
3.2	Background: Scattering Resonance . . . . .	29
3.3	Background: Pairing phases of bosons close to a Feshbach resonance in equilibrium	35
3.4	Background: Rydberg-polaritons . . . . .	39
3.5	Model . . . . .	41
3.6	Expected phases from symmetries . . . . .	43
3.7	Non-interacting case . . . . .	43
3.8	Effective action description for the atom-molecule model . . . . .	47
3.9	Understanding the phase diagram from phenomenological mean-field models .	60
3.10	MC-AC Ising transition . . . . .	72
3.11	Discussion . . . . .	74
3.A	Introducing the auxiliary $\phi$ field in the presence of 2-body loss and 3-body inter- actions . . . . .	76
3.B	Field equations derived from the 1-loop effective action . . . . .	77
3.C	$u_{am}$ flow equations . . . . .	79
4	CRITICAL BEHAVIOR NEAR THE MANY-BODY LOCALIZATION TRANSITION IN DRIVEN OPEN SYSTEMS	81
4.1	Introduction . . . . .	81
4.2	Background: Many-Body Localization . . . . .	83
4.3	Background: studying open-quantum systems using matrix-product states . . .	96
4.4	Hydrodynamic description of temperature fluctuations in the thermal phase . .	101
4.5	Resistor Network simulations . . . . .	104
4.6	MPS simulations . . . . .	107
4.7	Discussion . . . . .	113
5	TRAJECTORY DEPENDENT ENTANGLEMENT TRANSITION IN A FREE FERMION CHAIN – FROM EXTENDED CRITICALITY TO AREA LAW	117
5.1	Introduction . . . . .	117

## *Contents*

5.2	Background . . . . .	119
5.3	Model and method . . . . .	132
5.4	Entanglement Entropy and phase diagram . . . . .	140
5.5	Deviating trajectory ensembles . . . . .	143
5.6	Mutual information and correlation functions . . . . .	145
5.7	Discussion . . . . .	149
5.A	Higher moment evolution . . . . .	151
6	CONCLUSIONS AND OUTLOOK	153
	BIBLIOGRAPHY	155

# 1 INTRODUCTION

Recent years have seen great progress in the experimental techniques allowing the creation and manipulation of “synthetic quantum-matter” systems. These systems can be realized in a variety of platforms such as: ultracold-atoms [1], trapped ions [2], atoms in optical cavities [3] and superconducting circuit arrays [4]. The precise experimental control over those systems allows the engineering of lattice potentials and interaction couplings and opens the path for quantum simulation of a variety of physical models at scales which are out of reach for theoretical tools [5, 6]. These platforms are also the leading candidates for the realization of quantum computers [7–10], a research endeavor which has enjoyed tremendous interest and fast progress in the last years.

One thing that is common to all of the synthetic quantum-matter systems mentioned above, is that they are all strongly driven and constantly interacting with external (classical or quantum) electromagnetic-fields. Those are not just unwanted artifacts, but essential ingredients for the engineering of Hamiltonians, measurement and stabilization of interesting phases. Thus, a full description and understanding of the different phenomena which can occur in synthetic quantum-matter systems requires taking into account the fact that those systems are inherently open and driven out of equilibrium.

The main challenge in theoretical studies of many-body systems out of equilibrium stems from the fact that non-equilibrium systems are much less constrained than their equilibrium counterparts. Simply stated, the space of things that can happen out of equilibrium is much larger than the space of things which can happen under equilibrium conditions. As a consequence, many of the statistical-mechanics concepts which are crucial to the description of equilibrium many-body systems, such as free-energy and its associated thermodynamic intensive variables (temperature, chemical potential etc.), do not generically exist out of equilibrium. Hence a big part of the challenge is in identifying and developing alternative organizing concepts and tools to assist in taming the inherent complexity of many-body systems out of equilibrium.

In this thesis, we will limit ourselves to the investigation of a specific class of open systems whose interaction with the environment can be effectively described by a coupling to a collection of local Markovian baths. As a consequence, the dynamics of these system can be well described by the Lindblad quantum master-equation (QME) [11, 12]. While the theory of open quantum systems and the Lindblad QME description has been studied already since the 80s by pioneers in the field of quantum-optics, those earlier works dealt mainly with the physics of single-atoms. The type of systems we consider in this thesis are constituted of many interacting particles which puts them in the realm of quantum many-body open systems. This is a field which has emerged in the last decade and lies at the intersection of quantum-optics and condensed matter physics [13].

From a computational perspective, the increased difficulty in studying open many-body systems is manifested in the fact that instead of considering pure-states, as we would for example in the case of zero temperature physics or closed system dynamics, we have to consider a full descrip-

tion of the system in terms of a density matrix  $\rho$ . Considering for example a spin chain with  $N$  sites, this implies that we have to deal with  $(2^N)^2$  coefficients instead of  $2^N$  coefficients when only considering pure states. While thermal equilibrium states are also described by a mixed-state, they are constrained to be of the form  $\rho \sim e^{-\beta\hat{H}}$  (say for the canonical ensemble), hence we can infer their properties from the Hamiltonian eigenstates.

While studies of open quantum many-body systems pose new challenges, they also bring new opportunities. One promising direction is that of engineered dissipation and dissipative state preparation [14–16]. In many experiments with quantum simulators the goal is to prepare and study a ground-state (or low temperature state) of some model Hamiltonian of interest. While the final goal in this setting is to study equilibrium physics, the process of state preparation and stabilization leading to the target ground-state is inherently non-equilibrium process. In the context of dissipative state preparation we think of the dissipation which arises due to the coupling of the system to an environment as a friend instead of an enemy. The goal is to engineer the dissipative couplings such that the QME dynamics naturally lead an arbitrary initial state to a target state of interest.

Of course we are not limited to the goal of reproducing specific equilibrium states. Another research direction is a more general exploration and classification of the phases that arise as the non-equilibrium steady-states (NESS) of the QME. An interesting scenario occurs when, as a function of an external control parameter, some properties of the NESS change in a non-analytic way, this is known as a dissipative phase-transition. Understanding the similarities and differences between dissipative phase-transitions and their equilibrium counterparts is an active area of research [17–23]. In chapter 3 we will show how the interplay between two-particle coherent pump, particle losses and interactions in the vicinity of a scattering resonance, can lead to a stabilization of NESS characterized by different types of bosonic condensates.

Synthetic quantum matter systems are also uniquely suitable to study a variety of questions regarding non-equilibrium quantum-dynamics (in closed or open systems). A very active research area is that which concerns quantum thermalization of isolated interacting quantum systems after a quantum quench [24]. In this setup we consider an interacting system starting from some initial state  $|\psi_0\rangle$  which is not an eigenstate of the Hamiltonian, and then let it evolve under the unitary dynamics induced by the Hamiltonian  $|\psi_t\rangle = e^{-iHt}|\psi_0\rangle$ . At long times, generic quantum interacting systems are expected to thermalize. This means that their local observable properties are well described by a thermal state with a certain temperature determined by the initial energy-density (this kind of self-equilibration process is in fact crucial for the study of equilibrium phases of matter in ultracold atoms). However, there is a class of interacting systems which fail to thermalize when evolving in isolation, due to the effects of strong disorder. This phenomenon is known as many-body localization (MBL) [25, 26].

As a function of the disorder strength some systems are expected to undergo a phase transition between a thermalizing phase and an MBL phase [25, 27, 28]. This is a dynamical phase transition with no equilibrium analog, as it necessitates a dramatic change in the entanglement properties of all eigenstates of the Hamiltonian. Unlike equilibrium phase transitions, the MBL transition is expected to be sharp only in completely isolated systems, this leads to a difficulty in studying it in experiments where some coupling to the environment is inevitable. However, in chapter 4, we will show how one can nevertheless find signatures of the MBL transition in open systems. In

fact we will see that the open-system setting provides an advantage over the closed setting for numerical studies of the MBL transition.

Studies of dynamics of open quantum systems are also important for the understanding and characterization of quantum devices from the point of view of their ability to perform quantum computation. While quantum algorithms are often theoretically designed in terms of a sequence of coherent unitary operations on a register of qubits, one must take into account the noise processes the qubits are exposed to when such algorithms are implemented in the lab.

One recent line of research in this direction revolves around the dynamics of entanglement in systems evolving under unitary dynamics combined with non-unitary noise in the form of measurements. Generic unitary dynamics typically lead to generation of quantum states with large scale entanglement [29–31]. From a quantum computation perspective, preparation and manipulation of states with a large amount of entanglement is crucial for achieving any advantage over classical computers, since the dynamics of many-body states with low entanglement can be efficiently simulated classically [32, 33]. A main question which thus arises is: what is the maximal amount of noise under which the unitary dynamics can still generate an extensive amount of entanglement?

Recent works considered 1d spin chains evolving under random-unitary circuit dynamics in addition to projective or weak local-measurements which are performed at some rate  $p$  [34–37]. Those works considered the entanglement-entropy, averaged over different measurement trajectories. At a critical measurement rate a phase-transition of a new type was discovered. This is a transition between a phase where the trajectory states exhibit extensive volume-law entanglement at long times, and an area-law phase where the presence of measurements leads to low amount of entanglement. While the random-unitary evolution is believed to be a good representative of unitary evolution with generic interacting Hamiltonians, it is also interesting to look for entanglement transitions in more natural physical systems. In chapter 5 we will perform such an investigation for a model of free-fermions subject to continuous dephasing noise.

Let us now outline the content of the remaining chapters of this thesis and highlight the main results. We begin with a general introduction to open quantum systems in chapter 2. There we first introduce the Lindblad quantum-master equation which governs the dynamics of the class of Markovian open quantum systems we will investigate in this thesis. We sketch the QME derivation and explain under what physical assumptions it provides a good description of the dynamics. We then introduce the Keldysh formalism and explain how it can be used in order to derive a field-theory description of quantum open systems. Finally we provide a review of several experimental settings which allow the investigation of open quantum many-body systems.

In chapter 3 we consider a model of interacting bosons close to a scattering resonance, which are driven by a two-particle coherent pump and experience particle loss. This chapter is based on work done in collaboration with Alessio Chiocchetta and Sebastian Diehl. The model we consider is inspired by recent advancements in experiments with Rydberg-polariton systems [38–40]. We use the Keldysh formalism in order to construct an effective field theory description which forms a basis for our exploration. Earlier theoretical works, concerning equilibrium states of bosonic ultracold-atoms close to a Feshbach resonance, predicted the existence of a novel type of molecule condensate phase in addition to a more standard atomic condensate [41, 42]. Here, we find that a similar situation might occur in the driven-dissipative setting. As a function of the two-pump frequency and distance from the scattering resonance, we find a rich phase diagram which include

a molecule and atom condensate phases in addition to bistability regions. Our work also indicates the existence of a dissipative Ising phase transition between the molecule condensate and atom condensate phases, which can be observed by tuning in addition to first order phase transitions in certain parameter regimes.

Chapter 4 deals with signatures of the MBL transition in open systems. Parts of this chapter have been published in:

- Lenarčič, Z.\*, Alberton, O.\*, Rosch, A., Altman, E. (2020). *Critical Behavior near the Many-Body Localization Transition in Driven Open Systems*. [Physical Review Letters](#), 125(11), 116601. (\*equal contribution)

In this chapter we consider a situation in which a  $1d$  system undergoing an MBL transition is weakly coupled to non-equilibrium Markovian baths. While a coupling to an external bath is typically considered detrimental to localization, we show how in this setup the steady-states of the system contain signatures of the MBL transition. We find that the strength of the coupling to the non-thermal baths plays a similar role to that of a finite temperature in a  $T = 0$  quantum phase transition. By probing the response of the system to weak bath coupling we are able to detect the divergence of the dynamical exponent when approaching the transition from the thermal side. This is shown by solving the Lindblad QME numerically using matrix-product operator techniques, and suggests a new numerical method for exploration of the MBL transition at scales much larger than those accessible by exact-diagonalization studies of closed systems.

Finally in chapter 5 we turn to an investigation of the entanglement transition in measurement trajectories, using a naturally motivated free-fermion model. Parts of this chapter were included in the following preprint (currently under peer-review):

- Alberton, O., Buchhold, M., Diehl, S. (2020). *Trajectory dependent entanglement transition in a free fermion chain – from extended criticality to area law*. [arXiv/2005.09722](#).

In this chapter we consider free-fermions with nearest-neighbor hopping on a  $1d$  chain, which experience local dephasing noise. The dephasing noise can be interpreted as a continuous measurement of the fermion density at each site, hence this model describes a competition between the entangling unitary Hamiltonian dynamics and the non-unitary dephasing noise which tends to reduce entanglement. Similar to previous works on the entanglement transition, we consider the trajectory averaged entanglement-entropy  $\bar{S}_{\text{vN}}$ . Our main finding is that at weak dephasing strength, there exist an extensive region where  $\bar{S}_{\text{vN}}$  exhibits logarithmic scaling, similar to that which is observed in conformal-field theories describing  $1d$  quantum critical points. For some measurement protocols we find that at critical dephasing rate the system undergoes an entanglement transition to an area-law phase. Our work suggests free-fermion systems as an appealing simple model system to further study trajectory entanglement transitions.



# 2 BACKGROUND: QUANTUM OPEN SYSTEMS

## 2.1 THE QUANTUM MASTER EQUATION

This thesis is concerned with phenomena which occur in open systems, that is, systems which are coupled to an external environment. This external environment is also referred to as a “bath”. By an “environment” we refer to some large collection of degrees of freedom which we do not have access to experimentally. In other words, we do not have any access to information about the dynamics of the environment. One prominent example is the quantized electromagnetic field in the vacuum, which often plays the role of the bath in systems with strong light-matter coupling.

Even though we cannot track the dynamics of the bath, we still want to understand the effect it has on the system of interest. In this section we will explain how to obtain an approximate description, deriving an equation for the dynamics of a system coupled to a Markovian bath. Discussions and derivations of the quantum master equation can be found in several textbooks (e.g. [11, 12, 43]), most typically those which deal with quantum optics, the original context in which much of the theory for open quantum systems have been developed. Here we will follow the discussion in [11].

We will show that under the assumption of a Markovian bath the time evolution of the reduced density matrix of the system  $\rho_S$  can be described by the Lindblad quantum master equation (QME)<sup>1</sup>:

$$\begin{aligned}\partial_t \rho_S(t) &= -i[H_S, \rho_S(t)] + \mathcal{D}[\rho_S(t)] \equiv \mathcal{L}\rho_S(t), \\ \mathcal{D} &\equiv \sum_i \gamma_i \left[ L_i \rho_S(t) L_i^\dagger - \frac{1}{2} \{L_i^\dagger L_i, \rho_S(t)\} \right].\end{aligned}\tag{2.1}$$

Where  $\mathcal{D}$  is known as the dissipator,  $L_i$  termed Lindblad operators and  $\mathcal{L}$  is the Liouvillian. The first term in the RHS represents the unitary evolution generated by the system Hamiltonian  $H_S$ . The dissipator represents the irreversible non-unitary dynamics induced by the coupling with the bath, where  $\gamma_i$  are dissipation rates associated with specific dissipative processes represented by  $L_i$ . Importantly Eq. (2.1) is trace preserving, as can be seen from  $\partial_t \text{tr} \rho_S = \text{tr} \mathcal{L} \rho_S = 0$ . While Eq. (2.1) can be derived microscopically in certain settings note that it is the most general form of a Markovian trace preserving evolution [11].

The Hamiltonian describing the dynamics of the system and the bath is given by

$$H = H_S + H_B + H_{SB}.$$

---

<sup>1</sup>Here, and for the rest of this thesis we work in units where  $\hbar = 1$ , with the exception of a few sections where we want to make contact with well known quantum optics expressions.

## 2 Background: Quantum open systems

Here  $H_S$  ( $H_B$ ) is the system (bath) Hamiltonian, which contains only system (bath) operators. The last term  $H_{SB}$  describes the interaction between the system and the bath. For simplicity we will assume that  $H$  is time independent, but the derivation can be generalized for the case of a time dependent Hamiltonian. The full density-matrix describing the joint system and bath state  $\rho(t) = |\psi(t)\rangle\langle\psi(t)|$  obeys the von-Neumann equation

$$\partial_t \rho(t) = -i[H, \rho(t)].$$

We are interested in the reduced state describing the dynamics of the system only, which is obtained by tracing out degrees of freedom in  $B$ ,  $\rho_S(t) = \text{tr}_B \rho(t)$  and obeys the evolution equation

$$\partial_t \rho_S(t) = -i \text{tr}_B [H, \rho(t)]. \quad (2.2)$$

The rest of this section is devoted to obtaining an approximation to the RHS of Eq. (2.2).

For the purpose of the derivation it is convenient to work in the interaction picture where the state is given by  $\rho_{Int}(t) = e^{i(H_S+H_B)t} \rho(t) e^{-i(H_S+H_B)t}$  and time evolution is generated only by  $H_I(t) = e^{i(H_S+H_B)t} H_{SB} e^{-i(H_S+H_B)t}$ . For the rest of this section we denote  $\rho(t) \equiv \rho_I(t)$ , and assume that all states are specified in the interaction picture. We can reformulate Eq. (2.2) as an integral equation

$$\partial_t \rho_S(t) = - \int_0^t \text{dstr}_B [H_I(t), [H_I(s), \rho(s)]] \quad (2.3)$$

where we assumed that  $\text{tr}_B [H_I(t), \rho(0)] = 0$ .

We now perform our first approximation, known as the *Born approximation*, where we assume

$$\rho(t) \approx \rho_S(t) \otimes \rho_B. \quad (2.4)$$

That is, we assume that the coupling between the system and the bath is weak, such that the effect on the bath is negligible (similar to the typical assumption taken when thinking of a bath in thermodynamics).

The second approximation is the *Markov approximation*, where we assume that excitations created in the bath decay very fast as compared to the typical time-scale of the system evolution. The Markov approximation allows us to perform two simplifications of the RHS of Eq. (2.3). First we can replace  $\rho_S(s) \rightarrow \rho_S(t)$ . Furthermore, we assume that the integrand in Eq. (2.3) vanishes for  $|t - s| \gg \tau_B$ , with  $\tau_B$  the time scale for the decay of bath correlations. This allows us to perform a change of variables  $s \rightarrow t - s$  and extend the limit of integration to infinity. Those approximations are justified as long as the typical time scale  $\tau_R$ , over which  $\rho_S$  varies appreciably, is large compared to  $\tau_B$ .

We thus obtain the following Markovian evolution equation in the Born-Markov approximation

$$\partial_t \rho_S(t) = - \int_0^\infty \text{dstr}_B [H_I(t), [H_I(t-s), \rho_S(t) \otimes \rho_B]]. \quad (2.5)$$

We can see that this evolution equation for  $\rho_S(t)$  is indeed of a Markovian form where the state  $\rho_S(t + dt)$  depends only on the state at  $\rho_S(t)$ .

To bring the evolution equation to the Lindblad form, we need to perform one last approximation. We decompose the system-bath coupling in the form

$$H_{SB} = \sum_{\alpha, \omega} A_{\alpha}(\omega) \otimes B_{\alpha} \quad (2.6)$$

with  $A(B)$  acting only on the system (bath), and  $A_{\alpha}(\omega)$  is an annihilation operator of a system excitation with energy  $\omega$ , that is  $[H_S, A_{\alpha}(\omega)] = -\omega A_{\alpha}(\omega)$ <sup>2</sup>. In practice, for a generic many-body Hamiltonian  $H_S$ , it will be exponentially hard to actually find the operators  $A_{\alpha}(\omega)$ , because this is equivalent to a full diagonalization of  $H_S$ <sup>3</sup>. Still, the fact that such a decomposition exists is useful for the rest of the derivation.

Plugging the decomposition in Eq. (2.6) into Eq. (2.5) we obtain

$$\partial_t \rho_S(t) = \sum_{\omega, \omega', \alpha, \beta} e^{i(\omega - \omega')t} \Gamma_{\alpha\beta}(\omega) [A_{\beta}(\omega) \rho_S(t) A_{\alpha}^{\dagger}(\omega') - A_{\alpha}^{\dagger}(\omega') A_{\beta}(\omega) \rho_S(t)] + \text{h.c.} \quad (2.7)$$

Here,  $\Gamma_{\alpha\beta}(\omega)$  is the Laplace transform of the bath correlation functions

$$\Gamma_{\alpha\beta}(\omega) \equiv \int_0^{\infty} ds e^{i\omega s} \text{tr}_B(B_{\alpha}^{\dagger}(s) B_{\beta}(0) \rho_B), \quad (2.8)$$

and we assumed that the state  $\rho_B$  is stationary. We now perform the last approximation, known as the *rotating-wave approximation*, where we neglect terms with  $\omega \neq \omega'$  in Eq. (2.7). This is justified if the typical intrinsic time scale of the system  $\tau_S \sim |\omega' - \omega|^{-1}$  (for  $\omega' \neq \omega$ ) is large compared to the relaxation time  $\tau_R$  induced due to the coupling with the bath, which is the typical time scale over which  $\rho_S$  varies appreciably. Performing the rotating-wave approximation results in

$$\begin{aligned} \partial_t \rho_S(t) &= -i[H_{LS}, \rho_S(t)] + \mathcal{D}(\rho_S(t)), \\ H_{LS} &= \sum_{\omega, \alpha, \beta} S_{\alpha\beta}(\omega) A_{\alpha}^{\dagger}(\omega) A_{\beta}(\omega), \\ \mathcal{D}(\rho_S(t)) &= \sum_{\omega, \alpha, \beta} \gamma_{\alpha\beta}(\omega) \left[ A_{\beta}(\omega) \rho_S A_{\alpha}^{\dagger}(\omega) - \frac{1}{2} \{A_{\alpha}^{\dagger}(\omega) A_{\beta}(\omega), \rho_S\} \right]. \end{aligned} \quad (2.9)$$

Where we denoted  $\Gamma_{\alpha\beta}(\omega) = \frac{1}{2} \gamma_{\alpha\beta}(\omega) + i S_{\alpha\beta}(\omega)$ . The term  $H_{LS}$  is known as the Lamb-shift and it represents the renormalization of the energy levels of the system due to the coupling with the bath. Finally, we can bring Eq. (2.9) to the standard Lindblad form Eq. (2.1) by diagonalizing the matrix  $\gamma_{\alpha\beta}(\omega)$ .

<sup>2</sup>Note that the sum extends also over negative frequencies and  $A_{\alpha}(-\omega) = A_{\alpha}^{\dagger}(\omega)$ , so the system-bath interaction can both annihilate or create excitations in the system.

<sup>3</sup>Often it is the case that we are interested in the situation where  $A_{\alpha}$  are annihilation or creation operators of the free part of  $H_S$ .

### 2.1.1 EXAMPLE: TWO-LEVEL SYSTEM INTERACTING WITH THE ELECTROMAGNETIC FIELD

To put the abstract derivation in the previous section on more concrete grounds, we will now consider the derivation of the QME for the simple example of a two-level atom interacting with an electromagnetic-field [11]. The system, bath and system-bath Hamiltonians are given by:

$$H_S = \frac{\omega_0}{2} \sigma^z, \quad (2.10)$$

$$H_B = \sum_{\mathbf{k}, \lambda=1,2} \omega_{\mathbf{k}} b_{\lambda}^{\dagger}(\mathbf{k}) b_{\lambda}(\mathbf{k}), \quad (2.11)$$

$$H_{SB} = -\mathbf{D} \cdot \mathbf{E}. \quad (2.12)$$

where  $\sigma^z = |e\rangle\langle e| - |g\rangle\langle g|$ , with  $|g\rangle(|e\rangle)$  the ground(excited)-state of the atom. The system-bath coupling is the usual expression in the dipole approximation with the system dipole operator given by  $\mathbf{D} = \mathbf{d}\sigma^- + \mathbf{d}^*\sigma^+$  (where the dipole moment is  $\mathbf{d} \propto \langle g|\hat{\mathbf{x}}|e\rangle$ ), and the electric-field operator is

$$\mathbf{E} = i \sum_{\mathbf{k}, \lambda=1,2} \sqrt{\frac{2\pi\omega_{\mathbf{k}}}{V}} \mathbf{e}_{\lambda}(\mathbf{k}) (b_{\lambda}(\mathbf{k}) - b_{\lambda}^{\dagger}(\mathbf{k})). \quad (2.13)$$

Thus, the explicit expression for  $H_{SB}$  is

$$H_{SB} = -i\sigma^- \otimes \sum_{\mathbf{k}, \lambda=1,2} \sqrt{\frac{2\pi\omega_{\mathbf{k}}}{V}} \mathbf{d} \cdot \mathbf{e}_{\lambda}(\mathbf{k}) [b_{\lambda}(\mathbf{k}) - b_{\lambda}^{\dagger}(\mathbf{k})] + \text{h.c.} . \quad (2.14)$$

Note that  $\sigma^- (\sigma^+)$  is the annihilation (creation) operator for  $H_S$ , so in this case  $H_{SB}$  is already of the form in Eq. (2.6) with  $A(\omega) = \sigma^-$ ,  $A(-\omega) = \sigma^+$ .

For this specific setting, the dissipator of Eq. (2.9) becomes

$$\mathcal{D}(\rho_S) = \gamma(-\omega_0) [\sigma^+ \rho_S \sigma^- - \frac{1}{2} \{\sigma^- \sigma^+, \rho_S\}] + \gamma(\omega_0) [\sigma^- \rho_S \sigma^+ - \frac{1}{2} \{\sigma^+ \sigma^-, \rho_S\}], \quad (2.15)$$

where  $\gamma(\omega_0) = \text{im} \int_0^{\infty} ds e^{i\omega_0 s} \langle (\mathbf{d}^* \cdot \mathbf{E}(s)) (\mathbf{d} \cdot \mathbf{E}(0)) \rangle$ . Assume that the radiation field is in a thermal state with temperature  $\beta^{-1}$ . In this case we have

$$\begin{aligned} \langle b_{\lambda}(\mathbf{k}) b_{\lambda'}(\mathbf{k}') \rangle &= 0, & \langle b_{\lambda}^{\dagger}(\mathbf{k}) b_{\lambda'}^{\dagger}(\mathbf{k}') \rangle &= 0 \\ \langle b_{\lambda}^{\dagger}(\mathbf{k}) b_{\lambda'}(\mathbf{k}') \rangle &= \delta_{\mathbf{k}, \mathbf{k}'} \delta_{\lambda, \lambda'} n_{BE}(\omega_{\mathbf{k}}), & \langle b_{\lambda}(\mathbf{k}) b_{\lambda'}^{\dagger}(\mathbf{k}') \rangle &= \delta_{\mathbf{k}, \mathbf{k}'} \delta_{\lambda, \lambda'} (1 + n_{BE}(\omega_{\mathbf{k}})) \end{aligned}$$

where  $n_{BE}(\omega) = [\exp(\beta\omega) - 1]^{-1}$  is the Bose-Einstein distribution. With these correlation functions we obtain

$$\gamma(\omega_0) = \gamma_0(1 + n_{BE}(\omega_0)), \quad \gamma(-\omega_0) = \gamma_0 n_{BE}(\omega_0), \quad (2.16)$$

where  $\gamma_0 = 4\omega_0^3 |d|^2 / (3c^3)$ .

Thus the interaction of the two-level system with the thermal radiation field results in the following QME (transformed back to the Schrödinger picture)

$$\partial\rho(t) = -i[H, \rho] + \gamma_0[1 + n_{BE}(\omega_0)]\mathcal{D}_{\sigma^-}[\rho] + \gamma_0 n_{BE}(\omega_0)\mathcal{D}_{\sigma^+}[\rho]. \quad (2.17)$$

The first dissipator term corresponds to spontaneous emission, and it exists also in the  $T = 0$  case when there are no thermal photons around and  $n_{BE} = 0$ . The second dissipator term corresponds to an excitation of the atom due to photon absorption (hence it vanishes at  $T = 0$  since there are no photons to absorb). Note that in the absence of drive term in  $H$ , the steady state of Eq. (2.17) is a thermal state with the same temperature as the photon bath.

Finally let us comment on the validity of the Markov approximation in the quantum optics example. We obtained that the typical relaxation rate of the system is given by  $\tau_R = \gamma_0^{-1}$ . On the other hand the correlation time of the bath is given by the typical frequency  $\omega_0$ . Hence the Markov approximation is valid if  $\gamma_0 \ll \omega_0$ . This condition is usually valid in quantum optics where the typical inverse lifetimes are of order  $10^7 - 10^9 \text{s}^{-1}$  while optical frequencies are usually of order  $10^{15} \text{s}^{-1}$  [11].

## 2.2 KELDYSH PATH-INTEGRAL DESCRIPTION OF OPEN QUANTUM SYSTEMS

Our goal in this thesis is to study the properties of the steady-state solutions ( $\partial_t \rho = 0$ ) of the quantum master equation [Eq. (2.1)], for different types of systems. In this section we will introduce a mapping of the quantum master equation to a path-integral using the Keldysh formalism [17, 44], which allows us to study of open quantum systems using field-theory methods. This formulation of the problem is convenient for the development of approximation schemes and techniques, opening new lines of attack on the otherwise intractable problem of solving the QME for a generic many-body problem. In particular the field theoretic formulation allows us to borrow tools and knowledge that have been developed for many years in e.g. high-energy [45] or equilibrium condensed-matter physics [46], and adapt these ideas to the open system setting.

### 2.2.1 CONSTRUCTION OF THE PATH INTEGRAL

To derive the Keldysh path-integral description for Eq. (2.1) we follow the approach outlined in [17]. Our starting point is the partition-function

$$Z = \lim_{t \rightarrow \infty} \text{tr}[\rho(t)], \quad (2.18)$$

Where  $\rho(t)$  is obtained via time evolution according to Eq. (2.1), starting from some initial state  $\rho(t_0)$ . We can formally express the time evolution operator in terms of the Liouvillian

$$\rho(t) = \exp^{(t-t_0)\mathcal{L}} \rho(t_0). \quad (2.19)$$

Note that for the special case of a closed system, Eq. (2.19) reduces to the expression  $\rho(t) = U(t, t_0)\rho(t_0)U^\dagger(t, t_0)$ , where the unitary time evolution operator is given by  $U(t, t_0) = \mathcal{T}e^{-i \int_{t_0}^t dt H(t)}$

( $\mathcal{T}$  being the time ordering operator). The astute reader will notice that  $Z = 1$  due to the fact that time evolution generated by the Liouvillian is trace preserving and  $\text{tr}\rho(t_0) = 1$  for a physical state. Nevertheless, we will later show how  $Z$  allows us to obtain expectation values of observables with respect to the system steady-state by introducing source terms.

To obtain a path-integral we take a similar approach to that taken in equilibrium field-theory which is to expand the Liouvillian exponential in a first order Trotter decomposition

$$\exp(t\mathcal{L}) = (\mathbb{1} + \delta t\mathcal{L})^N + O(\delta t^2), \quad \delta t = \frac{t}{N}, \quad (2.20)$$

and express the evolution over each time step  $\delta t$  via a set of coherent-state fields. After doing so we will take the limit  $N \rightarrow \infty$  to obtain the path-integral. This is similar to the derivation of the path-integral for the case of pure-state evolution, but here we will have two sets of fields corresponding to the ket and bra states of the density-matrix.

We assume that the Hamiltonian and the Lindblad operators can be expressed in terms of a set of creation and annihilation operators  $\{a_i\}, \{a_i^\dagger\}$ . Here we will assume that  $a_i$  are bosonic operators, but the construction can be easily done also in the fermionic case. To lighten the notation, we will present the derivation in the case of a single degree of freedom with annihilation operator  $a$ . The derivation can then be trivially generalized to the case with many degrees of freedom by adding an extra index.

An important ingredient of the derivation is the set of coherent states  $\{|\psi\rangle\}_{\psi \in \mathbb{C}}$ , associated with the annihilation operator  $a$ . The coherent states obey  $a|\psi\rangle = \psi|\psi\rangle$  and  $\langle\psi|a^\dagger = \langle\psi|\psi^*$ . Furthermore they provide a resolution of the identity

$$\mathbb{1} = \frac{1}{\pi} \int d\psi d\psi^* e^{-\psi^*\psi} |\psi\rangle\langle\psi|. \quad (2.21)$$

Consider the evolution of  $\rho$  over one time step  $\delta t$ , this is given by

$$\rho(t_{n+1}) = \rho(t_n) + \delta t\mathcal{L}\rho(t_n), \quad (2.22)$$

where  $t_n = n\delta t$ . We express  $\rho(t_n)$  in terms of its coherent states matrix elements

$$\begin{aligned} \rho(t_n) &= \frac{1}{\pi^2} \int d\psi_{+,n} d\psi_{-,n} d\psi_{+,n}^* d\psi_{-,n}^* \\ &\times e^{-|\psi_{+,n}|^2 - |\psi_{-,n}|^2} \langle\psi_{+,n}|\rho(t_n)|\psi_{-,n}\rangle |\psi_{+,n}\rangle\langle\psi_{-,n}|. \end{aligned} \quad (2.23)$$

To obtain the matrix elements  $\langle\psi_{+,n+1}|\rho(t_{n+1})|\psi_{-,n+1}\rangle$  we plug Eq. (2.23) into Eq. (2.22). We need to evaluate matrix-elements for operators acting from the left, right and from both sides of  $\rho(t_n)$ . Assume all operators in the Liouvillian are brought to normal-ordered form and are polynomials of single-particle creation and annihilation operators, then

$$\begin{aligned} [\hat{O}_L\rho(t_n)\hat{O}_R]_{\psi_{+,n+1},\psi_{-,n+1}} &= \int_n e^{\delta t(\psi_{+,n}^* \partial_t \psi_{+,n}^* + \psi_{-,n}^* \partial_t \psi_{-,n})} \\ &\times O_L[\psi_{+,n+1}^*, \psi_{+,n}] O_R[\psi_{-,n}^*, \psi_{-,n+1}] \rho(t_n)_{\psi_{+,n}, \psi_{-,n}}, \end{aligned} \quad (2.24)$$

where we denoted  $\int_n \equiv \frac{1}{\pi^2} \int d\psi_{+,n} d\psi_{-,n} d\psi_{+,n}^* d\psi_{-,n}^*$ , the discretized derivative  $\partial_t \psi_{+,n}^* \equiv (\psi_{+,n+1}^* - \psi_{+,n}^*)/\delta t$  and  $O[\psi_i^*, \psi_j] = (\psi_i^*)^p (\psi_j)^q$  for  $\hat{O} = (a^\dagger)^p a^q$ .

Collecting all terms in Eq. (2.22) and re-exponentiating we obtain

$$\begin{aligned} \langle \psi_{+,n+1} | \rho_{t_{n+1}} | \psi_{-,n+1} \rangle &= \int_n e^{i\delta t (-\psi_{+,n} i\partial_t \psi_{+,n}^* - \psi_{-,n}^* i\partial_t \psi_{-,n} - \mathcal{L}[\psi_{+,n+1}^*, \psi_{+,n}, \psi_{-,n}^*, \psi_{-,n+1}])} \\ &\times \langle \psi_{+,n} | \rho(t_n) | \psi_{-,n} \rangle + O(\delta t^2). \end{aligned} \quad (2.25)$$

Applying the formula for one time step recursively, and then taking the limit  $N \rightarrow \infty$  we can obtain the expression for the partition function

$$Z = \int \mathcal{D}[\psi_+, \psi_+^*, \psi_-, \psi_-^*] e^{iS}, \quad (2.26)$$

where the path-integral measure is  $\mathcal{D}[\dots] = \lim_{N \rightarrow \infty} \prod_{n=0}^N \prod_{\sigma=\pm} \frac{d\psi_{\sigma,n}^* d\psi_{\sigma,n}}{\pi}$  and the action is given by  $S = S_c + S_d$

$$S_c = \int_{-\infty}^{\infty} dt \sum_{\sigma=\pm} \sigma (\psi_\sigma^* i\partial_t \psi_\sigma - H[\psi_\sigma^*, \psi_\sigma]), \quad (2.27)$$

$$S_d = -i \int_{-\infty}^{\infty} dt \sum_{\alpha} \gamma_{\alpha} \left[ L_{\alpha,+} L_{\alpha,-}^* - \frac{1}{2} (L_{\alpha,+}^* L_{\alpha,+} + L_{\alpha,-}^* L_{\alpha,-}) \right]. \quad (2.28)$$

We denoted  $L_{\alpha,\sigma} = L_{\alpha}[\psi_{\sigma}^*, \psi_{\sigma}]$ . Note that in principle we need to also include the matrix-element corresponding to the initial state  $\langle \psi_+(t_0) | \rho | \psi_-(t_0) \rangle$  in the integrand in Eq. (2.26). However, this can be neglected under the assumption that the system at  $t \rightarrow \infty$  has lost the memory of the initial state due to the dissipative nature of the open system dynamics leading to a steady-state fixed point.

### 2.2.2 CORRELATION FUNCTIONS

Having obtained  $Z$  we would now want to do something useful with it, since as we have seen  $Z = 1$ , so at the moment Eq. 11 seems like a very complicated way to write 1. The key point is to notice that, on the one hand, we can repeat the construction above for the case of  $\langle O \rangle = \text{tr}(O\rho)$ . This leads to a connection between expectation values in the operatorial form and correlation functions of fields computed using the action  $S$

$$\begin{aligned} \text{tr} \hat{o}_n(t_n) \dots \hat{o}_1(t_1) \rho &= \int \mathcal{D}[\psi_+^*, \psi_+, \psi_-^*, \psi_-] \hat{o}_{n,+}(t_n) \dots \hat{o}_{1,+}(t_1) e^{iS} \equiv \langle o_{n,+}(t_n) \dots o_{1,+}(t_1) \rangle, \\ \text{tr} \rho \hat{o}_1(t_1) \dots \hat{o}_n(t_n) &= \int \mathcal{D}[\psi_+^*, \psi_+, \psi_-^*, \psi_-] \hat{o}_{n,-}(t_n) \dots \hat{o}_{1,-}(t_1) e^{iS} \equiv \langle o_{n,-}(t_n) \dots o_{1,-}(t_1) \rangle. \end{aligned}$$

where we assumed  $t_n > t_{n-1} > \dots > t_1$  and that all times are already in the steady-state regime. We see that correlation function of the  $+$  ( $-$ ) fields are related to (anti-) time-ordered expectation

## 2 Background: Quantum open systems

values of operators. On the other hand, note that we can obtain correlation functions of the fields by adding sources  $J_\sigma = (j_\sigma, j_\sigma^*)$  to the action

$$Z[J_+, J_-] \equiv \int \mathcal{D}[\psi_+^*, \psi_+, \psi_-^*, \psi_-] e^{iS + i \int \Sigma_\sigma (j_\sigma^* \psi_\sigma + c.c.)}, \quad (2.29)$$

such that derivatives of  $Z$  with respect to the sources generate correlation functions. For example, the two-point correlation functions are given by

$$-\left. \frac{\delta^{(2)} Z}{\delta j_\sigma^*(t) \delta j_{\sigma'}(t')} \right|_{J_+ = J_- = 0} = \langle \psi_{\sigma'}^*(t') \psi_\sigma(t) \rangle. \quad (2.30)$$

A convenient representation for analysing the properties of the action  $S$  is obtained by introducing the classical and quantum fields

$$\psi_c \equiv \frac{1}{\sqrt{2}}(\psi_+ + \psi_-), \quad \psi_q \equiv \frac{1}{\sqrt{2}}(\psi_+ - \psi_-). \quad (2.31)$$

The c/q basis is especially convenient for the analysis of the two-point correlation functions, also known as the Green's functions. In the non-equilibrium context there are three types of Green's functions- retarded ( $G^R$ ), advanced ( $G^A$ ) and Keldysh ( $G^K$ ), which are defined as [44]

$$iG^R(t, t') = \theta(t - t') \langle [\hat{\psi}(t), \hat{\psi}^\dagger(t')] \rangle = \langle \psi_c(t) \psi_q^*(t') \rangle, \quad (2.32a)$$

$$iG^A(t, t') = -\theta(t' - t) \langle [\hat{\psi}(t), \hat{\psi}^\dagger(t')] \rangle = \langle \psi_q(t) \psi_c^*(t') \rangle, \quad (2.32b)$$

$$iG^K(t, t') = \langle \{\hat{\psi}(t), \hat{\psi}^\dagger(t')\} \rangle = \langle \psi_c(t) \psi_c^*(t') \rangle, \quad (2.32c)$$

where we suppressed other field indices, such as position or momentum, in the expressions above. The physical interpretation of the different Green's functions will become clear in the next section.

### 2.2.3 EXAMPLE: FREE BOSONS WITH SINGLE-PARTICLE PUMP AND LOSS

To discuss several important properties of the Green's functions and the Keldysh action let us consider a concrete toy model of non-interacting bosons subject to incoherent single-particle loss and pump. This system is described by the following QME

$$\partial_t \rho = -i[H, \rho] + 2\gamma_p \int_{\mathbf{x}} \mathcal{D}_{\psi^\dagger(\mathbf{x})}[\rho] + 2\gamma_l \int_{\mathbf{x}} \mathcal{D}_{\psi(\mathbf{x})}[\rho], \quad H = \int_{\mathbf{x}} \psi^\dagger(\mathbf{x}) (-\nabla^2) \psi(\mathbf{x}),$$



where  $\int_{\mathbf{x}} \equiv \int d^d x$ , and we have rescaled the dissipation rates in order to avoid carrying factors of  $1/2$  around. Mapping to the Keldysh path-integral we obtain the following quadratic action (in Fourier space)

$$S = \int_{\omega, \mathbf{k}} (\psi_c^*(\omega, \mathbf{k}), \psi_q^*(\omega, \mathbf{k})) \begin{pmatrix} 0 & P^A \\ P^R & P^K \end{pmatrix} \begin{pmatrix} \psi_c(\omega, \mathbf{k}) \\ \psi_q(\omega, \mathbf{k}) \end{pmatrix}, \quad (2.33)$$

$$P^R = \omega - k^2 + i(\gamma_l - \gamma_p), \quad P^A = (P^R)^*, \quad P^K = 2i(\gamma_p - \gamma_l), \quad (2.34)$$

where  $\int_{\omega, \mathbf{k}} \equiv (2\pi)^{-(d+1)} \int d\omega \int d^d k$ . The structure of the action in Eq. (2.33) is the usual structure of the quadratic part of the Keldysh action. Importantly note that the fact that no  $\psi_c^* \psi_c$  term exists is an exact property of the Keldysh action, which will be preserved also when the action is renormalized due to interactions. This can be traced to the fact that the time evolution generated by the Liouvillian is trace preserving (probability preserving), which leads to the more general constraint on the Keldysh action  $S[\psi_c, \psi_c^*, \psi_q = 0, \psi_q^* = 0] = 0$  [17].

Adding sources to the action and using Eq. (2.30) we can obtain the Green's functions

$$G^R = (P^R)^{-1} = \frac{1}{\omega - k^2 + i\tilde{\gamma}}, \quad G^K = -G^R P^K G^A = \frac{2i\tilde{\gamma}}{(\omega - k^2) + \tilde{\gamma}^2}, \quad (2.35)$$

where we denoted  $\tilde{\gamma} = \gamma_l - \gamma_p$ . Let us assume for the moment that  $\gamma_l > \gamma_p$  such that  $\tilde{\gamma} > 0$  (the reason for this will become clear shortly).

Considering  $G^R(G^A)$  as a function of a complex frequency, we see it is analytic in the upper(lower) half of the complex plane. This observation is not limited to our simple toy model but is again a general property of the Keldysh action. To see why it must be so, first we start with a simple mathematical argument. In the time-domain  $G^R(t) \propto \theta(t)$ , hence for any point  $\omega^* \in \mathbb{C}^+$  the contour integral  $\oint_{\omega \in C} G^R(\omega)$ , around the contour  $\omega(\theta) = re^{i\theta} + \omega^*$ , is vanishing as  $r \rightarrow 0$

$$\left| \oint_{\omega \in C} G^R(\omega) \right| \leq r \int d\theta \int_0^\infty dt e^{-\text{Im}\omega^* t} |G^R(t)| \xrightarrow{r \rightarrow 0} 0. \quad (2.36)$$

This implies that there could be no pole of  $G^R(\omega)$  at any  $\omega^* \in \mathbb{C}^+$ .

To understand the physical meaning of  $G^R$ , consider coupling the system a weak classical external source with some frequency and momentum pattern (i.e.  $j(\omega, \mathbf{k}) = e^{i(\omega t - \mathbf{k} \cdot \mathbf{x})} j_0$ ). This leads to an addition of a drive term to the Hamiltonian  $H \rightarrow H + [j(\omega, \mathbf{k}) \hat{\psi}^\dagger(\mathbf{k}) + h.c.]$ . The source acts as a coherent particle pump, leading to a finite expectation value  $\langle \hat{\psi}(\omega, \mathbf{k}) \rangle = \langle \psi_c(\omega, \mathbf{k}) \rangle$ . The response of  $\langle \psi_c(\mathbf{k}) \rangle$  to an infinitesimal field is given by

$$\left. \frac{\delta \langle \psi_c(\omega, \mathbf{k}) \rangle}{\delta j_c^*(\omega, \mathbf{k})} \right|_{j_c=0} = - \left. \frac{\delta^{(2)} Z}{\delta j_c^*(\omega, \mathbf{k}) \delta j_q(\omega, \mathbf{k})} \right|_{j_c, j_q=0} = iG^R(\omega, \mathbf{k}). \quad (2.37)$$

Now assume we apply a weak field  $j(t_0, \mathbf{k}) = \int_{\omega} e^{-i\omega t_0} j(\omega, \mathbf{k})$  localized at time  $t = t_0$ . From Eq. (2.37) we can conclude that at time  $t > t_0$

$$\langle \psi_c(t, \mathbf{k}) \rangle - \langle \psi_c(t, \mathbf{k}) \rangle_0 = \int_{\omega} e^{-i\omega t} \langle \psi_c(\omega, \mathbf{k}) \rangle = j(k^2, \mathbf{k}) e^{-\tilde{\gamma}(t-t_0)} e^{-ik^2(t-t_0)}. \quad (2.38)$$

From this we see the physical meaning of the analyticity properties of  $G^R$  which guarantee that fluctuations generated due to weak perturbations are exponentially decaying with time. Requiring  $\tilde{\gamma} > 0$  guarantees stability of the steady-state value  $\langle \hat{\psi} \rangle = 0$  against arbitrary weak perturbations. Of course, we might want to consider a, physically relevant, situation where  $\gamma_p > \gamma_l$  and thus  $\tilde{\gamma} < 0$ . In order to discuss the instability of the system in this case, as we will do shortly, we will have to take interactions into account.

From the discussion above we see that the poles of  $G^R$  occur at a natural excitation frequencies of the system where the response to a weak external field will be strongest. The real part of the pole frequency is the excitation energy while the imaginary part  $\tilde{\gamma}$  is the decay rate. More generally, we can define the spectral function which encodes the spectral properties of the system, via the relation [46]

$$\mathcal{A}(\omega, \mathbf{k}) = -2\text{Im}G^R(\omega, \mathbf{k}). \quad (2.39)$$

In our simple, non-interacting, case we the spectral function has a Lorentzian form

$$\mathcal{A}(\omega, \mathbf{k}) = \frac{2\tilde{\gamma}}{(\omega - k^2)^2 + \tilde{\gamma}^2}, \quad (2.40)$$

which becomes a delta peak in the limit  $\tilde{\gamma} \rightarrow 0^-$ . For generic interacting systems we expect branch cuts to emerge in  $G^R(\omega, \mathbf{k})$  which represent a continuum of excitations as opposed to the isolated Lorentzian structure.

We turn now to the Keldysh Green's function. From Eq. (2.32c) we can see that, at equal times,

$$G^K(t, t; \mathbf{k}) = 1 + 2\langle \hat{\psi}^\dagger(t, \mathbf{k})\hat{\psi}(t, \mathbf{k}) \rangle. \quad (2.41)$$

For a time translation invariant steady-state we can obtain the occupation function of momentum states via

$$n_{\mathbf{k}} = \frac{1}{2} \left( i \int_{\omega} G^K(\omega, \mathbf{k}) - 1 \right). \quad (2.42)$$

Hence, we see that  $G^K$  encodes information about the statistical occupation of the available states. For our specific example we obtain

$$n_{\mathbf{k}} = \frac{\gamma_p}{\gamma_l - \gamma_p}. \quad (2.43)$$

We note that in our example all momentum modes are equally occupied, which makes sense as the Markovian pump and loss do not depend on energy or momentum. Of course this cannot be the case in a real physical system. This pathological behavior can be cured by a momentum cutoff (assuming the pump is ineffective at high momenta) and by the inclusion of interaction effects which will renormalize the pump and loss rate and induce a momentum dependence. Also note that when  $\gamma_l = \gamma_p$  we have a divergence of  $n_{\mathbf{k}}$  which is related to the instability we encounter in  $G^R$  in this case.

More generally, the Keldysh Green's function can be parametrized, for a scalar field, as

$$G^K(\omega, \mathbf{k}) = F(\omega, \mathbf{k})(G^R(\omega, \mathbf{k}) - G^A(\omega, \mathbf{k})) = -iF(\omega, \mathbf{k})\mathcal{A}(\omega, \mathbf{k}), \quad (2.44)$$

$$F(\omega, \mathbf{k}) \equiv 1 + 2n(\omega, \mathbf{k}). \quad (2.45)$$

Here  $n(\omega, \mathbf{k})$  can be interpreted as an occupation function since Eq. (2.44) together with Eq. (2.42) implies that  $n_{\mathbf{k}} = \int_{\omega} n(\omega, \mathbf{k}) \mathcal{A}(\omega, \mathbf{k})$ . In our example we have

$$F(\omega, \mathbf{k}) = \frac{\gamma_l + \gamma_p}{\gamma_l - \gamma_p}. \quad (2.46)$$

In equilibrium the occupation function is given by the Bose-Einstein distribution and  $1 + 2n(\omega, \mathbf{k}) = \coth(\omega/2T)$ . This implies that in the equilibrium the Keldysh and retarded Green's function are not independent

$$G^K = \coth\left(\frac{\omega}{2T}\right) 2i \text{Im} G^R(\omega, \mathbf{k}). \quad (2.47)$$

This is a manifestation of the fluctuation-dissipation theorem [46], and it is the reason why in equilibrium field-theory we only need one Green's function in order to describe the system. Eq. (2.47) does not hold in a general non-equilibrium setting, however it can be sometime used to define an effective temperature by a fit to the low frequency behavior of the ratio  $\text{Im}[G^K(\omega, \mathbf{k})/G^R(\omega, \mathbf{k})]$  (see e.g. [47, 48]). It can also happen that an effective temperature emerges at long wavelengths in the vicinity of a critical point, as was shown in a renormalization-group (RG) study of the interacting version of our example system in Ref. [18].

#### CONDENSATION INSTABILITY AT $\gamma_p = \gamma_l$

We now turn to discuss the instability we encountered when  $\gamma_p = \gamma_l$ . In order to consider this case we must add interactions and two-body loss processes to our model which means we can no longer obtain the exact Green's functions. Here we will be satisfied with a simple mean-field analysis. For a full RG study of the interacting model see Ref. [18].

The interaction Hamiltonian we consider is given by  $H_{\text{int}} = \frac{u}{2} \int_{\mathbf{x}} \hat{\psi}^\dagger(\mathbf{x}) \hat{\psi}^\dagger(\mathbf{x}) \hat{\psi}(\mathbf{x}) \hat{\psi}(\mathbf{x})$ , in addition we consider a two-body loss process described by a dissipator term  $\Gamma \int_{\mathbf{x}} \mathcal{D}_{\hat{\psi}(\mathbf{x}) \hat{\psi}(\mathbf{x})}$ . This two additions result in the following interaction action

$$S_{\text{int}} = - \int_{t, \mathbf{x}} \left\{ \frac{u + i\Gamma}{2} [(\psi_c^*)^2 + (\psi_q^*)^2] \psi_q \psi_c + c.c. - 2i\Gamma |\psi_q|^2 |\psi_c|^2 \right\}. \quad (2.48)$$

We have seen that having  $\gamma_p > \gamma_l$  signals an instability of  $\langle \psi_c \rangle$  (which is vanishing for  $\gamma_l < \gamma_p$ ) towards infinitesimal fluctuations. We can obtain an approximation to the value of  $\langle \psi_c \rangle$  in the steady-state using the saddle-point approximation where we assume an homogeneous value and neglect all effects of classical and quantum fluctuations. The expectation values of both  $\psi_c, \psi_q$  are obtained as a solution of

$$\frac{\delta S}{\delta \psi_c^*} = 0, \quad \frac{\delta S}{\delta \psi_q^*} = 0. \quad (2.49)$$

First note that the condition  $S[\psi_c, \psi_q = 0]$  implies that the first equation is identically zero when  $\psi_q = 0$ . Since  $\langle \psi_q \rangle = 0$  must hold by construction in the Keldysh formalism, we only

## 2 Background: Quantum open systems

need to consider the second equation evaluated at  $\psi_q = 0$ . We consider a solution of the form  $\psi_c(t, \mathbf{x}) = e^{i\mu t}\psi_c$ , we obtain

$$[i(\tilde{\gamma} + \frac{\Gamma}{2}|\psi_c|^2) + \mu - \frac{u}{2}|\psi_c|^2]\psi_c = 0. \quad (2.50)$$

For  $\tilde{\gamma} > 0$  Eq. (2.50) has only a trivial solution  $\psi_c = 0$ . However when  $\tilde{\gamma} < 0$  we get another solution

$$|\psi_c|^2 = -\frac{2\tilde{\gamma}}{\Gamma} = \rho_0, \quad (2.51)$$

with  $\mu = u/2|\psi_c|^2$ . We see that the regime of instability of the steady-state with  $\langle\psi_c\rangle = 0$  we saw in the previous section coincides with the regime where steady-state with a finite condensate value  $\langle\psi_c\rangle \neq 0$  exists.

To see that the condensate solution is stable, we can expand the action in fluctuations around the condensate value  $\psi_c = \sqrt{\rho_0} + \delta\psi_c$ ,  $\psi_q = \delta\psi_q$ . Since the presence of a finite condensate generates terms of the form  $\delta\psi_c^*\delta\psi_q^*$  it is convenient to introduce a Nambu spinor  $\delta\Psi_\alpha^T = (\delta\psi_\alpha(\omega, \mathbf{k}), \delta\psi_\alpha^*(-\omega, -\mathbf{k}))$  for  $\alpha = c, q$ . We obtain the action

$$S_{\text{fluc}} = \frac{1}{2} \int_{\omega, \mathbf{k}} (\delta\Psi_c^\dagger \quad \delta\Psi_q^\dagger) \begin{pmatrix} 0 & \mathcal{P}^A \\ \mathcal{P}^R & \mathcal{P}^K \end{pmatrix} \begin{pmatrix} \delta\Psi_c \\ \delta\Psi_q \end{pmatrix}, \quad (2.52)$$

with the inverse retarded function given by

$$\mathcal{P}^R(\omega, \mathbf{k}) = \begin{pmatrix} \omega - k^2 + (i\Gamma - u)\rho_0/2 & (-u - i\Gamma)\rho_0/2 \\ (-u + i\Gamma)\rho_0/2 & -\omega - k^2 - (i\Gamma + u)\rho_0/2 \end{pmatrix}, \quad (2.53)$$

where we used the fact that  $\tilde{\gamma} = -\frac{\Gamma}{2}\rho_0$  and  $\mu = u/2\rho_0$ .

The poles of  $G^R$ , and consequently the excitation spectrum of the system, can be obtained by a solution of  $\det(\mathcal{P}^R(\omega, \mathbf{k})) = 0$  which leads us to

$$\omega_\pm^R(\mathbf{k}) = -i\frac{\Gamma}{2}\rho_0 \pm \sqrt{k^2(k^2 + u\rho_0) - \Gamma^2\rho_0^2/4}. \quad (2.54)$$

We thus see that due to the non-linearity induced by the two-particle loss can stabilize a condensate solution, since  $\text{Im}\omega_\pm^R(\mathbf{k}) \geq 0$ . At small momentum we have  $\omega_+^R(\mathbf{k}) \approx -i2uk^2/\Gamma$ , which indicates the existence of a dissipative gapless Goldstone mode. This is related the breaking of the  $U(1)$  symmetry,  $\psi_\alpha \rightarrow e^{i\theta}\psi_\alpha$ , of the action in the condensate phase [18].

### 2.2.4 EFFECTIVE ACTION FORMALISM

In this section we describe the effective-action formalism which is one useful formulation of the many-body problem, especially when condensation phenomena is considered [17, 49, 50]. Consider a field-theory with a set of fields  $\Phi = (\phi_1, \dots, \phi_n)$ , where the index  $i = 1, \dots, n$  can be discrete or continuous (e.g. position, momentum, different species)<sup>4</sup>. The Keldysh effective-action  $\Gamma$  is a

<sup>4</sup>To lighten the notation we assume that we work with real fields here, but the derivation in the case of complex fields is equivalent.

functional of the fields expectation values  $\bar{\phi}_i \equiv \langle \phi_i \rangle$  such that the physical steady-state value of  $\bar{\Phi}$  is given by a stationary-point of the functional  $\Gamma[\bar{\Phi}]$ .

Given an action  $S$  we can define the generating functional of connected correlation functions  $W$  by coupling the fields to external sources

$$W[J_c, J_q] = -i \log Z[J_c, J_q], \quad (2.55)$$

$$Z[J_c, J_q] = \int \mathcal{D}[\Phi] e^{iS + i \int (J_q^T \Phi_c + J_c^T \Phi_q)} = \left\langle e^{i \int (J_q^T \Phi_c + J_c^T \Phi_q)} \right\rangle. \quad (2.56)$$

Here we collected (different Keldysh components of) the fields and sources into vectors  $J_\alpha^T = (j_{\alpha,1}, \dots, j_{\alpha,n})$ , and  $\Phi_\alpha^T = (\phi_{\alpha,1}, \dots, \phi_{\alpha,n})$ , and we denoted  $\Phi = (\Phi_c, \Phi_q)$ .  $W$  is a functional of the sources  $J_q, J_c$ , and derivatives of  $W$  with respect to the sources generate connected correlation functions:

$$\left. \frac{\delta^{(n)} W}{\delta j_{\alpha_1, i_1} \dots \delta j_{\alpha_n, i_n}} \right|_{J_q, J_c=0} = (-i)^{(n+1)} \left\langle \phi_{\alpha'_1, i_1} \dots \phi_{\alpha'_n, i_n} \right\rangle_{\text{connected}}, \quad (2.57)$$

where we introduced the notation  $c' = q, q' = c$  for the Keldysh index.

We now want to obtain an object which is a functional of the field expectation values, this is done by means of a Legendre transform

$$\Gamma[\bar{\Phi}_c, \bar{\Phi}_q] = W[J_c, J_q] - \int (J_c^T \bar{\Phi}_q + J_q^T \bar{\Phi}_c), \quad (2.58)$$

$$\frac{\delta \Gamma}{\delta \bar{\Phi}_c} = -J_q, \quad \frac{\delta \Gamma}{\delta \bar{\Phi}_q} = -J_c. \quad (2.59)$$

From Eq. (2.59) we see that in the absence of external sources  $J_c, J_q = 0$ , the field expectation values are given by the stationary point of  $\Gamma$ , that is

$$\frac{\delta \Gamma}{\delta \bar{\Phi}_\alpha} = 0. \quad (2.60)$$

At a first glance Eq. (2.60) looks similar to the classical equations of motion (EOM) obtained by looking for the stationary point of the bare action  $S$ . However, unlike the classical EOM, Eq. (2.60) is exact and includes the effects of all statistical and quantum fluctuations in determining  $\bar{\Phi}$ . The field-equation is exact only when an exact expression for  $\Gamma$  is available, which is generically not the case for interacting theories. However, by introducing approximations to  $\Gamma$ , Eq. (2.60) allows us to include beyond mean-field corrections in a systematic way.

## 2 Background: Quantum open systems

From the second variation of  $\Gamma$  we can obtain the full Green's functions of the theory, which as we have seen encode the stability properties of steady-states of the open system. To see this note that Eq. (2.59) implies

$$\begin{aligned} -\delta_{\alpha\beta}\delta_{ij} &= \frac{\delta}{\delta j_{\alpha',i}} \frac{\delta\Gamma}{\delta\bar{\phi}_{\beta,j}} = \sum_{\gamma,m} \frac{\delta\bar{\phi}_{\gamma,m}}{\delta j_{\alpha',i}} \frac{\delta\Gamma}{\delta\bar{\phi}_{\gamma,m}\delta\bar{\phi}_{\beta,j}} \\ &= i \sum_{\gamma,m} \frac{\delta^{(2)}W}{\delta j_{\alpha',i}\delta j_{\gamma',m}} \frac{\delta^{(2)}\Gamma}{\delta\bar{\phi}_{\gamma,m}\delta\bar{\phi}_{\beta,j}} = - \sum_{\gamma,m} G_{\alpha\gamma}(i,m) \Gamma_{\gamma\beta}^{(2)}(m,j), \end{aligned}$$

where we denoted  $\Gamma_{\gamma\beta}^{(2)}(m,j) \equiv \frac{\delta^{(2)}\Gamma}{\delta\bar{\phi}_{\gamma,m}\delta\bar{\phi}_{\beta,j}}$ . Hence we see that the second variation of  $\Gamma$  is the inverse connected Green's functions

$$\Gamma_{\alpha\beta}^{(2)}(i,j) = G_{\alpha\beta}^{-1}(i,j). \quad (2.61)$$

It can be shown that higher derivatives of  $\Gamma$  generate the 1PI vertex functions, also known as 1PI amputated correlation functions [45, 51]. A 1PI correlation function is defined as a correlation function whose representation in terms of sum of Feynman diagrams contains only 1PI diagrams. A 1PI diagram is a diagram which cannot be disconnected into two parts by cutting one propagator line. An amputated correlation function, or vertex function, is obtained from a connected correlation function by removing propagator factors corresponding to external legs in a diagrammatic representation. The 1PI vertex functions contain all renormalization effects, since the connected correlation functions can be computed from tree-level diagrams (without loops) composed out of the 1PI vertices and the full propagator.

A simple approximation which is often used is the one-loop approximation, which amounts to expanding  $S[\bar{\Phi} + \delta\Phi]$  in Gaussian fluctuations around  $\bar{\Phi}$ . This results in

$$\Gamma[\bar{\Phi}] = S[\bar{\Phi}] + i \text{tr} \log S^{(2)}[\bar{\Phi}], \quad (2.62)$$

with  $S_{\alpha\beta}^{(2)} \equiv \delta^{(2)}S/\delta\Phi_{\alpha}\delta\Phi_{\beta}$  and the trace running over frequency, momentum, Keldysh and any other indices of the fields. The first term in the RHS of Eq. (2.62) is the bare action evaluated at the stationary value  $\bar{\Phi}$ , keeping only this term is equivalent to the saddle-point approximation of the bare action  $S$ . The second term contains the contributions to the effective action due to quadratic quantum and statistical fluctuations around the condensate value.

A more explicit expression for the 1-loop contribution in Eq. (2.62) can be obtained by decomposing  $S^{(2)}[\bar{\Phi}] = G_0^{-1} + V[\bar{\Phi}]$ , where  $G_0^{-1}$  is the bare Green's function arising from the quadratic part of  $S$ . With this decomposition we can expand

$$\text{tr} \log S^{(2)}[\bar{\Phi}] = \text{tr} \log G_0^{-1} - \sum_{n=1}^{\infty} \frac{(-1)^n}{n} \text{tr}[(G_0 V[\bar{\Phi}])^n]. \quad (2.63)$$

Note that the term  $\text{tr}[(G_0 V)^n]$  is of order  $n$  in the interaction couplings, and is at least of order  $n$  in the condensate value  $\bar{\Phi}$ . It is also convenient to represent the different terms in Eq. (2.63) as Feynman diagrams with external lines representing the condensate fields (coming from the  $V$

terms) and inner lines representing the bare propagators  $G_0$ . The RHS of Eq. (2.63) generates all 1PI one-loop diagrams. Taking derivatives of Eq. (2.62) we can obtain the field equations at the 1-loop level

$$\frac{\delta\Gamma}{\delta\bar{\Phi}} = i\text{tr}(G_0^{-1} + V[\bar{\Phi}])^{-1}\partial_{\bar{\Phi}}V[\bar{\Phi}] = 0. \quad (2.64)$$

## 2.3 EXPERIMENTAL PLATFORMS

The work in this thesis deals largely with understanding different phenomena which can occur in open quantum systems using simplified theoretical models which are not strongly tied to a specific experimental implementation. It is nevertheless important to at least have some examples in mind of the type of systems we will be thinking about. For this end we provide a brief review of several relevant experimental platforms whose dynamics can be well described by the QME Eq. (2.1).

### 2.3.1 ULTRACOLD ATOMS IN OPTICAL LATTICES

In the last two decades systems of ultracold gases trapped in optical lattices have emerged as one of the leading platforms for quantum-simulation of many-body physics [1]. This success has been facilitated by the ability to control the interaction strength in those systems using Feshbach resonances [52], allowing to investigate strongly correlated regimes even at low densities, and the ability to create optical potentials in different dimensionalities allowing the exploration of low-dimensional quantum systems. Another important recent development is the realization of quantum-gas microscopes enabling detection of individual atoms at a single-site resolution [53].

Some experimental results obtained with ultracold atoms in optical lattices include: the realization of the Bose-Hubbard model and the observation of the Mott-superfluid phase transition [54]; measurements of charge and spin correlations in the Fermi-Hubbard model in one and two dimensions [55, 56]; and investigation of spin transport in the strongly correlated Mott regime of the Fermi-Hubbard model [57].

In addition, ultracold atoms play an important role in the investigation of non-equilibrium dynamics after a quantum quench and the questions regarding thermalization of closed quantum systems [24]. For example, the first experimental evidence for many-body localization has been observed using ultracold fermions trapped in a quasi-periodic potential in 1D [58] (see chapter 4 for more details on many-body localization).

Ultracold atoms are considered to be quite well isolated from their environment, as compared to solid-state systems where phonons are always present. However, there still exist sources of dissipation, due to photon scattering, which need to be taken into account when describing experiments. In the rest of this section we briefly describe two origins of dissipation in those systems, dephasing noise where the Lindblad operator is hermitian  $L_i = n_i$  and particle loss where  $L_i = a_i$ . We mainly follow here the discussion in Ref. [13], which can be consulted for further details.

At the microscopic level the Hamiltonian can be described as:

$$\hat{H}_{\text{atoms}} = \int_{\mathbf{x}} \hat{\psi}^\dagger(\mathbf{x}) \left[ \frac{\hbar^2}{2m} \nabla^2 + V_{\text{opt}}(\mathbf{x}) \right] \hat{\psi}(\mathbf{x}) + \frac{u}{2} \int_{\mathbf{x}} (\hat{\psi}^\dagger(\mathbf{x}))^2 \hat{\psi}^2(\mathbf{x}), \quad (2.65)$$

where  $\psi(\mathbf{x})$  is the annihilation operator of atom at position  $\mathbf{x}$ , and  $V_{\text{opt}}(\mathbf{x})$  is the optical lattice potential, and we introduced the notation  $\int_{\mathbf{x}} \equiv \int d^3x$ . In the low-energy limit the effects of the complicated atom-atom interaction potential  $U(\mathbf{x})$  can be effectively captured in the point approximation as  $u\delta(\mathbf{x})$  with  $u = 4\pi\hbar^2 a/m$  and  $a$  the S-wave scattering length [1] (for more details see chapter 3).

The optical lattice potential is generated by the interference of two counter-propagating laser beams resulting in a standing wave pattern. The origin of the optical potential as well as dissipation in the system can be understood by considering atoms with two relevant internal levels moving in the presence of an external classical electric field as done in Ref. [59]. The atomic Hamiltonian is given by

$$H_{\text{atom}} = \int_{\mathbf{x}} \left\{ \sum_{\alpha=g,e} \hat{\psi}_{\alpha}^{\dagger}(\mathbf{x}) \left[ -\frac{\nabla^2}{2m} + \Delta\delta_{\alpha e} \right] \hat{\psi}_{\alpha}(\mathbf{x}) - \left[ \frac{\Omega(\mathbf{x})}{2} \hat{\psi}_e^{\dagger}(\mathbf{x}) \hat{\psi}_g(\mathbf{x}) + h.c. \right] \right\}. \quad (2.66)$$

Here we are working in a rotating frame, rotating with the laser frequency  $\omega_L$ .  $\Delta = \omega_L - \omega_0$  is the detuning of the laser frequency and  $\Omega(\mathbf{x})$  is the spatially dependent Rabi frequency which is obtained from the dipole term  $-\mathbf{d} \cdot \mathbf{E}$  in the rotating wave approximation. In addition, spontaneous emission from the excited state can be described with a dissipator term [59]

$$\Gamma \int_{\mathbf{x}} \int d^2\mathbf{u} N(\mathbf{u}) \mathcal{D}_{C_{\mathbf{u}}(\mathbf{x})}[\rho], \quad C_{\mathbf{u}}(\mathbf{x}) = e^{-ik_0\mathbf{u} \cdot \hat{\mathbf{x}}} \hat{\psi}_g^{\dagger}(\mathbf{x}) \hat{\psi}_e(\mathbf{x}), \quad (2.67)$$

where  $k_0 = \omega_0/c$  is the momentum associated with the internal transition, and  $N(\mathbf{u}) \propto (1 - (\mathbf{u} \cdot \mathbf{d})^2)$  is the distribution of emitted photon directions which depends on the atom dipole moment.

In the limit of large detuning  $|\Delta| \gg \Omega, \Gamma$  we can adiabatically eliminate the excited state from the master equation and derive an effective equation for  $\rho_{gg}(\mathbf{x}, \mathbf{x}')$  alone. In [59] this was done using the optical Bloch equations, here we will show how to do this in the Keldysh technique. For simplicity we approximate the dissipator in Eq. (2.67) to be  $\Gamma \mathcal{D}_{\hat{\psi}_{\dagger}}$ , for a full treatment see Ref. [59]. The Keldysh action is given by  $S = S_g + S_e + S_{eg}$  where:

$$\begin{aligned} S_e &= -\Delta \int_{t,\mathbf{x}} [|\psi_{e,+}(t, \mathbf{x})|^2 - |\psi_{e,-}(t, \mathbf{x})|^2], \\ S_{eg} &= - \int_{t,\mathbf{x}} \sum_{\sigma=\pm} \sigma \left[ \frac{\Omega(\mathbf{x})}{2} \psi_{e,\sigma}^*(t, \mathbf{x}) \psi_{g,\sigma}(t, \mathbf{x}) + c.c. \right], \\ &\quad - i\Gamma \int_{t,\mathbf{x}} [\psi_{g,+}^* \psi_{e,+} \psi_{g,-} \psi_{e,-}^* - \frac{1}{2} (|\psi_{g,+}|^2 |\psi_{e,+}|^2 + |\psi_{g,-}|^2 |\psi_{e,-}|^2)], \end{aligned} \quad (2.68)$$

where for notational compactness we suppressed the time and space dependence of the fields in the quartic term. Here we neglected the dynamics of the atoms in the excited state as compared to the detuning scale  $|\Delta|$ . With this approximation we can integrate out the excited state, which is



equivalent to replacing  $\psi_{e,\sigma}$  with its saddle-point value given by the classical equations of motion  $\delta S / \delta \psi_{e,\sigma}^* = 0$ . From the equations of motion we obtain

$$\psi_{e,\sigma}(t, \mathbf{x}) \approx \frac{\Omega(\mathbf{x})}{2\Delta} \psi_{g,\sigma}(t, \mathbf{x}). \quad (2.69)$$

Physically we assumed that the dynamics related to the excited state population are much faster compared to external dynamics of ground state atoms. We work in an approximation where the excited state population instantaneously adjusts to changes in the ground state density, as can be seen from Eq. (2.69).

Plugging Eq. (2.69) in Eq. (2.68) we obtain the optical potential and the effective dissipation for the atoms in the ground state:

$$S_o = - \int_{t,\mathbf{x}} \sum_{\sigma} \sigma \frac{|\Omega(\mathbf{x})|^2}{4\Delta} |\psi_{g,\sigma}(t, \mathbf{x})|^2, \quad (2.70)$$

$$S_d = -i \int_{t,\mathbf{x}} \frac{\Gamma |\Omega(\mathbf{x})|^2}{4\Delta^2} [|\psi_{g,+}|^2 |\psi_{g,-}|^2 - \frac{1}{2} (|\psi_{g,+}|^4 + |\psi_{g,-}|^4)]. \quad (2.71)$$

The continuum QME we obtained can be mapped to a tight-binding model using Wannier wave-functions localized around the different minima of the optical potential. Working in an approximation where only the lowest Wannier band is populated  $\hat{\psi}(\mathbf{x}) \approx \sum_i w(\mathbf{x} - \mathbf{X}_i) \hat{b}_i$  one obtains the following lattice QME

$$\partial_t \rho = -i[H, \rho] + \gamma \sum_i [n_i \rho n_i - \frac{1}{2} \{n_i^2, \rho\}]. \quad (2.72)$$

Hence we see that the inelastic scattering from the excited internal state results in an effective dephasing noise with Lindblad operator  $L_i = n_i$ . In chapter 5 we will consider the effect of such dephasing noise on the entanglement properties of free-fermions hopping on a lattice.

In addition to the dephasing noise, photon scattering can lead to particle loss when the momentum recoil due to the emitted photon transfers the atom to a momentum state with energy larger than the trap potential. This can happen in experiments inadvertently due to collisions with some (un-trapped) background gas. Local particle losses can also be induced in a controlled manner by usage of a laser beam in quantum gas microscopes with single-site addressing capabilities [60]. In those cases the system can be described by a QME with the dissipator  $\gamma \sum_i \mathcal{D}_{\hat{b}_i}[\rho]$ , where  $\hat{b}_i$  is the annihilation operator of a particle at site  $i$ . This type of controlled single-particle loss has been used in Ref. [61] to investigate signatures of many-body localization in open systems (see chapter 4).

Finally, let us comment that an incoherent pump term of the form  $\gamma_p \sum_i \mathcal{D}_{\hat{a}_i^\dagger}[\rho]$  can be engineered by immersing the system in a gas of a second un-trapped atomic species [62]. In this setup atoms in higher Bloch bands of the lattice (which are not part of the “system” in our effective description) can decay to the lowest band due to interaction with the background gas, leading to an effective incoherent pump.

### 2.3.2 ATOMS IN CAVITIES

Another interesting platform for quantum simulation is implemented in experimental setups where cold quantum gases are coupled to the radiation field of a high-finesse optical cavity, a field also known as cavity-QED. This is a setting which allows to investigate systems with long-range atom-atom interactions, since those are mediated by the cavity photons. Examples of cavity QED quantum simulation experiments include the realization of an open system version of the Dicke model and its associated superradiance phase transition [63]; observation of magnetic self-ordering in spinor BECs [64, 65]; realization of photonic Laughlin states [66]; formation of a supersolid phase, accompanied by spontaneous symmetry breaking of a continuous translational symmetry [67] and quantum-simulation of dynamical phase transitions in the Lipkin-Meshkov-Glick model [68]. In this section we will briefly describe the realization of the dissipative Dicke phase transition, for a more general review see [3].

In the experiment by Baumann et al. [63] a BEC was trapped inside an optical cavity and driven using a pump laser in a direction transversal to the cavity mode. Here we denote the cavity axis as  $\hat{x}$  and the transversal pump axis as  $\hat{z}$ . The Hamiltonian after adiabatic elimination of an internal atomic excited state (similar to sec. 2.3.1) is given by

$$\begin{aligned}\hat{H}_{atom} &= \int_{\mathbf{x}} \hat{\psi}^\dagger(\mathbf{x}) \left[ -\frac{\partial_x^2 + \partial_z^2}{2m} + V_0 \cos^2(kz) \right] \hat{\psi}(\mathbf{x}), \quad \hat{H}_{photon} = -\Delta_c \hat{a}^\dagger \hat{a}, \\ \hat{H}_{p-a} &= \eta(\hat{a}^\dagger + \hat{a}) \int_{\mathbf{x}} \cos(kx) \cos(kz) \hat{\psi}^\dagger(\mathbf{x}) \hat{\psi}(\mathbf{x}) + U_0 \hat{a}^\dagger \hat{a} \int_{\mathbf{x}} \cos^2(k\mathbf{x}) \hat{\psi}^\dagger(\mathbf{x}) \hat{\psi}(\mathbf{x}),\end{aligned}\quad (2.73)$$

here  $\int_{\mathbf{x}} \equiv \int dxdz$ ,  $k$  is the momentum associated with the pump laser,  $V_0$  is the potential induced by the pump laser,  $\hat{a}$  is an annihilation operator of a cavity photon and  $\Delta_c$  is the cavity detuning with respect to the pump frequency.

Mapping of this model to the Dicke model can be done by considering momentum modes of the BEC. The photon-atom coupling  $H_{p-a}$  induces transitions between BEC state with zero momentum  $|p_x = 0, p_y = 0\rangle = (N!)^{-1/2}(\hat{\psi}_{\mathbf{p}=0}^\dagger)^N |0\rangle$  and a state  $\hat{\psi}_{\mathbf{p}=(\pm k, 0)}^\dagger \hat{\psi}_0 |0, 0\rangle \equiv |\pm k, 0\rangle$  while the coupling with the pump field can induce transitions which changes the momentum in the  $\hat{z}$  direction  $\hat{\psi}_{\mathbf{p}=(0, \pm k)}^\dagger \hat{\psi}_0 |0, 0\rangle \equiv |0, \pm k\rangle$ . A process where a cavity (pump) photon is absorbed and a pump (cavity) photon is emitted induces a transition between the state  $|0, 0\rangle$  and the state  $|\pm k, \pm k\rangle \equiv (1/2) \sum_{\sigma, \sigma'=\pm} |\sigma k, \sigma' k\rangle$  [63].

When considering the BEC momentum states the system can be described by the Dicke model Hamiltonian [69]:

$$H_{\text{Dicke}} = \omega_z J_z + \omega_0 a^\dagger a + \frac{\lambda}{\sqrt{N}} (a^\dagger + a)(J_+ + J_-). \quad (2.74)$$

In the usual description of the Dicke model  $J_z$ ,  $J_\pm$  are spin operators describing a spin of size  $N$ , where the large spin is realized by a collection of  $N$  two-level atoms interacting with the cavity

mode  $\hat{J}_z = \sum_i \sigma^z$ ,  $\hat{J}_+ = \sum_i \sigma^+$ . In the experiment [63] the analogy to the Dicke model is obtained by mapping the two-level systems to the momentum excitations of the BEC, such that

$$\hat{J}_+ = \frac{1}{2} \sum_{\sigma, \sigma' = \pm} \hat{\psi}_{\mathbf{p}=(\sigma k, \sigma' k)}^\dagger \hat{\psi}_{\mathbf{p}=0}.$$

Even though a high-finesse cavity is used in the experiment, there is still some leakage of photons outside of the cavity. This needs to be taken into account when describing steady-states of the system. Hence the full system is described by

$$\partial_t \rho = -i[H_{\text{Dicke}}, \rho] + \kappa \mathcal{D}_a[\rho]. \quad (2.75)$$

Note that from an experimental perspective the fact that some photons leak outside of the cavity is important, because it is measurement of these photons and their correlations which allows for an experimental characterization of the state inside the cavity.

The Dicke Hamiltonian has a discrete  $\mathbb{Z}_2$  symmetry and is invariant under  $P = e^{i\pi(J_z + a^\dagger a)}$ . Namely, the total parity of the spin + photon number is conserved. When considering the ground-state properties of  $H_{\text{Dicke}}$ , this symmetry is spontaneously broken at a critical value of the photon-spin coupling  $\lambda_c$  where  $J_x$ ,  $a + a^\dagger$  develop finite expectation values. The broken symmetry phase is also known as the superradiant phase since the photon number obtains a macroscopic value  $\langle a^\dagger a \rangle \sim N$ .

The transition still occurs in the presence of photon loss as was observed in the experiment. We can see this using the Keldysh formalism following Ref. [47]. The key is to perform a Holstein-Primakoff expansion which allows us to replace the spin operators with bosonic operators in the limit of large atom number  $J_z = -N/2 + b^\dagger b$ ,  $J_x \approx \sqrt{N}(b + b^\dagger) + O(N^{-1/2})$ . Keeping only up to  $O(N^0)$  terms [with higher order terms of order at least  $O(N^{-1})$ ] results in a quadratic Keldysh action

$$S = \int (a_c^* \quad b_c^* \quad a_q^* \quad b_q^*) \begin{pmatrix} 0_{2 \times 2} & P^A \\ P^R & P^K \end{pmatrix} \begin{pmatrix} a_c \\ b_c \\ a_q \\ b_q \end{pmatrix} \quad (2.76)$$

with

$$P^R = \begin{pmatrix} \omega - \omega_0 + i\kappa & -\lambda \\ -\lambda & \omega - \omega_z \end{pmatrix}, \quad (2.77)$$

and  $P^K = \text{diag}(2i\kappa, 0)$ . Note that this description is only valid for the symmetric phase and in order to describe the superradiant phase we need to also take into account the leading  $1/N$  correction. The value of  $\lambda_c$  can be obtained by looking for an instability where one of the poles of  $G^R$ , obtained from solving  $\det(P^R(\omega)) = (\omega - \omega_z)(\omega - \omega_0 + i\kappa) - \lambda^2 = 0$ , has a zero imaginary value. This occurs at the critical value

$$\lambda_c = \frac{1}{2} \sqrt{\omega_z} \sqrt{\frac{\kappa^2 + \omega_0^2}{\omega_0}}. \quad (2.78)$$

We can also compute the photon number  $n = \langle a^\dagger a \rangle$  using  $G^K(\omega)$  which results in  $\langle a^\dagger a \rangle \sim (\lambda_c - \lambda)^{-1}$ . This kind of mean-field critical behavior of  $n$  is the same as the one encountered in the closed system at finite temperature [69].

In the experiment [63] the superradiant transition is observed by tuning the external pump intensity which effectively tunes the coupling  $\lambda$ . Above a threshold pump strength a sharp increase is observed in the mean photon number and in addition peaks at  $\pm k\hat{x}$ ,  $\pm k\hat{z}$  appear in the momentum distribution of the condensate which is evidence for a finite expectation value  $\langle J_+ + J_- \rangle$ .

### 2.3.3 CIRCUIT QED

In recent years much progress has been made towards the realization of many-body phases of photonic matter using microwave photons in superconducting circuits, a field known as circuit-QED (cQED) [4]. A lot of the technological advances in these devices are driven by the fact that superconducting qubits are one of the leading platforms for the realization of quantum computers, as evidenced for example in a recent experiment which claimed to show the first demonstration of quantum advantage [70]. The same capabilities which makes superconducting circuits good qubit candidates, such as long coherent times and scalability, also makes it an appealing platform for the realization of strongly interacting synthetic photonic matter.

The basic building blocks in cQED are LC resonator circuits. A linear LC circuit consists of a capacitor with capacitance  $C$  and inductor with inductance  $L$ . Its quantized Hamiltonian is given by

$$H_{\text{LC}} = \frac{\hat{Q}^2}{2C} + \frac{\hat{\Phi}^2}{2L}, \quad (2.79)$$

where  $\hat{Q}$  is the charge operator and  $\hat{\Phi}$  is the flux. Since  $\hat{Q}$  and  $\hat{\Phi}$  are canonical conjugates, this is nothing but an harmonic oscillator

$$H_{\text{LC}} = \omega_r a^\dagger a, \quad (2.80)$$

with  $\omega_r = 1/\sqrt{LC}$ . In current devices  $\omega_r$  is typically in the microwave regime. Hence, one LC resonator realizes a lattice site where a non-interacting microwave photon mode resides.

By replacing the simple inductor with a Josephson junction (a tunneling junction between two superconductors) one gets a circuit with non-linear inductance, also known as the transmon

$$H_{\text{transmon}} = \frac{\hat{Q}^2}{2C} + E_J \cos(\hat{\Phi}) \quad (2.81)$$

This leads to an interaction term between the microwave photons in the resonator

$$H_{\text{transmon}} \approx \omega \hat{b}^\dagger \hat{b} + U \hat{b}^\dagger \hat{b}^\dagger \hat{b} \hat{b}, \quad (2.82)$$

where the interaction, also known as a Kerr non-linearity,  $U \approx -E_C/2$  (with  $E_C = e^2/(2C)$  the charging energy) is attractive. The non-linearity is also what allows to operate the circuit as a qubit as it results in the energy levels no long being equidistant and allows addressing only the  $|0\rangle, |1\rangle$  states of the oscillator. Tunneling between the interacting sites (or coupling of an harmonic-oscillator and a qubit) can be induced by capacitive coupling of two circuits which leads to a term of the form  $H_{12} = C_{12} \hat{V}_1 \hat{V}_2 = g(\hat{b}_1^\dagger + \hat{b}_1)(\hat{b}_2^\dagger + \hat{b}_2)$ . This term can be approximated as a

tunneling term in the rotating wave approximation. Therefore, with an array of transmon qubits it is possible to realize a photonic version of the Bose-Hubbard model with attractive interactions.

Since photon loss naturally occurs due to leakage from the circuit, one has to take into account a term of the form  $\gamma \sum_i \mathcal{D}_{b_i}[\rho]$  when describing circuit-QED setups. The loss needs to be counter-balanced in order to obtain a steady state with a finite photon number. The most promising route for preparing strongly correlated many-body states in those systems is by means of engineered dissipation such that the resulting QME steady-state is the state of interest [4]. For example, Ref. [71] suggested a scheme for dissipative stabilization of fractional quantum Hall states against photon loss by coupling each photonic site, via a two-photon pump, to an auxiliary qubit site with a fast relaxation rate. Ref. [72] suggested a scheme for stabilizing incompressible Mott-insulator states using engineered non-Markovian baths. Hence a full description of the open system dynamics in terms of a (possibly non-Markovian) quantum-master equation is especially important for superconducting circuit arrays.

In a recent experiment by Ma et al. [73] the dissipative preparation of a Mott insulator state of photons, with filling  $n = 1$ , was demonstrated in a 1D transmon qubit chain with seven sites. The interacting Bose-Hubbard chain was driven to a state where at high probability each site is occupied by one photon, with average Mott fidelity  $\langle |1\rangle\langle 1| \rangle \approx 0.88$ . This was done by coupling one end of the chain to a dissipative stabilizer site. The stabilizer consists of a transmon qubit whose two-photon state is coupled to an extra lossy site. A coherent pump drives a two-photon transition from the  $n = 0$  to the  $n = 2$  state of the transmon, and the photon loss due to the coupling to the reservoir drives the transmon site to the  $n = 1$  state. Intuitively, when such a stabilizer site is coupled to a BH chain it acts as a narrow-band single photon source which fills the system until all sites are in the  $n = 1$  state [73]. Once all sites are filled the stabilizer is unable to inject more photons into the system owing to the fact that the Mott state is incompressible (i.e. there is a gap  $\Delta_{\text{comp}}$  between the  $n = 1$  Mott state and the state with an extra photon).



# 3

## CONDENSATE PHASES OF COHERENTLY DRIVEN BOSONS CLOSE TO A SCATTERING RESONANCE

### 3.1 INTRODUCTION

In experiments with ultracold atoms the interaction between atoms can be tuned by means of a Feshbach resonance [1, 52]. When the scattering length is positive this gives rise to a molecule bound state in the two-particle spectrum, which has lower energy than the state of two free atoms. On the other hand if the scattering length is negative there exist no bound state. Hence by tuning the scattering length from positive to negative through the resonance, the two-particle ground state changes its nature from molecular to atomic. For a system with finite many-body density of fermionic atoms, this leads to the well studied BCS-BEC crossover between a BCS like superfluid of cooper pairs in the atomic side of the resonance and a Bose-Einstein condensate of molecules in the molecular side [74–77].

The situation is quite different in the case of bosonic atoms, where, instead of a crossover, a sharp Ising phase-transition between a molecule condensate phase and an atom condensate phase was predicted to occur [41, 42, 78, 79]. However, unlike the fermionic case, the molecule BEC and the phase transition are yet to be observed in experiments due to the inherent difficulty of stabilizing a Bose gas close to a Feshbach resonance. A main difficulty in studying the equilibrium properties of the Bose gas close to the resonance is the fact that in this regime 3-body inelastic loss processes are strongly enhanced [80–82]. Thus, the system might not have time to equilibrate on the experimental time-scale<sup>1</sup>. Moreover, it was pointed out that the molecule condensate is thermodynamically unstable in the dilute limit and molecule-molecule repulsive interactions together with large enough density are necessary in order to stabilize it [84].

Inspired by the predictions of Refs. [41, 42] we set out to explore whether similar phases and phase transitions could be realized in an alternative driven-dissipative setting. One such promising platform that we consider is a system of Rydberg-polaritons, a type of strongly interacting light-matter quasi-particles. It has been recently shown that it is possible to control the Rydberg-polariton interactions and realize scattering resonances [39, 40].

Rydberg-polariton systems are inherently driven-dissipative lossy systems and hence it is important to take into account the way in which a state with a finite density is stabilized. In previous work the many-body physics of a one-dimensional Rydberg-polariton system was analyzed by neglecting the effect of losses and assuming that in its steady-state the system effectively thermalizes

---

<sup>1</sup>Some progress has been made recently in studying the properties of Bose gas close to resonance in non-equilibrium quench experiments [82, 83].

to an equilibrium Gibbs-state with the temperature dependent on the initial energy density of the system [85]. Such an approach might be suitable in the regime of very weak pump and losses. In this paper we take a different approach and consider explicitly the effects of losses and external pump on the long time steady-state into account by using an effective quantum master equation description of the Rydberg-polariton system.

In particular, we consider a situation where a two-particle coherent pump is used in order to stabilize a finite particle density against losses. We choose this pumping scheme since it crucially does not break the Ising symmetry associated with the phase transition between the molecule condensate and an atom condensate. In addition, the pump frequency serves as a useful tuning parameter which allows controlling the pumping efficiency at different energies. We develop an effective model using the tools of Keldysh field theory and explore the different condensate phases that arise in this situation. We find a rich phase diagram which includes the molecule condensate phase, a phase where both atoms and molecules are condensed, and in addition several bistability regions. An initial mean-field analysis of the phase transition between the molecule condensate and atom condensate phase suggests that it belongs to the model A dynamical universality class [86].

## OUTLINE AND SUMMARY OF RESULTS

Let us provide a brief highlight of the different sections in this chapter. In sections 3.2- 3.4 we review background information which is helpful for framing and understanding the results of this chapter. In particular: Sec. 3.2 reviews the physics of two-particle quantum mechanical scattering including its description in terms of a field-theory. While the field-theory formulation is not new, here we use the Keldysh formalism to describe the problem in order to set the stage for later work in the dissipative setting. In Sec. 3.3 we review previous theoretical works on bosonic condensate phases in the vicinity of Feshbach resonance in equilibrium states of ultracold gases. Sec. 3.4 reviews the experimental platform of Rydberg-polaritons which might provide a realization of the theoretical driven dissipative model we consider in this chapter.

The description of our research work starts in section 3.5 where we introduce the model and its associated field-theory. Before performing any detailed analysis we review the different condensate phases which are expected to occur in the systems based on symmetry analysis in Sec. 3.6, see table 3.1. In particular we argue for the existence of a phase with a molecule condensate (MC) where the condensate consists of tightly bound pairs. In addition there is a phase where both a molecule condensate and a standard atom condensate exist (AC).

In Sec. 3.8, starting from the bare action of attractively interacting atoms with coherent pump, we derive an effective action describing interacting atoms coupled to interacting coherently pumped molecules [Eq. (3.89)]. The main findings of this section are: *(i)* We explicitly show the existence of the molecule bound state in the dissipative vacuum setting. *(ii)* We find that the loss destabilizes the infinite series of three-body Efimov bound states, expected to emerge in equilibrium, and hence they can be safely neglected from the many-body description *(iii)* We show explicitly how the two-particle pump generates an effective molecule pump, leading to a finite molecule condensate density.



In Sec. 3.9 we use a simplified phenomenological model, inspired by the effective-action atom-molecule action, to perform a detailed mean-field study together with stability analysis of quadratic fluctuations. The main result of this section are the phase diagram shown in Fig. 3.13. The analysis of the phenomenological model allows us to understand the essence of the MC-AC transition. This transition occurs due to enhancement of the effective two-particle pump felt by the atoms, via the coupling to the molecule condensate. The pump enhancement leads to closing of the atomic gap and results in a condensation instability. In addition we point out the atom photoluminescence as a possible experimental probe which is sensitive to the different phases.

Finally, in Sec. 3.10 we perform an initial exploration of the MC-AC Ising transition. We decompose the atom field into two Ising degrees of freedom, one of them becomes gapless at the transition while the other remains gapped. By integrating out the gapped degree of freedom we obtain an effective Gaussian theory for the transition. At this level of analysis we find that the transition is describe by an effective equilibrium dynamical transition at finite temperature, belonging to the model A universality class.

## 3.2 BACKGROUND: SCATTERING RESONANCE

In this section we describe the physics of a two-particle scattering resonance and explain how this quantum-mechanical phenomenon can be captured using a field theory description. We start with a very brief recap of scattering theory and how the scattering of two-particles can be described at low energies. This leads us to the concept of the *scattering amplitude* and the *S-wave scattering length*. We then show how the low energy physics of the scattering problem can be reproduced in terms of a field theory in the limit of vanishing particle density. This will form the basis of our discussion of many-body physics in the vicinity of a scattering resonance in later sections.

### 3.2.1 TWO-PARTICLE SCATTERING AT LOW ENERGIES

Let us consider a situation where two identical particles are interacting via a spherically symmetric potential  $V(\mathbf{r})$ , with  $\mathbf{r} = \mathbf{r}_1 - \mathbf{r}_2$  the relative coordinate. We can parametrize the two-particle wave function as  $\Psi(\mathbf{r}, \mathbf{R}; \mathbf{P}_{\text{cm}}) = e^{i\mathbf{P}_{\text{cm}} \cdot \mathbf{R}} \psi(\mathbf{r})$ , with  $\mathbf{R}(\mathbf{P}_{\text{cm}})$  the center of mass coordinate(momentum).  $\psi(\mathbf{r})$  obeys the Schrödinger equation:

$$i\partial_t \psi(\mathbf{r}) = \left[ \frac{P_{\text{cm}}^2}{4m} - \frac{\nabla_{\mathbf{r}}^2}{m} + V(\mathbf{r}) \right] \psi(\mathbf{r}), \quad (3.1)$$

Hence, solving the two-particle scattering problem is equivalent to solving the scattering problem of a single-particle from the potential  $V(\mathbf{r})$ . For the rest of this section we will consider the properties of  $\psi(\mathbf{r})$ . Since this is standard text-book material, we will just recapitulate some basic facts here, further information can be found in e.g. [87].

At low energies (i.e. small relative momentum  $\mathbf{k}$ ) it is possible to describe the scattering properties of the two atoms via a single parameter called the *S-wave scattering length*. Intuitively this can be understood by the fact that a low-momentum particle scattering from some potential cannot resolve the details of the potential at short length scales. It is thus only sensitive to long wavelength properties, which at the  $k \rightarrow 0$  limit can be described by one parameter.

### 3 Condensate phases of coherently driven bosons close to a scattering resonance

More concretely, we can decompose the two-particle wave function as an incoming plane wave with momentum  $\mathbf{k} = k\hat{z}$ , and a scattered outgoing radial wave:

$$\psi(\mathbf{r}) = e^{ikz} + f_k(\theta) \frac{e^{ikr}}{r}. \quad (3.2)$$

The *scattering amplitude*  $f_k(\theta)$  encodes all the information about the scattering process. The scattering length is then defined as the low-energy limit of the scattering amplitude (which becomes isotropic in that limit):

$$a \equiv -\lim_{k \rightarrow 0} f_k(\theta) \quad (3.3)$$

Another useful object to introduce is the *T matrix* which is defined as  $V|\psi\rangle = T|\mathbf{k}\rangle$ . The scattering amplitude is related to the *T*-matrix via:

$$f(\mathbf{k}', \mathbf{k}) = -\frac{4\pi m}{\hbar^2} \langle \mathbf{k}' | T | \mathbf{k} \rangle. \quad (3.4)$$

We will see that this is an object that comes up naturally when considering the field-theoretic formulation of the two-body scattering problem. Note that since the scattering is energy-conserving we have  $f(\mathbf{k}', \mathbf{k}) = \delta_{kk'} f_k(\theta)$ , with  $\theta = \cos(\hat{\mathbf{k}}' \cdot \hat{\mathbf{k}})$ .

In the case of a spherically symmetric potential, a systematic low-energy expansion of the scattering amplitude can be obtained by expanding the wave function in terms of spherical-harmonics. This expansion is termed the *partial wave expansion* and is given by

$$f_k(\theta) = \sum_{l=0}^{\infty} (2l+1) f_l(k) P_l(\cos \theta). \quad (3.5)$$

Here  $P_l(x)$  is the  $l$ th Legendre polynomial. The index  $l$  corresponds to different total angular momenta. The physical meaning of  $f_l(k)$  can be understood by expanding the incoming plane-wave in Eq. (3.2) in terms of spherical waves, and plugging in Eq. (3.5) which leads to the following asymptotic expression for the wave function

$$\psi(\mathbf{r}) = \sum_l (2l+1) \frac{P_l(\cos \theta)}{2ik} \left[ (1 + 2ik f_l(k)) \frac{e^{ikr}}{r} - \frac{e^{-i(kr-l\pi)}}{r} \right]. \quad (3.6)$$

We see that the total wave function can be represented as a sum of incoming and outgoing spherical waves with different angular-momenta. The scattering potential affects only the coefficient of the outgoing wave.

Probability conservation implies that the total probability flux through a spherical surface must vanish. In addition since angular momentum is conserved this statement must be true for each partial-wave separately (i.e. for each  $l$  in Eq. (3.6)). This means that the magnitude of the coefficient of the outgoing and incoming spherical-waves for each angular-momentum sector must be equal, which leads to the *unitarity relation*

$$|1 + 2ik f_l(k)| = 1. \quad (3.7)$$

The meaning of this constraint is that the effect of scattering can be parametrized in terms of a phase-shift  $e^{2i\delta_l(k)} = 1 + 2ikf_l(k)$ , which leads us to

$$f_l = \frac{1}{k \cot \delta_l(k) - ik}. \quad (3.8)$$

For atoms interacting via a short range potential, in the low  $k$  limit, the phase shifts scale as  $\delta_l(k) \sim k^{2l+1}$ . Hence, we see that higher angular momentum contributions are less important. For identical bosons or spinfull Fermions the leading term is the S-wave phase shift ( $l = 0$ ). For  $V(\mathbf{r})$  with a long-range tail (such as WdV interactions) higher angular momentum phase shifts are not so strongly suppressed, but they still contribute less than the S-wave phase shift.

We can expand the S-wave phase shift at low momentum

$$k \cot \delta_0(k) = -1/a + 1/2r_s k^2 - 1/4P_s k^4 + \dots \quad (3.9)$$

Where  $a$  is the scattering length,  $r_s$  is called the effective range, and  $P_s$  is called the S-wave shape parameter. Plugging the effective range expansion in the expression for  $f_0(k)$  (Eq. (3.8)) we obtain

$$f(k) \approx \frac{1}{-1/a + 1/2r_s k^2 - ik} \quad (\text{low energies}). \quad (3.10)$$

The low-energy expression for the scattering amplitude Eq. (3.10) is a basis for an approximation commonly used in theoretical models of ultracold atoms, where the full interaction potential  $V(\mathbf{r})$  is replaced by a contact delta-function potential

$$V(\mathbf{r}) \rightarrow \frac{4\pi\hbar^2 a}{m} \delta(\mathbf{r}). \quad (3.11)$$

This contact potential reproduces exactly the result for the S-wave scattering amplitude at the low-energy limit Eq. (3.10), when finite-range corrections are neglected (i.e. setting  $r_s = 0$ ). Hence, in the low-energy limit all the scattering properties are captured by one parameter, which is the scattering length.

In this chapter, we will be concerning ourselves with a situation where the S-wave scattering length  $a$  becomes very large. As we can see from Eq. (3.10) this means that the scattering-amplitude will obtain a large value as  $k \rightarrow 0$ , hence this situation is termed a scattering resonance. Will now see that the occurrence of a scattering resonance can be related to the existence of a bound-state in the two-particle interaction potential  $V(r)$  [87, 88].

Let us consider a simple toy-model of a potential well with a delta-function barrier

$$V(r) = -\frac{\kappa_0^2}{m} \Theta(R - r). \quad (3.12)$$

The Schrödinger equation for the radial part of the wave function is given by

$$\left[-\frac{1}{m} \partial_r^2 + V(r) - \frac{k^2}{m}\right] \chi(r) = 0 \quad (3.13)$$

### 3 Condensate phases of coherently driven bosons close to a scattering resonance

where  $E = k^2/m$  is the collision energy, and we denoted  $\chi(r) = r\psi(r)$ . We consider only S-wave scattering in the low-energy limit  $k \rightarrow 0$ . In this limit, and using Eq. (3.6) the wave function outside of the well can be written as  $\chi(r) \propto e^{i\delta} \sin(kr + \delta)$ . The wave function inside the potential well can be written as  $\chi_{\text{in}}(r) \propto \sin(\sqrt{\kappa_0^2 + k^2}r)$ .

Our goal is to find the S-wave phase shift  $\delta$ . This can be done by matching the logarithmic derivatives at the point  $r = R$

$$\frac{\chi'(R)}{\chi(R)} = \frac{\chi'_{\text{in}}(R)}{\chi_{\text{in}}(R)}. \quad (3.14)$$

This results in an expression for  $\cot \delta(k)$ , which in the limit of  $k \rightarrow 0$  is given by

$$k \cot \delta(k) = \kappa_0 \cot(\kappa_0 R) = -\frac{1}{a} \Rightarrow a = -\kappa_0^{-1} \tan(\kappa_0 R). \quad (3.15)$$

We see that the scattering length diverges when  $\kappa_0 R = \pi/2 + n$ , which is also a condition on the depth of the well such that it has a bound-state energy exactly at  $E_b = 0$ . Hence, we see that the existence of a bound-state inside the scattering potential  $V(r)$  with energy close to zero leads to a large scattering length.

#### 3.2.2 FIELD-THEORY DESCRIPTION OF THE SCATTERING PROBLEM

Having reminded ourselves about the basics of the two-particle scattering problem, we will explain in this section how it can be described in a field-theoretical formulation [89–91]. While this might be an overkill for the two-particle setting, the field-theory formulation forms a basis which can be extended to describe the many-body problem where finite particle density is introduced. Even though the  $T = 0$  vacuum can be conveniently described by means of imaginary-time equilibrium field-theory, we will explicitly use the Keldysh formalism here as preparation for the next sections. We note that in this chapter we always assume to work in  $3d$ .

We consider atoms interacting via a contact-potential  $u_a$  at zero temperature in the vacuum. The Keldysh action for this problem at  $T = 0$  is given by  $S = S_0 + S_{\text{int}}$

$$S_a = \int_{\omega, \mathbf{k}} \left[ \psi_q^*(\omega, \mathbf{k}) \left( \omega - \frac{\mathbf{k}^2}{2m} + i\epsilon \right) \psi_c(\omega, \mathbf{k}) \right] + c.c. + 2i\epsilon \text{sign}(\omega) |\psi_q|^2, \quad (3.16)$$

$$S_{\text{int}} = -u_a \int_{t, \mathbf{r}} |\psi_+|^4 - |\psi_-|^4, \quad (3.17)$$

where we defined  $\int_{\omega, \mathbf{k}} \equiv (2\pi)^{-4} \int d\omega d^3k$  and  $\int_{t, \mathbf{r}} \equiv \int dt d^3r$  (this notation will be used in other sections of this chapter as well). The field  $\psi$  is associated with the annihilation operator of an atom, and  $\epsilon \rightarrow 0$  is an infinitesimal regularization of the path-integral. The term  $\sim \text{sign}(\omega) |\psi_q|^2$  enforces the  $T = 0$  equilibrium condition, and can be also viewed as arising from a coupling to a zero-temperature thermal bath [44].

The emergence of a bound state from the attractive interaction between atoms can be described by the inclusion of an auxiliary field via a Hubbard-Stratonovich (HS) transformation [46]. The HS transformation amounts to decoupling the quartic interaction using the identity

$$e^{i \int (\Psi\Psi)^\dagger U_a (\Psi\Psi)} = \int \mathcal{D}[\phi] e^{i \int \Phi^\dagger U_a^{-1} \Phi + \sum_{\sigma=\pm} \sigma \phi_\sigma^* \psi_\sigma \psi_\sigma + c.c.}, \quad (3.18)$$

where  $\phi$  is an auxiliary complex field,  $[\Psi\Psi]^T = (\psi_+^2, \psi_-^2)$ ,  $\Phi^T = (\phi_+, \phi_-)$  and  $U_a = -u_a \sigma^z$ . The resulting action can be rewritten as

$$S = S_a + S_m + S_{am}, \quad (3.19a)$$

$$S_m = \int_{t,r} [\phi_q^* (-\tilde{\nu} + i\eta) \phi_c + c.c. + 2i\eta \phi_q^* \phi_q], \quad (3.19b)$$

$$S_{am} = \int_{t,r} g [2\phi_c^* \psi_c \psi_q + \phi_q^* (\psi_c^2 + \psi_q^2) + c.c.], \quad (3.19c)$$

here  $\eta \rightarrow 0$  is an infinitesimal regularization, similar to  $\epsilon$ , the parameters  $\tilde{\nu}$  and  $g$  are related to the interaction as

$$u_a = -\frac{2g^2}{\tilde{\nu}}. \quad (3.20)$$

By means of the HS transformation, we replaced the quartic interaction  $u_a$  by introducing an auxiliary field which is coupled to the atoms. The two-point correlation function of  $\phi$  encodes the two-atom scattering properties. We introduced a parameter  $\tilde{\nu}$ , which can be related to the inverse scattering length and hence to the distance of the system from a scattering resonance, as we will soon see.

Note, that we could view the action in Eq. (3.19) as the microscopic starting point for the description of ultracold atoms in the vicinity of a Feshbach resonance [52]. In this setup a two-atom state is coupled to a molecule bound-state which exists as a bound state of a closed scattering channel. This situation can be described by Eq. (3.19) if we neglect the bare dynamics of the molecule, which is justified in the case of a broad Feshbach resonance. In experiments the atom-molecule coupling is used in order to tune the atom-atom scattering length, which is achieved by tuning the energy of the molecule bound-state via a magnetic-field, related to  $\tilde{\nu}$  in our description.

To see the connection between the field  $\phi$  and the scattering-amplitude of two atoms, we use the fact that the scattering amplitude can be extracted from the time-ordered connected 4-point function  $\langle \mathbb{T} \psi \psi \psi^\dagger \psi^\dagger \rangle_c$ . More conveniently the two-particle scattering properties can be extracted from the amputated 4-point function  $i\mathcal{A}$  which we define as  $\langle \mathbb{T} \psi(Q_1) \psi(Q_2) \psi^\dagger(Q_3) \psi^\dagger(Q_4) \rangle = (2\pi)^{d+1} \delta(Q_1 + Q_2 - Q_3 - Q_4) [\Pi_i G^\mathbb{T}(Q_i)] i\mathcal{A}(Q_1, Q_2, Q_3, Q_4)$ , where we introduced the notation  $Q_i = (\omega_i, \mathbf{q}_i)$ . According to the LSZ reduction formula the  $T$  matrix is obtained from  $\mathcal{A}$  by requiring all external frequencies to be on shell, that is  $\omega_i = \mathbf{q}_i^2/(2m)$  [45, 89].

In the Keldysh formalism the time-ordered correlation function is given by  $\langle \psi_+^* \psi_+^* \psi_+ \psi_+ \rangle$ , which in our case is given by the tree-level Feynman-diagram shown in Fig. 3.1a. Hence we see that the amputated 4-point function  $\mathcal{A}$  is proportional to the molecule field propagator  $\langle \phi_+^* \phi_+ \rangle$ . Denoting the molecule Green's functions by  $D$ , at zero-temperature equilibrium we obtain the

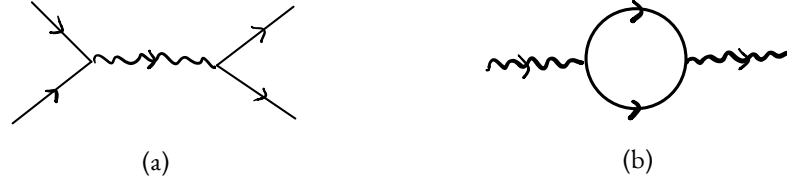


Figure 3.1: Diagrams involved in calculation of the atom-atom scattering amplitude. Straight lines correspond to an atom propagator while wiggly lines correspond to a molecule propagator. (a) The diagram for the atom connected 4-point function (b) The self-energy correction to the molecule propagator.

following relation between the time-ordered Green's function and the retarded/advanced Green's functions:

$$D^{\mathbb{T}}(\omega, \mathbf{k}) = \Theta(\omega)D^R(\omega, \mathbf{k}) + \Theta(-\omega)D^A(\omega, \mathbf{k}), \quad (3.21)$$

where we used the fact that in  $T = 0$  equilibrium  $D^K(\omega, \mathbf{k}) = \text{sign}(\omega)[D^R(\omega, \mathbf{k}) - D^A(\omega, \mathbf{k})]$ .

Thus, we see that the scattering properties of two atoms are encoded in the retarded Green's function of the  $\phi$  field. At the bare-level the field  $\phi$  has no dynamics, and the frequency and momentum dependence of the Green's function is given by the self-energy shown in Fig. 3.1b

$$[D_{\text{eq}}^R(\omega, \mathbf{k})]^{-1} = -\tilde{\nu} - i\eta - \Sigma_{\text{m,eq}}^R(\omega, \mathbf{k}). \quad (3.22)$$

We note here that the diagram in Fig. 3.1b gives the exact self-energy in vacuum since the atom propagator is not renormalized in vacuum. This is a consequence of the fact that there is no background particle density for the propagating atom to interact with. Mathematically, this physical observation is manifested by the fact that every diagram with closed momentum loop (i.e. a closed loop when following the momentum arrows) is vanishing in vacuum. This results in a massive simplification as compared to the finite density case, since it leads to a closed hierarchy of equations where the  $n$ -particle Green's function depends only on the  $1, \dots, n-1$ -particle Green's functions [14, 90].

Turning to the computation of the retarded self-energy, it is given by

$$\begin{aligned} \Sigma_{\text{m,eq}}^R(K)/(4ig^2) &= \int_P G^R(K/2 - P)G^K(K/2 + P) \\ &= \int_P \frac{\text{sign}(\omega + \omega_0/2)}{(\frac{\omega_0}{2} - \omega - \frac{(\mathbf{k}/2 - \mathbf{p})^2}{2m} + i\epsilon)(\frac{\omega_0}{2} + \omega - \frac{(\mathbf{k}/2 + \mathbf{p})^2}{2m} + i\epsilon)} \\ &= -i \int_{\mathbf{p}} \frac{1}{\omega_0 - \frac{k^2}{4m} - p^2 + 2i\epsilon}, \end{aligned} \quad (3.23)$$

where we denoted  $K = (\omega_0, \mathbf{k})$ ,  $P = (\omega, \mathbf{p})$ . Performing the integral over momentum we obtain

$$\Sigma_{\text{m,eq}}^R(\omega, \mathbf{k}) = \frac{g^2 m^{\frac{3}{2}}}{\pi} \sqrt{\frac{k^2}{4m} - i2\epsilon - \omega} - \int_{\mathbf{q}} \frac{4g^2 m}{q^2}. \quad (3.24)$$

### 3.3 Background: Pairing phases of bosons close to a Feshbach resonance in equilibrium

We see that  $\Sigma^R$  includes a UV diverging term (the second term in the RHS of Eq. (3.24)). In order to deal with the UV divergence we first regularize it by introducing a finite momentum UV cutoff  $\Lambda$ , such that  $\Sigma^R = I_{IR}(\omega, \mathbf{k}) + I_\Lambda$  with  $I_\Lambda = 2g^2m/\pi^2\Lambda$  and  $I_{IR}$  independent of  $\Lambda$ . We then perform renormalization by representing the bare detuning  $\tilde{\nu}$  as a sum of a physical coupling  $\nu$  and a diverging counter-term  $\tilde{\nu} = \nu + \delta\nu$ , where we choose  $\delta\nu = -I_\Lambda$ . With this choice of renormalization condition we obtain the renormalized Green's function

$$[D^R(\omega, \mathbf{k})]^{-1} = -\nu - \frac{g^2m^{\frac{3}{2}}}{\pi} \sqrt{\frac{k^2}{4m} - i2\epsilon - \omega}. \quad (3.25)$$

We now have to relate the parameter  $\nu$  appearing in our theory to some physical observable. Using the connection between  $D^R$  and the atom-atom  $T$ -matrix we can obtain the S-wave scattering amplitude in terms of  $\nu$

$$f(k) = -mT(k)/(4\pi) = -mg^2/\pi D^R(k^2/m, 0) = [\pi\nu/(mg^2) - ik]^{-1}. \quad (3.26)$$

comparing to the expression for the S-wave scattering amplitude in Eq. (3.10) we see that  $\nu$  is related to the scattering length via

$$\nu = -\frac{g^2m}{\pi a}. \quad (3.27)$$

In particular we see that  $\nu = 0$  corresponds to the resonance position where  $a \rightarrow \infty$ .

Looking at the Green's function we see that for  $\nu < 0$  it has a pole at

$$\omega^R(\mathbf{k}) = \frac{k^2}{4m} - \frac{\pi^2\nu^2}{m^3g^4} - i2\epsilon. \quad (3.28)$$

This means that for negative  $\nu$  the field  $\phi$  indeed describes a molecule bound state, a fact which is also seen from the  $T$ -matrix having a pole at the binding energy

$$E_b = -\frac{\pi^2\nu^2}{m^3g^4} = -\frac{1}{ma^2}. \quad (3.29)$$

In addition to the molecule pole,  $D^R$  also has a branch-cut for  $\omega(k) = k^2/(4m) - i2\epsilon$ , which is related to the continuum of two-atom scattering states. Hence the field  $\phi$  represents in general a mixture of a molecule bound-state (giving rise to the pole) and two-atom pairs  $\hat{\psi}(\mathbf{k})\hat{\psi}(-\mathbf{k})$  (giving rise to the branch-cut). At  $\nu \geq 0$  there is no longer a pole, which means that the molecule bound-state does not exist. Furthermore one can see that the bound-state pole residue is continuously decreasing as  $\nu \rightarrow 0^-$ .

### 3.3 BACKGROUND: PAIRING PHASES OF BOSONS CLOSE TO A FESHBACH RESONANCE IN EQUILIBRIUM

In this section we review previous theoretical works which examined condensate phases of attractively interacting bosons. The question of condensation in attractive Bose gases was considered already in the 80s by Nozières and Saint-James [78], in the context of excitons in semiconductors.

This problem has received revived interest when it was later considered in the context of a Feshbach resonance in ultracold gases by Radzihovsky et al. [41] and Romans et al. [42]. The main insight from these works is that in the presence of attractive interactions a new type of condensate phase can occur where the bosonic atoms condense only as strongly bound molecules. Tuning the interaction strength changes the bound-state energy, eventually making it more energetically favorable for atoms to form a more standard atomic condensate composed of single particles.

Ref. [41] used a two-channel model which is often used as a theoretical starting point for the description of a Feshbach resonance in ultracold atoms [92]. The model describes atomic and molecular degrees of freedom which are coupled to each other via an inter-conversion mechanism, where the imaginary time action is given by:

$$S = \int_0^\beta d\tau \int_{\mathbf{r}} [\psi^* \hat{h}_a \psi + \frac{u_a}{2} |\psi|^4 + \phi^* \hat{h}_m \phi + \frac{u_m}{2} |\phi|^4 + u_{am} |\psi|^2 |\phi|^2 - g(\psi^* \psi^* \phi + \text{c.c.})], \quad (3.30)$$

with the field  $\psi$  ( $\phi$ ) originating from the annihilation operator of an atom (molecule), and  $\hat{h}_\sigma = \partial_\tau - \nabla^2/(2m_\sigma) - \mu_\sigma$  is the single-particle Hamiltonian. Here,  $\mu_a = \mu$  and the molecule chemical potential is shifted by the detuning from resonance  $\mu_m = 2\mu - \nu$ .

In a typical ultracold atom experiment the number of particles is fixed. The phase-diagram of interest is in terms of the temperature  $T$  and the total particle density  $n$ . This can be done by relating the density to the chemical potential in the dilute limit via the condition  $n = -\partial\mathcal{F}/\partial\mu$  [41].

Let us denote  $\phi_0 = \langle \hat{\phi} \rangle$ ,  $\psi_0 = \langle \hat{\psi} \rangle$ , and consider first the  $T = 0$  case. When  $\mu_a, \mu_m < 0$  it is energetically beneficial for the system to be in the normal phase where  $\phi_0 = 0, \psi_0 = 0$ . When  $\nu < 0$  is large enough in magnitude, the molecule chemical potential can become positive leading to a molecule condensate phase (MC). By decreasing  $\mu$  the system can then be driven through another phase transition where the atomic chemical potential becomes positive leading to atomic condensation. The transition between the MC phase and the atom condensate (AC) phase is accompanied by a breaking of a  $\mathbb{Z}_2$  symmetry ( $\psi \rightarrow -\psi$ ), hence it is expected to be in the Ising universality class. Due to the Yukawa coupling  $g\psi^2\phi^* + \text{c.c.}$ , atom condensation necessarily implies molecule condensation. This is because the atomic condensate acts as an external field for the molecule condensate.

In order to determine the temperature for the normal-MC and normal-AC transitions, one can approximate the free-energy with the non-interacting one in the dilute limit:

$$f_0 = \frac{1}{\beta V} \int_{\mathbf{k}} \sum_{\sigma=a,m} \log(1 - e^{-\beta[k^2/(2m_\sigma) - \mu_\sigma]}), \quad n = -\frac{\partial f_0}{\partial \mu_a} - 2\frac{\partial f_0}{\partial \mu_m}. \quad (3.31)$$

Taking the derivatives of  $f_0$  and performing the momentum integration results in the following relation for the total density:

$$n = \frac{1}{\lambda_T^d} \left[ g_{d/2}(e^{\beta\mu}) + 2^{1+d/2} g_{d/2}(e^{\beta(\mu-\nu)}) \right] \quad (3.32)$$



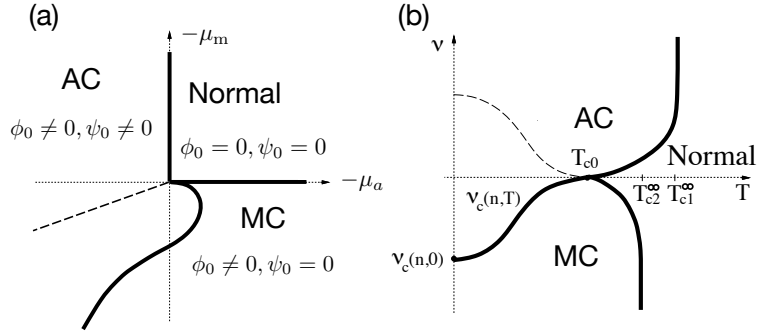


Figure 3.2: Phase diagrams obtained from analysis of an atom-molecule model (Eq. (3.30)) describing a Bose-gas in the vicinity of a Feshbach resonance, as obtained by Radzihovski et al. [41]. (a) Zero temperature phase diagram obtained in the grand-canonical ensemble, where  $\mu_a = \mu$ ,  $\mu_m = 2\mu - \nu$ . (b) Phase diagram at fixed density. (Figures adapted from [41]).

with  $g_\alpha = \sum_{n=1}^{\infty} z^n / n^\alpha$  and  $\lambda_T = \sqrt{2\pi\beta m}$  the thermal de-Broglie wave-length. Solving this equation for the case  $\mu_a = 0$  ( $\mu_m = 0$ ) allows finding the critical temperature for atom (molecule) condensation. For positive detuning,  $\nu > 0$ , atoms are energetically less expensive and will condense first, where the transition temperature  $\beta_{c,a}$  is determined by plugging-in  $\mu = 0$  in Eq. (3.32). On the other hand, for negative detuning the molecules are energetically favorable and will hence condense first, where  $\beta_{c,m}$  is determined by plugging-in  $\mu = \nu/2 < 0$  in Eq. (3.32).

The simplest method to find the AC-MC phase transition line is to perform a stability analysis of the atomic fluctuations in the MC phase [41]. To perform the analysis the action is expanded in fluctuations around the condensate values  $\psi = \psi_0 + \delta\psi$ ,  $\phi = \phi_0 + \delta\phi$ , keeping terms only up to quadratic order in  $\delta\psi, \delta\phi$ . This leads to the following action for the atom fluctuations in momentum space

$$S_{2,a} = \int_{\omega, \mathbf{k}} \frac{1}{2} \delta\Psi^\dagger(-i\omega, \mathbf{k}) G_a^{-1}(-i\omega, \mathbf{k}) \delta\Psi(-i\omega, \mathbf{k}), \quad (3.33)$$

where we defined the Nambu-spinor  $\delta\Psi^T = (\delta\psi(-i\omega, \mathbf{k}), \delta\psi^*(i\omega, -\mathbf{k}))$ . The inverse Matsubara Green's function is given by

$$G_M^{-1}(-i\omega, \mathbf{k}) = \begin{pmatrix} -i\omega - \epsilon_{a,k} & g\phi_0 \\ g\phi_0 & i\omega - \epsilon_{a,-k} \end{pmatrix}, \quad (3.34)$$

with  $\epsilon_{a,k} \equiv k^2/2m - \mu + u_{am}|\phi_0|^2$ . We can find the atom fluctuation dispersion by solving for  $\det G_M^{-1}(-i\omega, \mathbf{k}) = 0$ , which leads to the poles at

$$\omega_{a,\pm}^*(\mathbf{k}) = \pm i \sqrt{\left(\frac{k^2}{2m} - \mu + u_{am}|\phi_0|^2\right)^2 - 4g^2\phi_0^2} \quad (3.35)$$

### 3 Condensate phases of coherently driven bosons close to a scattering resonance

The MC phase becomes unstable when the atomic gap closes  $\omega_{a,+}^*(0) = 0$ . At  $T = 0$  we can use that  $|\phi_0|^2 = \mu_m/u_m$  in the MC phase, in order to eliminate  $\mu$  from Eq. (3.35). We thus obtain the following expression for the atomic gap in the MC phase

$$E_{\text{gap},a} = \sqrt{[-\nu/2 - (u_m/2 - u_{am})\rho_m]^2 - 4g^2\rho_m} \quad (3.36)$$

From Eq. (3.36) we see that for negative detuning, decreasing  $|\nu|$  leads to a decrease in the atom excitation gap which at a critical value of  $\nu$  will lead to a condensation instability. To find the critical value for the detuning leading to a quantum phase transition between the MC and AC phase, we can use the fact that at  $T = 0$  in the MC phase the density is given by  $n = 2\rho_m$ . This leads to

$$\nu_c(n, T = 0) = -(u_m/2 - u_{am})n - 2g\sqrt{2n}. \quad (3.37)$$

To compute the critical temperature for an MC-AC phase transition, Radzihovski et al. [41] obtain an expression for the molecule condensate density at finite  $T$  by taking into account the contribution of quadratic fluctuations to the free-energy. This results in the phase-diagram shown in Fig. 3.2b.

The analysis of Ref. [41] neglected the effect of dressing of the molecule action due to the coupling with the atoms (arising from a self-energy correction as in Sec. 3.2.2). Neglecting these effects is appropriate when the system is not too close to the Feshbach resonance, but they are important in the vicinity of the resonance. In [42] these dressing effects were taken into account. The self-energy corrections lead to the modification of the molecule chemical potential as

$$\mu_m = 2\mu - \epsilon_m, \quad \epsilon_m = -\nu - \frac{g^4 m^3}{2\pi^2} (\sqrt{1 - 4\pi^2 \nu / (m^3 g^4)} - 1) \quad (3.38)$$

Note that close to the resonance, when  $\pi^2 |\nu| / (m^3 g^4) \ll 1$ , we have  $\epsilon_m \approx E_b$  with  $E_b$  the binding energy computed in Eq. (3.29). In addition one has to work with renormalized molecule fields  $\phi = Z^{-1/2} \phi$ , with  $Z^{-1} = 1 + g^2 m^{3/2} / (2\pi \sqrt{|\epsilon_m|})$ . The expression for the atomic gap in the MC phase (Eq. (3.36)) is now

$$E_{\text{gap},a} = \sqrt{[-\epsilon_m/2 - (Z^2 u_m/2 - Z u_{am})\rho_m]^2 - 4g^2 Z \rho_m} \quad (3.39)$$

This will lead to a shift in the critical detuning value  $\nu_c(n, 0)$  for the MC-AC quantum phase-transition.

Finally, let us note that in Refs. [78,79] the MC-AC transition was analyzed in a model containing only attractively interacting atoms. This is relevant to the case of a broad Feshbach resonance, which is equivalent to the model we introduced in Sec. 3.2.2 at finite density. There it was shown explicitly that the  $T = 0$  MC-AC transition occurs when the extent of the molecule bound-state (which scales as  $\sim a$ ) is of the order of the mean interparticle distance  $n^{1/3}$ .

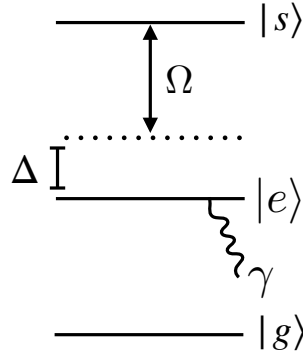


Figure 3.3: Level scheme of the atomic medium in the Rydberg-polariton system.  $|g\rangle$  is the atomic ground state,  $|s\rangle$  is a long-lived excited Rydberg state, and  $|e\rangle$  is an intermediate excited state with decay rate  $\gamma$ .

### 3.4 BACKGROUND: RYDBERG-POLARITONS

In this section we will discuss the experimental platform of Rydberg-polaritons, which might serve as a platform for realizing a driven-dissipative version of the physics discussed in the previous section. Rydberg-polaritons are light-matter quasi-particles originating from the hybridization of photons in an electromagnetically induced transparency (EIT) [93] configuration and Rydberg excitations. The distinctive features of Rydberg-polaritons are long lifetime, and a strong inter-particle interaction, inherited from the Rydberg excitations [94–97]. While Rydberg-polaritons have been realized in different setups [38, 98–102], in the following we will focus on the configuration of Ref. [38, 98, 99].

We consider a beam of photons propagating along the  $\hat{z}$ -axis and impinging on a cloud of atoms. For each atom only the optically active levels are considered, and consequently it can be modelled as a three-level system, with a ground state  $|g\rangle$ , a long-lived excited Rydberg state  $|s\rangle$  and an intermediate excited state  $|e\rangle$  with a finite lifetime  $\gamma^{-1}$  (see Fig. 3.3). The states  $|s\rangle$  and  $|e\rangle$  are coupled via an external control field with Rabi frequency  $\Omega$  and detuning  $\Delta = \omega_s - \omega_e - \omega_c$ , with  $\omega_s, \omega_e$  the level frequencies and  $\omega_c$  the control field frequency.

Now, consider photons with frequency  $\tilde{\omega}$  propagating inside the medium. When  $\tilde{\omega}$  is approximately satisfying the EIT condition  $\tilde{\omega} \approx \omega_p - \omega_g + \Delta$ , the photons can hybridize with the Rydberg state  $|s\rangle$  via a two-photon process, and propagate in the Rydberg medium in the form of a dark-state polariton [103] which is a superposition of a photon and an atomic Rydberg excitation  $|s\rangle$ . The dark polariton wave function does not have an overlap with the intermediate lossy state  $|e\rangle$  and hence it experiences only small losses when propagating through the medium.

Importantly, the dark Rydberg-polaritons inherit a strong interparticle interaction from their Rydberg component [94–97], as two Rydberg atoms at distance  $r$  experience a strong van der Waals interaction  $V(\mathbf{r}) = C_6/r^6$ .

In addition to the dark-polariton, the system has two other quasi-particle branches, namely the bright polaritons, which experience large losses as these states contain contributions from the intermediate state  $|e\rangle$ . The polariton basis, which includes the dark polariton and the two bright polariton states diagonalizes the non-interacting part of the photon-atom Hamiltonian. However

the Rydberg-Rydberg interaction is diagonal in terms of the atomic states and therefore has off-diagonal elements in the polariton basis.

A simple, effective description of the dark-polaritons can however be obtained by integrating out the bright-polariton modes [39, 40]. The presence of bright polaritons renormalizes the scattering properties of the dark polaritons, leading to an effective interaction potential between the dark polaritons  $U(\mathbf{r})$ , which can be tuned via experimentally controllable parameters. Importantly the potential  $U(\mathbf{r})$  can be tuned to be either repulsive or attractive.

At low energies the scattering properties can be encoded in the S-wave scattering length  $a$ , as we have explained in Sec. 3.2.1. The full potential  $U(\mathbf{r})$  can then be replaced with a contact interaction  $(4\pi\hbar^2 a/m)\delta(\mathbf{r})$  which reproduces correctly the low energy scattering properties of  $U(\mathbf{r})$  [1].

When  $U(\mathbf{r})$  is attractive and strong enough, it can support two-body bound states of Rydberg-polaritons, as was previously experimentally observed [38, 99]. Remarkably, theoretical predictions show that the value of the potential  $U(\mathbf{r})$  can be tuned through a scattering resonance, where  $a$  diverges and changes sign, allowing one to explore both the regime of effective repulsive contact interactions and attractive contact interactions between dark Rydberg polaritons [39, 40].

By taking into account the approximation of  $U(\mathbf{r})$  as a contact potential, the effective Hamiltonian of the dark Rydberg-polaritons in three-dimensions is given by [40]

$$\mathcal{H}_{\text{RP}} = \int_{\mathbf{r}} \left[ \hat{\psi}^\dagger(\mathbf{r}) \left( -iv_g \partial_z - \frac{\partial_z^2}{2m_z} - \frac{\partial_\perp^2}{2m_\perp} \right) \hat{\psi}(\mathbf{r}) + u_a \hat{\psi}^\dagger(\mathbf{r})^2 \hat{\psi}(\mathbf{r})^2 + u_3 \hat{\psi}^\dagger(\mathbf{r})^3 \hat{\psi}(\mathbf{r})^3 \right], \quad (3.40)$$

where here  $\hat{\psi}^\dagger(\mathbf{r})$  is the creation operator of a Rydberg-polariton at position  $\mathbf{r}$  and  $\perp$  denotes the directions transverse to the propagation direction  $\hat{z}$ . The existence of a drift term  $v_g \partial_z$  is related to the experimental setup, where the incoming photon beam is propagating along the  $\hat{z}$  direction. The drift term can be eliminated by working in a co-moving frame, and we will assume this from now on. The transformation to a co-moving frame is done by a Galilean transformation of momentum and frequency  $k_z \rightarrow k_z - k_0, \omega \rightarrow \omega - k_0^2/(2m_z)$  with  $k_0 \equiv m_z v_g$ . The longitudinal and transverse masses  $m_z, m_\perp$  are functions of the experimental control parameters and in general have different values, although it is possible to choose experimental values where they are equal [40].

In addition  $\mathcal{H}_{\text{RP}}$  includes a repulsive three-body interaction  $u_3$ . Although it is usually less relevant than the quartic interaction  $u_a$ , the inclusion of this term becomes necessary when attractive two-particle interactions are considered at finite density, in order to avoid the collapse of the Bose gas [84, 104]. In Rydberg-polariton systems this three-body interaction emerges as a consequence of the Rydberg blockade [105]. It was shown that when two Rydberg-polaritons are in the vicinity of a third Rydberg-polariton, the two polaritons are non interacting among themselves due to the strong shift of the Rydberg levels. This means that a three-body interaction with the same magnitude and opposite sign to the 2-body interaction exists. A more detailed calculation done by integrating out effects of high-momentum modes showed that the three-body interactions can also be tuned using the experimentally controllable parameters [105].

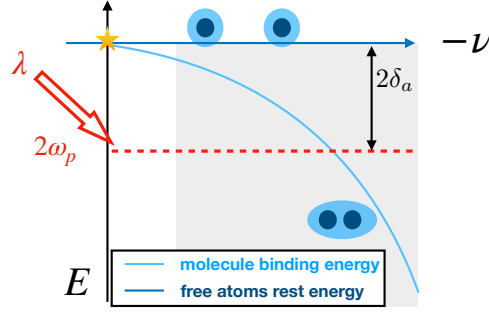


Figure 3.4: Schematic plot of the considered scheme and relevant parameters. The figure shows the possible two-particle states in vacuum, with energies  $E$ , as a function of detuning  $\nu$  from the scattering resonance (starred point), which is connected to the scattering length as  $\nu \propto -a^{-1}$ . For  $\nu < 0$  there exist a two-particle molecule bound state (bright-blue line) in addition to the unbound two-particle state (dark-blue line). Since particles experience losses the system needs to be pumped. Finite density is introduced using a two-particle pump with strength  $\lambda$  and frequency  $2\omega_p$ . In this paper we are interested in mapping the phase diagram as a function of  $\nu$  and  $\omega_p$ . We concentrate on the parameter regime shown in the shaded region, where the atoms pump is red-detuned (to avoid atom condensation instabilities at finite momenta) and not too close to the resonance point (where the theory becomes strongly coupled and challenging to deal with).

### 3.5 MODEL

We consider a microscopic model of polaritons with attractive interactions, and single- and two-particle losses, described in Sec. 3.4. In this chapter we consider the case of a three-dimensional system. As we are interested in exploring condensate phases of this system, we have to introduce a pumping mechanism to compensate for particle losses. Here we choose to work with a two-particle coherent pump of the form  $\sim \lambda e^{i2\omega_p t} \hat{\psi}^2 + \lambda^* e^{-i2\omega_p t} (\hat{\psi}^\dagger)^2$ . The state of the many-body system subject to these processes is given by the following quantum master equation

$$\partial_t \rho = -i[H, \rho] + 2\gamma_a \mathcal{D}_{\hat{\psi}}[\rho] + 2\Gamma_a \mathcal{D}_{\hat{\psi}\hat{\psi}}[\rho], \quad (3.41)$$

The second and third terms in Eq. (3.41) describe the single- and two-particle losses, with strength  $\gamma_a$  and  $\Gamma_a$  respectively, with the dissipator  $\mathcal{D}_{\hat{O}}$  given by

$$\mathcal{D}_{\hat{O}}[\rho] \equiv \int_{\mathbf{r}} \left[ \hat{O}(\mathbf{r}) \rho \hat{O}(\mathbf{r})^\dagger - \frac{1}{2} \{ \hat{O}(\mathbf{r})^\dagger \hat{O}(\mathbf{r}), \rho \} \right]. \quad (3.42)$$

The Hamiltonian  $H$  in Eq. (3.41) contains the effects described in Sec. 3.4 together with the two-particle coherent pump. In the rotating-frame (rotating with the frequency  $\omega_p$ ),  $H$  is given by:

$$H = \int_{\mathbf{r}} \left[ \hat{\psi}^\dagger \left( -\frac{\nabla^2}{2m} + \delta_a \right) \hat{\psi} + \frac{\lambda}{2} (\hat{\psi}^2 + \hat{\psi}^{\dagger 2}) + u_a \hat{\psi}^{\dagger 2} \hat{\psi}^2 + u_3 \hat{\psi}^{\dagger 3} \hat{\psi}^3 \right], \quad (3.43)$$

### 3 Condensate phases of coherently driven bosons close to a scattering resonance

with  $\delta_a = \omega_a - \omega_p$  the detuning between the atoms' natural frequency  $\omega_a$  and half of the drive frequency  $\omega_p$ ,  $\lambda$  the drive strength, and  $u_a$  and  $u_3$  the strength of the two- and three-particle interactions.

In the following we will focus only on the regime where  $\delta_a > 0$ , so that finite-momentum instabilities do not occur in the non-interacting problem. While  $\lambda$  is in general a complex number, one can redefine the fields so that only  $|\lambda|$  enters the Hamiltonian, as  $\hat{\psi} \rightarrow \hat{\psi} e^{-i \arg \lambda/2}$ ,  $\hat{\psi}^\dagger \rightarrow \hat{\psi}^\dagger e^{i \arg \lambda/2}$ , with  $\arg \lambda$  the angle of  $\lambda$  in the complex plane. For this reason, in the following we will assume  $\lambda > 0$  without loss of generality.

To explore the steady-states of the QME Eq. (3.41) we will use a Keldysh description, where the system is described by the action  $S = S_a + S_{\text{int}}$ . The free part  $S_a$  is given by:

$$S_a = \int_{t,\mathbf{r}} \left[ \psi_q^* \left( i\partial_t + \frac{\nabla^2}{2m} - \delta_a + i\gamma_a \right) \psi_c + \text{c.c.} \right. \\ \left. + 2i\gamma_a \psi_q^* \psi_q - \lambda (\psi_q^* \psi_c^* + \psi_c \psi_q) \right]. \quad (3.44)$$

As we discussed in Sec. 3.2.2, when describing the scattering problem it is advantageous to decouple the interaction terms with an Hubbard-Stratonovich transformation. Performing the HS transformation here we obtain  $S_{\text{int}} \rightarrow S_m + S_{\text{am}}$  with:

$$S_m = \int_{t,\mathbf{r}} [\phi_q^* (-\tilde{\nu} + i\eta) \phi_c + \text{c.c.} + 2i\eta \phi_q^* \phi_q], \quad (3.45a)$$

$$S_{\text{am}} = \int_{t,\mathbf{r}} \left\{ g [2\phi_c^* \psi_c \psi_q + \phi_q^* (\psi_c^2 + \psi_q^2) + \text{c.c.}] \right. \quad (3.45b)$$

$$\left. - u_{\text{am}} [\phi_q^* \phi_c (|\psi_c|^2 + |\psi_q|^2) + \psi_q^* \psi_c (|\phi_c|^2 + |\phi_q|^2) + \text{c.c.}] \right\}. \quad (3.45c)$$

Note that in the presence of the 3-body interaction  $u_3 |\psi|^6$  the equivalence between  $S_{\text{int}}$  and  $S_m + S_{\text{am}}$  is only approximate [89]. Other than the  $u_{\text{am}}$  term, the action in Eq. (3.45) is similar to the one we obtained in the equilibrium case, Eq. (3.19). However, here  $\eta$  is no longer an infinitesimal regularization but rather related to the two-body loss rate  $\Gamma_a$ . The parameters  $\tilde{\nu}, \eta$  and  $g$  are related to the bare polariton interaction  $u_a$  and two-particle loss  $\Gamma_a$  via

$$u_a = -\frac{2g^2 \tilde{\nu}}{\eta^2 + \tilde{\nu}^2}, \quad \Gamma_a = \frac{2g^2 \eta}{\eta^2 + \tilde{\nu}^2}. \quad (3.46)$$

From Eq. (3.46) we see that the complex detuning parameter  $-\tilde{\nu} + i\eta$  controls the distance of the system from the scattering resonance, as the coherent two-body interaction and two-body loss are diverging when both  $\tilde{\nu}$  and  $\eta$  are vanishing. Comparing to the case with only coherent interaction we see that presence of finite two-body losses  $\eta > 0$  leads to a broadening of the scattering-resonance and a finite value of  $u_a$  at  $\tilde{\nu} = 0$ . We also note the similarity of the  $\eta > 0$  case to the setup of an optical Feshbach resonance [52], where an effective two-atom loss is generated due to the coupling of atoms to an excited bound-state that has a finite life-time.

To see how the  $u_{am}$  term gives rise to the 3-body interaction term  $u_3|\psi|^6$  and for some further details on the introduction of the auxiliary field  $\phi$  in the presence of 3-body interactions, refer to App. 3.A.

### 3.6 EXPECTED PHASES FROM SYMMETRIES

Before delving into a more detailed analysis of the atom-molecule model let us consider possible phases from the perspective of symmetry. First we note that the two-particle pump  $\lambda$  breaks the  $U(1)$  symmetry of the action, given by  $\psi_\alpha \rightarrow e^{i\theta}\psi_\alpha$ ,  $\phi_\alpha \rightarrow e^{i2\theta}\phi_\alpha$ . Hence we expect that the system is always in a condensed phase. However, there still exists a residual  $\mathbb{Z}_2$  symmetry given by  $\psi \rightarrow -\psi$ . Hence we expect two possible phases: (i)  $\mathbb{Z}_2$  symmetric phase. In this phase particles condense only as molecules ( $\langle\phi_c\rangle \neq 0$ ) but not as atoms ( $\langle\psi_c\rangle = 0$ ). We will denote this phase as molecule condensate (MC). (ii)  $\mathbb{Z}_2$  broken phase. Particles condense both as molecules and atoms ( $\langle\phi_c\rangle \neq 0$ ,  $\langle\psi_c\rangle \neq 0$ ). We will denote this phase as atom-molecule condensate (AC).

Considering the MC phase itself, we will see that a bi-stability can occur where the system admits different solutions not related by  $U(1)$  rotation (i.e. solutions with different values of  $|\langle\phi_c\rangle|^2$ ). This situation occurs often in the presence of a symmetry breaking coherent pump, and is related to the phenomenon known as optical bistability [106,107]. For an intuitive explanation, consider first the simpler situation where an external magnetic field breaks a discrete symmetry in an Ising model. This leads to two distinct solutions in the ferromagnetic phase. In equilibrium it is assumed that the system is in the solution which is the global minimum of the free-energy, but out of equilibrium there is no such construction in general and the system is bi-stable. Coming back to the  $U(1)$  case consider the equilibrium case where the free-energy density for an homogeneous condensate solution is given by  $f(\phi) = \mu|\phi|^2 + u|\phi|^4 + \lambda\text{Re}\phi$ . Using the density-phase representation  $\phi \equiv \sqrt{\rho}e^{i\theta}$  we find that the minimum of  $f$  is always at  $\theta = \pi$  (assuming  $\lambda > 0$ ). The free-energy density is thus given by  $f(\rho) = \mu\rho + u\rho^2 - \lambda\sqrt{\rho}$ , which is equivalent to the case of the Ising model with an external magnetic field. This explains intuitively why we can expect a bi-stability in the non-equilibrium case, we will show that this happens explicitly in Sec. 3.9.1.

We expect the two-particle pump frequency  $\omega_p$ , or equivalently the atom detuning  $\delta_a$ , and the molecule bound state energy  $E_b$  to play a central role in driving transitions between the phases described above. The phase diagram is expected to display different features depending on  $\delta_a$  being  $\delta_a \simeq 0$  (pump resonant with atomic lowest energy mode, i.e. its ground state energy in vacuum) or  $\delta_a \simeq E_b/2$  (pump resonant with molecule lowest energy mode, i.e. the molecule binding energy in vacuum with respect to the atom ground state energy).

### 3.7 NON-INTERACTING CASE

Before going further with the investigation of the atom-molecule model let us consider the simpler case of non-interacting atoms subjected to a two-particle pump. That is, in this section we consider a model where  $S = S_a$ . This simpler case will help us build understanding and intuition of the effect of the two-particle pump term  $\lambda$ , and we will see how it can lead to condensation of the atoms.

### 3 Condensate phases of coherently driven bosons close to a scattering resonance

MC	molecule condensate ( $\langle \phi_c \rangle \neq 0, \langle \psi_c \rangle = 0$ )
AC	molecule and atom condensate ( $\langle \phi_c \rangle, \langle \psi_c \rangle \neq 0$ )
MC2	bi-stability: two MC solutions, “high-density” and “low-density” with $ \langle \phi_c \rangle_{\text{high}}  >  \langle \phi_c \rangle_{\text{low}} $ .
AC2	bi-stability: two AC solutions with different values of condensate density.
AC/MC	bi-stability: one “low-density” MC solution, and one AC solution (with higher molecule condensate density).

Table 3.1: A summary of the different phases found in our analysis and their notation.

Since the pump term  $\lambda$  in Eq. (3.43) induces anomalous correlations between the atoms, it is useful to collect the fields in a Nambu basis as

$$\Psi^T \equiv (\psi_c(\omega, \mathbf{k}) \quad \psi_c^*(-\omega, -\mathbf{k}) \quad \psi_q(\omega, \mathbf{k}) \quad \psi_q^*(-\omega, \mathbf{k})). \quad (3.47)$$

The quadratic part of the action can be rewritten in terms of  $\Psi$  as

$$S_a = \frac{1}{2} \int_{\omega, \mathbf{k}} \Psi^T(\omega, \mathbf{k}) G^{-1}(\omega, \mathbf{k}) \Psi(\omega, \mathbf{k}). \quad (3.48)$$

The  $4 \times 4$  matrix  $G^{-1}(\omega, \mathbf{k})$  reads

$$G^{-1}(\omega, \mathbf{k}) = \begin{pmatrix} 0 & P^A(\omega, \mathbf{k}) \\ P^R(\omega, \mathbf{k}) & P^K(\omega, \mathbf{k}) \end{pmatrix}, \quad (3.49)$$

where  $P^R(\omega, \mathbf{k}) = (P^A)^\dagger(\omega, \mathbf{k})$  and

$$P^R(\omega, \mathbf{k}) = \begin{pmatrix} \omega + i\gamma - \epsilon_k & \lambda \\ \lambda & -\omega - i\gamma - \epsilon_k \end{pmatrix}, \quad P^K(\omega, \mathbf{k}) = 2i\gamma_a \mathbb{1}. \quad (3.50)$$

Here  $\epsilon_k = k^2/(2m) + \delta_a$ . The  $2 \times 2$  structure of the Green’s functions reflects the presence of anomalous correlations between the bosonic fields.

The Hamiltonian (3.43) couples creation and annihilation operators (similarly to a Bogoliubov Hamiltonian for interacting Bose gases [108]). One typically resorts to a Bogoliubov transformation in order to diagonalize it and unveil the quasiparticles. Here we derive the spectrum of excitations by looking at the poles of  $G^R$ , i.e, by solving  $\det P^R(\omega, \mathbf{k}) = 0$  for  $\omega$  [17]. This yields:

$$\omega_a(\mathbf{k}) = -i\gamma_a \pm \sqrt{\epsilon_k^2 - \lambda^2}. \quad (3.51)$$

As in an equilibrium condensate, there exist positive and negative excitation branches, arising from the mixing between particle and hole-like excitations. The spectrum presents two different regimes, which are shown in Fig. 3.5: (i) for  $\lambda \leq \delta_a$ , the damping rates (imaginary part) of the two branches are independent of  $\mathbf{k}$  and given by  $\gamma_a$ , while the dispersion (real part) presents a



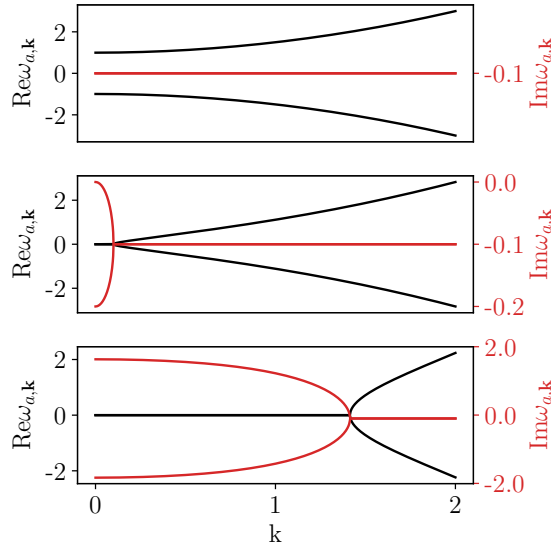


Figure 3.5: Excitation spectrum of the non-interacting polaritons with two-particle pump, given by Eq. (3.51), shown for (top)  $\lambda < \delta_a$  (middle)  $\lambda = \sqrt{\delta_a^2 + \gamma_a^2}$  (bottom)  $\lambda > \sqrt{\delta_a^2 + \gamma_a^2}$ . Solid lines correspond to the positive excitation branch and dashed lines correspond to the negative branch.

gap given by  $2\sqrt{\delta_a^2 - \lambda^2}$ , which closes at  $\lambda = \delta_a$ , leading to a linear dispersion at low momenta. (ii) For  $\lambda > \delta_a$ , the damping rates acquire a  $k$  dependence, while the dispersion vanishes for momenta below  $k^* = \sqrt{2m(\lambda - \delta_a)}$ . Eventually, when the condition

$$\lambda^2 = \delta_a^2 + \gamma_a^2, \quad (3.52)$$

is satisfied, the damping rate of one branch vanishes for small momenta as  $\sim k^2$ , signalling the emergence of a long-lived mode and, ultimately, of a condensation instability, which we discuss below in Sec. 3.9.1.

Further insight can be obtained from the momentum distribution, which can be evaluated from the diagonal part of  $G^K$  by using Eq. (2.42) and reads:

$$n_a(\mathbf{k}) = \frac{\lambda^2}{\left(\frac{k^2}{2m} + \delta_a\right)^2 + \gamma_a^2 - \lambda^2}. \quad (3.53)$$

As expected the momentum distribution develops a singularity at  $k = 0$  when the condition (3.52) is satisfied, signalling the onset of condensation at  $k = 0$ . Integrating over momentum we obtain the total atom density, in the case where  $\lambda > \gamma_a$ :

$$n_a = \frac{1}{\sqrt{2\pi}} \frac{m^{3/2} \lambda^2}{\sqrt{\delta_a + \sqrt{\lambda^2 - \gamma_a^2}} + \sqrt{\delta_a - \sqrt{\lambda^2 - \gamma_a^2}}}. \quad (3.54)$$

### 3 Condensate phases of coherently driven bosons close to a scattering resonance

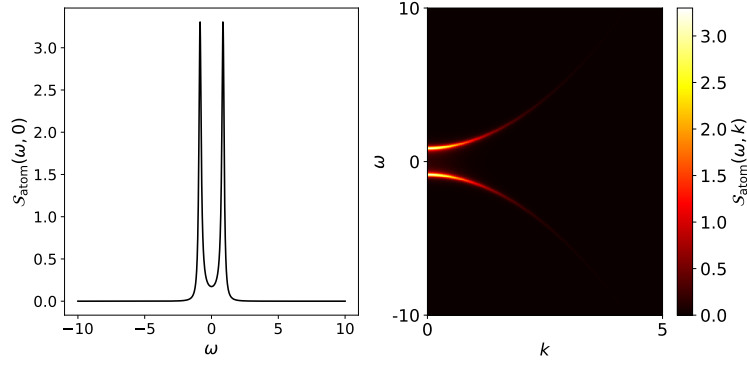


Figure 3.6: Photoluminescence spectrum for the non-interacting case (Eq. (3.58)). Parameters  $\lambda = 0.5\delta_a$ ,  $\gamma = 0.1\delta_a$ ,  $\delta_a = 1$ .

We see that for large detuning  $n_a$  is small and behaves as  $\sim \lambda^2/\sqrt{\delta_a}$ . For the case where  $\gamma_a \gg \lambda$  we get  $n_a \sim \lambda^2/\sqrt{\gamma_a}$ .

From the off-diagonal element of the Keldysh Green's function  $G_{12}^K$  we obtain the atom pair correlations

$$\langle \hat{\psi}(\mathbf{k})\hat{\psi}(-\mathbf{k}) \rangle = \frac{\lambda \left( \frac{k^2}{2m} + \delta_a + i\gamma_a \right)}{\left( \frac{k^2}{2m} + \delta_a \right)^2 + \gamma_a^2 - \lambda^2}. \quad (3.55)$$

We see that a finite  $\lambda$  leads to non-vanishing atom pairing correlations in a similar manner to the role of the condensate in a BEC. For low momentum and large detuning the pair correlation scales as  $\langle \hat{\psi}(\mathbf{k})\hat{\psi}(-\mathbf{k}) \rangle \sim \lambda/\delta_a$ .

Unlike the case of  $n_a(k)$ , the integral over pairing correlations diverges  $\int_{\mathbf{k}} \langle \hat{\psi}(\mathbf{k})\hat{\psi}(-\mathbf{k}) \rangle \sim \Lambda_{\text{pump}}$ , with  $\Lambda_{\text{pump}}$  some UV momentum cutoff above which our theory, which ignores a variety of short range effects, is no longer valid. This is a result of the fact that the two-particle pump term we introduced acts at all momentum scales and the single-particle loss is independent of momentum. In a physical situation there will exist a momentum cutoff at which the two-particle pump is no longer efficient. We will discuss how to deal with this divergence in Sec. 3.8.4.

Another observable we can consider is the photoluminescence which is defined by

$$\mathcal{S}_{\text{atom}}(\omega, \mathbf{k}) = \int_{\tau} e^{i\omega\tau} \langle \hat{\psi}_{\mathbf{k}}^{\dagger}(\tau) \hat{\psi}_{\mathbf{k}}(0) \rangle. \quad (3.56)$$

$\mathcal{S}_{\text{atom}}(\omega, \mathbf{k})$  can be observed experimentally in the correlations of photons exiting the system. The photoluminescence can be computed in the Keldysh formalism using the relation

$$\mathcal{S}_{\text{atom}}(\omega, \mathbf{k}) = \frac{i}{2} [G^K(\omega, \mathbf{k}) + G^A(\omega, \mathbf{k}) - G^R(\omega, \mathbf{k})]. \quad (3.57)$$

We compute the photoluminescence in the non-interacting case using Eq. (3.57), this results in the following analytic formula:

$$\mathcal{S}_{\text{atom}}(\omega, \mathbf{k}) = \frac{2\gamma\lambda^2}{[(\omega + i\gamma)^2 - E_{\mathbf{k}}^2][(\omega - i\gamma)^2 - E_{\mathbf{k}}^2]}, \quad (3.58)$$

with  $E_{\mathbf{k}}^2 = (k^2/(2m) + \delta_a)^2 - \lambda^2$ . We plot  $\mathcal{S}_{\text{atom}}(\omega, \mathbf{k})$  for some exemplary set of parameters in Fig. 3.6. We see that  $\mathcal{S}_{\text{atom}}(\omega, \mathbf{k})$  provides information about both dispersion branches with positive and negative energies where the signal is peaked. This implies that excitations at negative frequencies are also occupied, unlike the typical scenario in equilibrium. Since the system is non-interacting, the slight broadening of the signal is only due to the external single-particle loss  $\gamma_a$  (which is taken to be rather small in Fig. 3.6).

### 3.8 EFFECTIVE ACTION DESCRIPTION FOR THE ATOM-MOLECULE MODEL

Having understood the effects of the two-particle pump in the non-interacting case, we are ready to take a step forward towards understanding of the implications in the interacting case. Our starting point is the bare atom-molecule action  $S = S_a + S_m + S_{\text{am}}$  described by Eqs. (3.44) and (3.45). We will make use of the effective-action formalism in the 1-loop approximation which is suitable for determining the different condensate phases of the model. Recall that the effective action  $\Gamma$  is a function of the field expectation values  $\bar{\phi}_\alpha = \langle \phi_\alpha \rangle$ ,  $\bar{\psi}_\alpha = \langle \psi_\alpha \rangle$ , and in the 1-loop approximation it is given by

$$\begin{aligned} \Gamma[\bar{\psi}, \bar{\phi}] &= S[\bar{\psi}, \bar{\phi}] + i \text{tr} \log S^{(2)}[\bar{\psi}, \bar{\phi}] \\ &= S[\bar{\psi}, \bar{\phi}] - i \sum_{n=1}^{\infty} \frac{(-1)^n}{n} \text{tr}[(\mathcal{G}_0 V[\bar{\phi}, \bar{\psi}])^n] + i \text{tr} \log \mathcal{G}_0^{-1}. \end{aligned} \quad (3.59)$$

Here  $\mathcal{G}_0$  denotes the bare Green's function in the absence of condensates. The term  $\sim \text{tr}[(\mathcal{G}_0 V)^n]$  can be represented by all 1-loop Feynman diagrams with  $n$  interaction vertices insertions, where a diagram with  $m$  external molecule legs (denoted as wiggly lines) and  $k$  external atom legs (denoted as straight lines) contributes to the 1PI vertex  $\sim \bar{\phi}^m \bar{\psi}^k$ .

Our main goal is to obtain the condensate densities and determine the different steady-state phases characterized by atom and molecule condensation, similar to previous works done in the equilibrium settings [41, 42], which we reviewed in Sec. 3.3. Given the effective action, the steady-state values of the fields are determined from the stationarity conditions  $\delta_{\bar{\phi}} \Gamma, \delta_{\bar{\psi}} \Gamma = 0$ . The field equations can be obtained directly by taking a derivative of the RHS in the first line of Eq. (3.59). In Sec. 3.8.1 we derive the field equations and solve them in order to get a first glimpse into the phase diagram of the model.

However in the dynamical setting it is also crucial to consider the stability properties of the solutions  $\bar{\phi}, \bar{\psi}$  against fluctuations, by examining the imaginary part of the Green's functions obtained by the second derivative of  $\Gamma$ . For the purpose of stability analysis we need to derive an approx-

imate dynamical action for the molecule, including quartic molecule-molecule interactions, and we need to resort to a truncation of the infinite series in Eq. (3.59).

Our strategy, and the plan for the rest of this section is as follows:

1. Working in vacuum,  $\lambda = 0$ , we derive the dynamical part of the molecule action arising from the term  $\text{tr}(\mathcal{G}_0 V)^2$  (Sec. 3.8.2).
2. Still in vacuum, we derive the quartic molecule-molecule interaction term  $|\bar{\phi}|^4$  which is necessary for the stability analysis of a molecule condensate solution. This is done by computing contributions from the  $\text{tr}(\mathcal{G}_0 V)^3$ ,  $\text{tr}(\mathcal{G}_0 V)^4$  terms. (Sec. 3.8.3)
3. We include the leading contribution of the pump  $\lambda$  which is an effective molecule coherent pump, resulting from the term  $\text{tr}(\mathcal{G}_0 V)$ . (Sec. 3.8.4)
4. In Sec. 3.8.2 we also examine numerically the effect of finite pump  $\lambda \neq 0$  on the molecule dispersion.

### 3.8.1 MEAN-FIELD PHASE DIAGRAM

In this section we use the one-loop approximation of the effective-action to derive the field-equations for the condensate values, allowing us to obtain a phase diagram of the atom-molecule system. Here we work in the simplest case where  $u_{am} = 0$ . Taking the derivative of Eq. (3.59) with respect to the quantum-fields

$$\frac{\delta \Gamma}{\delta \bar{\phi}_q^*} = 0, \quad \frac{\delta \Gamma}{\delta \bar{\phi}_q} = 0,$$

we obtain the set of equations (see App. 3.B for details):

$$(-\delta_a + i\gamma_a - u_a |\psi_0|^2) \psi_0 + (\lambda + 2g\phi_0) \psi_0^* = 0, \quad (3.60a)$$

$$(-\nu + i\eta) \phi_0 + 2g\psi_0^2 + i2g \int_{\omega, \mathbf{k}} G_{12}^K(\omega, \mathbf{k}; \phi_0, \psi_0) = 0, \quad (3.60b)$$

with  $\psi_0 = \bar{\psi}_c$ ,  $\phi_0 = \bar{\phi}_c$  the atomic and molecular condensate, respectively. Here  $G_{12}^K[\psi_0, \phi_0] = \delta^{(2)} S / \delta \psi_q^* \delta \psi_c^*$ , and note that  $\int_{\omega, \mathbf{k}} G_{12}^K(\omega, \mathbf{k}; \phi_c, \psi_c) = \langle \psi_c^2(t, x) \rangle \propto \lambda$ . Hence, we can understand the appearance of the last term in Eq. (3.60b) as follows: the presence of a finite two-particle atom pump  $\lambda \neq 0$  generates a finite density of atom pairs. The atom pairs in turn act as a coherent pump term which can generate molecules via the conversion term  $g\phi^*\psi^2$ .

In order to simplify the solution of the field equations we performed an approximation in their derivation, where we neglected the hybridization of atoms and molecules, assuming all atom-molecule Green's functions are vanishing  $\langle \phi_\alpha^* \psi_\beta \rangle = 0$ . Those correlation functions are non-vanishing only in the AC phase, due to the fact that the term leading to hybridization of atomic and molecular excitations is of the form  $g\langle \psi_c \rangle \phi_c^* \psi_q + c.c..$  This approximation could be justified in the regime of small atom condensate density  $|\psi_0| \ll 1$ .

In Sec. 3.7 we have seen that in the non-interacting case an atom condensation instability arises when  $\lambda$  is larger than some critical threshold value. This kind of instability could be cured by a finite atom condensate  $\psi_0 \neq 0$ , only in the presence of quartic atom-atom interactions  $\sim u_a |\psi|^4$ .

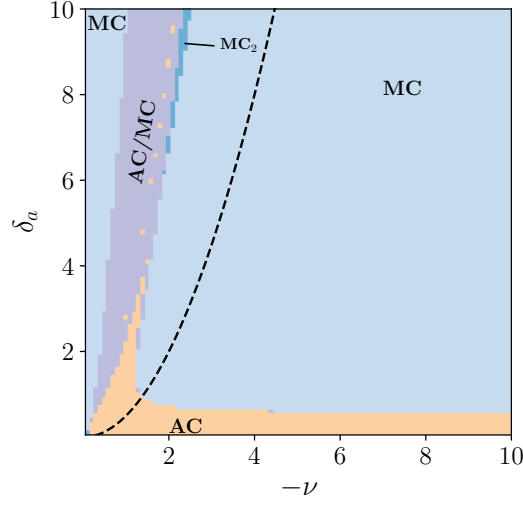


Figure 3.7: Phase diagram obtained from solutions of Eq. (3.60). Parameters used:  $\gamma_a = 0.1$ ,  $\lambda = 0.5$ ,  $u_a = 1$ ,  $\eta = 0.005$ ,  $g = 1$ ,  $u_{am} = 0$ . The different phases denoted in the phase diagram are defined in table 3.1. For reference, we denoted the line where the atomic detuning is equal to half the molecule binding energy  $\delta_a = |E_b|/2$ , as a dashed black line. Here it doesn't seem to be of importance, but this will change when molecule-molecule interactions are properly taken into account.

Although we decoupled the quartic term present in the bare action when we introduced the molecule-field, the quartic interaction term would be regenerated in the full expression for the effective action. Hence we include such a term phenomenologically at the level of the field equations derived from the 1-loop approximation, in order to allow for a stable atomic condensate phase.

After finding the mean-field solutions we perform stability analysis by considering the retarded Green's function

$$(G^R)^{-1} = \frac{\delta^2 S[\phi_c, \psi_c]}{\delta\psi_q^* \delta\psi_c}. \quad (3.61)$$

From the poles of the Green's functions in Eq. (3.61) we obtain the following quasi-particle dispersion:

$$\omega_{a,\mathbf{k}} = -i\gamma_a \pm \sqrt{\left(\frac{\mathbf{k}^2}{2m} + \tilde{\delta}_a\right)^2 - |\tilde{\lambda}|^2} \quad (3.62)$$

with  $\tilde{\delta}_a = \delta_a + 2u_a|\psi_0|^2$ ,  $\tilde{\lambda} = \lambda + 2g\phi_0 - u_a\psi_0^2$ . We emphasize that at this point we do not take into account corrections to the quasi-particle dispersion due to fluctuations, which can lead for example to appearance effective molecule-molecule interactions and have important effect on the stability properties. We will deal with these effects on a more phenomenological level in Sec. 3.9.

In Fig. 3.7 we show a phase diagram resulting from solutions of Eq. (3.60). As a function of the atom detuning  $\delta_a$  and the detuning from resonance  $\nu$  we observe four different regimes of the phase diagram. When the magnitude of the atomic detuning  $|\delta_a|$  is below a threshold set by  $\lambda$ , only an AC condensate solution exists. For larger values of  $|\delta_a|$ , several regimes exist depending on the value of the detuning from resonance  $\nu$ . Far-away from resonance and also close to it, the only stable solution is that of a molecule condensate. For intermediate values of  $\nu$  the system exhibits two different bistable regions where several different steady-state solutions co-exist. We note that in Fig. 3.7 the value of the molecule binding energy does not seem to play a big role. We will see that this will change when we take the effect of molecule-molecule interaction into account. We will do this in Sec. 3.9 using a phenomenological mean-field model, which will also allow us to understand the origin of the different phases.

### 3.8.2 MOLECULE DYNAMICS

In this section we first compute the molecule Green's function in vacuum where  $\lambda = 0$  and  $\bar{\phi}_c, \bar{\psi}_c = 0$ . The computation is almost identical to the one we performed in the zero temperature equilibrium case in Sec. 3.2.2, since we already presented the computation in the Keldysh framework there. The main difference is that the imaginary parts obtained here are finite due to the external losses.

The single particle properties of the molecule are contained in the corresponding retarded and Keldysh Green's functions,  $D^R$  and  $D^K$ , respectively. Recall that  $D^R, D^K$  can be evaluated from the effective action using the definition [17]:

$$\begin{pmatrix} D^K & D^R \\ D^A & 0 \end{pmatrix}^{-1} = \begin{pmatrix} \frac{\delta^2 \Gamma}{\delta \phi_c^* \delta \phi_c} & \frac{\delta^2 \Gamma}{\delta \phi_q^* \delta \phi_q} \\ \frac{\delta^2 \Gamma}{\delta \phi_q^* \delta \phi_c} & \frac{\delta^2 \Gamma}{\delta \phi_q^* \delta \phi_q} \end{pmatrix}_{\bar{\phi}_c = \bar{\phi}_q = 0}, \quad (3.63)$$

where we only consider  $U(1)$  symmetric Green's functions, as the vacuum model is  $U(1)$ -symmetric and, accordingly, all the anomalous Green's functions are identically zero.

Let us first focus on  $(D^R)^{-1}$ , which encodes the spectral properties of the molecule. Plugging in the expansion in Eq. (3.59) we obtain

$$\begin{aligned} (D_{\text{vac}}^R)^{-1}(K) &= \frac{\delta^{(2)}}{\delta \bar{\phi}_q^*(K) \delta \bar{\phi}_c(K)} \left[ S - \frac{i}{2} \text{tr}(\mathcal{G}_0 V)^2 \right] \Big|_{\lambda, \bar{\phi}, \bar{\psi}=0} \\ &\equiv -\tilde{\nu} - i\eta - \Sigma_{\text{m,vac}}^R(K), \end{aligned} \quad (3.64)$$

where  $K \equiv (\omega, \mathbf{k})$  and we defined the retarded self-energy

$$\Sigma_{\text{m,vac}}^R(K) \equiv \frac{i}{2} \frac{\delta^{(2)}}{\delta \bar{\phi}_q^*(K) \delta \bar{\phi}_c(K)} \text{tr}(\mathcal{G}_0 V)^2 \Big|_{\lambda, \bar{\phi}, \bar{\psi}=0}. \quad (3.65)$$

In vacuum  $\Sigma^R$  is given by the diagram in Fig. 3.1b. As we explained in Sec. 3.2.2 the expression for  $D^R$  in Eq. (3.64) obtained from the 1-loop expansion of  $\Gamma$  is in fact exact in vacuum.

Performing the loop integration, similar to Sec. 3.2.2, we obtain the self-energy

$$\Sigma_{\text{m,vac}}^R(K) = \frac{g^2 m^{\frac{3}{2}}}{\pi} \sqrt{\frac{k^2}{4m} - i2\gamma_a - \omega} - \int_{\mathbf{q}} \frac{4g^2 m}{q^2}. \quad (3.66)$$

this expression is identical to Eq. (3.24) except of the fact that  $\gamma_a \neq 0$  is finite due to the finite loss.

The similarity to the equilibrium case can be understood by considering the fact that the main difference between the zero- $T$  Keldysh action and the action we consider here is that in the zero- $T$  case the Keldysh element of the inverse atom Green's function is  $P_{\text{eq}}^K(\omega) = 2i\epsilon\text{sign}(\omega)$  while here it is  $2i\gamma_a$ . Since the molecule self-energy in vacuum is obtained only from a particle-particle diagram, frequency integration results in evaluating the  $P^K(\omega)$  only at a positive frequency  $\omega = k^2/(2m) > 0$  where  $P_{\text{eq}}^K(\omega) = 2i\epsilon$ . This would not be the case when working with finite density where we expect to see differences between the equilibrium and dissipative case.

As in the equilibrium case we encounter the UV divergence, which is cured by introducing a counter term in the bare action  $\tilde{\nu} = \nu + \delta\nu$  such that  $\nu = 0$  is the resonance position and the scattering length is given by

$$a = -\frac{g^2 m}{\pi(\nu - i\eta)}. \quad (3.67)$$

Note that the presence of a finite two-body loss  $\eta \neq 0$  results in a complex scattering length. The result we obtained here is similar to the scenario of an optical Feshbach resonance where atoms are optically coupled to a molecular state with a finite lifetime [52].

It is interesting to note that although both the real and imaginary part of the bare molecule mass term  $(\tilde{\nu} - i\eta)$  have the same (bare) scaling dimension, we only need one real counter-term  $\delta\nu$  in order to absorb the UV divergence. This can be understood from the fact that the UV divergence occurs due to contributions from high momentum modes to the atom-atom scattering amplitude, which is encoded here in the self-energy of the auxiliary field  $\phi$ . At high momenta the kinetic energy dominates over other terms in the atom propagator, hence the UV contribution is real. This would no longer be true in the presence of diffusion, where the atom kinetic mass  $m$  can be complex. However since we are dealing with the quantum mechanical scattering problem in vacuum the atoms propagation remains completely coherent and  $m$  is strictly real. Also note that since the UV divergence appearing in the retarded self-energy is real, the Keldysh self-energy, which obeys  $\Sigma_m^K = 2\text{Im}\Sigma_m^R$  in vacuum, has no UV divergence.

Taking the renormalization of  $\nu$  into account, the molecule retarded Green's function is given by:

$$[D_{\text{vac}}^R(\omega, \mathbf{k})]^{-1} = -\nu + i\eta - \frac{g^2 m^{\frac{3}{2}}}{\pi} \sqrt{\frac{k^2}{4m} - i2\gamma_a - \omega} \quad (3.68)$$

The (complex) dispersion of the molecule  $\omega_{\text{m}}(\mathbf{k})$  corresponds to the pole of the retarded Green's function, hence the dispersion is obtained from the condition  $(D^R)^{-1}(\omega_{\text{m}}(\mathbf{k}), \mathbf{k}) = 0$ . Similar to the equilibrium case (Sec. 3.2.2) a pole exists only for  $\nu < 0$ , in which case:

$$\omega_{\text{m}}(\mathbf{k}) = \frac{k^2}{4m} + E_b - i\gamma_{\text{m}}, \quad (3.69)$$

where  $E_b$  describes the bound state energy and  $\gamma_m$  the molecule inverse lifetime, and are given by

$$E_b = -\frac{\pi^2(\nu^2 - \eta^2)}{g^4 m^3}, \quad \gamma_m = 2\left(\gamma_a - \frac{\pi^2 \eta \nu}{g^4 m^3}\right). \quad (3.70)$$

Let us comment on the properties of the molecule dispersion displayed by Eq. (3.69). First of all, as in equilibrium systems, the molecule acquires a dispersion quadratic in the momentum  $\mathbf{k}$ , with a mass corresponding to twice the mass of the single atoms. Moreover, in absence of single- and two-particle losses ( $\gamma_a$  and  $\eta$ , respectively), the molecule lifetime is expectedly infinite as  $\gamma_m = 0$ , and the binding energy  $E_b < 0$  recovers its equilibrium value [52]. While a finite value of single-particle losses  $\gamma_a$  only induces a finite molecule lifetime, the presence of finite two-body losses  $\eta$  affects both the molecule binding energy and life-time. In particular,  $E_b$  is reduced by the two particle losses, and eventually vanishes for  $\eta = |\nu|$ , indicating that the bound state breaks down and that the molecule ceases to be a well-defined degree of freedom. Moreover, a finite value of  $\eta$  also increases the molecule damping rate  $\gamma_m$  (notice that  $\nu < 0$ ).

We also notice that at the resonance,  $\nu = 0$ , the loss rate becomes  $\eta$  independent  $\text{Im}[\omega_m(k)] = 2\gamma_a$ . This means that at  $\nu = 0$  the molecule becomes decoupled from the two-particle loss process. Intuitively this can be understood by the fact that as  $\nu \rightarrow 0$  the extent of the molecule bound state becomes very large, such that the two bound-together atoms are on average far from each other. Since the two-particle loss is a local term acting only on two atoms which are in the same position, the two atoms will be less affected by it when they are in a bound state with a large extent.

#### SELF-ENERGY CORRECTIONS AT FINITE PUMP $\lambda \neq 0$

We now turn to analyze the effects of the two-particle pump on the spectral properties of the molecule as compared to the vacuum case. In the presence of finite  $\lambda$  we can no longer obtain exact results for the self-energy  $\Sigma_m^R$ . Furthermore as we will see later on in this chapter a finite value of  $\lambda$  necessarily implies a finite value of  $\bar{\phi}_c$ , hence the full 1-loop expression for the molecule self-energy includes contributions from all terms in the expansion (3.59)

$$\Sigma_\lambda^R[\bar{\phi}]_{ij} = i \frac{\delta^2}{\delta \bar{\Phi}_{q,i}^* \delta \bar{\Phi}_{c,j}} \left[ \sum_{n=2}^{\infty} \frac{(-1)^n}{n} \text{tr}(\mathcal{G}_0 V)^n \right], \quad (3.71)$$

where we introduced the Nambu spinor  $\Phi_\alpha^T(K) = (\phi_\alpha(K), \phi_\alpha^*(-K))$ . When the molecule condensate density is small we can neglect the  $n > 2$  terms in Eq. (3.72) and we remain with the contribution from the term  $\text{tr}(\mathcal{G}_0 V)^2$

$$\Sigma_\lambda^R[\bar{\phi}]_{ij} \approx \frac{i}{2} \frac{\delta^{(2)}}{\delta \bar{\Phi}_{q,i}^*(K) \delta \bar{\Phi}_{c,j}(K)} \text{tr}(\mathcal{G}_0 V)^2 \Big|_{\lambda \neq 0}. \quad (3.72)$$



The self-energy is obtained from the loop integrals

$$\Sigma_{\lambda,11}^R(K) = -4ig^2 \int_P [G_0^R]_{11}(K-P; \lambda) [G_0^K]_{11}(P; \lambda), \quad (3.73)$$

$$\Sigma_{\lambda,12}^R(K) = -2ig^2 \int_P [G_0^K]_{12}(K+P; \lambda) [G_0^R]_{12}(P; \lambda). \quad (3.74)$$

Where here  $G_0(P; \lambda)$  denotes the bare atom Green's function in the presence of two particle pump (introduced in Sec. 3.7). The expression in Eq. (3.73) is structurally similar to the expression obtained in the vacuum case, however due to the presence of finite  $\lambda$  we can no longer evaluate the full integrals analytically. We can expand the atom Green's functions in powers of  $\lambda$  to obtain a perturbative analytical expression for the momentum independent parts of the self-energy. Performing the integrations using *Mathematica* we obtain the leading correction for the self-energy (of order  $\lambda^2$ ):

$$\Sigma_{11,(2)}^R(\omega_0, 0) = -i \frac{m^{3/2} g^2 \lambda^2}{2\sqrt{2}\pi\gamma_a^2} \left( \frac{\gamma_a \sqrt{\Delta_a - \omega_0/2}}{|\Delta_a - \omega_0/2|} - 2\text{Im}\sqrt{\Delta_a - \omega_0/2} \right) \quad (3.75)$$

$$\Sigma_{12,(2)}^R(\omega_0, 0) = \frac{m^{3/2} g^2 \lambda^2}{2\sqrt{2}\pi\gamma_a^2} \left( \sqrt{\Delta_a^* - \omega_0/2} - 1/\sqrt{\Delta_a - \omega_0/2} \right) \quad (3.76)$$

where we denoted the complex atom detuning  $\Delta_a = \delta_a + i\gamma_a$ . The shift in the binding energy<sup>2</sup> can be estimated from  $-\text{Re}\Sigma_{11,(2)}^R(-|E_b|, 0) \sim -\sin(\arg(\Delta_a + |E_b|))\lambda^2/(\gamma_a \sqrt{|\Delta_a + |E_b||}) < 0$ .

We compute  $\Sigma_\lambda^R$  numerically and obtain the spectrum of molecule excitations solving the equation  $\det(D^R)^{-1}(\omega, \mathbf{k}) = 0$ . In Fig. 3.8 we show a comparison between the excitation spectrum in vacuum and the spectrum with finite  $\lambda$ . We can see that the two-particle pump lowers the binding energy of the molecule and in addition it has the effect of slightly increasing the effective mass of the molecule as can be obtained numerically from the kinetic energy coefficient (the coefficient of  $k^2$  in the molecule dispersion). We also note that when the pump is weak, the molecule spectrum is qualitatively similar to the vacuum one, at least at low momenta. From this we conclude that in order to simplify the initial exploration of the phase diagram of our system it is reasonable to neglect the molecule self-energy corrections due to finite  $\lambda$ .

### 3.8.3 MOLECULE-MOLECULE INTERACTIONS

In order to perform stability-analysis of the steady-state solutions obtained from the field equations, it is important to include molecule-molecule interaction processes that will be generated due to atomic fluctuations, as interactions are crucial for the stabilization of condensates. Since the two-particle pump  $\lambda$  breaks  $U(1)$  symmetry explicitly, it will in principle lead to the generation of non-charge conserving interaction terms. At order  $O(\lambda^0)$  (that is in the absence of two-particle pump) only charge-conserving interactions are generated. For an initial analysis of the model we will neglect the effect of interaction couplings which do not conserve charge, as

<sup>2</sup>Note that in the presence of finite  $\lambda$  corrections, the molecule binding energy is less well defined since the off-diagonal terms will tend to induce pairing correlations in momentum space.

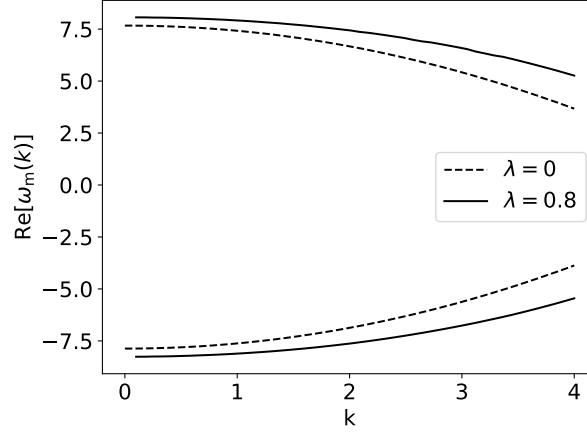


Figure 3.8: Molecule spectrum in the presence of finite two-particle pump, as obtained from solving  $\det(D^R)^{-1}(\omega^*, k) = 0$ . Numerical parameter values:  $\lambda = 0.8, \delta_a = 1, \gamma_a = 0.1, g = 1, \nu = -1, \eta = 0$ .

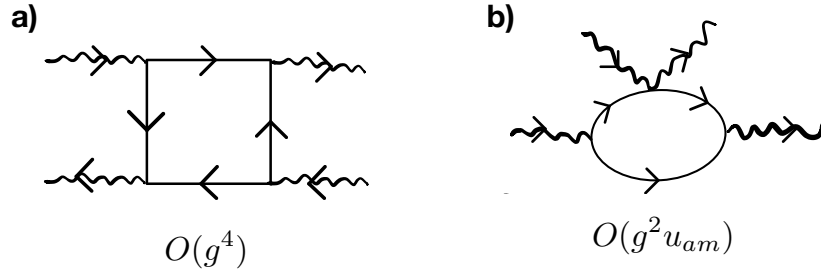


Figure 3.9: Diagrams contributing to molecule-molecule interaction in vacuum. (a) The contribution from  $\text{tr}(G_0 V)^4$  in Eq. (3.59). (b) The contribution from  $\text{tr}(\mathcal{G}_0 V)^3$  term in Eq. (3.59) which is due to the 3-body interactions. Note that the contribution from diagram (a) alone results in an attractive molecule-molecule interaction, and the contribution from (b) is necessary for the molecule-molecule interaction to be repulsive.

those are generated at higher orders in  $\lambda$ . We find that the atom fluctuations generate an effective quartic molecule-molecule interaction:  $\sim |\phi|^4$ , where the corresponding diagrams are shown in Fig. 3.9.

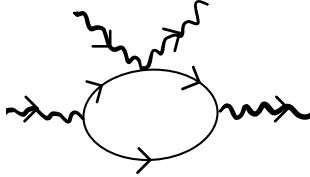
To organize the computation we introduce further notation:

$$V \equiv gV_g + u_{am}V_{am} = S_g^{(2)} + S_{am}^{(2)} \quad (3.77)$$

$$V_g = \begin{pmatrix} V_{g,\phi} & V_{g,\psi} \\ V_{g,\psi}^* & 0 \end{pmatrix} \quad (3.78)$$

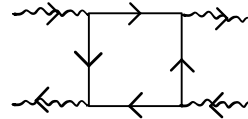
$$V_{am} = \begin{pmatrix} V_{am,\phi\phi} & V_{am,\psi\phi} \\ V_{am,\psi\phi}^\dagger & V_{am,\psi\psi} \end{pmatrix} \quad (3.79)$$

The first diagram, which arises only in the case of non-vanishing atom-molecule coupling  $u_{am}$ , arises from the term  $\frac{1}{3}\text{tr}(\mathcal{G}_0 V)^3$  in Eq. (3.59). Here we evaluate it in the vacuum limit  $\lambda, \bar{\phi}_c, \bar{\psi}_c = 0$



$$= ig^2 u_{am} \text{tr}(G_0 V_{g,\phi} G_0 V_{g,\phi} G_0 V_{am,\phi\phi}) \equiv I_3, \quad (3.80)$$

with  $G_0$  denoting the bare atom Green's function in the absence of pump ( $\lambda = 0$ ). The second diagram we need to compute is obtained from the  $\text{tr}(\mathcal{G}_0 V)^4$  term in Eq. (3.59), and arises only due to the Yukawa coupling



$$= -\frac{ig^4}{4} \text{tr}(G_0 V_{g,\phi})^4 \equiv I_4 \quad (3.81)$$

In order to obtain  $u_m$ , we compute the coefficient of the term  $\bar{\phi}_q^* \bar{\phi}_c |\bar{\phi}_c|^2$  as we expect all non-vanishing terms to have the same coefficient, due to the fact that the dissipative-vacuum is equivalent to the equilibrium vacuum in the limit  $\gamma_a \rightarrow 0$ . We also use the fact that in vacuum we have  $G_{11}^K = G_{11}^R - G_{11}^A$ .

In principle evaluating the diagrams in Eqs. (3.80), (3.81) at non-vanishing external momenta and frequencies will lead to momentum and energy dependent interaction vertices. And often used approximation, in the so-called derivative expansion of the action, is to neglect the complicated momentum dependence and approximate  $u_m(K_1, K_2, K_3, K_4) \approx u_m(0, 0, 0, 0)$ . In the case of negative detuning when a molecule bound-state with energy  $-|E_b|$  exists, it is more appropriate to approximate  $u_m$  by evaluating the diagrams at external frequencies corresponding to the molecule binding energy  $u_m \approx u_m(\omega_i = -|E_b|)$ .

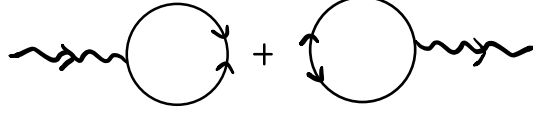


Figure 3.10: The leading contribution at finite pump, generating an effective molecule pump term  $\sim \lambda_m \bar{\phi}_q + c.c.$

We thus obtain:

$$\begin{aligned} \frac{1}{2} \delta_{\bar{\phi}_q^* \bar{\phi}_c^* \bar{\phi}_c \bar{\phi}_c} I_3 / (-i 16 g^2 u_{am}) = \\ \int_K \left[ G^A(-K + P_0) G^R(-K + P_0) G^R(K + P_0) + G^R(-K + P_0)^2 G^R(K + P_0) \right. \\ \left. - G^A(-K + P_0) G^A(-K + P_0) G^R(K + P_0) \right], \end{aligned} \quad (3.82)$$

$$\begin{aligned} \frac{1}{2} \delta_{\phi_q^* \phi_c^* \phi_c \phi_c} I_4 / (32 g^4 i) = \\ \int_K G^K(K + P_0) G^A(K + P_0) G^R(-K + P_0) [G^R(-K + P_0) + G^R(K + P_0)], \end{aligned} \quad (3.83)$$

where we denoted  $K \equiv (\omega, \mathbf{k})$ ,  $P_0 \equiv (-|E_b|/2, 0)$ , and  $G_{11}^x = G^x$ . Performing the integration in *Mathematica* we obtain

$$u_m = \frac{g^2}{\pi \sqrt{\delta_a + |E_b|/2}} \left( 3\sqrt{2} u_{am} - \frac{g^2}{4\sqrt{2}(\delta_a + |E_b|/2)} \right) \quad (3.84)$$

Note that in the absence of the atom-molecule interaction,  $u_{am} = 0$ , the effective molecule-molecule interaction is attractive  $u_m < 0$ . This shows that a finite  $u_{am}$  is needed in order to stabilize a molecule condensate, as an attractive interaction cannot stabilize the molecule condensate, as was also pointed out in the equilibrium context in Refs. [84, 109].

#### 3.8.4 EFFECTIVE MOLECULE PUMP

In this section we compute the leading order to the effective-action at  $\lambda \neq 0$ , which arises from the term  $\text{tr} G_0 V$  in Eq. (3.59), represented by the diagrams in Fig. 3.10. This leads to a linear term in the effective-action

$$\Gamma_1[\bar{\phi}, \bar{\psi}] = \lambda_m \bar{\phi}_q + c.c. \quad (3.85)$$

Due to probability conservation no terms linear in  $\bar{\phi}_c$  can appear as it will imply finite value of  $\bar{\phi}_q$ . Also note that due to the  $\mathbb{Z}_2$  symmetry of the bare-action  $S$  (corresponding to  $\psi \rightarrow -\psi$ ) no effective single-particle pump term  $\sim \bar{\psi}_q$  can be generated.

Evaluating the first diagram in Fig. 3.10 we obtain

$$\lambda_m = 2ig \int_{\omega, \mathbf{k}} [G_0^K]_{12}(\omega, \mathbf{k}; \lambda). \quad (3.86)$$

Recall that  $[G_0^K]_{12}(\omega, \mathbf{k}; \lambda) \equiv \langle \psi_c(\omega, \mathbf{k}) \psi_c^*(-\omega, -\mathbf{k}) \rangle$ , hence the effective molecule pump is proportional to the atomic off-diagonal correlations  $\langle \hat{\psi}^2 \rangle$ .

In the limit of small pump  $\lambda \ll \gamma_a, \delta_a$ , we can approximate Eq. (3.86) to leading order in  $\lambda$ . Performing the loop integral we obtain

$$\lambda_m = -\frac{\sqrt{2}gm^{3/2}\lambda}{\pi}\sqrt{\Delta_a^*} + \frac{2gm\lambda\Lambda_{\text{pump}}}{\pi^2}. \quad (3.87)$$

where  $\Delta_a = \delta_a + i\gamma_a$  is the complex atom-detuning as before. Here we denoted by  $\Lambda_{\text{pump}}$  a momentum cutoff for the pump.  $\Lambda_{\text{pump}}$  arises due to the fact that the two-particle wave function of a pair created by the coherent pump is not localized at a point but rather has a finite extent with some scale  $a_p$  which is much larger than the microscopic short-length scale (given typically by the van der Waals length  $a_{\text{vdW}}$ ).

In order to eliminate the dependence of the action on the cutoff  $\Lambda_{\text{pump}}$  we can use the additive renormalization procedure, similar to the one we introduced for the bare detuning  $\tilde{n}u$  in Sec. 3.2.2. To do so we add a “counter-term” of the form  $\delta\lambda_m\phi_q^* + c.c.$  to the bare molecule action in Eq. (3.45a). In order to determine the value of  $\delta\lambda_m$ , we need to choose a renormalization condition, which connects  $\lambda_m$  to some physical parameter. In the case of the detuning  $\tilde{\nu}$  we chose  $\delta\nu$  such that the scattering resonance occurs at  $\nu = 0$  which allowed us to connect the renormalized parameter  $\nu$  to the physical parameter which is the scattering length  $a$ . For  $\lambda_m$  we will make the simple choice that

$$\delta\lambda_m = -\frac{2gm^{3/2}\lambda\Lambda_{\text{pump}}}{\pi^2}. \quad (3.88)$$

This choice guarantees that  $\lambda_m|_{\lambda=0} = 0$ , that is that we don’t induce any molecule pump in the absence of a two-particle atom pump.

We can rewrite the cutoff independent part of Eq. (3.87) as  $\lambda_m \propto (\lambda/|\Delta_a|)|\Delta_a|^{3/2}$ . If we take the limit  $|\Delta_a| \rightarrow 0$  while keeping the ratio  $\alpha = \lambda/|\Delta_a|$  fixed at  $\alpha \gg 1$  to satisfy the weak pumping limit, we see that  $\lambda_m$  vanishes as  $|\Delta_a|^{3/2}$ . Physically this could be understood from the fact that in this limit the two-particle pump is resonant with the atoms which means that it will mostly pump atom pairs instead of molecules.

## 3.8.5 SUMMARY OF THE APPROXIMATE ATOM-MOLECULE EFFECTIVE ACTION

Summarizing all the contributions to the effective-action discussed in the previous sections we end up with:

$$\Gamma = \Gamma_a + \Gamma_{m,\text{eff}} + \Gamma_{\text{am}}, \quad (3.89a)$$

$$\Gamma_a = \int_{t,\mathbf{r}} \bar{\psi}_q^* \left( i\partial_t + \frac{\nabla^2}{2m} - \delta_a + i\gamma_a \right) \bar{\psi}_c + \lambda \bar{\psi}_q^* \bar{\psi}_c^* + c.c. + 2i\gamma_a \bar{\psi}_q^* \bar{\psi}_q \quad (3.89b)$$

$$- u_a \int_{t,\mathbf{r}} \bar{\psi}_q^* \bar{\psi}_c [\bar{\psi}_c^* \bar{\psi}_c + \bar{\psi}_q^* \bar{\psi}_q] + c.c., \quad (3.89c)$$

$$\Gamma_{m,\text{eff}} = \int_{t,\mathbf{r}} \left[ Z_m \bar{\phi}_q^* \left( i\partial_t + \frac{\nabla^2}{4m} - \delta_m + i\gamma_m \right) \bar{\phi}_c + c.c. + 2i\gamma_m |\bar{\phi}_q|^2 + \lambda_m \bar{\phi}_q + \lambda_m^* \bar{\phi}_q^* \right] \quad (3.89d)$$

$$- u_m \int_{t,\mathbf{r}} \bar{\phi}_q^* \bar{\phi}_c [\bar{\phi}_c^* \bar{\phi}_c + \bar{\phi}_q^* \bar{\phi}_q] + c.c.,$$

$$\Gamma_{\text{am}} = g \int_{t,\mathbf{r}} [2\bar{\phi}_c^* \bar{\psi}_c \bar{\psi}_q + \bar{\phi}_q^* (\bar{\psi}_c \bar{\psi}_c + \bar{\psi}_q \bar{\psi}_q) + c.c.] \quad (3.89e)$$

$$- u_{am} \int_{t,\mathbf{r}} [\bar{\phi}_q^* \bar{\phi}_c (|\bar{\psi}_c|^2 + |\bar{\psi}_q|^2) + \bar{\psi}_q^* \bar{\psi}_c (|\bar{\phi}_c|^2 + |\bar{\phi}_q|^2) + c.c.]. \quad (3.89f)$$

The quadratic part of  $\Gamma_m$  in Eq. (3.89d) was obtained from the single particle pole in the molecule propagator given in Eq. (3.68). This was done by writing  $D_{\text{vac}}^R$  in the form:

$$D_{\text{vac}}^R = \frac{Z_m^{-1}}{\omega - \omega_m(k)} + f(\omega, k) \quad (3.90)$$

with  $\omega_m$  given in Eq. (3.69) and  $f$  an analytic function around  $\omega_m(k)$ , which we neglect (structureless background of scattering states). Doing so we obtain :

$$\delta_m = 2\delta_a - \frac{\pi^2(\nu^2 - \eta^2)}{g^4 m^3}, \quad \gamma_m = 2\left(\gamma_a + \frac{\pi^2 \eta |\nu|}{g^4 m^3}\right), \quad Z_m^{-1} = \frac{2\pi^2}{g^4 m^3}(i\eta - \nu). \quad (3.91)$$

Note that the molecule propagator residue  $Z_m^{-1}$  is vanishing at the resonance point  $\nu \rightarrow 0, \eta \rightarrow 0$ , where our approximation breaks down. This is a manifestation of the fact that the molecule state becomes unbound, hence the propagator of the field  $\phi$  encodes only atom-atom scattering.

In order to include other effects giving rise to a residual effective repulsion between the atoms, we also included a repulsive atom-atom interaction parametrized by  $u_a > 0$ . Although this term is absent in the bare action obtained after the HS transformation, it would be nevertheless be generated by fluctuations. Including this term is crucial for obtaining stable steady state solutions in the saddle-point analysis that follows.

## 3.8.6 EFIMOV BOUND STATES

A well known phenomenon that occurs in a system of interacting Bosons at a scattering resonance is the appearance of an infinite tower of 3-body bound states called Efimov states [89]. In ultracold atom systems the presence of Efimov bound states results in large 3-body losses, and it is in fact one of the main obstacles for an experimental realization of a unitary Bose-gas with finite density. In this section we examine the effect of the coherent pump and losses present in our model on the Efimov states.

In this section we show that understanding the fate of Efimov bound states in the presence of loss and pump can be done using a functional-renormalization group (FRG) framework, which was originally used in the zero- $T$  equilibrium case in Ref. [91]. In FRG one considers the effective action at scale  $k$ , denoted  $\Gamma_k$ .  $\Gamma_k$  is the action obtained by integrating all quantum and classical fluctuations with momenta  $q \in [k, \Lambda]$ , where  $\Lambda$  is the UV-cutoff. Starting from the action at the UV scale  $\Gamma_\Lambda = S$  [given by Eqs. (3.44) - (3.45)], we can obtain the effective action  $\Gamma_k$  using the formally exact Wetterich equation [110]

$$\partial_k \Gamma_k = \frac{i}{2} \text{Tr} \left[ \partial_k R_k (\Gamma_k^{(2)} + R_k)^{-1} \right] \equiv \frac{i}{2} \text{Tr} \tilde{\partial}_k \log (\Gamma_k^{(2)} + R_k). \quad (3.92)$$

Here  $R_k$  is an IR cutoff function which suppresses fluctuations at all momenta  $q < k$  with  $k$  the running cutoff scale.  $\Gamma_k^{(2)}$  is the second variation of the effective action with respect to the fields, and the trace is take over all momenta, frequencies and Keldysh indices. The scale derivative  $\tilde{\partial}_k$  is defined as acting only on the cutoff function  $R_k$ , this allows us to represent the RHS of Eq. (3.144) in terms of an expansion in Feynman diagrams. It is also useful to define  $t = \log(k/\Lambda)$  such that the flow starts from  $t = 0$  and flows toward  $t = -\infty$ .

The object of interest is the scale dependent atom-molecule coupling  $u_{am}(t)$  appearing in Eq. (3.45c). In the FRG framework Efimov bound states are expected to be manifested as periodic divergences in  $u_{am}(t)$  during the RG flow, where divergences occurs at momenta determined by the 3-body bound-state energies [89]. In the RG language the Efimov effect is manifested as a limit-cycle flow.

The flow equation for  $u_{am}$  is depicted diagrammatically in Fig. 3.11. Since the dependence on the two-particle pump strength  $\lambda$  comes only from atom Green's functions, and there are no diagrams containing off-diagonal Green's functions in the flow equation, the leading order correction will be of order  $O(\lambda^2)$  which we neglect.

It has been shown in Ref. [91] that in order to obtain the periodic limit cycle behavior, it is enough to work in a point approximation where momentum dependence of  $u_{am}$  is neglected (this does not produce an accurate quantitative value for the limit cycle period). Using the point approximation we evaluate the diagrams in Fig. 3.11 and obtain the flow equation for  $u_{am}$ . See App. 3.C for details of the FRG computation.

Solutions of the flow equations for different values of the atom-detuning  $\delta_a$  and atom loss  $\delta_a$  are shown in Fig. 3.12. We see that introducing even a small drive frequency of order  $10^{-1}$ , no divergences are encountered during the flow. This is a manifestation of the fact that  $\delta_a$  and  $\gamma_a$  act as relevant perturbations taking the system away from the unitary point.

From the RG computation we see that for finite  $\delta_a$  and  $\gamma_a$ , the system is in a regime where either no Efimov states exist or maybe just one Efimov state is present (since the energy of the first

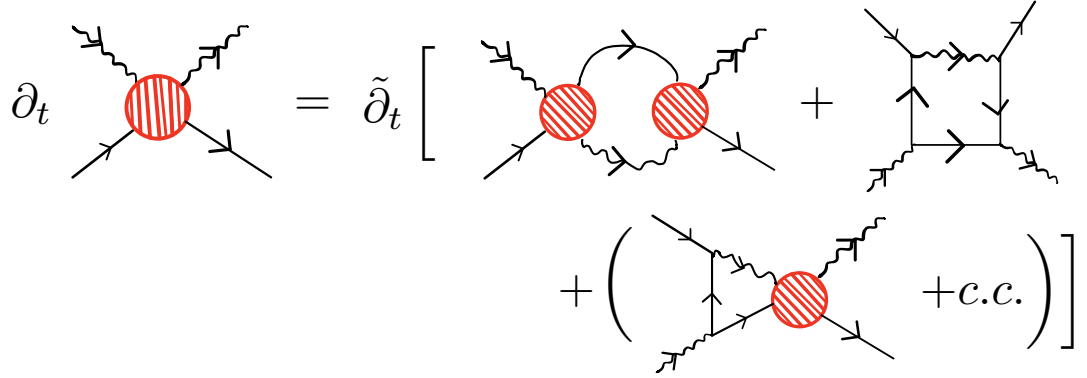


Figure 3.11: Diagrammatic representation of the FRG flow equation for the atom-molecule vertex  $u_{am}(t)$  (with  $t = \log(k/\Lambda)$ ). Solid lines denote atom propagators, wiggly lines denote molecule propagators and the red line-filled circle denotes the renormalized 3-body vertex.  $\tilde{\partial}_t$  acts only on the cutoff function  $R_k$ .

Even if the Efimov bound state is non-universal we cannot rule out this scenario based on our qualitative RG computation). Even if it is the case that the system supports an Efimov state, we expect it to not play an important role in determining the phase diagram of the system as long as the pump frequency is far enough detuned from the Efimov bound state energy  $E_{\text{efimov}}$ . Since there is no infinite-tower of Efimov states in the presence of pump and loss, we can work in a parameter regime of  $\nu$  and  $\delta_a$  where  $|E_{\text{efimov}}| \gg |E_b|, |\delta_a|$ .

### 3.9 UNDERSTANDING THE PHASE DIAGRAM FROM PHENOMENOLOGICAL MEAN-FIELD MODELS

In order to gain better understanding of the effects of different couplings in the effective action in Eq. (3.89), we consider in the following sections mean-field phase diagrams obtained in simplified settings where some of the couplings are not present. We will use phenomenological atom-molecule models inspired by the structure of the action (3.89), where we assume that the different couplings are independent of each-other. Ignoring the fact in principle some couplings depend on others when derived from the more microscopical bare action Eq. (3.45). Our approach here is somewhat similar to that taken in Refs. [41, 42], which studied condensation of molecules and atoms close to a Feshbach resonance using two-channel models.

The phenomenological mean-field equations we consider in this section are given by:

$$0 = \left( -\delta_a + i\gamma_a - u_a|\psi_0|^2 - u_{am}|\phi_0|^2 \right) \psi_0 + (\lambda + 2g\phi_0)\psi_0^* \quad (3.93a)$$

$$0 = \left( -\delta_m + i\gamma_m - u_m|\phi_0|^2 - u_{am}|\psi_0|^2 \right) \phi_0 + g\psi_0^2 + \lambda_m \quad (3.93b)$$

This set of phenomenological equations can be obtained from the approximate Eq. (3.89) by considering  $Z_m \approx 1$  and ignoring the dependence of  $Z_m$  on  $\nu$ . Away from resonance we expect that



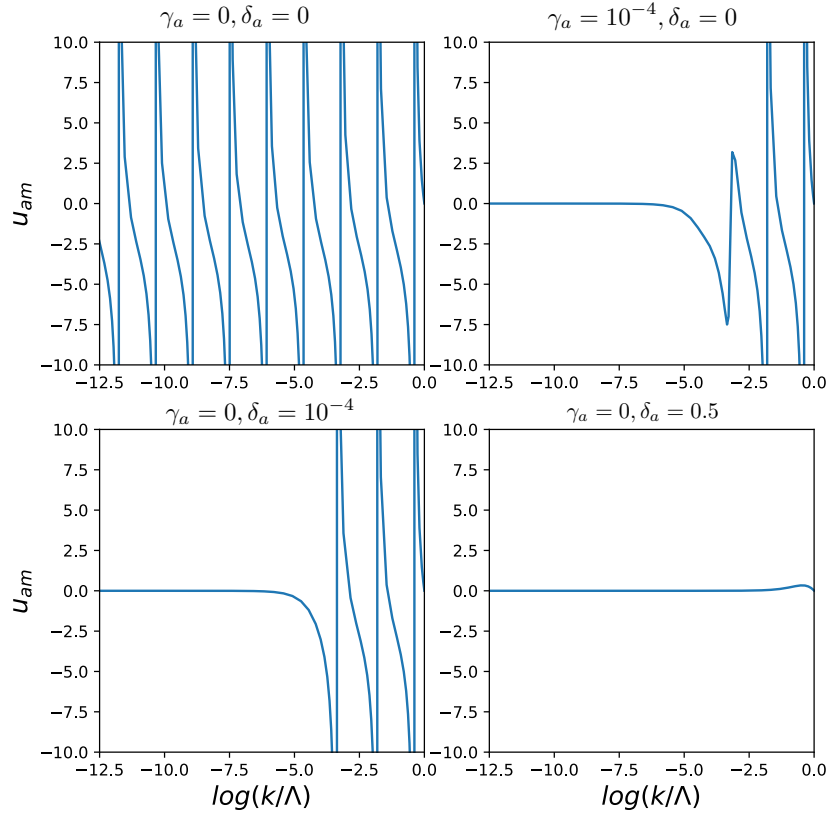


Figure 3.12: FRG flow of the atom-molecule coupling  $u_{am}$  obtained from numerical solution of the flow equation for  $u_{am}$ . **(upper-left)**: flow in the resonant case where  $\gamma_a, \eta, \delta_a, \nu = 0$  and  $u_{am}(\Lambda) = 0.1$  divergences during the flow are due to the presence of Efimov bound states. **(upper-right)** and **(lower-left)**: effects of very small deviations from resonance due to finite atom loss or finite drive frequency, only a few Efimov states exist at high-energies. **(lower-right)**: Introducing a drive frequency of order  $10^{-1}$  no Efimov bound states are encountered during the flow.

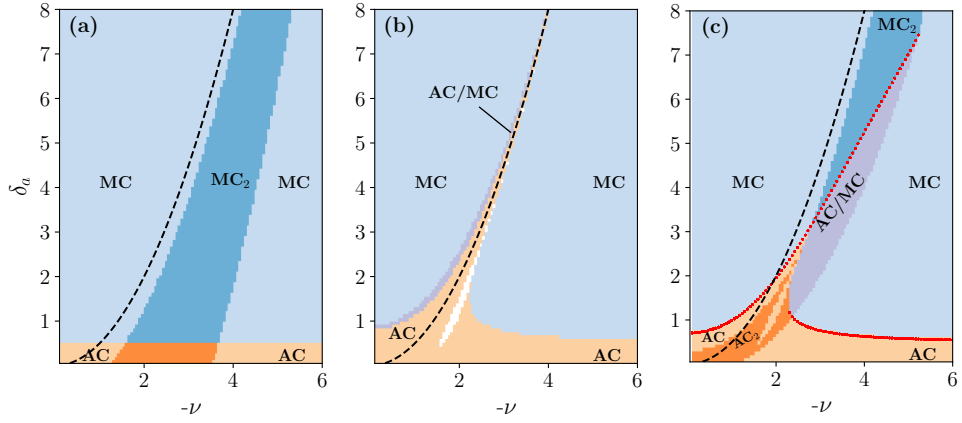


Figure 3.13: Phase diagrams obtained via solution of the mean-field equations of the phenomenological model Eq. . The dashed black line marks half the molecule binding energy in vacuum. (a) Phase diagram in the absence of atom-molecule coupling ( $g = 0$ ). (b) Phase diagram for the case of a non-interacting molecule ( $u_m = 0$ ) (c) Phase diagram for the full phenomenological model. See definition of the different phases in table 3.1. In all cases, the values of the parameters (when not explicitly set to zero) are:  $\gamma_a = 0.1$ ,  $\gamma_m = 0.2$ ,  $\lambda = 0.5$ ,  $\lambda_m = 1.0$ ,  $g = 1$ ,  $u_a = 1$ ,  $u_m = 0.5$ ,  $u_{am} = 0.1$ .

the results obtained in this way are qualitatively similar to the results obtained when taking  $Z_m$  into consideration. In addition we ignore the dependence of  $\lambda_m$  on  $\delta_a$ ,  $\gamma_a$ ,  $\lambda$  and replace it with a phenomenological constant which helps simplifying the analysis and focusing on the main physical phenomena. In order to connect with experimentally tunable parameters we retain the dependency of the molecular detuning  $\delta_m$  on the atom detuning  $\delta_a$  and the detuning from resonance  $\tilde{\nu}$ ,  $\delta_m = 2\delta_a - \frac{\pi^2 \tilde{\nu}^2}{g^4 m^3}$ .

The retarded Green's function  $\mathcal{G}^R = (\mathcal{P}^R)^{-1}$  used for stability analysis of fluctuation around the MF solution is given by:

$$\mathcal{P}^R = \begin{pmatrix} P_a^R & P_{am}^R \\ (P_{am}^R)^\dagger & P_m^R \end{pmatrix} \quad (3.94a)$$

$$P_a^R = \begin{pmatrix} \omega - \epsilon_{a,\mathbf{k}} + i\gamma_a - \frac{\partial \mathcal{U}}{\partial \rho_a} & \lambda_{\text{eff}} \\ \lambda_{\text{eff}} & -\omega - \epsilon_{a,\mathbf{k}} - i\gamma_a - \frac{\partial \mathcal{U}}{\partial \rho_a} \end{pmatrix} \quad (3.94b)$$

$$P_m^R = \begin{pmatrix} \omega - \epsilon_{m,\mathbf{k}} + i\gamma_m - \frac{\partial \mathcal{U}}{\partial \rho_m} & -u_m \phi_0^2 \\ -u_m (\phi_0^*)^2 & -\omega - \epsilon_{m,\mathbf{k}} - i\gamma_m - \frac{\partial \mathcal{U}}{\partial \rho_m} \end{pmatrix} \quad (3.94c)$$

$$P_{am}^R = \begin{pmatrix} -u_{am} \psi_0 \phi_0^* + 2g\psi_0^* & -u_{am} \phi_0 \psi_0 \\ -u_{am} \phi_0^* \psi_0^* & -u_{am} \phi_0 \psi_0^* + 2g\psi_0 \end{pmatrix} \quad (3.94d)$$

with  $\mathcal{U} = u_a \rho_a^2 + u_m \rho_m^2 + u_{am} \rho_a \rho_m$  and  $\lambda_{\text{eff}} = \lambda + 2g\phi_0 - u_a \psi_0^2$ .

The mean-field equations (3.93) are a set of multivariate polynomial equations in the real and imaginary parts of the condensate fields. As such they are generically not analytically solvable,

but there exist efficient numerical methods that are able to find all possible roots of multivariate-polynomials without requiring a good initial guess (unlike Newton methods for solving general non-linear equations). Specifically we use here the homotopy-continuation method as implemented by the Julia package *HomotopyContinuation.jl* [111].

In what follows, we consider several specific cases where some of the couplings are not present in Eq. (3.93). This allows us to obtain analytical expressions in some cases and to better understand the role of the different couplings.

### 3.9.1 CASE 1: ATOMS AND MOLECULES DECOUPLED ( $g = u_{am} = 0$ )

We start by analyzing the case where atoms and molecules are completely decoupled, that is we set  $g = 0, u_{am} = 0$  in Eq. (3.89). This allows us to consider the condensation mechanisms of atom and molecule degrees of freedom separately.

Considering steady-state homogeneous solutions, the saddle-point equations in the fully decoupled case are given by:

$$\left(-\delta_a + i\gamma_a - u_a|\psi_0|^2\right)\psi_0 + \lambda\psi_0^* = 0, \quad (3.95a)$$

$$\left(-\delta_m + i\gamma_m - u_m|\phi_0|^2\right)\phi_0 + \lambda_m = 0. \quad (3.95b)$$

Since the two equations are completely decoupled we can consider them separately.

#### CONDENSATION OF ATOMS WITH TWO-PARTICLE PUMP

We now discuss possible solutions of Eq. (3.95a) and analyze their stability properties. We already discussed the condensation instability due to two-particle pump in the  $u_a = 0$  case in Sec. 3.7. Here we generalize the discussion for the case  $u_a \neq 0$  which is crucial for having a stable condensate solution.

First we note that Eq. (3.95a) always has a trivial solution with  $\psi_0 = 0$  where atoms are not condensed, however this solution is not always stable as we will see below.

Let us consider solutions where  $\psi_0 \neq 0$ . In this case we can recast Eq. (3.95a) into a simple quadratic equation for the atomic condensate density  $\rho_a \equiv |\psi_0|^2$  by taking the absolute value:

$$(\delta_a + u_a\rho_a)^2 + \gamma_a^2 = |\lambda|^2, \quad (3.96)$$

$$\rho_a = \frac{-\Omega \pm \sqrt{\Omega^2 - u_a^2 r}}{u_a^2}, \quad (3.97)$$

where we denoted  $\Omega \equiv \delta_a u_a$  and  $r \equiv \delta_a^2 + \gamma_a^2 - |\lambda|^2$ . We are only interested in physical solutions where  $\rho_a \geq 0$ .

We consider only the case  $\delta_a > 0$  (the case  $\delta_a < 0$  leads to finite-momentum instability which we will not be considered in this work). Thus, we have  $\Omega > 0$  and positive solution for Eq. (3.97) exists only when  $r < 0$ . Hence, the condition on  $\lambda$  for atom condensation to occur is

$$|\lambda|^2 > \lambda_c^2 = \delta_a^2 + \gamma_a^2. \quad (3.98)$$

Expanding in small  $r$ , we see that close to the transition we have

$$|\psi_0| \approx \sqrt{-r}, \quad (r < 0, \quad |r|/\delta_a^2 \ll 1). \quad (3.99)$$

The trivial solution  $\psi_0 = 0$  is stable as long as the poles of the retarded Green's function, denoted by  $\omega_a(k)$ , lie in the lower half of the complex plane. In the case of  $\psi_0 = 0$  the atom retarded Green's function is identical to the non-interacting case discussed in Sec. 3.7. Examining the dispersion in Eq. (3.51) we see that the trivial solution is stable as long as  $|\lambda|^2 < \lambda_c^2$ . At the critical value of the pump strength we have  $\omega_a(k=0) = 0$  which indicates a closing of the dissipative gap and the system undergoes a second order phase transition into the atomic condensate phase.

Note that the inclusion of the atom-atom interaction  $u_a$  in the model is crucial in order to obtain a stable atom-condensate solution. In the presence of an atom-condensate the dispersion in Eq. (3.51) changes to

$$\omega_a(k) = -i\gamma_a \pm \sqrt{\left(\frac{k^2}{2m} + \delta_a + 2u_a|\psi_0|^2\right)^2 - |\lambda - u_a\psi_0^2|^2}. \quad (3.100)$$

Hence the atom-condensate occurring at  $|\lambda| > \lambda_c$  can be stable only when  $u_a > 0$ .

#### CONDENSATION OF MOLECULES WITH SINGLE-PARTICLE PUMP

We now turn to analyze the solutions for Eq. (3.95b). Equating the modulus of both sides of the equation, we obtain an equation for the molecule condensate density  $\rho_m \equiv |\phi_0|^2$ :

$$\rho_m = \frac{|\lambda_m|^2}{(\delta_m + u_m\rho_m)^2 + \gamma_m^2}. \quad (3.101)$$

We remind the reader that the molecule detuning is given by  $\delta_m = 2\delta_a - |E_b|$  with  $|E_b| \sim \tilde{\nu}^2$  the molecule binding energy. Unlike the case of atoms with two-particle pump, in the molecule case only solutions with  $\rho_m > 0$  exist. This is a manifestation of the fact that  $U(1)$  symmetry is explicitly broken by the two-particle pump.

In the case of  $u_m = 0$  we can see that the largest condensate value is obtained when  $\delta_m = 0$ , which occurs when  $\delta_a = |E_b|/2$ . Simply stated, the maximum value of the condensate occurs when the two-particle pump is resonant with the molecule bound state. In this case we have  $\rho_m = |\lambda_m|^2/\gamma_m^2$ .

In the interacting case,  $u_m \neq 0$ , the interaction shifts the condensate energy such that the effective detuning of the pump is  $\tilde{\delta}_m = \delta_m + u_m\rho_m$ . When  $\delta_m < 0$  (red-detuned) this can lead to a situation where the interaction induced detuning shift leads to  $\tilde{\delta}_m \approx 0$  and the pump becomes effectively resonant. In this case  $\rho_m$  increases with decreasing  $\delta_m$ .

Solving Eq. (3.101) we observe the behavior illustrated in Fig. 3.14. For  $\delta_m > 0$  ( $\delta_a > |E_b|/2$ ) there exist only one solution, which is similar to the non-interacting solution. For negative detuning  $\delta_m$  below some threshold  $\delta_1^*$  two stable solutions exist, we refer to these solutions “high-density condensate” and “low-density condensate”. The low-density solution behaves similar to the non-interacting case where the condensate density decreases as  $\delta_m$  is further increased beyond resonance at  $\delta_m \approx 0$ . The condensate density of the high-density solution keeps increasing as

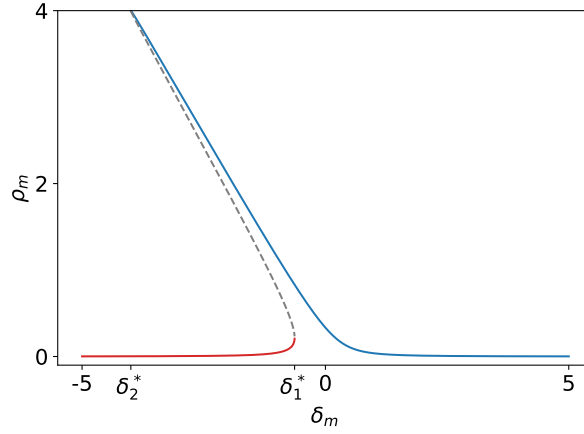


Figure 3.14: Behavior of molecule condensate with coherent molecule pump (solutions to Eq. (3.101)). When the detuning  $\delta_m$  is in the interval  $[\delta_2^*, \delta_1^*]$  the system is bistable with a “high-density condensate” solution (blue) and “low-density condensate” solution (red). The dashed gray line corresponds to an unstable solution.

$\delta_m$  is decreased. Once the system is red-detuned below a second critical value  $\delta_2^*$  the high-density solution no longer exist. This is related to the finite decay rate of molecules  $\gamma_m$ .

In addition to triggering a bi-stability the introduction of molecule interaction  $u_m$  also creates finite density of non-condensed molecules. Expanding in quadratic fluctuations around the saddle-point solution we obtain the expression for the non-condensed molecule density  $n_m(k)$

$$n_m(k) = \frac{u_m^2 \rho_m^2}{\left(\frac{k^2}{4m} + \delta_m + u_m \rho_m\right)^2 - u_m^2 \rho_m^2 + \gamma_m^2}. \quad (3.102)$$

We see that in our non-equilibrium setup  $n_m(k) \propto u_m^2 \rho_m^2$  which means that the fraction of non-condensed molecules increases with increasing  $\rho_m$ . This can be viewed as an increase of an effective temperature due to molecule-molecule interactions.

Having described the mechanisms for atom and molecule condensation in our setup, let us emphasize the differences between them. As we have seen the atom condensation due to two-particle pump is triggered by a closing of the dissipative gap and results in breaking of the  $\mathbb{Z}_2$  symmetry  $\psi \rightarrow -\psi$ , hence it is expected to be a sharp phase transition. In contrast the molecule condensate is always present due to the explicit breaking of the  $U(1)$  symmetry by the two-particle pump. There is however a crossover to a regime with high molecule condensate density which also shows bistability. Unlike the atom case no closing of a gap occurs for the molecule.

#### PHASE DIAGRAM IN THE DECOUPLED CASE

We are now in a position to understand the phase diagram obtained from the solution of Eqs. (3.95), which we show in Fig. 3.13a. Keep in mind that changing the detuning  $\nu$ , modifies only the molecule detuning, while changing the atom detuning changes both atom and molecule detuning simultaneously. As  $\delta_a$  is decreased below the pump strength  $\lambda$  the atoms become unstable

towards condensation due to the gap closing described above, this is the reason for the straight phase boundary between the AC phases and the MC phase. For  $\delta_a$  above the threshold set by the pump strength only molecule condensation occurs.

Detuning the system away from resonance (increasing  $-\nu$ ) has the effect of decreasing the pump detuning  $\delta_m$ . We see that the boundary between the MC region with a single low-density solution to the bistability region (MC2), where both a low-density and high-density molecule condensate solutions exist, follows roughly the dashed red curve which denotes the parameter values for which the pump is exactly at resonance with the molecule energy and  $\delta_m = 0$ . As the system is detuned further away from resonance the region with high-density solution terminates, due to molecule losses (weaker molecule losses will correspond to a broader bi-stability region). Finally, we note that the presence of the region where two AC solutions exist (denoted AC2) is only due to the coexistence of a molecule condensation bi-stability and atom condensation.

#### 3.9.2 DIGRESSION: BISTABILITY IN COHERENTLY DRIVEN OPEN SYSTEMS

We have seen that the presence of the molecule pump  $\lambda_m$ , leads to a bi-stability where several dynamically stable solutions to the mean-field equations exist. The existence of bistable regions will remain a feature of our mean-field phase diagram also when we switch on all interaction and couplings between atom and molecules. When several stable solutions exist in an equilibrium setting one determines the state of the system by choosing the solution which has the minimal free-energy value. In the non-equilibrium setting the notion of free-energy minimization does not exist, and one has to in principle consider the dynamical evolution of the system including noise and information of the initial state in order to determine the fate of the system in the bistable region.

The appearance of a bi-stability in mean-field solution of a coherently driven field is not surprising and has been discussed previously in the literature. It is known to occur in a variety of systems such as a single-cavity with Kerr non-linearity [106], driven-dissipative Bose-Hubbard model in an array of cavity resonators [107, 112–114], Rydberg-atoms lattices [115–117], and in driven-dissipative spin models [118–120]. The fate of the mean-field bi-stability when correlations are taken into account depends on the dimensionality of the system.

In Ref. [106] the case of an optical bi-stability in a single cavity with coherent drive and loss (also known as the Kerr model) was considered. In that case it is possible to obtain an analytic solution for the quasiprobability phase space distribution in the P representation. The analytical solution shows that when quantum fluctuations are considered, there is always a unique steady state in the single cavity case.

In our case in addition to quantum fluctuations, also classical spatial fluctuations of the condensate have to be taken into account in order to understand the fate of the bi-stability beyond the saddle-point solution. In 1D it was shown, using matrix-product operator techniques, that correlations beyond mean-field wash-out the bi-stability region and turn it into a crossover between the high-density and the low-density phases [119, 120]. In the case of the 2D driven-dissipative Bose-Hubbard model, calculations using the truncated Wigner approximation indicate that the bi-stability becomes a sharp first-order transition due to fluctuations [107, 121]. Since fluctuations usually play a more important role in lower-dimensional systems, it is not clear what is the fate of

the mean-field bi-stability in 3D. Indeed, in the infinite-dimensional limit mean-field is expected to be exact and the system will exhibit a true bi-stable behavior [118].

### 3.9.3 CASE 2: ATOMS COUPLED TO NON-INTERACTING MOLECULES

We now consider the case where atoms and molecules are coupled via the interconversion term  $g$ , but the molecule interactions  $u_m$  and atom-molecule interactions  $u_{am}$  are switched off. In this case the saddle-point equations for the steady-state homogeneous configurations are

$$(-\delta_a + i\gamma_a - u_a|\psi_0|^2)\psi_0 + (\lambda + 2g\phi_0)\psi_0^* = 0, \quad (3.103a)$$

$$(-\delta_m + i\gamma_m)\phi_0 + g\psi_0^2 + \lambda_m = 0. \quad (3.103b)$$

From Eq. (3.103b) we obtain an expression for  $\phi_0$

$$\phi_0 = \frac{g\psi_0^2 + \lambda_m}{\delta_m - i\gamma_m}. \quad (3.104)$$

Plugging Eq. (3.104) in Eq. (3.103a) and taking the absolute value, we obtain an equation for the atom condensate density  $\rho_a$  which is exactly the same form as Eq. (3.96) but with effective interaction and pump

$$u_{a,\text{eff}} = u_a - \frac{2g^2}{\delta_m - i\gamma_m}, \quad (3.105)$$

$$\lambda_{\text{eff}} = \lambda + \frac{2g\lambda_m}{\delta_m - i\gamma_m}. \quad (3.106)$$

The interpretation of Eq. (3.106) is that the molecule condensate acts as an effective two-particle pump for the atoms (atom pairs can be created from the condensate). When the external two-particle pump frequency is on resonance with the molecule binding energy and  $\delta_m \approx 0$ , this can lead to a large enhancement of the two-particle pump amplitude experienced by the atoms and trigger atomic condensation. Also note that the effective interaction  $u_{a,\text{eff}}$  has an imaginary part, which means that the molecule condensate creates a two-particle loss for the atoms.

Looking for a non-trivial solution for  $\psi$ , the equation for the condensate density  $\rho_a$  is now given by

$$\rho_a = \frac{-\Omega_{\text{eff}} \pm \sqrt{\Omega_{\text{eff}}^2 - |u_{a,\text{eff}}|^2 r_{\text{eff}}}}{|u_{a,\text{eff}}|^2}. \quad (3.107)$$

with

$$\Omega_{\text{eff}} = (\delta_a \text{Re} u_{a,\text{eff}} - \gamma_a \text{Im} u_{a,\text{eff}}), \quad (3.108)$$

$$r_{\text{eff}} = \delta_a^2 + \gamma_a^2 - |\lambda_{\text{eff}}|^2. \quad (3.109)$$

If  $\Omega_{a,\text{eff}} > 0$  the condition for atom condensation is similar to the one discussed in Sec. 3.9.1

$$|\lambda_{\text{eff}}|^2 > \lambda_c^2 = \delta_a^2 + \gamma_a^2. \quad (3.110)$$

We also have to consider the case  $\Omega_{\text{eff}} < 0$  which might occur when  $u_{a,\text{eff}} < 0$  (effective attractive interactions). In this case there still exists a non-trivial atom condensate solution when  $|\lambda_{\text{eff}}| > \lambda_c$ . In addition there is a region with two non-trivial solutions (with different values for  $\rho_a$ ) when

$$\lambda_c^2 - \frac{\Omega_{\text{eff}}^2}{|u_{a,\text{eff}}|^2} < |\lambda_{\text{eff}}|^2 < \lambda_c^2. \quad (3.111)$$

Note that in this case the trivial solution with  $\rho_a = 0$  is still stable.

In Fig. 3.13b we show numerical solution of Eq. (3.103), taking into account also stability properties of the solutions. We indeed see that the effective pump for the atoms is enhanced in a region where  $|E_b| \approx 2\delta_a$ , which is manifested in atom condensation occurring in a region along the molecule bound state energy line (dashed black line).

In addition we see that a bistability region emerges, where both the AC and MC phase coexist. This occurs due to the fact that in that regime the effective mean-field atom interaction  $u_{a,\text{eff}}$  becomes attractive. As we saw above this leads to a situation where an atom condensate solution exists but the trivial solution with  $\rho_a = 0$  is also stable. We also note that the phase diagram has instability regions, where no saddle point solution is stable. The reason for this instability is that the effective attractive interaction for the atoms is not compensated by other repulsive mechanism, such as the ones provided by  $u_m, u_{am}$ , here neglected.

To summarize, from the analysis above we learn that the coupling of the atoms to a non-interacting molecule state acts as an effective two-particle pump for the atoms. Even when the strength of the bare two-particle pump  $|\lambda|$  is smaller than the critical pump strength for atom condensation  $\lambda_c$ , atom condensation can still occur if the effective pump is above threshold  $|\lambda_{\text{eff}}| > \lambda_c$ . This occurs when the pump frequency is in resonance with the molecule bound state energy. Thus, the atom-molecule coupling enables a new mechanism for atom condensation which can be triggered by tuning the pump frequency close to the molecule bound state energy.

### 3.9.4 CASE 3: ATOMS COUPLED TO INTERACTING MOLECULES

We now consider the case where both atoms and molecules are interacting, given by Eq. (3.93) with all interaction couplings present. In this case the features of the two previous cases are expected to merge. In particular, a bistability region with two MC solutions should emerge as a consequence of the molecule-molecule interaction. A numerical solution of the full set of equations is shown in Fig. 3.13c.

Due to the molecule interaction  $u_m$  we can no longer write an explicit solution for the molecule condensate  $\phi_0$  in terms of  $\psi_0$  alone. We can still understand intuitively the effect of finite molecule condensate  $\phi_0$  on the atoms by seeing that it enters Eq. (3.93a) in the same way as the two-particle pump term  $(\lambda + 2g\phi_0)\psi_0^*$ . Hence a large value of the molecule condensate density can create a large effective two-particle pump for the atoms and trigger atomic condensation.

Our intuition is confirmed by the numerical solutions of Eq. (3.93b) as seen in Fig. 3.13c. We see that a finite value of  $u_m$  gives rise to a region of molecule condensation bistability, whose origins were discussed in Sec. 3.9.1. As  $\nu$  is decreased the system exhibits an extended region where there exist an AC solution which breaks the  $\mathbb{Z}_2$  symmetry in addition to the low-density MC solution. This is due to the fact that the molecule condensate-density is increasing with decreasing  $\nu$  in the high-density MC solution (as we have seen in Fig. 3.14), hence at some point the effective



atom pump  $\lambda + 2g\phi_0$  reaches the critical value and a closing of the atom dissipative gap occurs, leading to atom condensation instability. Finally, we see that increasing the pump frequency  $\omega_p$  causes also the low-density MC solution to become unstable towards atom condensation, since it decreases the value of the critical pump strength  $\lambda_c$  below the value of the effective atom pump.

Finally, we can consider the effect of the atom-molecule interaction term  $u_{am}|\psi_0|^2|\phi_0|^2$ . In the presence of the atom-molecule interaction the atom dispersion in the MC phase ( $\psi_0 = 0$ ) is given by

$$\omega_a(\mathbf{k}) = -i\gamma_a \pm \sqrt{[k^2/(2m) + \delta_{a,\text{eff}}(\phi)]^2 - |\lambda_{\text{eff}}(\phi)|^2}, \quad (3.112)$$

where we denoted  $\lambda_{\text{eff}}(\phi_0) \equiv 2g\phi_0 + \lambda$  and  $\delta_{a,\text{eff}}(\phi) \equiv \delta_a + u_{am}|\phi_0|^2$ . Hence, the molecule condensate has two competing effects : (i) increasing the effective pump, which leads to decrease of the atom dissipative gap (ii) increasing the effective atom detuning, which increases the atom dissipative gap.

Having examined the phase diagrams obtained by numerical solution of Eq. (3.93) we can now examine the condition for an atom condensation instability in order to obtain an equation determining some of the phase boundaries. Specifically, let us consider the condition for a transition between a solution with only molecule condensate and a solution with an atom condensate. In the case of a second-order phase transition, the condition for the transition can be obtained by assuming  $|\psi_0| = \epsilon \ll 1$  in Eq. (3.93a) and then taking the limit  $\epsilon \rightarrow 0$  which results in a condition

$$|\lambda_c|^2 \equiv |(\delta_a - i\gamma_a + u_{am}|\phi_0|^2)|^2 = |\lambda + 2g\phi_0|^2 \equiv |\lambda_{\text{eff}}|^2 \quad (3.113)$$

plugging Eq. (3.93b) we obtain

$$|\tilde{\Delta}_m|^4 [(\delta_a + u_{am}\rho_m)^2 + \gamma_a^2] = \left[ |\tilde{\Delta}_m|^2 \lambda - \lambda_m(\delta_m + u_m\rho_m) \right]^2 + (\gamma_m\lambda_m)^2 \quad (3.114)$$

with  $\tilde{\Delta}_m \equiv \delta_m + u_m\rho_m - i\gamma_m$ .

We solve Eq. (3.114) numerically and plot the phase boundary curves  $(\nu_c, \delta_{a,c})$  on top of the phase-diagram in Fig. 3.13. This allows us to identify phase boundaries which correspond to a second-order transition (when the system follows one of the solution branches in the case of a bistability), corresponding to the red curves. On the converse, phase boundaries in Fig. 3.13c where condition (3.113) is not satisfied are expected to correspond to first order transitions. It also confirms that the MC-AC transition is indeed a consequence of the atomic gap closing due to the molecule condensate acting as an effective pump as we discussed in Sec. 3.9.3.

### 3.9.5 CHARACTERIZATION OF THE PHASES

We now turn to characterize some observable properties of the different phases. First let us look at the dependence of the order parameters  $\rho_a, \rho_m$  as a function of the detuning from resonance  $\nu$ . This is shown in Fig. 3.15 for different values of  $\delta_a$ . For relatively large atom detuning  $\delta_a = 5.5$  (Fig. 3.15a) starting from  $\nu \approx -2$  and increasing the detuning away from resonance we see that the molecule condensate density  $\rho_m$  continuously increases with increasing  $|\nu|$ . When the high-density branch of  $\rho_m$  reaches a critical value at  $\nu = \nu_c$  it triggers atom condensation and a new solution with  $\rho_a > 0$  emerges, as expected. In addition we see the emergence of a low-density

### 3 Condensate phases of coherently driven bosons close to a scattering resonance

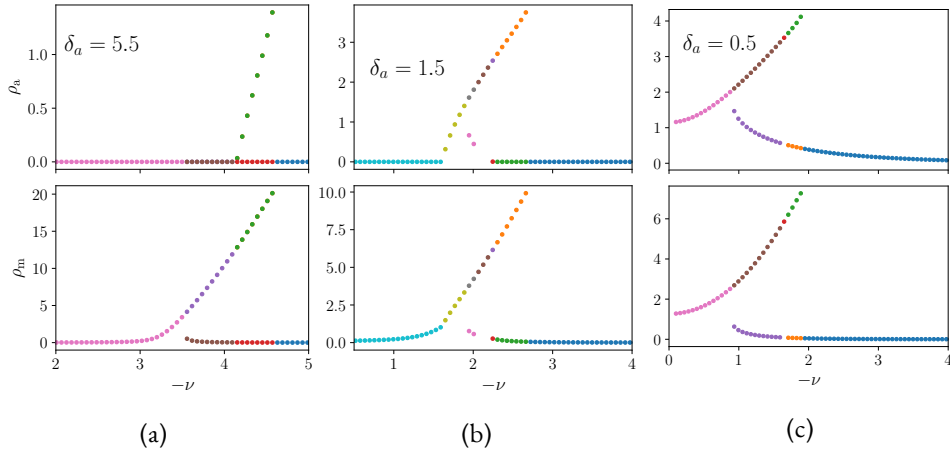


Figure 3.15: Condensate densities as a function of the detuning  $\nu$  for different values of the atomic detuning  $\delta_a$  corresponding to horizontal cuts in the phase diagram in Fig. 3.13c. In all cases we see that at large  $|\nu|$  the high-density solutions become unstable and in the low density solution the condensate densities tend to zero.

branch  $0 < \rho_m \ll 1$  at  $\nu_b > \nu_c$ . For  $|\nu|$  large enough only the low-density MC solution exists and  $\rho_m$  decreases with increasing  $|\nu|$ .

For smaller value of atom detuning  $\delta_a = 1.5$ , shown in Fig. 3.15b, a slightly different scenario occurs. Here the atom condensation transition occurs before any bistability emerges. Furthermore we observe that for a small range of detuning values a bistability region exists with both a high density atom-molecule condensate solution and a low-density atom-molecule condensate solution. Finally at larger value of  $|\nu|$  the low-density molecule condensate solution emerges. We also observe that in the high-density atom-molecule condensate solution the  $\rho_a$  ( $\rho_m$ ) is higher (lower), as compared to the case with higher  $\delta_a$  (Fig. 3.15a).

When the atom detuning is below a threshold determined by the two-particle pump strength  $\lambda$ , an atom condensate solution always exists, as shown in Fig. 3.15c for  $\delta_a = 0.5$ . In this case, as  $|\nu|$  is increased a bistable region emerges with a low-density atom-molecule condensate solution. We see that lowering  $\delta_a$  results in even higher (lower) values of  $\rho_a$  ( $\rho_m$ ) as compared to the two previous cases. This is physically expected, since as we lower the atom detuning the two-particle pump becomes more resonant with the atoms and less resonant with the molecules.

Another useful quantity to consider is the atom photoluminescence, given in Eq. (3.56). The photoluminescence encodes both information about the excitation spectrum of the system and the occupation of excitations. In Fig. 3.16 we plot the atom photoluminescence for different values of  $\delta_a$  at a fixed  $\nu$ , exploring different phases. We observe distinct behavior in each phase, which can serve as an experimental probe. In the MC-high phase we see a shift of the peak with respect to the vacuum case. In the AC phase we see four different peaks, this is related to the fact that the quasi-particle excitations in the AC phase are a mixture of molecule and atoms. At the phase transition between the MC high-density phase and the AC phase the photoluminescence spectrum exhibits a gap closing as anticipated, as can be seen in Fig. 3.16 for  $\delta_a \approx 5.25$ . Hence, the photoluminescence spectrum displays a clear signature of the different phases and the phase transition.

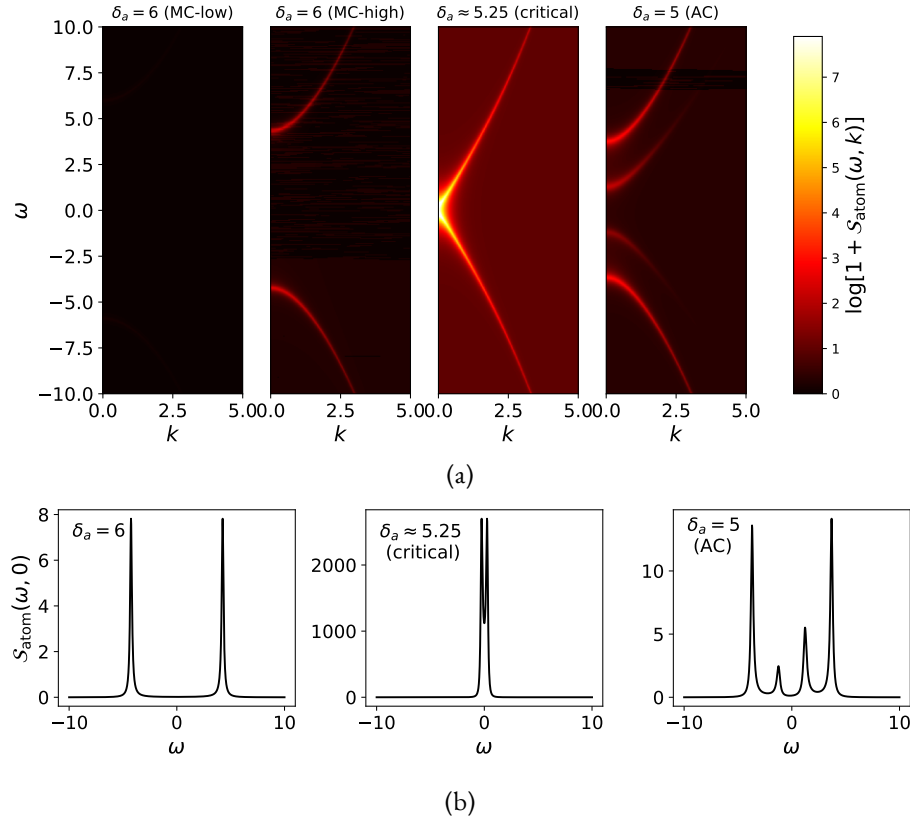


Figure 3.16: (a) Atom photoluminescence  $S_{\text{atom}}(\omega, k)$  for different values of  $\delta_a$  at fixed detuning  $\nu = -4$  (corresponding to points in the phase-diagram in Fig. 3.13c.). (b) Cuts showing the photoluminescence at zero momentum  $S_{\text{atom}}(\omega, k = 0)$  at the MC-high, critical and AC phase.

In the MC phase where  $\langle \psi_0 \rangle = 0$  we can write an analytic expression for  $\mathcal{S}_{\text{atom}}(\omega, k)$ :

$$\mathcal{S}_{\text{atom}}(\omega, k) = \frac{2\gamma_a |\lambda_{\text{eff}}|^2}{[(\omega + i\gamma_a)^2 - E_k^2][(\omega - i\gamma_a)^2 - E_k^2]}, \quad (3.115)$$

$$E_k^2 \equiv \left( \frac{k^2}{2m} + \delta_a + u_{am} |\phi_0|^2 \right)^2 - |\lambda_{\text{eff}}|^2, \quad \lambda_{\text{eff}} \equiv 2g\phi_0 + \lambda.$$

From Eq. (3.115) we see that the photoluminescence spectrum is symmetric with respect to  $\omega$ . This means that both negative energy modes with energy  $-E_k$  and positive energy modes with energy  $E_k$  are equally occupied. For real frequencies  $\mathcal{S}_{\text{atom}}(\omega, k)$  has peaks at  $\omega = \pm E_k$ , where

$$\mathcal{S}_{\text{atom}}(\pm E_k, k) = \frac{2|\lambda_{\text{eff}}|^2}{\gamma_a^2 + 4E_k^2}. \quad (3.116)$$

It is interesting to compare the photoluminescence spectrum in our system to the expression for  $\mathcal{S}_{\text{eq}}(\omega, k)$  for a regular equilibrium BEC at finite temperature

$$\mathcal{S}_{\text{eq}}(\omega, k) = n_{\text{BE}}(\beta\omega) \left[ \frac{\epsilon_k + \mu + \tilde{E}_k}{\tilde{E}_k} \delta(\omega - \tilde{E}_k) - \frac{\epsilon_k + \mu - \tilde{E}_k}{\tilde{E}_k} \delta(\omega + \tilde{E}_k) \right].$$

Where  $n_{\text{BE}}$  is the Bose-Einstein distribution,  $\tilde{E}_k \equiv \sqrt{k^2(k^2 + \mu)}$ ,  $\mu$  is the chemical potential and  $\beta$  is the inverse temperature. In the equilibrium case the weight of the peaks is momentum dependent and furthermore, the weight of the peak at positive frequency is always higher than the weight of the negative peak. This is in stark contrast to what we see in the case of an atom with a two-particle coherent pump where both peaks are equal.

### 3.10 MC-AC ISING TRANSITION

We will now derive an effective field theory which describes the Ising transition between the MC phase with high-density and the AC phase. We ignore here the fact that our mean-field calculation predicts a bistability region, and assume that the entire system is in a state with a specific value of the molecule condensate  $\psi_0$ . That is we want to describe the situation where the state of the system follows the high-density branch of  $\rho_m(\nu)$  shown in Fig. 3.15a.

To obtain the effective theory we first express the quadratic part of the atoms action in terms of real fields by defining

$$\tilde{\psi}_\alpha = e^{i \arg(\lambda + \phi_0)/2} \psi_\alpha, \quad \tilde{\psi}_\alpha(t, x) = \eta_\alpha(t, x) + i\chi_\alpha(t, x). \quad (3.117)$$

Defining the vector  $v^T \equiv (\eta_c, \chi_c, \eta_q, \chi_q)$ , we can write the action as

$$S = \int_{\omega, \mathbf{k}} \frac{1}{2} v^T(-\omega, -\mathbf{k}) \begin{pmatrix} 0 & P^A \\ P^R & P^K \end{pmatrix} v(\omega, \mathbf{k}) \quad (3.118)$$

$$P^R(\omega, \mathbf{k}) = \begin{pmatrix} |\lambda_{\text{eff}}| - \xi_k & i\omega - \gamma_a \\ -i\omega + \gamma_a & -|\lambda_{\text{eff}}| - \xi_k \end{pmatrix} \quad (3.119)$$

$$P^K = 2i\gamma_a \mathbb{1}. \quad (3.120)$$

where as before  $\lambda_{\text{eff}} \equiv \lambda + 2g\phi_0$ , and  $\xi_k \equiv k^2/(2m) + \delta_a + u_{am}|\phi_0|^2$ .

In the absence of loss, we see that the field  $\eta$  will become massless at the critical point where  $|\lambda_{\text{eff}}| = \xi_0$  while the field  $\chi$  stays gapped. Hence we can integrate out  $\chi$  to obtain a theory for the critical mode only. Doing so we obtain the following theory for the field  $\eta$

$$\begin{aligned} \mathcal{L}_\eta = & \frac{1}{2} \eta_q(-\omega, -\mathbf{k}) \left[ \frac{(\omega + i\gamma_a)^2}{|\lambda_{\text{eff}}| + \xi_k} - (\xi_k - |\lambda_{\text{eff}}|) \right] \eta_c(\omega, \mathbf{k}) + c.c. \\ & + 2i\gamma_a \left( 1 + \frac{\gamma_a^2}{(|\lambda_{\text{eff}}| + \xi_k)} \right) \eta_q(-\omega, -\mathbf{k}) \eta_q(\omega, \mathbf{k}), \end{aligned} \quad (3.121)$$

where note that  $\eta_\alpha^*(\omega, k) = \eta_\alpha(-\omega, -k)$  (since it is the Fourier transform of a real field). For finite  $\gamma_a$  we can neglect the term  $\sim \omega^2$  and the  $k$  dependence of the denominator of the frequency coefficient (when we want to describe the critical behavior), this result in the effective low frequency Lagrangian

$$\begin{aligned} \mathcal{L}_\eta \approx & \frac{1}{2(|\lambda_{\text{eff}}| + \xi_0)} \eta_q(-\omega, -\mathbf{k}) [2i\gamma_a\omega - (\xi_k - |\lambda_{\text{eff}}|)(\xi_0 + |\lambda_{\text{eff}}|) - \gamma_a^2] \eta_c(\omega, \mathbf{k}) + c.c. \\ & + 2i\gamma_a \left[ 1 + \frac{\gamma_a^2}{(|\lambda_{\text{eff}}| + \xi_0)} \right] \eta_q(-\omega, -\mathbf{k}) \eta_q(\omega, \mathbf{k}). \end{aligned}$$

The pole of the retarded Green's function is at

$$\omega_\eta(\mathbf{k}) = -\frac{i}{2\gamma_a} \left[ (|\lambda_{\text{eff}}| + \xi_0) \left( \frac{k^2}{2m} + \xi_0 - |\lambda_{\text{eff}}| \right) + \gamma_a^2 \right]. \quad (3.122)$$

We see that the  $\eta$  mode is completely dissipative close to the transition, since  $\omega_\eta(\mathbf{k})$  has no real part. In particular, the dissipation rate at zero momentum is given by

$$\omega_\eta(0) = -\frac{i}{\gamma_a} (\xi_0^2 + \gamma_a^2 - |\lambda_{\text{eff}}|^2) \xrightarrow{|\lambda_{\text{eff}}| \rightarrow \lambda_c} 0. \quad (3.123)$$

Thus we see that  $\eta$  is indeed the right field which describes the critical theory at the  $\mathbb{Z}_2$  transition.

The model we obtain at the quadratic level is equivalent to model A in the Hohenberg-Halperin classification of classical dynamical criticality [86, 122]. From the relation between the noise term and the frequency coefficient we can read off the effective temperature

$$T_{\text{eff}} = \frac{1}{2}(|\lambda_{\text{eff}}| + \xi_0) \left( 1 + \frac{\gamma_a^2}{(|\lambda_{\text{eff}}| + \xi_0)^2} \right) \quad (3.124)$$

We see that even in the limit  $\gamma_a \rightarrow 0$  (which implies  $|\lambda_{\text{eff}}| = \xi_0$ ), the critical Ising degree of freedom is at effective finite temperature  $T_{\text{eff}} = \xi_0$ . The result we obtain here is similar to that obtained in Ref. [123] which formulated an effective Keldysh field-theory for the transverse-field Ising model subject to dissipation described by a Lindblad operator  $L_i = \sigma_i^-$ .

### 3.11 DISCUSSION

Let us now summarize the results of this chapter and provide some outlook. We considered a model of attractively interacting bosonic atoms close to a scattering resonance. The atoms experience Markovian single- and two-particle losses and are not coupled to any equilibrium bath, a setting which is naturally realized in Rydberg-polariton systems.

First, we considered the case without particle pump processes. By means of a Keldysh-field theory description, we showed that a molecule bound state exists in this setup, with spectral properties similar to the equilibrium vacuum. The main differences here is that due to the losses, on the one hand, the molecule bound state acquires finite life-time, and on the other hand its binding energy is decreased. Furthermore, we explored the possibility of three-particle Efimov bound states, which are known to exist in the equilibrium vacuum case. Using an FRG calculation we have shown that the single-particle losses are detrimental to the Efimov bound states. At relatively weak loss no Efimov states appear. This allows us to ignore them when considering many-body effects.

In order to explore steady-states with a finite many-body density we introduced a two-particle coherent pump. This pump explicitly breaks  $U(1)$  symmetry, inducing a finite molecular condensate density. Tuning the frequency of the coherent pump, it is possible to drive a phase transition from a molecule condensate (MC) phase to a phase with an atom condensate (AC). This is shown by a mean-field study of a phenomenological model, whose form is inspired by considering the leading corrections to the effective action at weak pumping.

The phase transition is associated with a breaking of a  $\mathbb{Z}_2$  symmetry. We identify the mechanism behind the atom condensation instability to be an enhancement of the coherent pump due to the molecule condensate. This enhancement is most pronounced when the pump is resonant with the molecule binding energy, hence we see how the many-body phase diagram emerges from the properties of the two-particle vacuum. Photoluminescence measurements provide an experimental probe which is able to detect the different phases and the gap closing at the phase transition.

The work in this chapter suggests several future directions. First let us consider the pumping mechanism. The advantage of a coherent pump over an incoherent Markovian one, is that the former allows targeting a specific energy by tuning the pump frequency. This energy selectivity is crucial to unveil the molecular physics: a Markovian pump would inject the same energy at all

frequencies, favouring always atomic condensation and thus washing out the phase transition. However, we pay the price of breaking explicitly the  $U(1)$  symmetry, which eliminates a possible phase transition between the molecular BEC and a normal phase. In this respect, an appealing option is to consider recently proposed and experimentally realized non-Markovian incoherent pumping schemes which allow to pump particles into a specific narrow band of energies [72, 73], while preserving  $U(1)$  symmetry.

Another feature which merits further investigation is the fate of the bistability regions beyond mean-field. In order to investigate this, one option would be to consider the dynamical evolution of the condensate fields in the presence of noise. One approach for this is to derive and solve semi-classical stochastic Gross-Pitaevskii equations describing the time evolution of non-homogeneous condensate profiles  $\phi_0(x, t)$ ,  $\psi_0(x, t)$  in the presence of classical stochastic noise. This was done, for example, in a similar driven-dissipative model in one and two-dimensions [107]. Another approach to include beyond mean-field corrections could be to use the 2PI formalism in order to derive and solve a set of coupled equations describing both the condensate evolution and the evolution of two-point correlation functions [124–126].

Yet another interesting direction would be to consider specifically the case of very weak pumping and loss strength. There, it is possible that particle collisions, happening at a faster rate than loss or pump events, cause the system to effectively thermalize. In this case the steady-state could be well described by a thermal state with an effective temperature and chemical potential determined by the ratio of the pump and loss strength [127, 128]. This regime might allow to reproduce more faithfully the equilibrium physics suggested in [41, 42], whereas the main challenge would be to derive and solve the equations for determining the effective temperature and chemical potentials induced by the external baths.

## APPENDICES TO CHAPTER 3

 3.A INTRODUCING THE AUXILIARY  $\phi$  FIELD IN THE PRESENCE OF 2-BODY LOSS AND 3-BODY INTERACTIONS

In this appendix we provide details regarding the equivalence between the atom-molecule action  $S_m + S_{am}$  introduced in Eq. (3.45) and an atom only action with 2-body loss and 3-body interaction with the Lagrangian

$$\mathcal{L}_{\text{int}} = \sum_{\sigma=\pm} \sigma [u_a - i\sigma\Gamma_a |\psi_\sigma|^4 + u_3 |\psi_\sigma|^6] - i\Gamma_a \psi_+^2 (\psi_-^*)^2 \quad (3.125)$$

The equivalence will be shown by integrating out the molecule field  $\phi$ . For this purpose it is convenient to write the action in Eq. (3.45) in the  $\pm$  basis,

$$\mathcal{L}_m = \sum_{\sigma=\pm} \sigma (-\nu - i\eta\sigma) \phi_\sigma \phi_\sigma^* - 2i\eta \phi_-^* \phi_+ \quad (3.126)$$

$$\mathcal{L}_{am} = \sqrt{2}g\sigma \sum_{\sigma=\pm} (\psi_\sigma^2 \phi_\sigma^* + c.c.) - u_{am}\sigma \sum_{\sigma=\pm} |\psi_\sigma|^2 |\phi_\sigma|^2 \quad (3.127)$$

where we suppressed time and space indices.

To eliminate the  $\phi$  field, we replace it with its stationary value given by the solution of  $\delta S/\delta\phi = 0$ <sup>3</sup> [89]. The stationary values for  $\phi$  are given by:

$$\phi_+ = \frac{\sqrt{2}g\psi_+^2}{-i\eta + \nu + u_{am}|\psi_+|^2} \quad (3.128a)$$

$$\phi_- = \frac{\sqrt{2}g(\eta\psi_-^2 + i\nu\psi_-^2 + iu_{am}\psi_-^2|\psi_+|^2 - 2\eta\psi_+^2)}{(i\eta + u_{am}|\psi_-|^2 + \nu)(\eta + i\nu + iu_{am}|\psi_+|^2)} \quad (3.128b)$$

$$\phi_+^* = \frac{2\sqrt{2}g\eta(\psi_-^*)^2}{(i\eta + u_{am}|\psi_-|^2 + \nu)(\eta + i\nu + iu_{am}|\psi_+|^2)} \quad (3.128c)$$

$$+ \frac{\sqrt{2}g(\psi_+^*)^2}{-i\eta + \nu + u_{am}|\psi_+|^2} \quad (3.128d)$$

$$\phi_-^* = \frac{\sqrt{2}g(\psi_-^*)^2}{i\eta + u_{am}|\psi_-|^2 + \nu} \quad (3.128e)$$

<sup>3</sup>In the absence of the  $u_{am}$  term this procedure is completely equivalent to Gaussian integration of  $\phi$ . For  $u_{am} \neq 0$  it is equivalent to gaussian integration only up to a  $\log \det D(u_{am}|\psi|^2)$  with  $D$  the molecule bare Green's function.



Plugging in the solutions (3.128) in the action  $S_m$  we obtain:

$$\frac{2g^2\psi_+^2(\psi^*)_+^2}{u_{am}\psi_+\psi^*_+-i\eta+\nu} - \frac{2g^2\psi_-^2(\psi^*)_-^2}{u_{am}\psi_-\psi^*_-+i\eta+\nu} \quad (3.129)$$

$$+ \frac{4g^2\eta(\psi^*)_-^2\psi_+^2}{(u_{am}\psi_-\psi^*_-+i\eta+\nu)(iu_{am}\psi_+\psi^*_++\eta+i\nu)} + \dots \quad (3.130)$$

where ... denotes terms with  $\psi^6$  in the numerator. The leading contribution is obtained by ignoring  $u_{am}|\psi|^2$  terms in the denominator, which results in terms quartic in  $\psi$ .

The real terms generated correspond to coherent interaction, and the terms with imaginary coefficient correspond to two-body loss. This results in the following two-body interaction and loss:

$$u_a = -\frac{2g^2\nu}{\eta^2 + \nu^2}, \quad \Gamma_a = \frac{2g^2\eta}{\eta^2 + \nu^2} \quad (3.131)$$

Expanding up to order  $O(\psi^6)$  we also obtain a 3-body interaction term:

$$-\frac{6g^2u_{am}(\nu^2 - \eta^2)(|\psi_+|^3 - |\psi_-|^3)}{(\eta^2 + \nu^2)^2} \quad (3.132)$$

In the presence of finite  $\eta$ , extra terms are generated, which cannot clearly be traced back to having been originated from a coherent Hamiltonian evolution  $[H, \rho]$  or a Lindblad term in some effective quantum master equation:

$$-\frac{12ig^2\eta\nu u_{am}}{(\eta^2 + \nu^2)^2} [-(\psi^*)_-^2\psi_+^3 - \psi_- (\psi^*)_-^3\psi_+^2 + \psi_-^3(\psi^*)_-^3 + (\psi^*)_+^3\psi_+^3] \quad (3.133)$$

$$-\frac{12g^2u_{am}\eta^2}{(\eta^2 + \nu^2)^2} ((\psi^*)_-^2\psi_+^3\psi^*_+-\psi_- (\psi^*)_-^3\psi_+^2) \quad (3.134)$$

These terms are  $O(\eta|\psi|^6)$  and  $O(\eta^2|\psi|^6)$ , and can be neglected in the limit of small two-body loss and atom condensate density.

### 3.B FIELD EQUATIONS DERIVED FROM THE 1-LOOP EFFECTIVE ACTION

In this appendix we derive the field equations using the 1-loop expression for the 1PI effective action Eq. (3.59). As explained in the main text, the equations are derived from the stationary condition  $\delta\Gamma/\delta\phi_q^*, \delta\Gamma/\delta\psi_q^* = 0$ . Taking the derivatives with respect to the quantum fields we obtain:

$$(-\delta_a + i\gamma_a - u_a|\psi_0|^2)\psi_0 + (\lambda + 2g\phi)\psi_0^* + i\text{tr}(\partial_{\bar{\psi}_q^*}\mathcal{G}^{-1})\mathcal{G}(\phi_0, \psi_0) = 0, \quad (3.135)$$

$$(-\nu + i\eta)\phi_0 + 2g\psi_0^2 + i\text{tr}(\partial_{\bar{\phi}_q^*}\mathcal{G}^{-1})\mathcal{G}(\phi_0, \psi_0) = 0. \quad (3.136)$$

### 3 Condensate phases of coherently driven bosons close to a scattering resonance

We denoted here the  $8 \times 8$  Green's function as

$$\mathcal{G}^{-1} \equiv \frac{\delta^{(2)} S}{\delta \chi_\alpha^* \delta \chi_\beta}, \quad \chi \equiv (\Psi_c \quad \Psi_q \quad \Phi_c \quad \Phi_q), \quad (3.137)$$

$$\Psi_\alpha(K) = (\psi_\alpha(K) \quad \psi_\alpha^*(-K)), \quad \Phi_\alpha(K) = (\phi_\alpha(K) \quad \phi_\alpha^*(-K)), \quad (3.138)$$

with  $K \equiv (\omega, \mathbf{k})$ . We added the atom interaction  $u_a$  by hand in order to stabilize the atom condensate. It is not possible to describe a stable atom condensate in the absence of  $u_a$ . This coupling will be in principle generated due to higher order contributions at finite-density.

Evaluating the derivatives of  $\mathcal{G}^{-1}$  at  $\phi_q = \psi_q = 0$  we obtain

$$\begin{aligned} \partial_{\bar{\phi}_q^*} \mathcal{G}^{-1} = & \begin{pmatrix} 0 & 0 & 0 & 0 & 2g & 0 & 0 & 0 \\ 0 & 0 & 0 & 0 & -u_{am}\phi_c^* & -u_{am}\phi_c & 0 & 0 \\ 0 & 0 & 0 & 0 & 0 & 0 & 2g & 0 \\ 0 & 0 & 0 & 0 & 0 & 0 & -u_{am}\phi_c^* & -u_{am}\phi_c \\ -u_{am}\phi_c & 0 & 0 & 0 & -u_{am}\psi_c & 0 & 0 & 0 \\ -u_{am}\phi_c^* & 2g & 0 & 0 & 0 & -u_{am}\psi_c & 0 & 0 \\ 0 & 0 & -u_{am}\phi_c & 0 & 0 & 0 & -u_{am}\psi_c & 0 \\ 0 & 0 & -u_{am}\phi_c^* & 2g & 0 & 0 & 0 & -u_{am}\psi_c \end{pmatrix} \\ \partial_{\bar{\phi}_q^*} \mathcal{G}^{-1} = & \begin{pmatrix} -u_{am}\phi_c & 0 & 0 & 0 & -u_{am}\psi_c & 0 & 0 & 0 \\ 2g & -u_{am}\phi_c & 0 & 0 & -u_{am}\psi_c^* & 0 & 0 & 0 \\ 0 & 0 & -u_{am}\phi_c & 0 & 0 & 0 & -u_{am}\psi_c & 0 \\ 0 & 0 & 2g & -u_{am}\phi_c & 0 & 0 & -u_{am}\psi_c^* & 0 \\ 0 & 0 & 0 & 0 & 0 & 0 & 0 & 0 \\ -u_{am}\psi_c^* & -u_{am}\psi_c & 0 & 0 & 0 & 0 & 0 & 0 \\ 0 & 0 & 0 & 0 & 0 & 0 & 0 & 0 \\ 0 & 0 & -u_{am}\psi_c^* & -u_{am}\psi_c & 0 & 0 & 0 & 0 \end{pmatrix} \end{aligned}$$

We also denote the different  $4 \times 4$  blocks of the Green's function as:

$$\mathcal{G} \equiv \begin{pmatrix} G & G_{am} \\ G_{ma} & D \end{pmatrix}. \quad (3.139)$$

Using these expressions we get:

$$\text{tr}(\partial_{\phi_q^*} \mathcal{G}^{-1}) \mathcal{G} = 2g \int_P G_{12}^K \quad (3.140)$$

$$\begin{aligned} & - 2u_{am} \left[ \phi_c \int_P G_{11}^K + \psi_c \int_P [G_{am}^K]_{11} + \psi_c^* \int_P [G_{am}^K]_{12} \right] \\ \text{tr}(\partial_{\psi_q^*} \mathcal{G}^{-1}) \mathcal{G} &= 2g \int_P ([G_{am}^K]_{11} + [G_{am}^K]_{22}) \\ & - 2u_{am} \left[ \psi_c \int_P D_{11}^K + \phi_c \int_P [G_{am}^K]_{11} + \phi_c^* \int_P [G_{am}^K]_{12} \right] \end{aligned} \quad (3.141)$$

In the limit of small or vanishing atom-condensate  $|\psi_c| \ll 1$  we can neglect all atom-molecule correlation functions  $G_{am}$ . In this limit the mean-field equations are given by

$$(-\delta_a + i\gamma_a - u_a |\psi_0|^2) \psi + (2g\phi_0 - \lambda) \psi_0^* = 0 \quad (3.142a)$$

$$\left( -\nu + i\eta - 2iu_{am} \int_{\omega, \mathbf{k}} G_{11}^K \right) \phi_0 + 2g\psi_0^2 + 2ig \int_{\omega, \mathbf{k}} G_{12}^K = 0 \quad (3.142b)$$

If we further neglect the contribution of  $\psi_c$  to the atom Green's functions, we can write the atom inverse retarded Green's function in this limit as

$$P_a^R = \begin{pmatrix} \omega - \epsilon_{a, \mathbf{k}} + i\gamma_a - u_a |\phi|^2 & \lambda + 2g\phi \\ \lambda + 2g\phi^* & -\omega - \epsilon_{a, \mathbf{k}} - i\gamma_a - u_a |\phi|^2 \end{pmatrix} \quad (3.143)$$

### 3.C $u_{am}$ FLOW EQUATIONS

In this appendix we provide details on the derivation of the FRG flow equation for the atom-molecule coupling  $u_{am}$ .

The main object examined in the FRG formalism is the effective action at momentum scale  $k$ , denoted  $\Gamma_k$ , which is the action obtained by integrating all quantum and classical fluctuations with momenta  $q \in [k, \Lambda]$ , where  $\Lambda$  is the UV-cutoff. Starting from the action at the UV scale  $\Gamma_\Lambda = S$ , we can obtain the effective action  $\Gamma_k$  using the formally exact Wetterich equation

$$\partial_k \Gamma_k = \frac{i}{2} \text{Tr} \left[ \partial_k R_k (\Gamma_k^{(2)} + R_k)^{-1} \right] \equiv \frac{i}{2} \text{Tr} \tilde{\partial}_k \log(\Gamma_k^{(2)} + R_k). \quad (3.144)$$

Here  $R_k$  is an IR cutoff function which suppresses fluctuations at all momenta  $q < k$  with  $k$  the running cutoff scale.  $\Gamma_k^{(2)}$  is the second variation of the effective action with respect to the fields, and the trace is taken over all momenta, frequencies and Keldysh indices. The scale derivative  $\tilde{\partial}_k$  is defined as acting only on the cutoff function  $R_k$ , this allows us to represent the RHS of Eq. (3.144) in terms of an expansion in Feynman diagrams. It is also useful to define  $t = \log(k/\Lambda)$  such that the flow starts from  $t = 0$  and flows toward  $t = -\infty$ .

Due to the fact that in vacuum only particle-particle diagrams are non-vanishing the flow equations for the  $n$ -body sector of the effective-action (which we define as the set of vertices of the form  $\phi^m \psi^r$  with  $r + 2m = 2n$ ) are decoupled from all higher order sectors. In particular the 1-body

sector (i.e. atom propagator) remains unnormalized [90]. This vacuum hierarchy allows us to introduce separate cutoffs for the atom and molecule. In particular choosing  $R_{a,k}(\mathbf{p}) = k^2$  for the atom allows for an exact integration of the flow equation for the molecule propagator in vacuum and we obtain the result in Eq. (3.68).

To obtain the flow-equations for the three-body sector, namely for the coupling  $u_{am}$ , we introduce a sharp momentum cutoff for the molecule  $R_{m,k}(\mathbf{p}) = \Theta(p - k)$ . The action of the scale derivative  $\partial_t$  on this cutoff results in  $\tilde{\partial}_t R_{m,k} = -k\delta(p - k)$  such that all momentum integrals are just evaluated at the cutoff scale.

In order to obtain the Efimov limit-cycle it was shown in [91] that it is enough to work in the point approximation where we neglect momentum dependence of the 3-body coupling  $u_{am}$ . The structure of the most generic three-body vertex in the point approximation is of the form:

$$\Gamma^{(3)} = \int_{Q_1, Q_2, Q_3, Q_4} (u_{am})_{\alpha, \beta}^{\alpha', \beta'} \phi_\alpha(Q_1) \phi_{\alpha'}^*(Q_2) \psi_\beta(Q_3) \psi_{\beta'}^*(Q_4) \delta(Q_1 + Q_3 - Q_2 - Q_4) \quad (3.145)$$

However, we find that in vacuum where the only dissipative processes are one and two particle loss the structure of the 3-body sector remains similar to the second term in Eq. (3.45) and we have to consider only one coupling  $u_{am}(t)$  which is independent of the Keldysh indices.

In order to derive the flow-equation for  $u_{am}(t)$  we can evaluate the diagrams in Fig. 3.11 with zero external-momenta and frequencies and a specific set of external Keldysh indices, e.g. corresponding to  $\phi_q^* \phi_c \psi_c^* \psi_c$ .

Defining the following dimensionless couplings:

$$\hat{\gamma}_a = \frac{\gamma_a}{k^2}, \quad \hat{\delta}_a = \frac{\delta_a}{k^2}, \quad \hat{\eta} = \frac{\eta}{k}, \quad \hat{u}_{am} = k^2 u_{am} \quad (3.146)$$

we obtain the following flow equations by evaluating the diagrams in Fig. 3.11:

$$\begin{aligned} \partial_t \hat{u}_{am} = & - \frac{4\hat{u}_{am}^2}{\pi \left( -4\pi(\hat{\nu} + i\hat{\eta}) + \sqrt{3}g^2 \sqrt{1 - 4i\hat{\gamma}_a - 4\hat{\delta}_a} \right)} \\ & - \frac{32g^2 \hat{u}_{am}}{\pi \left( 1 - 2i\hat{\gamma}_a - 2\hat{\delta}_a \right) \left( -4\pi(\hat{\nu} + i\hat{\eta}) + \sqrt{3}g^2 \sqrt{1 - 4i\hat{\gamma}_a - 4\hat{\delta}_a} \right)} \\ & - \frac{64g^4}{\pi \left( 1 - 2i\hat{\gamma}_a - 2\hat{\delta}_a \right)^2 \left( \sqrt{3}g^2 \sqrt{1 - 4i\hat{\gamma}_a - 4\hat{\delta}_a} - 4\pi(\hat{\nu} + i\hat{\eta}) \right)} \\ & + 2\hat{u}_{am} \end{aligned} \quad (3.147)$$

and

$$\partial_t \hat{\gamma}_a = -2\hat{\gamma}_a, \quad \partial_t \hat{\delta}_a = -2\hat{\delta}_a, \quad \partial_t \hat{\nu} = -\hat{\nu} \quad \partial_t \hat{\eta} = -\hat{\eta} \quad (3.148)$$

# 4 CRITICAL BEHAVIOR NEAR THE MANY-BODY LOCALIZATION TRANSITION IN DRIVEN OPEN SYSTEMS

## 4.1 INTRODUCTION

Many-body localization is a state of interacting quantum systems, which fail to thermalize subject to their intrinsic dynamics due to the effect of strong disorder [25, 26]. An important question, currently under intense theoretical study and debate, concerns the nature of the phase transition between the ergodic and localized phases. This transition represents a new class of dynamical quantum phase transitions, which involves a fundamental change of the entanglement structure in all, or at least many, of the eigenstates.

Unlike equilibrium phase transitions, the many-body localization transition is sharp only if the system is completely isolated, which imposes severe limitations on the ability to study it using standard theoretical, numerical, and experimental approaches. In particular, the requirement of a closed system appears to preclude experiments with solid state materials, which, due to coupling to a thermal phonon bath cannot be many-body localized. Even in experiments with small systems of ultracold atoms and ion traps, which are usually considered to be exquisitely isolated, signatures of many-body localization are visibly polluted by extrinsic decay processes that may mask the critical point [129–132]. At the same time, numerical experiments are also severely limited. In order to study the MBL transition in a closed system one needs to either have access to a large number of eigenstates in order to extract full spectral properties or to simulate close systems dynamics. These requirements have led to numerical studies being mostly restricted to exact diagonalization (ED) of very small systems [27, 133–138]. There is increasing evidence that such simulations are overwhelmed by transient finite-size effects that supersede the critical scaling behavior [139, 140].

In this chapter, we show a way to overcome the limitations posed by closed systems, by studying sharp signatures of the MBL transition in weakly open driven systems. Specifically we consider a situation where a disordered system is coupled to non-equilibrium baths. We assume that the coupling is such that the dynamics of the system density matrix can be described by a Lindblad quantum master equation

$$\dot{\rho} = -i[H, \rho] + \epsilon \sum_{\nu} \left( L_i^{\nu} \rho L_i^{\nu\dagger} - \frac{1}{2} \{ L_i^{\nu\dagger} L_i^{\nu}, \rho \} \right). \quad (4.1)$$

Where the Hamiltonian  $H$  undergoes an MBL transition as a function of disorder strength in the absence of the coupling to the Lindblad operators. We will show how the weak coupling to the baths allows probing the underlying MBL transition.

In a previous work by Lenarčič et al. [141] it was shown that in the limit of vanishing  $\epsilon$ , the MBL transition shows up as a singular change in the temperature variations across the sample. On the thermalizing side of the critical point (i.e. for sufficiently weak disorder) the temperature fluctuations vanish in the limit  $\epsilon \rightarrow 0$ , while they remain finite on the MBL side.

In this chapter we build upon the work in [141] and extend it by considering the case of a small, but non-vanishing, coupling to the external baths  $\epsilon > 0$ . In this situation we expect that the sharp transition which is observed in the temperature fluctuations at  $\epsilon \rightarrow 0$  will broaden into a crossover governed by the critical point located at  $\epsilon \rightarrow 0$ . The finite coupling to the bath has a similar effect to that of a finite-temperature in a quantum phase transition, where the dependence of the order parameter on temperature contains information on the properties of the underlying quantum-critical point [142].

By studying the leading dependence of the spatial temperature fluctuations on  $\epsilon$  in the vicinity of the critical point we will show that we can extract the critical properties of the MBL transition, where our main interest in this chapter is extracting the dynamical critical exponent  $z$ . The MBL transition in one dimensional systems is believed to be preceded by a thermal Griffiths regime where  $z$  changes continuously as a function of the disorder strength (i.e. the tuning parameter of the MBL transition), and diverges at the critical point. This scenario explains the subdiffusive transport which was observed in numerical studies when approaching the MBL transition from the ergodic sides [143–158].

The relative coupling to the different Lindblad terms in Eq. (4.1) can be arranged such that the steady state density matrix is well described by a matrix product operator with low bond dimension, allowing efficient computation. Using a matrix product operator ansatz to solve for the steady-state of Eq. (4.1), enables us to numerically compute the dependence of temperature variations on  $\epsilon$ . Doing so we find a sharp signature of the Griffith regime with a continuously varying dynamical exponent that diverges at the critical point.

Before proceeding we note the connection to Ref. [159], where Griffiths exponents have been computed numerically for a similar spin-chain coupled to Lindblad operators placed at the two ends of the chain to drive a steady state current. Because in our case the coupling to the drive and the bath are in the bulk the calculation can converge faster and we are therefore able to access parameter regimes much closer to the MBL transition.

## OUTLINE AND SUMMARY OF RESULTS

Let us now present an outline for the rest of this chapter and a highlight of our key results. Sections 4.2 and 4.3 contain background information. In Sec. 4.2 we provide background on the MBL phase and the corresponding transition. In Sec. 4.3 we elaborate on the numerical method we use to find the steady state of the QME by means of a matrix-product state ansatz.

The presentation of our research results starts in Sec. 4.4. As explained in the introduction, the main idea is to explore the effect of weak coupling to the baths  $\epsilon$  (see Eq. (4.1)) on the local temperature fluctuation order parameter which was first introduced in Ref. [141]. This order parameter is defined as  $\delta T / \bar{T}$ , where  $\delta T$  is the variance of local temperatures, and  $\bar{T}$  is the mean temperature (both averaged over different disorder realizations). This order parameter can be equivalently

defined using the inverse local temperatures. Our key result is the extraction of the dynamical exponent  $z$  from the dependence of  $\delta T/\bar{T}$  on  $\epsilon$ , shown in Fig. 4.7.

The path leading to the extraction of  $z$  from  $\delta T/\bar{T}(\epsilon)$  consists of three main parts:

1. In Sec. 4.4 we use a long wavelength effective hydrodynamic description to show that in the ergodic side of the transition temperature fluctuations obey  $\sqrt{\langle \delta T^2 \rangle} \sim \epsilon^{1/(2z)}$  in  $1d$ .
2. In Sec. 4.5 we use an effective resistor-network model of thermal islands with fluctuating temperatures connected via conducting links with random conductances. Here the Griffiths physics, the distance from the MBL transition and the strength of the bath coupling  $\epsilon$  are encoded into the model as parameters controlling the distribution of conductances. We obtain anumerical solution of the resistor-network model for large systems up to size  $N = 1000$ . By assuming the dependence obtained from the hydrodynamic description,  $O_T \sim \epsilon^{1/(2z)}$ , we find that the dynamical exponent diverges with the correlation length  $z \sim \xi^{-1}$  ( see Fig. 4.4). This scaling of  $z$  agrees with observations from previous works [28, 145] (which used alternative probes for  $z$ ). Hence, the resistor-network computation substantiates our claim that  $z$  can be extracted by studying  $O_T(\epsilon)$ .
3. Finally, in Sec. 4.6, we use time-evolving block decimation (TEBD) to simulate a microscopic model of an XXZ spin chain with random  $h_z, h_x$  fields, coupled to non-equilibrium baths. The dynamics are described by Eq. (4.1). Analyzing the dependence of temperature fluctuations in the non-equilibrium steady-state on  $\epsilon$  we observe a divergence of  $z$  as the system approaches the MBL transition from the ergodic side. See Fig. 4.7.

From the numerical TEBD data, and the assumption  $z \sim |h - h_c|^{-\nu}$  we extract a critical exponent  $\nu \approx 4.0 \pm 0.9$  which is consistent with the Harris bound [160] and is in agreement with the results from previous phenomenological RG studies [28, 161]. This suggests that our open system approach is less sensitive to the finite-size effects encountered in ED studies, whose results are in contradiction to the Harris bound. We conjecture that this is related to level broadening due to finite dissipation.

## 4.2 BACKGROUND: MANY-BODY LOCALIZATION

In this section we provide theoretical background on the concept of many-body localization, as occurring in closed systems. The typical scenario which is considered is that of a quantum quench in a closed system, where the system is initialized in some state  $|\psi_0\rangle$  and evolves under unitary Hamiltonian dynamics with some Hamiltonian  $H$ . That is,  $|\psi(t)\rangle = e^{-iHt}|\psi_0\rangle$ . Typically, for an interacting system, it is expected that the interactions between subparts of the system will lead to a thermal steady-state at long times [24]. More precisely, this means that expectation values of local observables are time independent and can be captured by an expectation value with respect to a thermal density matrix:

$$\langle \psi(t \rightarrow \infty) | \hat{O} | \psi(t \rightarrow \infty) \rangle = \frac{\text{tr} \hat{O} e^{-\beta H}}{Z}, \quad (4.2)$$

where the inverse temperature  $\beta$  is determined by the initial energy density  $\langle \psi_0 | H | \psi_0 \rangle$ , and  $Z = \text{tr} e^{-\beta H}$ . In case the system in question possesses extra conservation laws beyond energy (e.g. charge), the thermal steady state will be the one described by the corresponding statistical ensemble (e.g. Grand-canonical if charge is conserved). A system which thermalizes in such a way is called an ergodic system.

Note that strictly speaking the closed system is always described by a pure quantum state  $|\psi(t)\rangle$ . However, Eq. (4.2) implies that locally (at length scales  $\ell$  much smaller than the system size  $L$ ) it is indistinguishable from a thermal state. In turn this means that any initial quantum information encoded in the state cannot be retrieved by local measurements and is for all practical purposes “erased”.

The property of thermalization at long-times can be connected to the eigenstates of the Hamiltonian  $\{|\alpha\rangle\}_\alpha$  by considering the infinite-time average of an observable

$$\langle \hat{O} \rangle_\infty \equiv \lim_{T \rightarrow \infty} \frac{1}{T} \int_0^T \langle \psi(t) | \hat{O} | \psi(t) \rangle = \sum_\alpha p_\alpha \hat{O}_{\alpha\alpha}, \quad (4.3)$$

with  $\hat{O}_{\alpha\alpha}$  the diagonal matrix elements in the eigenstates basis and  $p_\alpha$  are determined by the initial projection of  $|\psi_0\rangle$  on the eigenstates. In order to ensure that  $\langle \hat{O} \rangle_\infty$  behaves in a thermal way according to Eq. (4.2), we must require that the expectation values of local operators in individual eigenstates  $\langle \alpha | \hat{O} | \alpha \rangle$  agree with those obtained from the micro-canonical ensemble with energy  $E_\alpha$ . This explanation of thermalization of closed quantum many-body systems is known as the *eigenstate thermalization hypothesis* (ETH) [162, 163]. A quantum system whose eigenstates obey the ETH is called an ergodic system.

In contrast, Many-body localization (MBL) is a phase of matter in which an interacting closed quantum-system fails to thermalize due to the effects of strong disorder. An MBL system has vanishing conductivity even at finite temperatures  $\sigma(T) = 0$ . This is opposed to conventional insulators which exhibit finite conductivity at finite temperatures  $\sigma(T) \propto \exp(-\Delta/T)$  (with  $\Delta$  the gap between the Fermi-energy and the conductance band). Vanishing conductance at finite energy density is an obstruction to thermalization, since it prohibits flow of energy and other conserved quantities between different parts of the system. As opposed to ergodic systems the eigenstates of the Hamiltonian of an MBL system do not obey ETH, a statement which can also be taken as a defining property of the MBL phase.

#### 4.2.1 ANDERSON LOCALIZATION

The insulating behavior due to disorder in the non-interacting case was first studied by Anderson in his seminal paper already in 1958 [164], and is known as Anderson localization. This is a single-particle phenomenon whose essence is destructive interference which leads to localized single-particle wave-function. To understand the phenomenon of Anderson localization, consider a tight-binding Hamiltonian of fermions hopping on a square lattice and subject to a random on-site potential,

$$H_{\text{Anderson}} = t \sum_{\langle\langle i,j \rangle\rangle} (c_i^\dagger c_j + h.c.) + \sum_i \epsilon_i c_i^\dagger c_i, \quad (4.4)$$



where  $\epsilon_i \sim U([-W/2, W/2])$  and  $\sum_{\langle\langle i,j \rangle\rangle}$  denotes sum over nearest neighbors only. In one and two dimensions it is known that disorder will always lead to localized single-particle eigenstates  $\psi_\alpha(\mathbf{r}) \sim \exp(-|\mathbf{r} - \mathbf{r}_\alpha|/\xi)$  with  $\xi$  the localization length (which becomes smaller with stronger disorder) [165]. In three dimensions, there is a critical value of disorder  $W_c$  above which all single-particle states are localized. As the disorder strength is reduced below  $W_c$  extended states appear, where localized and extended states reside in different parts of the energy band and the boundary separating them is called the *single particle mobility-edge*. Finally for very weak disorder in three dimensions practically all states are extended.

In the limit of  $t = 0$  the eigenstates of  $H_{\text{Anderson}}$  will be localized on a single-site  $\psi_i = |i\rangle$  with energies  $E_i = \epsilon_i$ . To show that localization can remain stable for weak but finite hopping  $0 < t \ll W$  Anderson considered a perturbative expansion in the hopping. The perturbation induces corrections to the localized wave-function  $|i\rangle$  transforming it into  $|\tilde{i}\rangle$ , which will have some overlap with other sites  $\langle j|\tilde{i}\rangle \neq 0$ . For sites which are at distance  $n$  from  $i$  on the graph, the overlap will come from  $n$ th order in perturbation theory and will be of the form

$$\langle j|\tilde{i}\rangle \sim \frac{t}{(\epsilon_i - \epsilon_{m_1})} \cdots \frac{t}{(\epsilon_{m_{n-1}} - \epsilon_j)}. \quad (4.5)$$

Since the energies are distributed uniformly in  $[-W/2, W/2]$ , the denominators are typically of order  $|\epsilon_i - \epsilon_{i'}| \sim W$ . Consider now the probability of finding the particle at some site which is at distance  $n$  from  $i$ , it can be naively estimated as

$$p_n \sim \left( \frac{Kt}{W} \right)^{2n}, \quad (4.6)$$

where  $K$  is known as the connectivity of a regular graph, and is defined such that the number of non self-intersecting paths of length  $n$  starting from any point is  $\sim K^n$  (for example the cubic lattice in 3D has  $K \approx 4.5$ ). Hence, we see that as long as  $Kt/W \ll 1$  the wave-function is still exponentially localized, which leads to the naive criterion for the critical hopping strength  $2Kt_c/W = 1$ .

In [164] Anderson considered the so-called “locator expansion” of the Green’s function in the basis of localized states:

$$G_{ij}(E) = \langle i | \frac{1}{E - H} | j \rangle. \quad (4.7)$$

The return probability  $p_0(t)$ , which is the probability of a particle initially placed on site  $i = 0$  to be found there at later times, is given by

$$p_0(t) = -\frac{1}{2\pi i} \lim_{\eta \rightarrow 0^+} \int dz e^{-izt} G_{00}(z + i\eta). \quad (4.8)$$

When the system is localized, we expect  $p_0(t)$  to stay finite at large times, while if it is delocalized we expect an exponential decay of the return probability  $p_0(t) \propto e^{-t/\tau}$  (in the thermodynamic

limit). The Green's function can be written as  $G_{00}(E) = (E - \epsilon_0 - \Sigma_0(E))^{-1}$  with the self energy given by a sum over all paths which start and end at  $i = 0$ :

$$\Sigma_0(E) \equiv \sum_{n=1}^{\infty} \sum_{m_1, \dots, m_n \neq 0} \frac{t_{0m_n} \dots t_{m_2 m_1} t_{m_1 0}}{(E - \epsilon_{m_n}) \dots (E - \epsilon_{m_2})(E - \epsilon_{m_1})}. \quad (4.9)$$

Note that finite decay rate  $\tau > 0$  is generated due to the hopping only if  $\text{Im} \lim_{\eta \rightarrow 0^+} G_{00}(E + i\eta) \neq 0$  for a finite range of energies, which can occur only when  $\text{Im} \lim_{\eta \rightarrow 0^+} \Sigma_0(E + i\eta) \neq 0$  [164, 166].

It can be shown that whenever the sum in Eq. (4.9) converges  $\text{Im} \lim_{\eta \rightarrow 0} \Sigma_0(E + i\eta) = 0$ , which implies that the particle initially placed at  $i = 0$  remains localized there. The question of whether a particle remains localized reduces to the question of the probability of finding resonant paths with large transition amplitudes which cause the sum in Eq. (4.9) to diverge. This analysis leads to the improved criterion for the critical hopping

$$eK\lambda_c \log(1/\lambda_c) = 1, \quad \lambda \equiv \frac{2t}{W}. \quad (4.10)$$

The criterion in Eq. (4.10) have been shown to be in agreement with an exact solution in the case of the Bethe lattice [167] (which can be considered as an infinite-dimensional case). However, as we noted above the analysis does not give the correct results for the 1- and 2-dimensional cases (where all state are always localized), since it doesn't take into account the possibility of destructive interference and cancellation of paths.

#### 4.2.2 MBL AS ANDERSON LOCALIZATION IN FOCK-SPACE

In Ref. [25] Basko, Aleiner and Altshuler (BAA) provided arguments for the stability of Anderson localization to finite interaction, by considering the problem of placing a single particle excitation on top of a many-body eigenstate and mapping it to an Anderson localization problem in Fock-space. BAA considered the Hamiltonian written in the basis of the single-particle eigenstates of the disordered quadratic part

$$H = \sum_{\alpha} \epsilon_{\alpha} c_{\alpha}^{\dagger} c_{\alpha} + \frac{1}{2} \sum_{\alpha\beta\gamma\delta} V_{\alpha\beta\gamma\delta} c_{\alpha}^{\dagger} c_{\beta}^{\dagger} c_{\gamma} c_{\delta}. \quad (4.11)$$

For a disordered system with strong enough disorder, the single-particle wave functions are localized in space.

Now, consider placing a single-particle excitation on top of some eigenstate of the many-body Hamiltonian  $|\Psi_k\rangle$ , such that the system is initialized in the state  $|\psi(t = 0)\rangle = c_{\alpha}^{\dagger} |\Psi_k\rangle$ . The interaction term  $V_{\gamma\delta\alpha\beta}$  connects this initial state with states containing three particle-hole excita-

tions and we can intuitively view this kind of scattering as a “hopping” process over a lattice whose sites are the Fock states<sup>1</sup>

$$|n_\alpha = 1, n_\beta = 1, n_\gamma = 0, n_\delta = 0, \dots\rangle \rightarrow |n_\alpha = 0, n_\beta = 0, n_\gamma = 1, n_\delta = 1, \dots\rangle. \quad (4.12)$$

Hence, we expect that for strong enough interaction the initial single-particle excitation can spread over states with three particle-hole excitations, which then spread over states with five excitations and so on, until eventually the initial localized excitation decays completely as it spreads over a continuum of many-body states. In a different scenario with weak interaction it is possible that the initial excitation spreads only over a limited number of states with a few excitations, and hence remain localized.

To find the criterion for many-body localization consider the Fourier components of  $|\psi(t)\rangle$

$$(\epsilon + E_k - H)|\psi(\epsilon)\rangle = c_\alpha^\dagger |\Psi_k\rangle. \quad (4.13)$$

Eq. (4.13) can be solved iteratively in perturbation theory, as

$$|\psi(\epsilon)\rangle = \frac{1}{\epsilon - \epsilon_\alpha} (|\psi^{(0)}(\epsilon)\rangle + |\psi^{(1)}(\epsilon)\rangle + |\psi^{(2)}(\epsilon)\rangle + \dots). \quad (4.14)$$

The zeroth order is just the initial-state which is a single-particle excitation  $|\psi^{(0)}(\epsilon)\rangle = c_\alpha^\dagger |\Psi_k\rangle$ . The first order contains 3-particle excitations

$$|\psi^{(1)}(\epsilon)\rangle = \sum_{\beta\gamma\delta} \frac{V_{\delta\gamma\beta\alpha}}{\epsilon - \Omega_{\gamma\delta}^\beta} c_\delta^\dagger c_\gamma^\dagger c_\beta |\Psi_k\rangle, \quad (4.15)$$

where we denoted the energy of the three-particle excitation  $\Omega_{\gamma\delta}^\beta \equiv \epsilon_\gamma + \epsilon_\delta - \epsilon_\beta$ . Similar to single-particle Anderson localization, the main question is the probability of finding large terms in Eq. (4.15). If all terms are non-resonant and the first order correction is small, this is an indication for MBL since the state  $|\psi(t)\rangle$  has considerable overlap with the initial state  $c_\alpha^\dagger |\Psi_k\rangle$ .

Since the interaction is short-ranged, non-vanishing matrix elements appear only for single-particle states which are within one localization volume (i.e. they are localized around points at most  $\sim \xi$  from each other, with  $\xi$  the localization length), hence the denominators in Eq. (4.15) are random numbers which are of order of the single-particle level spacing within the localization cell  $\delta_\xi$ . The single-particle level spacing is related to the localization length via  $\delta_\xi = (\nu \xi^d)^{-1}$ , with  $\nu$  the density of states. For weak interactions,  $\lambda = \max |V_{\alpha\beta\gamma\delta}| / \delta_\xi \ll 1$ , most of the terms in the sum will be small, and it will be dominated by resonant terms for which the energy denominators are small compared to the interaction element.

Assume there are  $K$  terms in the sum in Eq. (4.15) with non-vanishing matrix elements,  $K$  is the connectivity of the state  $c_\alpha^\dagger |\Psi_k\rangle$  to other many-body states with three-particle excitations.

---

<sup>1</sup>Strictly speaking the many-body eigenstate  $|\Psi_k\rangle$  will be a superposition of Fock-states, but the intuitive picture is still useful.

Since the denominators are  $\sim U([- \delta_\xi, \delta_\xi])$ , the smallest denominator is of order  $\delta_\xi/K$ . Hence the criterion for the probability of finding a resonant term in Eq. (4.15) is

$$K\lambda \sim \frac{KV}{\delta_\xi} \sim 1. \quad (4.16)$$

The connectivity  $K$  can be estimated as the number of Fock-states connected to the initial state  $c_\alpha^\dagger |\Psi_k\rangle$ . Those are states with non-vanishing matrix elements  $V_{\delta\gamma\beta\alpha} \neq 0$  and for which  $c_\delta^\dagger c_\gamma c_\beta |\Psi_k\rangle$  is non-zero. BAA argue that the energies of allowed particle-hole excitations on top of  $|\Psi_k\rangle$  are constrained by the temperature<sup>2</sup> via  $-T < \epsilon_\gamma, \epsilon_\delta; \epsilon_\beta < T$ . In addition the interaction matrix elements are non-vanishing only when the energy difference corresponding to the transitions  $\alpha \rightarrow \delta, \beta \rightarrow \gamma$  (or the same with  $\delta \leftrightarrow \gamma$ ) are not larger than the level spacing  $\delta_\xi$ . This leads BAA to the estimate  $K \sim T/\delta_\xi$ . Using the Anderson criterion for delocalization this leads to a criterion for the critical “temperature” (energy density) at which the interaction leads to delocalization

$$\frac{T_c}{\delta_\xi} \lambda |\log \lambda| \sim 1, \quad \lambda = \frac{V}{\delta_\xi}. \quad (4.17)$$

Since the above arguments are heuristic and also depend on some assumptions on the connectivity of the graph of many-body Fock-states, BAA provide further evidence for the stability of localization to interactions via a computation of the imaginary part of the self-energy (which we have seen is related to localization of an initial excitation) using the Keldysh formalism. The computation is done using the self-consistent Born approximation which takes into account only a certain class of scattering processes. Specifically, only processes where at each step one excitation decays into the maximal number of allowed excitations are considered (in terms of Fock-state hopping only transitions from Fock-state with  $n$  excitations to a state with  $n+2$  excitations are considered).

One mechanism for delocalization which was not taken into account by the perturbative computation of BAA, is the effect of rare thermal regions inside the MBL phase, as pointed out by De-Roeck et al. [168]. The main idea is that a rare thermal inclusion inside an otherwise localized system might act as a bath which can thermalize the other parts of the system. Consider a rare region with  $\ell$  sites in which the on-site energies  $\epsilon_i$  are all resonant (they are within  $V$  from each other). The probability of such a region is  $p(\ell) \approx (V/W)^\ell$ , and the typical size of such a region in a system of length  $L$  is  $\ell_{\text{typ}}(W) \sim \log L / \log(W/V)$ . Assume there is a critical size  $\ell_c \gg 1$ , such that the presence of a rare thermal region with  $\ell > \ell_c$  leads to the entire system becoming ergodic. This leads to a criterion for a critical disorder strength for which  $\ell_{\text{typ}}(W) = \ell_c$  (to avoid de-localization due to rare inclusion we need  $W > W_c$ ),

$$W_c(L) \sim VL^{1/\ell_c}. \quad (4.18)$$

The criterion in Eq. (4.18) implies that MBL cannot exist in the thermodynamic limit, however it would be hard to observe this effect in finite-size systems to the very slow drift of  $W_c$  with  $L$ .

<sup>2</sup>Note that we are considering a closed system so the temperature should be thought of as a Lagrange multiplier which should be determined by the energy density of the state  $|\Psi_k\rangle$ .

In light of the possibility of de-localization due to rare thermal regions, the stability of the MBL phase in  $d \geq 2$  in the thermodynamic limit is still an open research question. However, the existence of MBL in  $1d$  has been proven rigorously by Imbrie [169].

#### 4.2.3 EMERGENT INTEGRABILITY IN THE MBL PHASE

An important idea which allows us to understand the MBL phase and explains much of the observed phenomenology is the emergence of an extensive set of local conserved quantities, or local integrals of motion (LIOM), reminiscent of integrable systems. A key property of the MBL phase which allows to construct the LIOMs is that all of the eigenstates exhibit area-law entanglement. This property of the MBL phase, which has been observed numerically [170, 171], can be in fact considered as a defining property of the phase. This is in sharp contrast to high-energy eigenstates of generic ergodic systems, which obey the ETH and exhibit volume-law entanglement.

The fact that the eigenstates of an MBL system have low entanglement, implies that they can be connected to an un-entangled product state using a series of quasi-local unitary transformations [171]. To be more concrete, consider the random field XXZ model, which is one of the typical model systems used to study MBL,

$$H = \sum_i h_i \sigma_i^z + J_z \sum \sigma_i^z \sigma_{i+1}^z + J \sum (\sigma_i^x \sigma_{i+1}^x + \sigma_i^y \sigma_{i+1}^y), \quad (4.19)$$

where  $h_i$  are random fields drawn uniformly from  $[-W, W]$ . In the limit  $J = 0$ ,  $H$  commutes with  $\sigma_i^z$  for all  $i$  and hence the eigenstates are simple product-states of the form  $|\sigma\rangle = |\sigma_1, \sigma_2, \dots, \sigma_N\rangle$  with  $\sigma_i = \uparrow, \downarrow$ .

Turning on the kinetic term  $J \neq 0$ , but assuming it is weak enough such that the system is still many-body localized,  $\{\sigma_i^z\}$  no longer commute with  $H$ . The new eigenstates can be obtained from  $|\sigma\rangle$  by applying a quasi-local unitary of the form

$$U = \Pi_i \dots U_{i,i+1,i+2}^{(3)} U_{i,i+1}^{(2)}, \quad (4.20)$$

where the important property is that long-range unitaries in the decomposition of  $U$  are exponentially close to the identity  $\|1 - U_{i,i+1,\dots,i+n}^{(n)}\|_F^2 < e^{-n/\xi}$  (i.e. their effect is exponentially small and they do not introduce much correlations between far away spins). The fact that quasi-local unitaries suffice to transform the product-state  $|\sigma\rangle$  to an eigenstate  $|E\rangle$  of  $H$ , can be understood from the fact that  $|E\rangle$  has low entanglement hence only unitaries which entangle nearby spins are essential. This is in contrast to a generic ergodic Hamiltonian, whose eigenstates can also be built by applying a unitary  $U$  to an initial product-state, but in this case the  $U$  will be highly non-local in order to build the volume-law entanglement which is expected in that case.

The quasi-local unitary  $U$  transforms the original spin-z operators  $\sigma_i^z$  into quasi-local conserved operators  $\tau_i^z = U^\dagger \sigma_i^z U$ , which can be written as

$$\tau_i^z = Z \sigma_i^z + \sum_n V_i^{(n)} \hat{O}_i^{(n)}. \quad (4.21)$$

The operator  $\hat{O}_i^{(n)}$  has support only on sites which are at most distance  $n$  from  $i$ . Crucially, each  $\tau_i^z$  has a finite overlap  $Z \neq 0$  with the original spin  $\sigma_i^z$  and the contributions from higher order operators decay exponentially  $V_i^{(n)} \sim e^{-n/\xi}$ . Here  $\xi$  can be viewed as the localization length. The Hamiltonian in the MBL phase is diagonal in the  $\tau_i^z$  basis

$$H_{\text{MBL}} = \sum_i \tilde{h}_i \tau_i^z + \sum_{ij} J_{ij} \tau_i^z \tau_j^z + \sum_{ijk} J_{ijk} \tau_i^z \tau_j^z \tau_k^z + \dots \quad (4.22)$$

Where the interaction couplings decay exponentially with the distance between the involved LIOMs. We note again that for every Hamiltonian we can in principle build an extensive set of conserved quantities similar to Eq. (4.21), however in the generic case  $\tau_i^z$  will be a highly non-local operator with vanishing overlap with the bare  $\sigma_i^z$ .

The phenomenological LIOM Hamiltonian (4.22) explains all the phenomenology observed in the MBL phase [171, 172]. First, it is clear that the existence of the set of localized conserved quantities  $\{\tau_i^z\}$  is an obstruction to thermalization, since the dynamics is constrained to keep a memory of the initial values of extensive set of local expectation values which may have greatly varying values at different regions of the system. Secondly, the emergent integrability explains the Poisson statistics of the energy spectrum which is one of the numerical signatures of the MBL phase [27, 134]. Furthermore, the LIOM picture also explain the observed unbounded logarithmic growth of entanglement entropy in an MBL system after a quench [173, 174], this phenomenon can be explained by  $\{\tau_i^z\}$  configuration dependent phases which are generated during time evolution due to the couplings  $J_{i\dots j}$  between the LIOMs [175].

#### 4.2.4 EXPERIMENTAL OBSERVATION OF MBL

The question of MBL as we framed it so far is whether an isolated system can self-thermalize due to its internal interactions or not. We expect that coupling a system to a thermal-bath will eventually lead to thermalization, even if the underlying Hamiltonian is MBL. Hence, it is hard to observe MBL in experiments with solid-state systems which are always coupled to a thermal-bath of phonons. The first systems in which MBL was observed were synthetic quantum matter systems, which can be isolated from their environment to a high-degree, such as ultracold atoms [58, 176], trapped Ions [177] and superconducting qubit arrays [178].

The first observation of MBL was in a system of ultracold fermions with a quasi-periodic lattice potential (obtained by superimposing two lattices with incommensurate periods) [58]. The system is described by the following Hamiltonian:

$$H = -J \sum_{i,\sigma} (\hat{c}_{i,\sigma}^\dagger \hat{c}_{i+1,\sigma} + h.c.) + \Delta \sum_{i,\sigma} \cos(2\pi\beta i + \phi) \hat{n}_{i,\sigma} + U \sum_i \hat{n}_{i,\uparrow} \hat{n}_{i,\downarrow}. \quad (4.23)$$

The non-interacting part of  $H$  is known as the Aubry-André model, and it exhibits a localization transition at a critical value of the quasi-periodic potential strength  $\Delta = 2J$  [179]. Hence here  $\Delta$  plays a similar role to the disorder strength in the Anderson model.

In the experiment the system was prepared in an initial highly non-equilibrium state, consisting of a charge-density wave in which only the even lattice sites are occupied. This state is characterized by a high imbalance  $\mathcal{I} = (N_e - N_o)/(N_e + N_o)$ , with  $N_{e(o)}$  the number of particles residing on

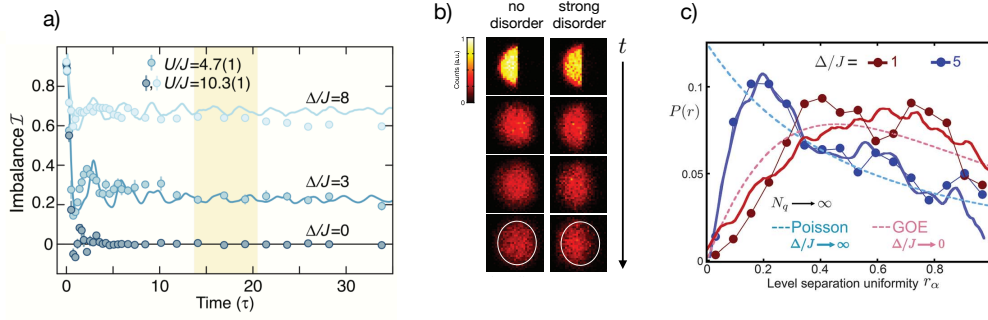


Figure 4.1: Experimental signatures of MBL. (a) Evolution of an initial density imbalance  $\mathcal{I} = (N_e - N_o)/(N_e + N_o)$  for different values of disorder strength  $\Delta$ , as observed in a 1D chain of ultracold interacting fermions. For strong disorder  $\mathcal{I}(t)$  retains a finite value even at long times indicating lack of thermalization (figure taken from [58]). (b) Indications for MBL in 2D system, as observed in the remnants of an initial density domain-wall at long times (figure adapted from [176]). (c) Experimental measurement of the energy level statistics  $P(r)$  for two photons in a 9 site Bose-Hubbard chain implemented in a superconducting qubit array.  $P(r)$  exhibits a change from Wigner-Dyson statistics at weak disorder to poisson statistics at strong disorder, which is an indication for a localized phase (figure taken from [178]).

even(odd) sites. Then the system is evolved and the imbalance  $\mathcal{I}(t)$  is tracked. In the absence of the quasi-periodic potential,  $\Delta = 0$ , the initial imbalance was observed to quickly relax to zero, while for  $\Delta > \Delta_c$  the imbalance remained at a finite value after an initial relaxation implying the lack of thermalization (see Fig. 4.1a).

Further experimental examples include the investigation of MBL in a 2D system of ultracold fermions [176], where the system was initialized with a density domain wall. There, for strong enough disorder, remnants of the density imbalance are still visible at long times, as opposed to the case with no disorder (see Fig. 4.1b). Signatures of localization were also observed in an experiment with superconducting qubits, where a novel spectroscopic method was used to directly measure the energy level statistics [178] (see Fig. 4.1c).

#### 4.2.5 THE MBL TRANSITION

Starting from the case of strong disorder and weak interactions, where the system is many-body localized, and decreasing the strength of disorder, an MBL system will eventually undergo a phase transition to an ergodic thermalizing phase. This MBL transition is very different than typical quantum (or classical) phase transitions studied in equilibrium settings, since the MBL properties are encoded in all the eigenstates of the Hamiltonian<sup>3</sup>. At the transition the eigenstates undergo a radical change in their entanglement properties from area-law in the MBL side to volume-law in the ergodic side. This is in contrast to  $T = 0$  quantum phase transitions which are between two different ground-states each having area-law entanglement. In a sense the MBL transition can be thought of as a transition between quantum and classical behavior. Indeed in the MBL phase

<sup>3</sup>In principle there could exist a many-body mobility edge, separating localized and ergodic eigenstates, but we ignore such complication in the qualitative discussion here.



quantum information encoded in the initial state persists to arbitrary long time. On the other hand quantum information is quickly scrambled and becomes inaccessible in the thermal phase, whose long time dynamics are well described by classical hydrodynamics.

So far, a clear simple thermodynamic quantity which serves as an order parameter for the MBL transition is not known, and in fact it could very well be that such an order parameter does not exist. Hence numerical studies of the MBL transition require analysis of dynamical and spectral properties, which are quantities that involve a large number of eigenstates. For this reason numerical studies of the transition are challenging and have been mainly limited to ED studies of small systems [27, 133–138].

A variety of quantities can be studied numerically using ED to detect the transition. Due to the emergent integrability, the energy levels are expected to exhibit Poisson behavior in the MBL phase, and Wigner-Dyson behavior in the ergodic phase. This can be seen numerically by studying the average of the ratio  $r_n = \min\{\delta_n, \delta_{n-1}\} / \max\{\delta_n, \delta_{n-1}\}$  with  $\delta_n = E_{n+1} - E_n$ . As a function of the disorder strength a transition from  $\langle r \rangle \approx 0.52$  (predicted by random matrix theory) in the ergodic phase to  $\langle r \rangle \approx 0.38$  (Poisson) in the MBL phase is observed [134]. Another quantity one can study is the eigenstate entanglement-entropy  $S_A$  of a subsystem  $A$  (averaged over disorder and eigenstates), which is expected to be independent of subsystem size in the MBL phase and scale linearly with size in the ergodic phase [135, 136, 180]. Furthermore the standard deviation of  $S_A$  over the disorder ensemble shows a peak at the transition, and it is thus analogous to a susceptibility.

In the ED studies the critical exponent  $\nu \approx 1$  is found [135, 180]. This result is inconsistent with the Harris bound  $\nu > 2/d$  which is a criterion for the stability of classical and quantum critical points in disordered systems [160, 181], which was argued to hold also for the MBL case [182]. This implies that ED studies suffer from strong finite-size effects which make observing the true critical behavior challenging.

A different approach for studying the MBL transition is by means of phenomenological RG schemes, which were first introduced by Vosk et al. [28] and Potter et al. [161]. For example, the RG description in [28] considers a set of blocks which represent insulating and thermal regions of a 1d system close to the MBL transition (where we expect both kind of regions to exist). Each block is described by a many-body level spacing  $\Delta_i \sim 2^{-\ell_i}$  and thermalization rate  $\Gamma_i$  (time for entanglement propagation). Together these two parameters form a dimensionless quantity  $g = \Gamma/\Delta$ , where  $g \gg 1$  for a thermal region and  $g \ll 1$  for an insulating region. In addition neighbouring blocks are coupled with rates  $\Gamma_{ij}$ . The RG coarse-graining step is comprised by merging the two block with the largest coupling  $\Gamma_{ij}$  and computing the new  $\Gamma_{\text{eff}}, \Delta_{\text{eff}}, \tilde{\Gamma}_{ij}$  according to a set of phenomenological rules. This can be viewed as reducing a cutoff  $\Omega = \max \Gamma_{ij}$ . Depending on the parameters of the merged block, this can lead to the new block becoming more insulating or more thermal.

As the RG steps are taken the average block size  $\ell$  increases. The main point is to examine the scaling of the typical value of  $g$  as a function of  $\ell$ . In the MBL phase blocks become more and more insulating as they are coarse grained  $g \sim e^{-\ell/\xi_{\text{RG}}}$ , while in the ergodic phase we expect  $g \sim e^{s\ell}$  at large scales with  $s$  the entropy density. Numerical simulation of the phenomenological RG shows a transition between these two regime as a function of the disorder strength which enters via the disorder in the initial distribution of  $g_i$ . This RG scheme, as well as the slightly different



(but similar in spirit) scheme in [161], predicts  $\nu \approx 3.3$  which is in agreement with the Harris bound.

#### 4.2.6 GRIFFITHS EFFECTS CLOSE TO THE MBL TRANSITIONS

One remarkable property of the transition between the ergodic and MBL phase in  $1d$  is the prediction of a continuously increasing dynamical exponent  $z$  which diverges at the critical point similarly to the localization length  $z \sim \xi \sim (h - h_c)^{-\nu}$ . This is a manifestation of Griffiths effects which are due to rare localized regions appearing in the thermal side of the transition.

The idea that rare regions in disordered systems can lead to singularities in dynamical correlation functions was originally introduced by Griffiths [183] and McCoy [184] in the context of classical disordered spin systems. The key idea of the Griffiths effects in the case of the MBL transition is the effect of rare insulating regions which are embedded in an otherwise thermal system. In a one-dimensional system these rare insulating regions act as a bottleneck for transport.

To understand the origin of the divergence of  $z$ , we bring here the intuitive scaling argument provided in Ref. [28]. In the ergodic phase, the density of insulating (or critical) regions of length  $\ell$  decays exponentially with the length and scales as <sup>4</sup>

$$p(\ell) \sim \frac{1}{\xi^2} e^{-\ell/\xi}, \quad (4.24)$$

where  $\xi$  is the length scale which diverges at the transition. Here we are assuming that the system size  $L$  is much larger than  $\xi$ . While long insulating regions are exponentially rare they act as a strong bottle-neck to transport with transport time  $\tau(\ell) \sim \tau_0 \exp(\ell/a)$  (with  $a, \tau_0$  some microscopic length and time scales respectively). For a long system of size  $L \gg \xi$ , the number of thermal regions with length  $> \ell$ , is given by  $N_L(\ell) = L \int_\ell^\infty ds p(s) = (L/\xi) e^{-\ell/\xi}$ . The longest region we will typically find in the system can be estimated from the condition  $N_L(\ell_m) = 1$ , which leads to  $\ell_m(L) \sim \xi \log(L/\xi)$ . Close enough to the MBL transition we can assume that the rare insulating regions will serve as the main bottleneck for transport, which leads to transport time

$$\tau \sim \tau_0 \exp(\xi/a \log(L/\xi)) \sim L^{\xi/a} \equiv L^z. \quad (4.25)$$

Hence we see that the dynamical exponent diverges as the correlation length  $z \sim \xi$  as we approach the critical point. Beyond the heuristic scaling argument, the divergence of  $z$  at the MBL transition was observed in the RG study of [28], where the phenomenological RG scheme allows one to extract the typical transport time of a block  $\tau_{tr} = (\ell/\ell_0) \Gamma^{-1}$ .

Typically for a weakly disordered system, propagation of particles can be described via a random-walk process due to a series of scattering events, and hence the equation governing dynamics of the density is a diffusion equation  $\partial_t n = D \partial_x^2 n$ . This leads to the common diffusive scaling with  $z = 2$  and transport time  $\tau \sim L^2$ . The arguments above suggest that close to the MBL transition sub-diffusive (i.e.  $z > 2$ ) transport is expected. This was observed numerically in several works using ED studies [145, 159, 185].

In particular Agarwal et al. [145] used both ED and an effective resistor-network model to study Griffiths signatures in the low-frequency behavior of the optical conductivity  $\sigma(\omega)$  and in the

<sup>4</sup>Note that by integrating  $p(\ell)$  we obtain that the total density of critical regions in the thermal bulk is  $\sim 1/\xi$ .

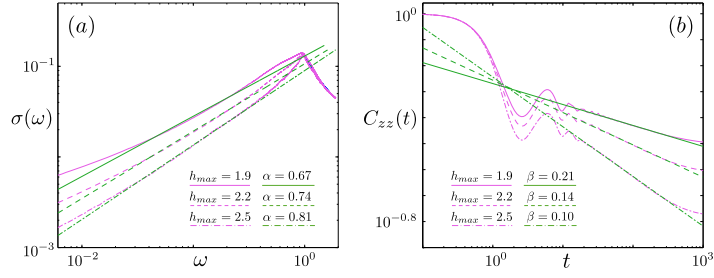


Figure 4.2: Power-law behavior of the optical conductivity  $\sigma(\omega)$  and return probability  $C_{zz}(t)$  close to the MBL transition in the ergodic side, obtained via ED study of the random-field XXZ model [145]. The power-law behavior indicates a sub-diffusive behavior which is a prediction of the Griffiths picture. Here the exponent  $\beta$  is related to the dynamical exponent via  $\beta = 1/z$ , and  $\alpha \approx 1 - 2\beta$ . Figure taken from Ref. [145].

return probability  $C_{zz}(t) \sim \langle S_i^z(t) S_i^z(0) \rangle$ . The study is done using the disordered XXZ model (Eq. (4.19)), where the infinite temperature limit of the optical conductivity is computed from the eigenstates using a linear-response formula  $T\sigma(\omega) \approx (LZ)^{-1} \sum_{mn} |\langle m | \sum_i j_i | n \rangle|^2 \delta(\omega - \omega_{mn})$  with  $j_i$  the spin current operators. The numerical results for a system of size  $L = 14$  show that both observables exhibit a power-law behavior  $\sigma(\omega) \sim \omega^\alpha$ ,  $C_{zz}(t) \sim t^{-\beta}$  on the ergodic side close to the MBL transition (see Fig. 4.2). The scaling relation observed between the exponents is  $\alpha + 2\beta \approx 1$ , which can be predicted by identifying  $z = 1/\beta$ . Specifically, it is observed that  $\beta$  decreases towards zero as the MBL transition is approached. In the case of diffusive transport  $C_{zz}(t) \sim 1/\sqrt{t}$  is expected, so  $\beta < 1/2$  indicates sub-diffusive transport indeed. Agarwal et al. further show that an effective resistor-network model, with a power-law distribution of resistances  $P(R) \sim R^{-\tau}$ , reproduces the numerical results of the microscopic model. This serves as evidence that the origin of the sub-diffusive transport is indeed due to the effects of rare insulating regions.

#### 4.2.7 MBL IN OPEN SYSTEMS

So far we have discussed MBL in the context of closed system dynamics, and we have seen that in a many-body localized system the interactions fail to thermalize the system. However, if we take an MBL system and connect it to a large thermal bath, for example phonons in a solid-state system, we would expect that the system will eventually reach thermal equilibrium as the coupling to phonons leads to transport via variable-range hopping. For this reason MBL has been hard to observe in real materials.

Experiments observing MBL have been so far performed in systems of synthetic matter of ultracold atoms or trapped ions [58, 176]. In those systems there are no phonons since the lattice is created via laser potentials. While ultracold atom systems can be isolated to a much better degree than solid-state systems, dissipation still exists in those systems (e.g. particle loss). Hence, it is important to study the effect of weak dissipation on the experimental signatures of MBL (which in AMO systems can be usually well described in terms of a Markovian Lindblad quantum master-equation).

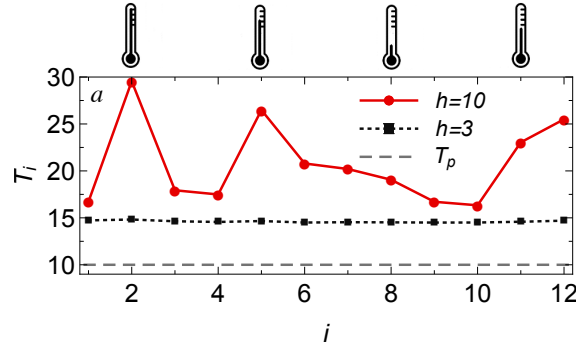


Figure 4.3: Lenarčič et al. used local temperature fluctuations to study the MBL transition in a system weakly coupled to phonons and drive with coupling strength  $\epsilon$  [141]. The figure shows the numerically calculated local temperature, in the limit  $\epsilon \rightarrow 0$ , for different values of the disorder strength  $h$ . For small  $h$  the system is in the thermal phase and the temperature profile is uniform. For large  $h$  the system is in the MBL phase and the weak coupling to the baths leads to large fluctuation of the local temperature, due to the existence of an extensive number of local integrals of motion. (Figure taken from [141])

Fischer et al. [147] considered the effects of coupling a system deep in the MBL phase to a dephasing noise  $L_i = n_i$  or particle loss  $L_i = c_i$ . Existence of LIOMS allows them to derive an effective classical master equation. The main goal is to explore the effect of the dissipation on the dynamics of a density imbalance  $\mathcal{I} = \langle n_e - n_o \rangle / \langle n_e + n_o \rangle$  (where  $n_e$  ( $n_o$ ) is the occupation of even (odd) sites) which is imprinted on the initial state. In the MBL phase, in the absence of dissipation, we expect the initial imbalance to decay to a finite value and retain a non-vanishing asymptotic value. Ref. [147] finds that dissipation leads to decay of the initial imbalance with a stretched exponential form, which is reminiscent of the dynamical behavior of classical glasses.

Lüschen et al. [61] performed an experimental study using ultracold fermions with controlled dephasing. They study ultracold fermions in a  $1d$  quasi-periodic optical lattice which realizes the interacting Aubry-André model, Eq. (4.23). Dephasing with a controlled rate is induced via a dedicated plane-wave laser which is tuned to induce internal atomic transition leading to photon scattering (which corresponds to a density “measurement”). The system is initialized in a charge-density with density imbalance  $\mathcal{I}$  close to unity.

The experimental measurements of the imbalance dynamics agree with the theoretical prediction of stretched exponential decay  $\mathcal{I}(t) \sim e^{(-\Gamma_{\mathcal{I}} t)^\beta}$  in Ref. [147]. The imbalance relaxation rate  $\Gamma_{\mathcal{I}}$  is found to be linearly increasing with the photon scattering rate  $\gamma$  (strength of dephasing noise). Furthermore, defining the susceptibility to dephasing via  $\Gamma_I = \chi\gamma + \Gamma_{bg}$ , it is found that  $\chi$  increases with interaction strength close to the MBL transition. Even though the experimental results show that dephasing eventually destroys MBL properties at long times, for weak enough dephasing rate it is possible to observe an intermediate regime where the imbalance is finite which allows for an experimental observation of MBL. One can think of  $\gamma$  having similar effect as temperature on a QCP, where the true properties of the QCP only exist at  $T = 0$ , but nevertheless one can observe signatures and crossovers also at  $T > 0$ .

A recent work by Lenarčič et al. [141] (of which our work in this chapter is a continuation of) suggested a route for observing the MBL transition in open-systems by coupling the system to an additional non-equilibrium drive. They considered a disordered interacting system which is weakly coupled to phonons and irradiated by light. In the limit of vanishing strength of drive and phonon coupling  $\epsilon_d, \epsilon_p \rightarrow 0$ . Ref. [141] observed that the variance of local temperatures acts as an order parameter for the MBL transition, and it is possible to extract the critical exponent  $\nu$  by examining its dependence on the disorder strength (see Fig. 4.3). Remarkably, even though the system sizes studied in [141] are quite small  $N \leq 12$ , the extracted critical exponent  $\nu \approx 2.6$  obeys the Harris bound  $\nu > 2/d$ . This is in stark contrast to previous numerical ED studies done on closed systems, which obtain  $\nu \approx 1$  in contradiction with the Harris bound.

To understand why the local temperature fluctuations are expected to act as an order parameter for the weakly open-driven MBL system, recall the fact that the MBL phase is characterized by an extensive set of quasi-local conserved quantities  $\tau_i^z$ . Previous works by Lenarčič, Lange and Rosch [127, 128] have shown that the steady-states of integrable systems which are weakly driven and coupled to baths can be well described by a generalized Gibbs ensemble  $\rho \sim \exp(\sum_i \lambda_i C_i)$ . Here, the expectation values of conserved quantities  $\langle C_i \rangle$ , and equivalently the Lagrange multipliers  $\lambda_i$ , are determined by the ratios of the drive strength and coupling to a bath. While the LIOMs in the MBL phase are different than the conserved quantities in integrable systems, we still expect a similar effect where the non-equilibrium steady-state will be characterized by an extensive set of widely varying local temperatures (Lagrange multipliers), leading to a large variance  $\delta T \sim O(1)$ . On the other hand, in the ergodic phase only the global energy is conserved (in the absence of bath coupling and drive) and hence following the results of [128] we expect the state of the system to be well described by a thermal Gibbs ensemble with one global temperature leading to no variance  $\delta T = 0$ .

### 4.3 BACKGROUND: STUDYING OPEN-QUANTUM SYSTEMS USING MATRIX-PRODUCT STATES

In this section we provide background on the main numerical technique used in our work, which is the representation of the density matrix in terms of a matrix-product density operator (MPDO) and time-evolution of the MPDO using the time-evolving block decimation (TEBD) algorithm [32, 186]. Here we provide just a brief review of the use of matrix-product state (MPS) techniques for simulation of quantum states of open systems, readers who want to learn more may want to refer to existing reviews such as Refs. [33, 187, 188].

Consider a  $1d$  spin chain of length  $N$ . The first step we take in order to simulate the dynamics described by the QME in Eq. (4.1) is using Choi's isomorphism to map the density matrix to a state in a doubled Hilbert space and the Liouvillian to a matrix which acts on states in this Hilbert space [189]:

$$\rho = \sum_{\sigma, \tau} \rho_{\sigma, \tau} |\sigma\rangle\langle\tau| \quad \rightarrow \quad |\rho\rangle = \sum_{\sigma, \tau} \rho_{\sigma, \tau} |\sigma, \tau\rangle, \quad (4.26)$$

where we denoted  $\sigma = (\sigma_1, \dots, \sigma_N)$  and similar for  $\tau$ . The Liouvillian acting on the vectorized density-matrix  $|\rho\rangle$  is given by the non-hermitian operator

$$\hat{\mathcal{L}} = -i(H \otimes \mathbb{1} - \mathbb{1} \otimes H^T) + \sum_i \gamma_i \left[ L_i \otimes L_i^* - \frac{1}{2}(L_i^\dagger L_i \otimes \mathbb{1} + \mathbb{1} \otimes L_i^T L_i) \right]. \quad (4.27)$$

Starting from some initial density matrix  $\rho_0$  the state of the system at time  $t$  can be obtained as:

$$|\rho_t\rangle = e^{t\hat{\mathcal{L}}}|\rho_0\rangle. \quad (4.28)$$

The steady-state can be obtained as the eigenstate of  $\hat{\mathcal{L}}$  with eigenvalue  $\lambda = 0$ . For a spin chain of size  $N$ ,  $|\rho\rangle$  is a vector of length  $4^N$  and  $\hat{\mathcal{L}}$  is a matrix of size  $4^N \times 4^N$ . Hence performing exact time evolution or finding the steady-state by means of exact diagonalization (ED) of  $\hat{\mathcal{L}}$  is exponentially expensive in the system size  $N$  and limits computations to small system sizes  $N \sim 12$ .

In order to simulate the dynamics of larger systems one has to abandon the idea of representing the quantum state of the system exactly and resort to some sort of approximation which allows representing the state of the system with a number of parameters which is polynomial in the system size  $N$ . The approach we will describe here is that of matrix-product states which is an efficient method to represent quantum states with low entanglement, and is often the best method for performing computations in 1-dimensional systems. Since we have seen that the problem of simulating the QME dynamics can be mapped to that of non-unitary evolution of a pure state  $|\psi\rangle$  in an enlarged Hilbert space, we will first describe the method considering time-evolution of pure states. After doing so we will give some comments regarding the application of the method in the context of QME dynamics.

A general quantum state of a 1D spin chain can be represented by a tensor  $c_{\sigma_1, \dots, \sigma_N}$  written as

$$|\psi\rangle = \sum_{\sigma} c_{\sigma_1, \dots, \sigma_N} |\sigma\rangle \quad (4.29)$$

where the entries in the tensor  $c_{\sigma_1, \dots, \sigma_N}$  are the probability amplitudes of the basis states  $|\sigma\rangle$ . As we explained above the number of coefficients in  $c_{\sigma}$  scales exponentially with the system size  $N$ .

The simplest approximation one can use is that of a product-state where we assume that the tensor  $c$  is completely factorizable, that is  $c_{\sigma} = c_{\sigma_1} c_{\sigma_2} \dots c_{\sigma_N}$ , which leads to the following state:

$$|\psi\rangle = \bigotimes_i \left( \sum_{\sigma_i = \pm 1} c_{\sigma_i} |\sigma_i\rangle \right). \quad (4.30)$$

In the case where  $c_{\sigma_i}$  are independent of  $i$ , the product-state ansatz is also known as the mean-field approximation. Using the product-state ansatz reduces the number of complex coefficients from  $2^N$  to  $2N$ . However, product-states are very limited since they cannot represent any connected correlations or entanglement between spins on different sites, as we will see below.

Matrix-product states (MPS) are a generalization of product states where instead of factorizing the high-dimensional tensor  $c_{\sigma}$  as a product of numbers, we factorize it as a product of matrices:

$$|\psi\rangle = \sum_{\sigma} M_{\alpha_1}^{\sigma_1} M_{\alpha_1 \alpha_2}^{\sigma_2} \dots M_{\alpha_{N-1}}^{\sigma_N} |\sigma\rangle \quad (4.31)$$

where  $M_{\alpha_{i-1} \alpha_i}^{\sigma_i}$  is a matrix of dimension  $\chi_{i-1} \times \chi_i$  (for each site there are two matrices corresponding to  $\sigma_i = \pm 1$ ), with  $\chi_i$  known as the bond-dimension of bond  $i$ . The total number of parameters scales as  $O(N\chi)$  with  $\chi = \max_i \{\chi_i\}$ .

A product-state is a special case of an MPS with bond-dimension 1. On the other hand any quantum-state can be represented exactly as an MPS when using a bond-dimension which grows exponentially with the system size. The key insight is that states with moderate amount of entanglement can be represented efficiently as an MPS with a bond-dimension that is independent of the system-size. To see the connection between bond-dimension and entanglement we consider a bi-partition of the spin-chain at bond  $\ell$ :

$$|\psi\rangle = \sum_{\sigma_L, \sigma_R} \Psi_{\sigma_L, \sigma_R} |\sigma_L\rangle |\sigma_R\rangle, \quad (4.32)$$

where we denoted  $\sigma_L = \{\sigma_1, \dots, \sigma_\ell\}$ ,  $\sigma_R = \{\sigma_{\ell+1}, \dots, \sigma_N\}$ . The Schmidt decomposition of the state can be obtained from a singular-value decomposition (SVD) of the matrix  $\Psi$ , and is given by

$$|\psi\rangle = \sum_{i=1}^r \Lambda_i |\alpha_i^L\rangle |\alpha_i^R\rangle, \quad (4.33)$$

where  $\{|\alpha_i^L\rangle\}$  ( $\{|\alpha_i^R\rangle\}$ ) is an orthonormal basis of the left (right) subsystem, and  $\Lambda_i \geq 0$  are the Schmidt values (or singular values). Here we denoted the number of non-zero Schmidt values by  $r$ . Note that since  $|\psi\rangle$  is normalized we have  $\sum_i \Lambda_i^2 = 1$ .

Given the Schmidt decomposition, we can easily compute the entanglement-entropy of the bi-partition:

$$\rho_L = \text{tr}_R |\psi\rangle \langle \psi| = \sum_i \Lambda_i^2 |\alpha_i^L\rangle \langle \alpha_i^L| \Rightarrow \quad (4.34)$$

$$S(\ell) = -\text{tr} \rho_L \log \rho_L = -\sum_{i=1}^r \Lambda_i^2 \log \Lambda_i^2 \leq \log r. \quad (4.35)$$

So we see that the amount of entanglement is bounded by the logarithm of the Schmidt rank  $r$ .

Consider now an MPS, and denote

$$U_{\sigma_L, \alpha_\ell} \equiv (M^{\sigma_1} M^{\sigma_2} \dots M^{\sigma_\ell})_{\alpha_\ell}, \quad V_{\alpha_\ell, \sigma_R} \equiv (M^{\sigma_{\ell+1}} \dots M^{\sigma_N})_{\alpha_\ell}. \quad (4.36)$$

The matrix representing the bi-partition is given by  $\Psi_{\sigma_L, \sigma_R} = U_{\sigma_L, \alpha_\ell} V_{\alpha_\ell, \sigma_R}$ . This means that the number of non-zero singular values of  $\Psi$  is bounded by the dimension of the index  $\alpha_i$ <sup>5</sup>.

<sup>5</sup>This is true because the rank of  $\Psi$  is equal to the number of non-zero singular values and in addition  $\text{rk} \Psi \leq \text{rk} V$  due to the fact that  $\ker V \subseteq \ker \Psi$ .

Hence, we see that the maximal entanglement for a bi-partition at bond  $\ell$  for an MPS with bond dimension  $\chi_\ell$  is  $S(\ell)_{\text{MPS-max}} = \log \chi_\ell$ . In particular we see that a product state where  $\chi_\ell = 1$  has no entanglement.

From the discussion above we expect that an MPS ansatz is indeed an efficient ansatz when the amount of entanglement of the state we want to approximate does not grow faster than logarithmically in system size. This is the case for ground-states of gapped local Hamiltonians in 1D, whose entanglement follows an area-law [190]. The MPS ansatz can also be used for approximating state of a system after a quantum quench  $|\psi(t)\rangle$ , however for generic systems the method is limited to short times due to the ballistic growth of the entanglement-entropy. For the mixed state case, note that an infinite temperature density-matrix can be represented exactly as a  $D = 1$  MPS, namely it is the product state of bell-pairs of the  $\sigma_i, \tau_i$  local spins  $|\rho_\infty\rangle = 2^{-L} \bigotimes_i (|\uparrow\uparrow\rangle_i - |\downarrow\downarrow\rangle_i)$ <sup>6</sup>. Hence we expect that density-matrices which are somewhat close to the infinite temperature state can be efficiently represented as an MPDO.

In our work in this chapter we use the time-evolving block decimation (TEBD) algorithm [32] in order to compute  $|\rho(t)\rangle = e^{t\mathcal{L}}|\rho_0\rangle$ . By evolving  $\rho(t)$  to long-times we can obtain an approximation for the steady-state of  $\mathcal{L}$ . The TEBD algorithm, initially introduced for real time coherent evolution of pure states  $|\psi(t)\rangle = e^{-iHt}|\psi_0\rangle$ , relies on a Trotter decomposition of the time-evolution operator  $U(t) = \exp(-iHt)$ . Assuming that  $H$  has at most two-site operators, we can write  $H = \sum_{b=1}^{L-1} h_b$ , with  $h_b$  having support only on sites  $b, b+1$ . The 1st order Trotter decomposition then reads

$$U(Ndt) \approx \left[ \prod_{b \in \text{odd}} e^{(-idth_b)} \prod_{b \in \text{even}} e^{(-idth_b)} \right]^N. \quad (4.37)$$

The error in this approximation is  $O(dt^2)$  per time step. Here we discuss the 1st order approximation for simplicity, but in practice we use a 4th order decomposition (see [33]) in our computations in this chapter.

The key component we need to understand is how to apply a two-site unitary of the form  $U_{b,b+1} = \exp(-idth_b)$  to a state represented as an MPS. In order to do so, we first need to introduce the concept of canonical form of an MPS. Note that the representation (4.31) is not unique as it is invariant under a gauge transformation  $M_i \rightarrow M_i G, M_{i+1} \rightarrow G^{-1} M_{i+1}$ , where  $G$  is an arbitrary invertible matrix. We say that an MPS tensor is left-orthonormal if  $A_{\alpha_{i-1}\alpha_i}^{[\sigma_i]} (A_{\alpha_{i-1}\alpha'_i}^{[\sigma_i]})^* = \delta_{\alpha_i\alpha'_i}$  and right-orthonormal if  $B_{\alpha_i\alpha_{i+1}}^{[\sigma_i]} (B_{\alpha'_i\alpha_{i+1}}^{[\sigma_i]})^* = \delta_{\alpha_i\alpha'_i}$ . We follow a convention where tensors denoted by  $A$  ( $B$ ) are assumed to be left(right)-orthonormal. An arbitrary MPS can be brought into a left(right)-canonical form, where all the matrices are left (right)-orthonormal via a series of QR decompositions.

To apply  $U_{b,b+1}$  we first bring  $|\psi\rangle$  to a mixed canonical form:

$$\begin{aligned} |\psi\rangle &= \sum_{\sigma} A^{\sigma_1} \dots A^{\sigma_b} B^{\sigma_{b+1}} \dots B^{\sigma_N} |\sigma\rangle \\ &\equiv \sum_{\alpha_{b-1}, \alpha_{b+1}, \sigma_b, \sigma_{b+1}} \Theta_{\alpha_{b-1}, \alpha_{b+1}}^{\sigma_b, \sigma_{b+1}} |\alpha_{b-1}\rangle |\sigma_b\rangle |\sigma_{b+1}\rangle |\alpha_{b+1}\rangle \end{aligned} \quad (4.38)$$

<sup>6</sup>This can be seen by transforming  $\rho_\infty = \bigotimes_i \mathbb{1}_i$  using Choi's isomorphism.

where the two site wave-function is  $\Theta_{\alpha_{b-1}, \alpha_{b+1}}^{\sigma_b, \sigma_{b+1}} \equiv A_{\alpha_{b-1} \alpha_b}^{\sigma_b} B_{\alpha_b \alpha_{b+1}}^{\sigma_{b+1}}$  and we defined the states

$$|\alpha_{b-1}\rangle = \sum_{\sigma_{1..b-1}} (A^{\sigma_1} \dots A^{\sigma_{b-1}})_{\alpha_{b-1}} |\sigma_1, \dots, \sigma_{b-1}\rangle, \quad (4.39)$$

$$|\alpha_{b+1}\rangle = \sum_{\sigma_{b+2..N}} (B^{\sigma_{b+2}} \dots B^{\sigma_N})_{\alpha_{b+1}} |\sigma_{b+2}, \dots, \sigma_N\rangle. \quad (4.40)$$

Due to the orthonormality properties of the  $A$  and  $B$  tensors,  $\{|\alpha_{b-1}\rangle\}$  and  $\{|\alpha_{b+1}\rangle\}$  are sets of orthonormal states.

Applying  $U_{b,b+1}|\psi\rangle$  results in an update to the two-site wave function

$$\Theta_{\alpha_{b-1} \alpha_{b+1}}^{\sigma_b \sigma_{b+1}} \rightarrow U_{\sigma'_b \sigma'_{b+1}}^{\sigma_b \sigma_{b+1}} \Theta_{\alpha_{b-1} \alpha_{b+1}}^{\sigma'_b \sigma'_{b+1}} \equiv \tilde{\Theta}_{\alpha_{b-1} \alpha_{b+1}}^{\sigma_b \sigma_{b+1}}. \quad (4.41)$$

To finish we want to bring  $U_{b,b+1}|\psi\rangle$  back to a mixed canonical form. This can be done by reshaping  $\tilde{\Theta}$  to a  $(2\chi_{b-1}) \times (2\chi_{b+1})$  matrix and performing an SVD decomposition

$$\tilde{\Theta}_{(\sigma_b \alpha_{b-1})(\alpha_{b+1} \sigma_{b+1})} = U_{(\sigma_b \alpha_{b-1}), \alpha_b} S_{\alpha_b} V_{\alpha_b, (\alpha_{b+1} \sigma_{b+1})}^\dagger \quad (4.42)$$

where  $S_{\alpha_b} \geq 0$  are the singular values which are assumed to be ordered by magnitude. We can now define  $A_{\alpha_{b-1}, \alpha_b}^{\sigma_b} = U_{(\sigma_b \alpha_{b-1}), \alpha_b}$  and  $B_{\alpha_b, \alpha_{b+1}}^{\sigma_{b+1}} = S_{\alpha_b} V_{\alpha_b, (\alpha_{b+1} \sigma_{b+1})}^\dagger$ .

Note that a consequence of the application of  $U_{b,b+1}$  is generically an increase of the bond dimension  $\chi_b \rightarrow 2\chi_b$ . The key idea of the TEBD algorithm is to keep only the most important Schmidt values at every unitary update and discard all Schmidt values such that the error introduced is below a cutoff  $\epsilon$ . Assume that  $\sum_{\alpha_b=d_c+1}^{2\chi_b} S_{\alpha_b}^2 \leq \epsilon$ , then the TEBD update is done via a truncated SVD decomposition

$$\tilde{\Theta}_{(\sigma_b \alpha_{b-1})(\alpha_{b+1} \sigma_{b+1})} \approx \frac{1}{\mathcal{N}} \sum_{\alpha_b=1}^{d_c} U_{(\sigma_b \alpha_{b-1}), \alpha_b} S_{\alpha_b} V_{\alpha_b, (\alpha_{b+1} \sigma_{b+1})}^\dagger \quad (4.43)$$

where the normalization factor  $\mathcal{N} = \sqrt{\sum_{\alpha_b=1}^{d_c} S_{\alpha_b}^2}$  ensures that the state remains normalized. Now we can update the tensors  $A^{\sigma_b}, B^{\sigma_{b+1}}$  as before, but using only  $d_c$  columns of  $U$  and  $d_c$  rows of  $\mathcal{N}^{-1} S V^\dagger$ .

The bond dimension after the update is  $d_c$  which can be much smaller than  $2\chi_b$  as long as the state is not too entangled, allowing for an efficient compression of the state. The error introduced by the state obtained via the truncated SVD update  $|\tilde{\psi}\rangle$  is bounded by the cutoff  $\| |\tilde{\psi}\rangle - U_{b,b+1}|\psi\rangle \|^2 \leq \epsilon$ .

Finally let us comment on two aspects which are special to the case of Liouvillian evolution of an MPDO  $|\rho\rangle$  using TEBD. When performing the update in the case of Hamiltonian evolution we relied on the fact that the two-site operator acting at bond  $b$  is unitary and hence the state remains in canonical form. This is not the case with non-unitary evolution and we have to bring back the MPDO to canonical form after every few update steps. Second, the normalization condition for a density-matrix is  $\text{tr} \rho = 1$  which in the vectorized form reads as  $(\mathbb{1}|\rho) = 1$ . However,



for applying MPS algorithms in general and TEBD in particular it is important to keep the vectorized state normalized according to  $\langle \rho | \rho \rangle = 1$ . Thus when computing expectation values of operators using the MPDO representation of  $|\rho\rangle$  we must divide by  $\text{tr} \rho$

$$\langle \hat{O} \rangle = \frac{\langle \rho | \hat{O} | \rho \rangle}{(\mathbb{1} | \rho)}.$$
 (4.44)

#### 4.4 HYDRODYNAMIC DESCRIPTION OF TEMPERATURE FLUCTUATIONS IN THE THERMAL PHASE

Having introduced the main ideas behind many-body localization, the transition between the ergodic phase and the MBL phase, and the expected divergence of the dynamical exponent  $z$  due to rare-region (Griffiths) effects close to the critical point, we are now ready to consider the possibility of probing the Griffiths physics by coupling the system to non-equilibrium baths.

We start by considering an effective hydrodynamic description for the temperature fluctuations in the thermal side of the MBL transition, in the presence of coupling to baths. The origin of the hydrodynamic description comes from a continuity equation for the energy density in the presence of an external energy source and sink, which in the absence of any other conserved quantities is given by  $\partial_t e + \nabla \cdot \mathbf{J} = \epsilon \theta I_{\text{source}} - \epsilon I_{\text{sink}}$ . By expressing the energy current in terms of a temperature gradient  $\mathbf{J}(\mathbf{r}) = -\kappa(\mathbf{r}) \nabla T(\mathbf{r})$ , with  $\kappa(\mathbf{r})$  a local heat conductivity, we obtain

$$\partial_t e - \nabla \cdot (\kappa(\mathbf{r}) \nabla T(\mathbf{r})) = -\epsilon g_1(\mathbf{r})(T(\mathbf{r}) - T_0) + \epsilon \theta g_2(\mathbf{r}).$$
 (4.45)

Effects of disorder are taken into account in Eq. (4.45) by weak fluctuations of the conductivity  $\kappa(\mathbf{r})$  and of the strength of external energy sources  $g_{1(2)}(\mathbf{r})$ :

$$\kappa(\mathbf{r}) = \bar{\kappa} + \delta\kappa(\mathbf{r}), \quad g_{1(2)}(\mathbf{r}) = \bar{g} + \delta g_{1(2)}(\mathbf{r}),$$
 (4.46)

where  $\delta\kappa(\mathbf{r}), \delta g_{1(2)}(\mathbf{r})$  are Gaussian random variables with zero mean. The average effective steady-state temperature is  $\bar{T} = T_0 + \theta$ , and is obtained by averaging both sides of Eq. (4.45) with respect to disorder.

We now consider the fluctuations of temperature around  $\bar{T}$  in the steady-state. This is done by denoting  $T(\mathbf{r}) = \bar{T} + \delta T(\mathbf{r})$  and linearizing Eq. (4.45) in the disorder strength, keeping only terms which are first order in the fluctuations  $O(\delta g), O(\delta T), O(\delta \kappa)$ . This leads to

$$(-\bar{\kappa} \nabla^2 + \epsilon \bar{g}) \delta T(\mathbf{r}) = \epsilon \theta \delta g(\mathbf{r}),$$
 (4.47)

where  $\delta g(\mathbf{r}) = \delta g_2(\mathbf{r}) - \delta g_1(\mathbf{r})$ . This equation can be solved for the local temperature variations by fourier transforming to momentum space resulting in

$$(\bar{\kappa} k^2 + \epsilon \bar{g}) \delta T_{\mathbf{k}} = \epsilon \theta \delta g_{\mathbf{k}}.$$
 (4.48)

We see that  $\delta T_{\mathbf{k}} = \tilde{G}(\mathbf{k}) \delta g_{\mathbf{k}}$ , with the Green's function given by  $\tilde{G}(\mathbf{k}) = (\bar{\kappa} k^2 + \epsilon \bar{g})^{-1}$ .

Now we can use the formalism of fractional calculus [191, 192] in order to generalize the linearized hydrodynamic Eq. (4.47) to describe the sub- and super-diffusive case. The key idea is

to modify the real-space Green's function  $G(\mathbf{r})$ , describing the response of temperature fluctuations to a random pump and drive  $\delta g(\mathbf{r})$ , by replacing the Laplace operator  $\nabla^2$  with the Riesz fractional derivative  $\nabla^z$ . The fractional derivative is defined via its Fourier transform  $\mathcal{F}$ ,

$$\mathcal{F}(\nabla^z y(\mathbf{r})) = -|k|^z \mathcal{F}(y(\mathbf{r})), \quad z > 0, \quad (4.49)$$

where  $y(\mathbf{r})$  is an infinitely differentiable function. Hence, the generalized continuity equation gives rise to the following Green's function in momentum space

$$G(\mathbf{k}) = \frac{1}{\bar{\gamma}|k|^z + \bar{g}\epsilon}. \quad (4.50)$$

Uncorrelated disorder  $\langle \delta g(\mathbf{r}) \delta g(\mathbf{r}') \rangle = (\delta g)^2 \delta(\mathbf{r} - \mathbf{r}')$  gives the following scaling of temperature fluctuations with the dimension  $d$  and fractional power  $z$

$$\begin{aligned} \langle \delta T^2 \rangle &= \frac{\epsilon^2 \theta^2}{L} \int G(\mathbf{r} - \mathbf{r}') G(\mathbf{r} - \mathbf{r}'') \langle \delta g(\mathbf{r}') \delta g(\mathbf{r}'') \rangle d\mathbf{r} d\mathbf{r}' d\mathbf{r}'' \\ &= \frac{\epsilon^2 \theta^2 \delta g^2}{(2\pi)^d} \int d\mathbf{k} \frac{1}{(\bar{\gamma}|k|^z + \epsilon \bar{g})^2} \\ &\sim \frac{\theta^2 \delta g^2}{\bar{g}^2} \frac{\bar{g}^{d/z}}{\bar{\gamma}^{d/z}} \frac{(z-d)}{z^2 \sin(d\pi/z)} \epsilon^{d/z}. \end{aligned} \quad (4.51)$$

By the replacement  $k^2 \rightarrow |k|^z$  in the hydrodynamic equation for  $\delta T$  we have obtained the scaling of the of the temperature fluctuations with small  $\epsilon$ :

$$\sqrt{\langle \delta T^2 \rangle} \sim \theta |\delta g / \bar{g}| (\bar{g} / \bar{\gamma})^{d/2z} \epsilon^{d/2z}. \quad (4.52)$$

Hence this implies that by exploring the response of the local temperature fluctuations to weak coupling to a bath  $\epsilon$ , we will be able to extract the value of the dynamical exponent  $z$ .

The derivation above provides a heuristic and intuitive explanation for the expected scaling form, and explains how  $z$  enters into the dependence on  $\epsilon$ . We note however, that using a disorder averaged Green's function to get this result may not be properly accounting for the effect of rare regions that dominate the transport in the Griffiths regime. In Sec. 4.5 we compute the temperature variations in a minimal model that takes this physics into account.

#### 4.4.1 HYDRODYNAMIC EQUATIONS AS AN EXPANSION OF THE QME

In this section we make the connection between the microscopic QME in Eq. (4.1), describing a disordered spin chain coupled to Markovian nonequilibrium baths represented by Lindblad operators, and the hydrodynamic Eq. (4.45) describing long wavelength temperature fluctuations. More specifically we show how Eq. (4.45) can be derived using an expansion in small temperature variations around a thermal density matrix, determined from the Liouville equation  $\dot{\rho} = (\hat{\mathcal{L}}_0 + \epsilon \hat{\mathcal{D}})\rho = 0$ , where  $\hat{\mathcal{L}}_0 \rho = -i[H, \rho]$  and  $\hat{\mathcal{D}}$  corresponds to the dissipator super-operator.

On the ergodic side, the system approaches a thermal state for  $\epsilon \rightarrow 0$  [141]. For small epsilon, we can therefore expand the steady state density matrix in weak temperature variations around the thermal state

$$\rho \approx \rho_0(\bar{T}) + \sum_j \delta T_j \frac{\partial \rho}{\partial T_j} \Big|_{T_j=\bar{T}} + \dots, \quad \rho_0(\bar{T}) \equiv \frac{e^{-H/\bar{T}}}{\text{tr}[e^{-H/\bar{T}}]}. \quad (4.53)$$

We will now use the expansion (4.53) in order to show how the phenomenological terms in Eq. (4.45) can emerge from the microscopic Liouville equation.

First of all, the term  $-\epsilon \bar{g}(T(\mathbf{r}) - \bar{T})$  ensures the relaxation towards the correct mean temperature  $\bar{T}$ , which is determined from the stationarity condition applied to the total rate equation for the energy [141],

$$\langle \dot{H} \rangle = \text{tr}[H(\hat{\mathcal{L}}_0 + \epsilon \hat{\mathcal{D}})\rho_0(\bar{\beta})] = \text{tr}[H \epsilon \hat{\mathcal{D}} \rho_0(\bar{\beta})] \stackrel{!}{=} 0, \quad (4.54)$$

where we use the fact that the thermal density matrix commutes with the Hamiltonian and hence  $\hat{\mathcal{L}}_0 \rho_0 = 0$ .

To see the emergence of the other terms in Eq. (4.45) we consider the behaviour of the local energy density  $\langle h_i \rangle$ , where  $H = \sum_i h_i$ , and  $h_i$  are terms with local support around bond  $i$  (in the model we consider they are at most two-site terms)

$$\frac{d}{dt} \langle h_i \rangle = \text{tr} \left[ h_i \hat{\mathcal{L}}_0 \rho \right] \quad (4.55)$$

$$+ \text{tr} \left[ h_i \epsilon \hat{\mathcal{D}} \rho_0(\bar{\beta}) \right] \quad (4.56)$$

$$+ \text{tr} \left[ h_i \epsilon \hat{\mathcal{D}} \sum_j \frac{\partial \rho}{\partial T_j} \Big|_{T_j=\bar{T}} \delta T_j \right] \quad (4.57)$$

$$+ \dots$$

Using the definition for the energy currents,  $j_{i,i+1} = i[h_i, h_{i+1}]$ , we can see that the right hand side of expression (4.55) equals to the difference in expectation value of energy currents across neighboring links. On the other hand, in a system with spatially varying local temperatures, local current expectation values are proportional to local temperature gradients

$$\text{tr} \left[ h_i \hat{\mathcal{L}}_0 \rho \right] = \text{tr} [(-j_{i,i+1} + j_{i-1,i})\rho] \quad (4.58)$$

$$= \Gamma_{i,i+1}(T_{i+1} - T_i) - \Gamma_{i-1,i}(T_i - T_{i-1})$$

$$\sim \nabla \cdot (\kappa(\mathbf{r}) \nabla T(\mathbf{r})), \quad (4.59)$$

where we denoted  $\Gamma_{i,i+1}$  the heat conductance between site  $i$  and site  $i + 1$ .

The term (4.56) corresponds to the gain and loss of local energy density due to the driving and dissipation, evaluated with respect to the homogeneous thermal state

$$\text{tr} \left[ h_i \epsilon \hat{\mathcal{D}} \rho_0(\bar{\beta}) \right] \sim \epsilon \theta g_2(\mathbf{r}). \quad (4.60)$$

Here  $\langle g_2(\mathbf{r}_i) \rangle = \frac{1}{\theta N} \sum_i \text{tr}[h_i \hat{D} \rho_0(\bar{\beta})] = 0$  due to Eq. (4.54).

Term (4.57) is of the same type, but comes from the next order expansion in the variation of local temperatures

$$\text{tr} \left[ h_i \epsilon \hat{D} \sum_j \frac{\partial \rho}{\partial T_j} \Big|_{T_j=\bar{T}} \delta T_j \right] \sim \epsilon g_1(\mathbf{r}) \delta T(\mathbf{r}). \quad (4.61)$$

Collecting the dominant terms in the fluctuation expansion, we get the hydrodynamic relation

$$\partial_t e - \nabla \cdot (\kappa(\mathbf{r}) \nabla T(\mathbf{r})) = -\epsilon g_1(\mathbf{r})(T(\mathbf{r}) - \bar{T}) + \epsilon \theta g_2(\mathbf{r}), \quad (4.62)$$

which can be identified with Eq. (4.45), except that  $T_0$  is replaced by  $\bar{T}$  (set by Eq. 4.54) and that the last term contains only the random part with a zero mean, i.e.,  $g_2(\mathbf{r}) = \delta g_2(\mathbf{r})$ .

## 4.5 RESISTOR NETWORK SIMULATIONS

As a minimal model for the Griffiths regime we consider in this section a chain of conducting islands, each characterized by its own temperature  $T_i$ , coupled by links representing insulating regions of size  $\ell$ . The essence of the Griffiths physics can be captured by the fact that in the ergodic phase an insulators are exponentially rare but they also act as a bottleneck for transport with and exponentially small conductance. To take this into account, the link (insulator) lengths are drawn from the probability distribution  $P(\ell) = \frac{1}{N} e^{-\ell/\xi}$ , where  $\xi$  is identified with the correlation length that diverges toward the MBL critical point. Each insulating region gives rise to a conductance exponentially small in its length  $\Gamma_{\text{ins}}(\ell) = \Gamma_0 e^{-\ell/a}$ , where  $a$  is a microscopic length scale.

Without the coupling to the drive and the bath, the distribution of insulating links leads to a power-law distribution of inter-island conductances

$$\begin{aligned} P(\Gamma) &= \frac{1}{N} \left| \frac{d\Gamma}{d\ell} \right|^{-1} P(\ell(\Gamma)) \\ &\sim \Gamma^{-1} \left( \frac{\Gamma}{\Gamma_0} \right)^{a/\xi} \\ &\sim \left( \frac{\Gamma}{\Gamma_0} \right)^{\alpha-1}, \end{aligned} \quad (4.63)$$

with  $\alpha = \frac{a}{\xi}$ . The range  $0 < \alpha < 1$ , for which the average resistance  $\langle \Gamma^{-1} \rangle$  diverges corresponds to the subdiffusive regime [145, 193].

Coupling this system to a bath and to an energy source ultimately destroys the insulating behavior of the links, adding a channel of conductance through the link with conductivity  $\epsilon \kappa_0$ . Thus we take the heat conductance through a link in presence of this coupling to be

$$\Gamma(\ell) = \epsilon \frac{\kappa_0}{\ell} + \Gamma_0 e^{-\ell/a}, \quad (4.64)$$

with an implicit short-range cutoff  $a$  (to ensure that the probability distribution of conductances is normalizable). The form in Eq. (4.64) is obtained by assuming that the conductance channel induced by the bath is connected in parallel to the intrinsic conductance channel of the insulator, and the conductance of the bath channel is obtained by assuming Ohm's law dependence  $\Gamma \propto L^{d-2}$ .

With the link conductances in hand, we can write the rate equation for the energy transport on the chain

$$\begin{aligned} \partial_t e_i - \Gamma_{i,i+1}(T_{i+1} - T_i) + \Gamma_{i-1,i}(T_i - T_{i-1}) \\ = -\epsilon g_{1,i}(T_i - T_0) + \epsilon \theta g_{2,i}. \end{aligned} \quad (4.65)$$

This is a discrete version of Eq. (4.45) with a physically motivated distribution of link conductances. We take  $g_{1(2),i} = \bar{g} + \delta g_{1(2),i}$  with  $\delta g_{1(2),i}$  drawn from a uniform distribution in the range  $[-\delta g_{1(2)}, \delta g_{1(2)}]$ .

Requiring that the system is in a steady-state  $\partial_t e_i = 0$ , Eq. (4.65) reduces to a system of linear equations which we solve numerically to obtain temperature profiles. We extract the normalized variation of local temperatures

$$O_T \equiv \frac{\delta T}{\bar{T}} \equiv \frac{\sqrt{\langle\langle \text{Var}(T_i) \rangle\rangle}}{\langle\langle \mathbb{E}(T_i) \rangle\rangle}. \quad (4.66)$$

Here  $\mathbb{E}$  and  $\text{Var}$  are the sample mean and variance, while  $\langle\langle \cdot \rangle\rangle$  denotes averaging over disorder realizations. For simplicity we assumed that the conducting islands are all of similar size.

The results of the numerical solution for  $\delta T/\bar{T}$  as a function of  $\epsilon$  are shown in Fig. 4.4 for different values of  $\alpha = a/\xi$ . We extract the dynamical exponent  $z$ , by assuming the dependence found in Eq. (4.52),  $\delta T \sim \epsilon^{1/2z}$ . In Fig. 4.4 we see that for  $0 < \alpha < 1$  the dynamical exponent grows with the correlation length as  $z \sim 1/\alpha = \xi/a$ , which agrees with findings of closed-system studies of the Griffith regime in the vicinity of the MBL transition [28, 145]. For  $\alpha > 1$  the dynamical exponent saturates to  $z = 2$ , as expected for a diffusive system. Thus we establish a direct relation between the leading dependence of the temperature fluctuations  $\delta T$  on  $\epsilon$  and the dynamical exponent  $z$ , which governs the sub-diffusive behavior in a closed system [28, 161]. Crucially we find that the dynamical exponent diverges together with the correlation length  $\xi$  on approaching the MBL transition [28, 161].

In solid state systems it is usually much easier to measure charge transport than the local temperature profile. It is therefore natural to seek signatures of MBL or the Griffiths regimes in the resistance of a weakly open system. In order to compute how the resistance scales with the external bath or drive coupling  $\epsilon$  we consider a charge resistor network described by the rate equations

$$\partial_t n_i - [\tilde{\Gamma}_{i,i+1}(\mu_{i+1} - \mu_i) - \tilde{\Gamma}_{i-1,i}(\mu_i - \mu_{i-1})] = 0. \quad (4.67)$$

Here  $\mu_i$  is the electro-chemical potential on island  $i$ .  $\tilde{\Gamma}_{i,j}$  are charge conductances on links, which are distributed exactly as the thermal conductances in Eq. (4.65). The main difference from Eq. (4.65), is that here there are no source or sink terms because the external couplings to the bath and the drive are assumed to conserve charge. In fact for these measurements we can con-

sider a system with just a drive or just tunable coupling to phonons. Both terms give rise to a parallel channel of ohmic conductivity proportional to  $\epsilon$  on the insulating links, so that

$$\tilde{\Gamma}(\ell) = \tilde{\Gamma}_0 e^{-\ell/a} + \epsilon \sigma_0 / \ell. \quad (4.68)$$

To gain analytic insight we calculate the average resistivity of the chain. Comparing the first term in Eq. (4.68) to the second we see that the insulating behavior dominates for  $\ell < \ell_* \approx a \log \epsilon^{-1} + a \log \log \epsilon^{-1}$ , while the bath or drive induced conductance dominates in longer links. When computing the average resistivity we can neglect contributions from the regime where conducting behavior dominates

$$\bar{\rho} = \bar{\ell}^{-1} \int d\ell P(\ell) \tilde{\Gamma}(\ell)^{-1} \approx \frac{1}{\bar{\ell} \tilde{\Gamma}_0} \int_a^{\ell_*} d\ell \xi^{-1} e^{\ell(a^{-1} - \xi^{-1})} \approx \frac{\alpha}{\bar{\ell} \tilde{\Gamma}_0} \left( \frac{\epsilon}{\log \epsilon^{-1}} \right)^{\alpha-1},$$

where  $\alpha = 1/z = a/\xi$  and  $\bar{\ell} = \int d\ell P(\ell) \ell \sim \xi$ . In Fig. 4.5 we show a numerical solution of the current in a one dimensional chain with a bias voltage, the current dependence  $j \sim \epsilon^{1-\alpha}$  together with the relation  $j \sim V/\bar{\rho}$  confirms the approximate analytic dependence of the resistivity on  $\epsilon$ . Thus it should be possible to measure the dynamical exponent  $z$  by varying the coupling  $\epsilon$  via controlled cooling of the phonon bath or by varying the strength of an external drive.

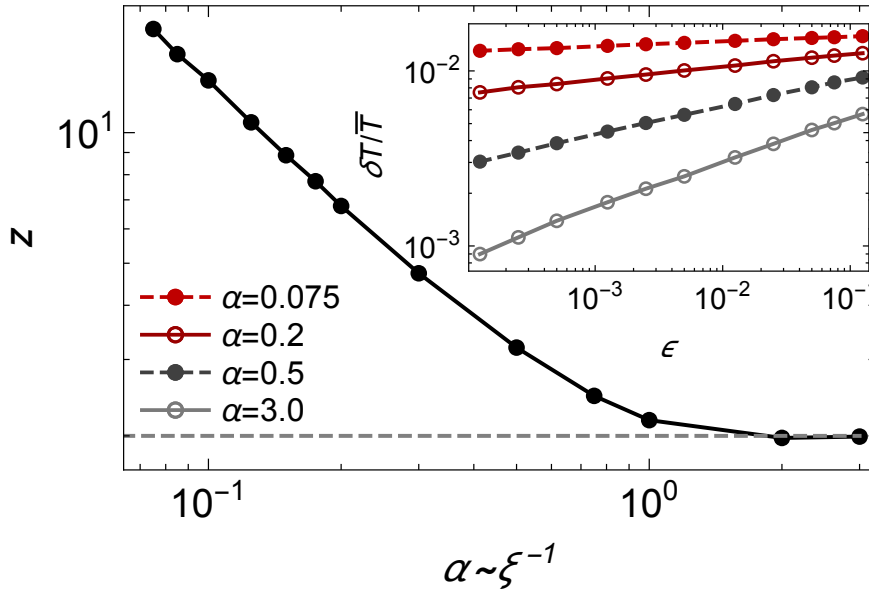


Figure 4.4: Fluctuations of the local temperatures,  $\delta T / \bar{T}$ , are computed from a resistor network model as function of the coupling strength  $\epsilon$  to a thermal bath and driving. For small  $\epsilon$ , temperature fluctuations are described by  $\delta T / \bar{T} \sim \epsilon^{1/2z}$  with  $z \sim \alpha^{-1} = \xi/a$  for  $0 < \alpha < 1$ , and  $z = 2$  in the diffusive regime,  $\alpha > 1$ . Parameters:  $\kappa_0 = 1$ ,  $a\Gamma_0 = 5.0$ ,  $T_0 = 1$ ,  $\delta g_1 = 0.05$ ,  $\delta g_2 = 0.05$ ,  $\theta = T_0$ ,  $N = 1000$ , averaged over  $M = 500$  configurations.

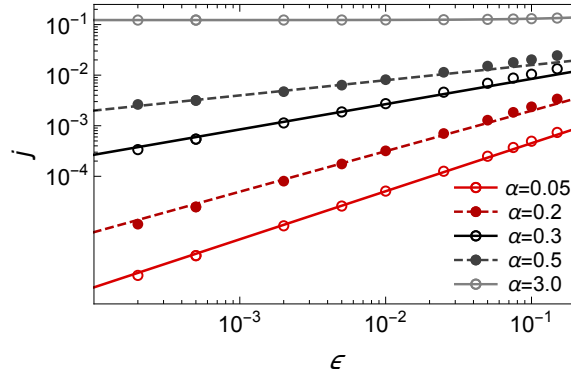


Figure 4.5: Dependence of particle current  $j$  on the strength of coupling to the baths  $\epsilon$  in  $d = 1$ . For  $\alpha < 1$ ,  $j \sim \epsilon^{1-\alpha}$  is observed. For diffusive  $\alpha > 1$ , on the other hand, a finite  $j(\epsilon \rightarrow 0)$  is observed. Parameters:  $\sigma_0 = 1$ ,  $a\tilde{\Gamma}_0 = 5.0$ ,  $N = 2000$ ,  $V = 0.1N$

## 4.6 MPS SIMULATIONS

Besides opening a new experimental route, consideration of weakly open driven systems, suggests a new approach for accessing the many-body localization transition numerically. Here we calculate how the local temperature variations in a spin-chain model change with the coupling to a weak drive that brings the system to a non thermal steady state.

The coherent part of the dynamics is governed by the Hamiltonian

$$H = \sum_i S_i \cdot S_{i+1} + h(\zeta_i^z S_i^z + \zeta_i^x S_i^x), \quad (4.69)$$

with open boundary conditions and disorder fields drawn uniformly from the range  $\zeta_i^{x,z} \in [-1, 1]$ . For simplicity we have chosen a model in which energy is the only conserved quantity, since the existence of extra conserved quantities will lead to extra slow modes entering the hydrodynamic equation (4.45) and coupling between those slow modes and temperature fluctuations might change the predicted dependence of  $\delta T$  on  $\epsilon$ . The MBL transition in the Hamiltonian (4.69) has been studied in Ref. [194] using ED.

We compute the properties of this system when it is weakly coupled to non-thermal baths described through the Lindblad formalism. The precise choice of Lindblad operators is not important, as long as the steady-state is non-trivial,  $\rho_\infty \neq \mathbb{1}$ . Therefore, at least one of the Lindblad operators has to be non-Hermitian. We choose a symmetric combination of several dissipators

$$\begin{aligned} L_i^{(1a)} &= \frac{1}{\sqrt{2}} S_i^+ \left( \frac{1}{2} \mathbb{1}_{i+1} - S_{i+1}^z \right), \quad L_i^{(1b)} = \frac{1}{\sqrt{2}} \left( \frac{1}{2} \mathbb{1}_i - S_i^z \right) S_{i+1}^+, \\ L_i^{(2a)} &= \frac{1}{\sqrt{2}} S_i^- \left( \frac{1}{2} \mathbb{1}_{i+1} + S_{i+1}^z \right), \quad L_i^{(2b)} = \frac{1}{\sqrt{2}} \left( \frac{1}{2} \mathbb{1}_i + S_i^z \right) S_{i+1}^-, \\ L_i^{(3)} &= S_i^z. \end{aligned} \quad (4.70)$$

The (unique) steady state  $\rho_\infty$  is obtained by solving the Lindblad time evolution in Eq. (4.1) using the time-evolving block decimation (TEBD) technique for a vectorized density matrix [186, 195], which we reviewed in Sec. 4.3.

The dephasing term  $L_i^{(3)}$ , Eq. (4.70), is used to ensure that the steady state is sufficiently close to an infinite temperature state, so that a bond dimension of  $\chi = 100$  is adequate to describe a system of  $N = 20$  sites for  $\epsilon \geq 0.01$ . Note that larger bond dimensions and longer propagation times are needed for smaller  $\epsilon$ , making computation in these cases more expensive, as we discuss below. At fixed  $h$ , the same set of disorder configurations is used for different values of  $\epsilon$ , while independent configurations are used at different values of  $h$ . We find that this procedure helps to determine the exponent  $z$  as the  $\epsilon$  dependence becomes less affected by the statistical ensemble. We average over 100 ( $h = 1, 2$ ) or 300-500 ( $h > 2$ ) disorder configurations.

The goal of the calculation is to obtain the spatial variation of the local temperature for varying values of the dissipative coupling  $\epsilon$ . To determine the local temperatures  $T_i$  we compare the reduced density matrix of 2 sites in the steady state  $\rho_\infty^{(i,i+1)}$  with a thermal state [196] by minimizing the cost function

$$F[\beta_i] = \text{tr} \left[ \left( \rho_\infty^{(i,i+1)} - \rho_{\text{th}}^{(i,i+1)}(\beta_i) \right)^2 \right]. \quad (4.71)$$

Here the thermal state is obtained by computing  $\rho_{\text{th}}(\beta) = Z^{-1} \exp(-\beta H)$  for each disorder realization, where the computation is done by means of imaginary time-evolution of a purified density matrix starting from the infinite temperature state (see [33] for details on this standard technique).

The (inverse) temperature variations  $\delta\beta/\bar{\beta}$ , obtained numerically as a function of  $\epsilon$ , are shown in Fig. 4.6 for a range of disorder strengths. We observe different  $\epsilon$  dependence in the MBL and ergodic phase, namely

$$\frac{\delta\beta}{\bar{\beta}}(\epsilon) \sim \begin{cases} \epsilon^{1/2z}, & h < h_c, \\ \frac{\delta\beta}{\bar{\beta}}|_{\epsilon \rightarrow 0} - b\epsilon + \mathcal{O}(\epsilon^2), & h \geq h_c \end{cases}. \quad (4.72)$$

In the MBL phase we see temperature variations of order one even in the limit  $\epsilon \rightarrow 0$  as predicted in Ref. [141]. At finite  $\epsilon$  we expect an analytic dependence on  $\epsilon$  due to the local nature of the MBL phase.

In the thermal regime, the temperature variations are expected to vanish in the limit  $\epsilon \rightarrow 0$  [141]. We see an increase of the temperature variations with  $\epsilon$  that fits well with the expected non analytic behavior  $\delta\beta/\bar{\beta} \sim \epsilon^{1/2z}$  at small values of  $\epsilon$  (see Fig. 4.6(b)). The fitted dynamical exponent  $z$ , shown in Fig. 4.7 changes continuously with disorder strength, growing rapidly as the MBL transition is approached. Error bars in Fig. 4.6c and Fig. 4.7 were obtained using a jackknife resampling. The usage of a resampling method for error estimates is necessary because statistical errors for different  $\epsilon$  at fixed  $h$  are strongly correlated in our setup. As discussed above, the dynamical exponent is expected to diverge together with the correlation length  $\xi$  at the MBL critical point. The apparent saturation of  $z$  is an artifact of the fit procedure; it is impossible to reliably fit a small exponent  $\alpha$  to the function  $\epsilon^\alpha$  for realistic values of  $\epsilon \gtrsim 0.01$ .

We obtain an estimate of the critical disorder strength  $h_c$  by recording the fraction  $P$  of disorder realizations showing  $\delta\beta/\bar{\beta}$  increasing with  $\epsilon$  near  $\epsilon = 0.01$  (see Fig. 4.6(c)). From the condition



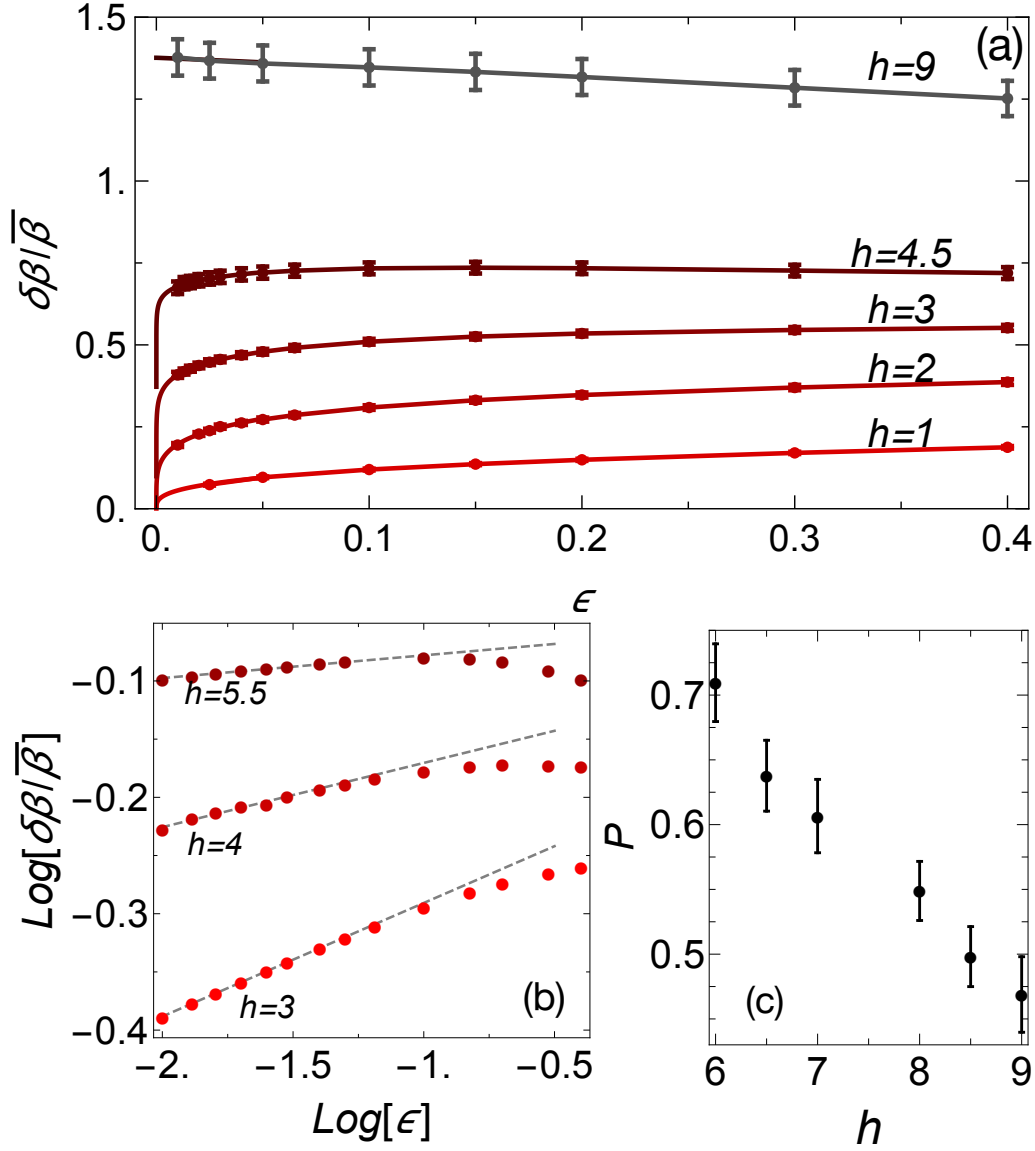


Figure 4.6: *Numerical Time Evolving Block Decimation results* – (a) The fluctuations of the inverse temperature,  $\delta\beta/\bar{\beta}$ , show two distinct dependences on  $\epsilon$ : while they vanish proportionally to  $\epsilon^{1/2z}$  on the ergodic side of the phase diagram, they obtain a finite value for  $\epsilon \rightarrow 0$  with a linear correction in the MBL phase. Errorbars show (a correlated) statistical error, while line correspond to the fits. (b) Fits (dashed lines) to  $\delta\beta/\bar{\beta}$  are used to obtain  $z(h)$  shown in Fig. 4.7. (c) We estimate  $h_c \approx 8.75 \pm 0.5$  from the condition that at  $h_c$  the probability  $P$  for  $\delta\beta/\bar{\beta}$  to have a positive slope at smallest  $\epsilon$  equals  $P = 0.5$ . That is, at  $h_c$  the sign of the slope is undetermined.

$P = 0.5$  we estimate  $h_c \approx 8.75 \pm 0.5$  for  $N = 20$ . Allowing for smaller  $\epsilon$  might lead to a slightly larger estimate of  $h_c$  for this system size. A previous ED study of the same model on 20 sites [194]

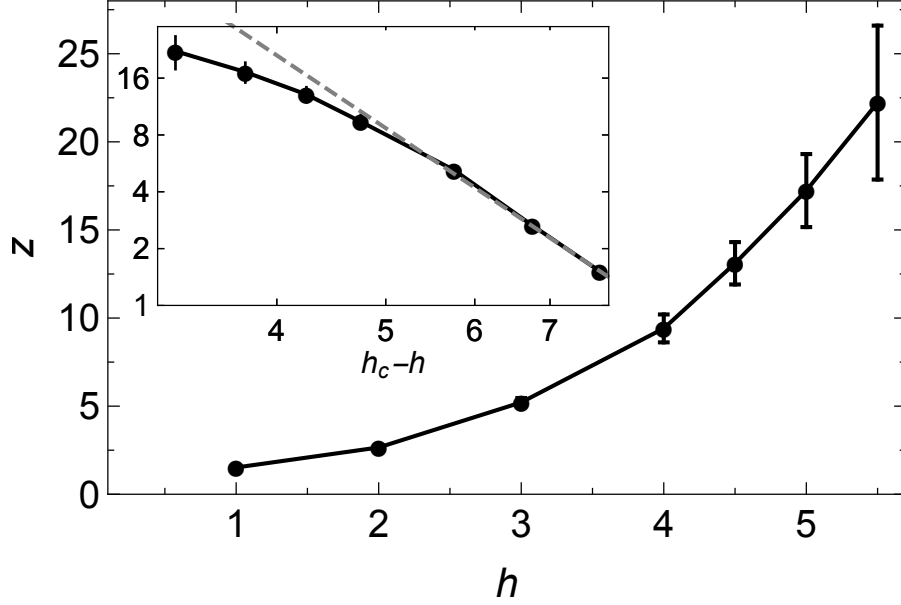


Figure 4.7: The dynamical exponent  $z$  increases strongly upon approaching the MBL phase transition. The apparent saturation of  $z$  is due to limitation to  $\epsilon \geq 0.01$ . Note that the error bars only reflect statistical errors but not finite size effects. Inset:  $z$  as function of  $h_c - h$  on log-log scale assuming  $h_c = 8.75$ . Using  $h_c = 8.75 \pm 0.5$ , our results are consistent with  $z \sim (h - h_c)^{-\nu}$  with critical exponent  $\nu = 4 \pm 0.9$ .

estimated a range of possible values for the critical disorder strength depending on the quantity being examined, from as low as  $h_c \sim 2 - 3$  to  $h_c \sim 7 - 8$ .

With  $h_c$  at hand we extract a correlation length exponent  $\nu$  from the divergence of  $z \sim \xi \sim (h_c - h)^{-\nu}$ . As shown in Fig. 4.7, fitting can be reliably performed for  $h \in [1, 4]$  when the error bars on  $z$  are taken into account. The result of this procedure gives the estimate  $\nu \approx 4.0 \pm 0.9$  (with large errorbars due to uncertainty in  $h_c$ ), which is consistent with the Harris-Chayes bound,  $\nu > 2/d$  [197, 198] and also in agreement with single parameter scaling fits to renormalization group results [28, 161]. In a previous study [141], Lenarčič et al. carried out a finite size scaling analysis of the local temperature variations in significantly smaller systems in the limit  $\epsilon \rightarrow 0$ , which gave the estimates  $\nu \approx 2.6$ . We note that recent works derived phenomenological two parameter RG flow equations, suggesting Kosterlitz-Thouless like behavior of the MBL transition [199, 200], which would result in  $z \sim \xi \sim e^{c/\sqrt{(h_c-h)}}$ . We cannot exclude this possibility based on our current numerical data. It is an interesting question how the "order parameter"  $\delta\beta/\bar{\beta}$  behaves at the critical point itself  $h = h_c$  in the limit  $\epsilon \rightarrow 0$ . Our results are consistent with a jump across the transition, but they also leave open the possibility of a slow logarithmic behavior as  $-1/\log \epsilon$ , which would allow a continuous change of  $\delta\beta/\bar{\beta}$  across the transition.

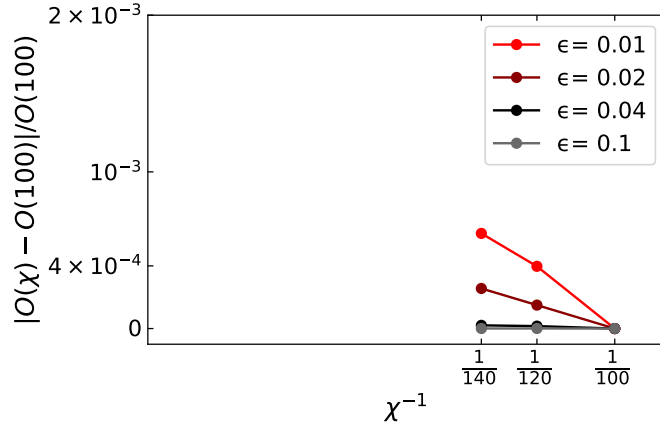


Figure 4.8: Relative error due to finite bond dimension  $\chi = 100$  can be estimated from the ratio  $|O(\chi) - O(\chi = 100)|/O(\chi = 100)$ ,  $O(\chi) = \frac{\delta\beta}{\beta}(\chi)$ . The error estimated from the  $\chi \rightarrow \infty$  extrapolation is below 0.1% for smallest  $\epsilon = 0.01$  used in our computations. Parameters:  $N = 20$ ,  $h = 4$ , with averaging over 60 realizations.

#### 4.6.1 CONVERGENCE IN SYSTEM SIZE, TIME AND BOND DIMENSION

In this section, we look more closely into what are the limiting factors of the calculation. We first investigate how our results on system size  $N = 20$  depend on the bond dimension. Fig. 4.8 shows the relative change of the expectation value of  $O = \delta\beta/\beta(\epsilon)$  with bond dimension  $\chi$  at steady state. We set  $\chi = 100$ , used for the results in the main text, as a baseline.  $O(\chi)$  is averaged over 60 disorder realizations, which are the same for different  $\chi$ . We find that the error extrapolated to  $\chi = \infty$  is small, e.g., for  $h = 4$  below 0.1%. We also note that the extrapolated error estimate grows with decreasing  $\epsilon$ , hence for smaller values of  $\epsilon$  a larger bond dimension will be required, increasing the costs of computations at small  $\epsilon$ .

In Fig. 4.9 we show the relaxation of temperature fluctuations  $O(t) = \frac{\delta\beta}{\beta}(t)$  to steady state in the TEBD time evolution. Specifically, we plot  $|O(t) - O(t_f)|$  with respect to the  $O(t_f)$  at the maximal propagation time  $t_f$ . As expected, we see exponential relaxation to the steady-state value with a characteristic rate which scales as  $\epsilon$ . Obtaining results for smaller  $\epsilon$  is thus increasingly hard with TEBD.

Assuming that the necessary bond dimension  $\chi$  is independent of system size, our approach should be scalable, with computational demands growing linearly with system size. Figs. 4.9(a,b) compare the convergence of  $O(t) = \frac{\delta\beta}{\beta}(t)$  for a single realization at  $N = 20, 40$  system sizes. While the computational time approximately doubles, the exponential convergence rate with TEBD evolution time  $t$  is comparable.

Finally, we present a finite size scaling analysis of the results. We show the dependence of the dynamical exponent  $z$ , obtained from our numerical scheme, on the system size. The exponent  $z$  is extracted by fitting a power law for the dependence of the temperature variance on  $\epsilon$  with  $\epsilon \geq 0.01$ , Eq.(9) in the main text. The results are shown in Fig. 4.10.

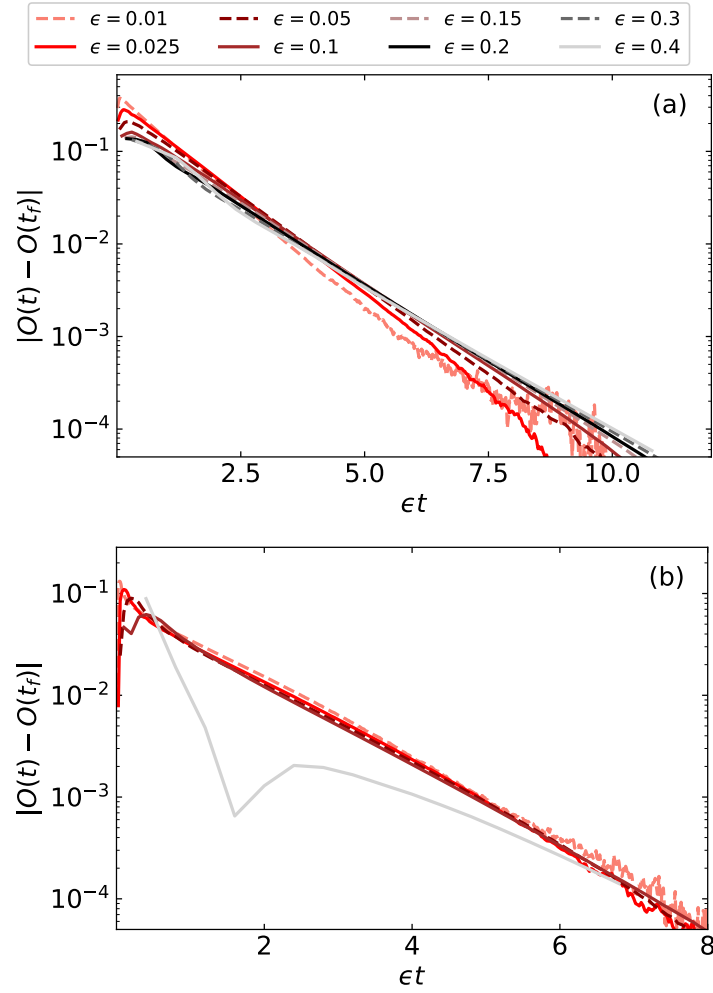


Figure 4.9: Evolution of  $O(t) = \frac{\delta\beta}{\beta}(t)$  (with respect to  $O(t_f)$  at maximal propagation time  $t_f$ ) during the TEBD computation, for one disorder realization at  $h = 4$ ,  $\chi = 100$ , for systems of size (a)  $N = 20$  and (b)  $N = 40$ . Note that the time axis is rescaled by  $\epsilon$  to reveal an exponential relaxation with a convergence rate proportional to  $\epsilon$ .

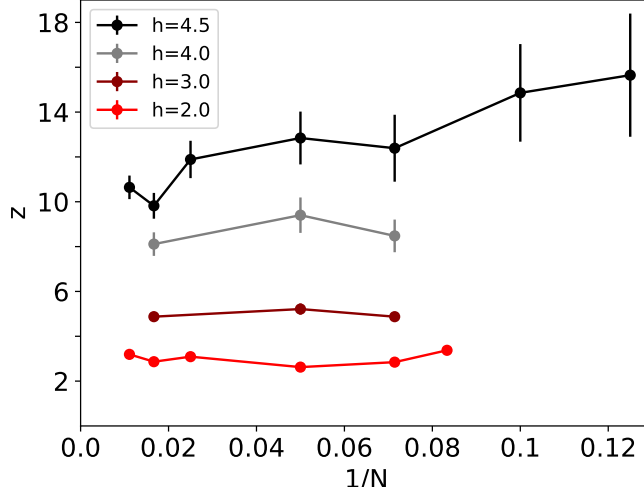


Figure 4.10: Finite-size analysis of the dynamical exponent  $z$  for  $h = 2.0, 3.0, 4.0, 4.5$ . Calculations are performed with bond dimension  $\chi = 100$  and  $\epsilon \geq 0.01$ . A different number of realizations is used for different points, e.g., at  $h = 2.0$  and  $N \in [12, 90]$ , 150 – 50 realizations are used, for  $h = 4.5$  and  $N \in [8, 90]$ , 790 – 190 realizations are used. Fit error bars are obtained with the jackknife resampling of data with  $\epsilon \geq 0.01$  and do not estimate systematic deviations from the  $z$  that would be obtained using  $\epsilon < 0.01$ , necessary for  $h > 4$ .

In systems with disorder strengths  $h = 2.0, 3.0, 4.0$  we do observe negligible finite size dependence. Recall that this is the range of  $h$  we used to extract the power law divergence of  $z \sim (h_c - h)^{-\nu}$  on approaching the critical point. It is encouraging to see that this behavior is unaffected by finite size. We do see a non systematic finite size dependence for disorder strength  $h = 4.5$ , which we attribute to uncertainty in fitting the dynamical exponent  $z$ . Indeed, as noted above, for  $h > 4$  ( $z > 8$ ) we can no longer extract a reliable power law fit to  $\frac{\delta\beta}{\beta} \sim \epsilon^{\frac{1}{2z}}$  in the range  $\epsilon \geq 0.01$ . In order to reliably obtain larger values of  $z$  close to the critical point one would have to reduce the cutoff  $\epsilon$  exponentially in  $z$  (equivalently, in  $\xi$ ). Thus it is the finite time cutoff ( $1/\epsilon$ ) rather than the finite size, which limits the calculation.

As noted above, calculations performed at smaller  $\epsilon$  might yield somewhat larger  $h_c$  as well, which would, in turn, impact the value of  $\nu$  obtained from  $z \sim (h_c - h)^{-\nu}$  fit.

## 4.7 DISCUSSION

We have demonstrated the advantages of investigating the MBL transition as a function of the coupling strength  $\epsilon$  to external non-equilibrium baths. In this approach the coupling gives rise to universal broadening of the critical point, governed by the coupling  $\epsilon$  in the same way that temperature broadens a conventional quantum critical point. In numerical computation, the finite coupling to a bath limits the operator entanglement entropy allowing the usage of powerful matrix-product operator methods on both sides of the phase transition. Thus we were able to

obtain quantitative information on quantum critical properties, including the dynamical exponent  $z$ , the correlation length exponent  $\nu$  and the critical disorder strength. Moreover, having a weak coupling to the baths seems to regulate the calculation by broadening the many-body energy levels facilitating faster convergence to the thermodynamic limit. Even though our calculations were performed on rather small system sizes, the approach is in principle scalable (the computational effort scales linearly with system size at fixed bond dimension) and thus offers an appealing alternative to non-scalable ED calculations.

Our numerical scheme is scalable in terms of the calculated spatial size. The limiting factor to approach the critical point is the time-scale imposed by the minimal value of the dissipative coupling  $\tau_c \sim 1/\epsilon$ . To reliably extract  $z$  from the fit to  $\delta T \sim \epsilon^{1/(2z)}$ , one would need to vary  $\delta T/\bar{T}$  over about an order of magnitude. Close to the critical point, this would require very small  $\epsilon \sim e^{-B\xi/a}$ , where  $\xi \sim z$  is the correlation length. This is a fundamental limitation stemming from the exponential dynamical scaling that characterizes the critical point. It would be a limiting factor even if we had a perfect quantum simulator at our disposal to study the MBL transition. In our current numerical scheme reaching small values of  $\epsilon$  is challenging, since it requires performing TEBD evolution for longer times in order to reach the steady-state of Eq. (4.1) and also requires larger bond dimensions. Thus, it is an interesting research direction to develop numerical approaches which are better suitable to compute QME steady-states at the limit of small  $\epsilon$ .

An interesting future direction is to go beyond the temperature-fluctuation order parameter in Eq. (4.66) and study the full statistical properties of the local temperatures. For example, one could investigate the distributions of thermal region sizes (regions with small temperature variance) on the MBL side of the transition. This might allow to test recent claims, based on phenomenological RG studies, that the MBL transition obeys Kosterlitz-Thouless scaling [199, 200]. It would be also interesting to apply our approach to a model where the MBL transition occurs due to a quasi-periodic potential instead of real disorder, where Griffiths effects are not expected to occur. In case we observe that  $z$  remains at a finite value in the quasi-periodic potential scenario, it will serve as further evidence to the rare-regions mechanism being the origin of sub-diffusive transport observed in models with real disorder.

Potentially even more exciting than the numerical advances are the experimental breakthroughs that the open system approach can facilitate in the study of MBL. In particular this approach may allow to study MBL and the MBL transition in solids in spite of the inevitable coupling to a phonon bath. The non-equilibrium conditions we considered here can be achieved by driving the system externally either with light, or with a bias voltage, to a steady state set by the ratio of couplings to the drive and the phonon bath. Both couplings can be controlled, the former through the strength of the driving field and the latter by changing the phonon temperature. We have shown that under these conditions the critical properties can be inferred from the dependence of local temperature variations on the coupling  $\epsilon$ . In principle local temperatures can be measured by comparing the Stokes and Anti-stokes response in a local (tip-enhanced) Raman spectroscopy experiment [201, 202]. However, a more natural measurement in solids would be a simple resistivity measurement. We have argued that dependence of the resistivity on  $\epsilon$  at small values of the coupling can also provide crucial information on the MBL transition.

We note that the sub-diffusive scaling in one dimensional systems  $\epsilon^{1/2z}$  may be hard to distinguish from true localization close to the transition, where the dynamical exponent becomes

very large  $z \gg 2$ . In two and three dimensional systems, however, we do not expect to observe sub diffusive scaling even close to a localization transition. Thus the open system approach is uniquely suitable for determining the fate of many body localization in two and three dimensional systems in view of recent arguments [203] and some numerical evidence [204] for absence of a sharp MBL transition in this case. For the purpose of numerically computing steady-states of Eq. (4.1) in  $2d$ , one could use the recently developed neural-network ansatz approach for solving the QME [205–208], which is expected to be competitive with tensor-network methods in this scenario.





# 5

## TRAJECTORY DEPENDENT ENTANGLEMENT TRANSITION IN A FREE FERMION CHAIN – FROM EXTENDED CRITICALITY TO AREA LAW

### 5.1 INTRODUCTION

Fingerprints of the competition between unitary and non-unitary dynamics are found in almost all aspects of modern quantum science. The spectrum ranges from radiative decay in driven two-level systems [209, 210] to dephasing of trapped ions and cold atoms due to laser noise [211] or phonon-induced dissipation in electronic devices and color centers [212, 213]. Non-unitary processes crucially affect quantum dynamics from single particles to the many-body realm, as we have also seen in previous chapters.

One fascinating example are phase transitions in the entanglement entropy, which have been recently discovered in systems undergoing random-unitary circuit evolution subject to local projective measurements [31, 34, 35, 214–216]. These works explored the entanglement properties of individual measurement trajectories  $|\psi_{\xi}\rangle$ . Here,  $\xi$  represents a specific realization of temporal randomness encountered during time evolution due to quantum mechanical measurements. For example, in the case of projective measurements in circuit dynamics,  $\xi$  encodes all the different measurement results and the times at which they were performed.

A particular quantity of interest is the entanglement entropy of the trajectory state  $|\psi_{\xi}\rangle$ , averaged over all trajectory realizations, denoted  $\bar{S}_{\text{vN}}$ . When examining the long time value of  $\bar{S}_{\text{vN}}$  in random-unitary circuits with measurements, two different phases have been found. For small enough measurement rate the steady-state value of  $\bar{S}_{\text{vN}}$  obeys volume-law scaling. This means that  $S_{\text{vN}}(\ell) \sim \ell$  for a given subsystem of length  $\ell$ , implying that the subsystem is strongly entangled with the rest of the system. On the other hand for large measurement rate  $\bar{S}_{\text{vN}}$  obeys area-law scaling, meaning that  $\bar{S}_{\text{vN}}(\ell) \sim \text{const.}$  for a large enough subsystem size. At a critical measurement rate an entanglement phase transition occurs, where  $\bar{S}_{\text{vN}}$  exhibits logarithmic scaling. This novel class of phase-transitions is currently under intense research [36, 37, 217–221], and has been reported in a plethora of setups, including non-unitary circuit models and chains of interacting bosons subject to continuous measurements [222–226].

A characteristic trait of these entanglement transitions is that they manifest themselves in the expectation value of *state-dependent* operators  $\text{tr}[\rho_{\xi}\hat{O}(\rho_{\xi})]$ , with  $\rho_{\xi} = |\psi_{\xi}\rangle\langle\psi_{\xi}|$ . For example, the entanglement entropy of a subsystem  $A$ , can be expressed as  $S_{\text{vN}}(A) = -\text{tr}[\rho_{\xi}\hat{O}_S(\rho_{\xi})]$  with  $\hat{O}_S(\rho_{\xi}) \equiv -\log \rho_A(\xi)$ . Here  $\rho_A(\xi)$  is the reduced density matrix on subsystem  $A$ . Hence we see that  $S_{\text{vN}}(A)$  is a highly nonlinear function of the trajectory state  $\rho_{\xi}$ . This implies that dif-

ferent measurement protocols, which are expected to lead to the same dynamics for the averaged state  $\rho(t) = \mathbb{E}_{\xi}[\rho_{\xi}(t)]$ , can result in qualitatively different dynamics of the trajectory-averaged entanglement-entropy  $\bar{S}_{\text{vN}}(t)$ . Therefore, when considering trajectory entanglement phase transitions, it is important to explore the effects of different measurement protocols.

Here we focus on one of the most elementary models for the competition between unitary and non-unitary dynamics, free fermions on a periodic chain, subject to coherent hopping and local, temporally random, and particle number conserving dephasing dynamics [227–230]. From a measurement theory point of view, the non-unitary dephasing evolution results from a continuous, weak measurement of the local fermion particle number, caused for instance by weak interactions with a monitored photon bath [231–234]. Hence this model describes competition between entangling Hamiltonian dynamics and disentangling measurement dynamics, similar to the case of random-unitary circuits with projective measurements.

The free-fermion model can be simulated efficiently [228], allowing us to investigate large system sizes, similarly to the case of random Clifford circuits [35, 220, 235]. In addition, it is natural in terms of physical implementations: this scenario arises, e.g., for ultracold fermions in optical lattices, which experience incoherent light scattering [227, 236], or in Rydberg atom arrays subject to phase noise in the driving laser [237, 238].

An important difference between the free-fermion model and random-unitary dynamics is that the former is an integrable model and as such it is not expected to capture the full phenomenology of generic interacting quantum-systems. However, integrable and non-integrable models do share some similar phenomenology as far as the closed system entanglement dynamics is concerned. In particular in both cases ballistic entanglement growth is observed after a quantum quench [29, 30], and in some models with tunable integrability breaking the same universal formula is obeyed by the entanglement in the integrable and non-integrable regimes [239]. Even if the free-fermion model does not capture the full phenomenology of generic trajectory entanglement transitions, its relative simplicity makes it an appealing model system. Furthermore, it can serve as a starting point for the exploration of the entanglement transition in the presence of weak-interactions.

## OUTLINE AND SUMMARY OF RESULTS

Before delving into the details of our work, let us present a high-level outline and summary of the main results. In Sec. 5.2 we provide background which helps understanding our results and putting them in context. In particular we review: previous studies of the entanglement transition in random-unitary circuits in Sec. 5.2.2; stochastic trajectory unravelings of the QME and their relation to monitoring in Sec. 5.2.3; and some properties of the entanglement-entropy and correlation functions expected in conformal-field theories in Sec. 5.2.4.

The description of our work starts Sec. 5.3 in where we introduce the concrete free-fermion model we consider, where the fermions are subjected to dephasing noise, resulting from interaction with a photon bath. The resulting quantum master equation dynamics for the averaged state contains Lindblad operators of the form  $n_i$ . In this work we are not interested in the averaged state, but rather in the conditioned state which is obtained when the state of the bath is monitored, which we also refer to as a measurement trajectory. We consider three different types of measurement trajectories: (i) the quantum state diffusion (QSD), describing a situation where

the photon bath is continuously monitored via homodyne detection [233, 240] (ii) quantum-jump (QJ) trajectories which describe the evolution of the state when photons are detected directly with a photon counter. [233, 241] (iii) The so called “raw” quantum-state diffusion [242], which mimics non-unitary quantum circuit evolution (QSDc).

Section 5.4 includes the main result of our chapter where we establish the entanglement phase diagram of the model Fig. 5.5. The phase diagram emerges as a result of a competition between the hopping rate  $J$  (which we fix to be  $J = 1$  from now on) and the dephasing rate  $\gamma$ . We observe three different regimes with different behavior of the entanglement-entropy of a subsystem of length  $L/2$  (equal bipartition of the system):

- For weak  $\gamma$  and small  $L$  we find a volume-law behavior of the entanglement  $\sim L$ .
- Increasing the system size we observe a cross-over between the volume-law behavior to logarithmic scaling of the entanglement-entropy  $\sim \log L$ . This logarithmic scaling is reminiscent of the entanglement scaling in CFTs, as we explained in Sec. 5.2.4. By examining the entanglement-entropy scaling we can extract a  $\gamma$  dependent effective central-charge. Similar behavior has also been observed very recently in a related free-fermion circuit-model including spatio-temporal randomness [226], and in measurement-only quantum circuits [243].
- For some types of trajectory-evolution we find area-law behavior  $\sim L^0$  for large enough  $\gamma$ . In this case a phase transition from the CFT regime to the area-law regime occurs at a critical dephasing rate  $\gamma_c$ , where the effective central-charge vanishes  $c(\gamma_c) = 0$ . On the other hand for a certain type of trajectory-evolution, which can be viewed as a continuous limit of the non-unitary circuit introduced in [226], we find that the system exhibits CFT like behavior for all  $\gamma$ .

By comparing different types of trajectory evolution, we find that the way monitoring is performed is essential for the qualitative properties of entanglement entropy dynamics – as noted, the area-law regime exists only for certain evolution protocols. In Sec. 5.5, we conjecture that a key ingredient for the existence of the area-law regime in the free-fermion system is whether probability is conserved exactly in the trajectory evolution, or only on average. While exact probability conservation is automatic in unitary dynamics, it may or may not be realized for non-unitary protocols – even though the average conservation is sufficient to guarantee a consistent open system quantum dynamics. In addition, we show that the different protocols lead to a very different picture when considering the full distribution trajectory entanglement-entropies.

Finally, in Sec. 5.6 we further substantiate the claim of a conformally invariant regime at weak monitoring, by considering the spatial dependence of mutual-information and connected density-density correlation functions. We observe a scaling behavior which agrees with the predictions of conformal-field theory.

## 5.2 BACKGROUND

### 5.2.1 ENTANGLEMENT OF PURE QUANTUM STATES

Let us consider a bipartition of one-dimensional spin chain at a bond  $x$ , denoting the subsystems  $A = [1, x]$ ,  $B = [x + 1, L]$ . Intuitively, we think about the entanglement between  $A$  and  $B$  as

representing the amount of non-classical correlations between them. It is maybe easiest to explain when two systems are not entangled. We say that  $A$  and  $B$  are not entangled, if the (pure) state of the system can be written as a product state of the form  $|\psi\rangle = |\psi_A\rangle \otimes |\psi_B\rangle$ . In this case  $A$  and  $B$  do not share any quantum correlations.

For pure states there exist a useful measure, the entanglement entropy, that can define bipartite entanglement in a positive way and quantify it. Given a state of the system  $|\psi\rangle$ , we denote the reduced density-matrix corresponding to the bipartition as

$$\rho(x) = \rho_A = \text{tr}_B |\psi\rangle\langle\psi|. \quad (5.1)$$

We can then define the von-Neumannn entanglement-entropy of the bipartite system as

$$S_{\text{vN}}(x) = -\text{tr} \rho(x) \log_2 \rho(x). \quad (5.2)$$

From the point of view of quantum information, this is a natural measure of bipartite entanglement for pure states. Consider two observers Alice and Bob, such that Alice (Bob) has access only to subsystem  $A(B)$ . It has been shown that given a sufficient amount of Bell-pairs shared by Alice and Bob, they can create an arbitrary many-body bipartite state only by means of local operations (on their respective subsystems) and classical communication (LOCC) [244]. The entanglement-entropy  $S_{\text{vN}}$  was shown to be equal to the amount of Bell pairs that are needed to be shared between Alice and Bob in order to generate the state  $|\psi\rangle$  via LOCC [244].

It is also useful to consider the set Rényi entropies

$$S_n(x) = \frac{1}{1-n} \log_2 \text{tr}(\rho(x))^n. \quad (5.3)$$

A useful property of the Rényi entropies is that they obey the inequality  $S_n(x) \leq S_{n-1}(x)$ . In particular  $S_{\text{vN}}$  is the  $n = 1$  Rényi entropy. Another special important case includes the Hartley entropy

$$S_0(x) = \text{rk} \rho(x), \quad (5.4)$$

which is equivalent to the bond-dimension required at bond  $x$  for an exact representation of the state  $|\psi\rangle$  as an MPS (see our discussion in Sec. 4.3). The Hartley entropy serves as an upper bound for all other Rényi entropies.

Another quantity that we consider in this chapter is the bipartite mutual information, defined for two subsystems  $A, B$  as

$$I_n(A, B) = S_n(A) + S_n(B) - S_n(A \cup B). \quad (5.5)$$

The mutual-information is useful because it quantifies the correlations between two subsystems  $A$  and  $B$  in a basis independent way. More percisely,  $I_{\text{vN}}(A, B)$  provides an upper bound on any connected correlation function between  $A$  and  $B$  [245]

$$I_{\text{vN}}(A, B) \geq \frac{\langle M_A M_B \rangle_c^2}{2 \|M_A\|^2 \|M_B\|^2}, \quad (5.6)$$

where  $M_{A(B)}$  is some observable on  $A(B)$  and  $\langle M_A M_B \rangle_c = \langle M_A M_B \rangle - \langle M_A \rangle \langle M_B \rangle$ . Hence, if the mutual information decays exponentially in the distance between  $A$  and  $B$ , it implies the same for the connected correlation functions. Note that in the special case we considered above, where  $A, B$  are obtained from a bipartition of the entire chain, the entanglement-entropy is twice the mutual information since in this case  $S_{\text{vN}}(A \cup B) = 0$ . Therefore,  $S_{\text{vN}}(x)$  also serves as an upper-bound on all correlation functions between the two parts of the system.

From a quantum computation perspective entanglement is a resource, and achieving any advantage over classical algorithms requires the preparation and manipulation of highly entangled states [246]. This claim can be understood from the fact that the dynamics of states with low entanglement can be efficiently simulated on classical computers by mean of tensor-network representation, as we discussed in the previous chapter.

#### EXPERIMENTAL MEASUREMENT OF THE ENTANGLEMENT ENTROPY

Since  $S_n$  is not a linear function of the density matrix  $\rho_A$ , we generally don't think about it as an observable which is directly measurable, as opposed to some Hermitian operator  $\hat{O}$ . However, in a recent experiment by Islam et al. [247], the 2nd Rényi entropy was directly measured in an ultra-cold atom system, realizing the Bose-Hubbard model with 4 sites. An increase of  $S_2$  in the ground-state was measured when adiabatically tuning the system from the Mott insulating phase (large interactions) to the superfluid phase (small interactions compared to hopping).

The main idea behind the experiment is to exploit the fact that the purity of a state  $\rho$  can be expressed as an expectation value of the SWAP operator  $V_2$  with respect to a state consisting of two replicas of  $\rho$

$$\text{tr} \rho^2 = \text{tr}(V_2 \rho \otimes \rho) = \langle V_2 \rangle_{\rho \otimes \rho}, \quad V_2(|\psi_1\rangle \otimes |\psi_2\rangle) = |\psi_2\rangle \otimes |\psi_1\rangle. \quad (5.7)$$

As seen from its definition, the SWAP operator exchanges the states between the two copies. Since  $V_2^2 = \mathbb{1}$ , its eigenvalues are  $\pm 1$ . Furthermore a pure state has  $\langle V_2 \rangle_{|\psi\rangle \otimes |\psi\rangle} = \text{tr}(\rho_\psi^2) = 1$  and hence it is contained in the symmetric subspace of  $V_2$ . When the two copies of the state are interfered via a 50-50 beam-splitter it can be shown that a pure-state input will lead to an even number of particles in the output state of the interferometer. Therefore, a measurement of the average parity of the output state is equivalent to measuring the purity  $\langle P \rangle = \langle V_2 \rangle_{\rho \otimes \rho}$ .

In the experiment the system was initialized with two copies of the ground-state of the Bose-Hubbard Hamiltonian on two adjacent 4-site 1d chains. The two copies were then interfered with each other via a 50-50 beam splitter, which was effectively implemented via a tunnel coupling between the two 1d chains. The quantum-gas microscope used in [247] can measure the site-resolved parity in the two chains systems after the interference, and in this way the purity of the reduced state  $\text{tr} \rho_A^2$  could be measured, allowing computation of  $S_2(A)$ .

Another scheme for measurement of the Rényi entropy in quantum simulators, based on randomized measurements, was suggested theoretically by Elben et al. [248] and subsequently realized in a trapped ion setup by Brydges et al. [249]. This scheme is based on application of random unitary matrices  $U_A$  drawn from the circular unitary ensemble, and estimating the statistical mo-

ments of projectors on the computational basis  $|\mathbf{s}\rangle\langle\mathbf{s}|$ . Defining  $P(\mathbf{s}) = \text{tr}[U_A \rho_A U_A^\dagger |\mathbf{s}\rangle\langle\mathbf{s}|]$ , one can use the relation

$$\langle P(\mathbf{s})^2 \rangle = \mathbb{E}_{U_A} \{ \text{tr}[(U_A \rho_A U_A^\dagger)^{\otimes 2} (|\mathbf{s}\rangle\langle\mathbf{s}|)^{\otimes 2}] \} \propto 1 + \text{tr}(\rho_A^2). \quad (5.8)$$

In contrast to the replica scheme used in [247], the randomized measurement scheme does not require a replicated state. This allowed Brydges et al. to measure the dynamics of the 2nd Rényi entropy of subsystems of up to 10 qubits, with the total length of the chain being  $N = 20$ . In this respect it seems that the randomized measurement scheme provides a promising route for eventually measuring  $S_2$  at scales which are out of reach for classical simulations.

### 5.2.2 ENTANGLEMENT PHASE TRANSITION IN RANDOM-UNITARY CIRCUITS WITH MEASUREMENTS

In this section we review the results of recent studies of the entanglement transition in systems evolving under random-unitary circuit (RUC) dynamics with projective or weak measurements.

The transition was first pointed out in Refs. [34, 35], both considered a similar hybrid 1D quantum circuit model describing evolution of a spin-1/2 chain. We will start by following the discussion in Ref. [34] which provides some analytical insight into the origin of the transition in addition to numerical result. The dynamical evolution consists of unitary steps and projective measurement steps. In the unitary step random two-site unitaries are applied to all the even or odd bonds:

$$|\tilde{\psi}_{i+1}\rangle = \begin{cases} \prod_{k=1}^{N/2} U_{2k-1, 2k} |\psi_i\rangle, & i \text{ odd} \\ \prod_{k=1}^{N/2} U_{2k, 2k+1} |\psi_i\rangle, & i \text{ even} \end{cases} \quad (5.9)$$

with  $U_{n, n+1}$  a random-unitary acting only on sites  $n, n+1$ , drawn from the Haar measure. After each unitary step a projective measurement is performed on each site with probability  $p$ . This is implemented at each site  $k$  by the mapping

$$|\tilde{\psi}_{i+1}\rangle \rightarrow \begin{cases} \frac{P_{\uparrow, k} |\tilde{\psi}_{i+1}\rangle}{\|P_{\uparrow, k} |\tilde{\psi}_{i+1}\rangle\|}, & \text{prob. } p \langle \tilde{\psi}_{i+1} | P_{\uparrow, k} | \tilde{\psi}_{i+1} \rangle \\ \frac{P_{\downarrow, k} |\tilde{\psi}_{i+1}\rangle}{\|P_{\downarrow, k} |\tilde{\psi}_{i+1}\rangle\|}, & \text{prob. } p \langle \tilde{\psi}_{i+1} | P_{\downarrow, k} | \tilde{\psi}_{i+1} \rangle \\ |\tilde{\psi}_{i+1}\rangle, & \text{prob. } 1 - p \end{cases} \quad (5.10)$$

where  $P_{\uparrow(\downarrow), k} = (\mathbb{1} + (-)\sigma_k^z)/2$ . The state resulting from the sequential application of the mapping (5.10) to all sites is defined as  $|\psi_{i+1}\rangle$ .

We note that all the entanglement measures mentioned above are defined for the case of pure-state evolution. For the evolution with projective measurements, averaging over the measurement results leads to a mixed-state, which in the long time limit is a structureless infinite-temperature state in the protocol considered here, irregardless of the measurement rate. The quantities we will consider here are the trajectory-averaged quantities. Specifically the trajectory averaged Rényi entropies are given by

$$\overline{S}_n(A) \equiv \mathbb{E}_{\mathbf{p}, \mathcal{U}} \frac{1}{1-n} \log_2 \text{tr}(\text{tr}_{\bar{A}} |\psi\{\mathbf{p}, \mathcal{U}\}\rangle \langle \psi\{\mathbf{p}, \mathcal{U}\}|), \quad (5.11)$$

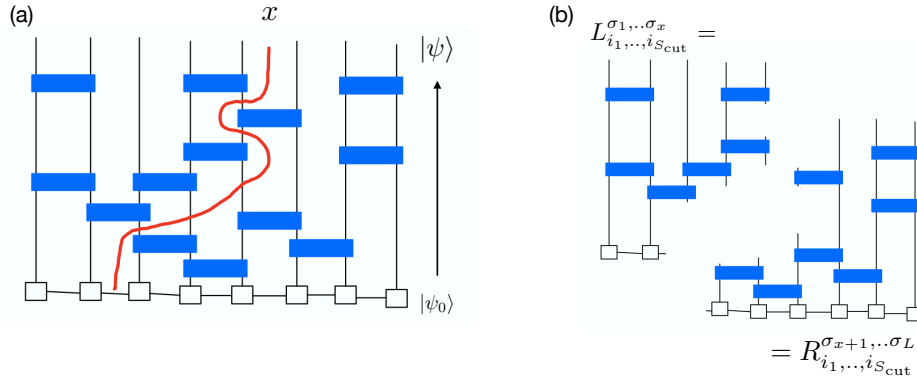


Figure 5.1: Bound on the Rényi entropy of a state obtained via RUC evolution, provided by an arbitrary cut through the RUC. The initial state is represented as an MPS (white boxes at the bottom), while the blue boxes represent two-site unitaries acting on the state. (a) The number of “legs” the red line passes through is denoted by  $S_{\text{cut}}$ , and it bounds the Rényi entropy  $S_n(x) \leq S_{\text{cut}}$ . In the example shown here  $S_{\text{cut}} = 5$ . (b) The cut induces a decomposition of the state  $|\psi\rangle$  as the product of two tensors  $L$  and  $R$ .

where  $\mathbf{p}$  denotes the set of projective measurements that were performed and their outcomes,  $\mathcal{U}$  is the set of random-unitaries applied to the initial state and  $\text{tr}_{\bar{A}}$  is the partial trace over all spins not in subsystem  $A$ . Note that  $\bar{S}_n(A)$  cannot be extracted from the mixed-state dynamics which arise when averaging over measurement results and times.

#### DYNAMICS OF $S_0$ , MINIMAL-CUT PICTURE AND MAPPING TO 2D PERCOLATION

First, let us consider the evolution of  $S_0(x)$  under RUC dynamics in the absence of measurements, which allows one to gain some analytical insight. Applying a random-unitary acting on sites  $\{x, x + 1\}$  at time-step  $t$ , it can be shown that  $S_0(x)$  obeys the following formula with probability 1 [31]:

$$S_0(x, t + 1) = \min\{S_0(x - 1, t), S_0(x + 1, t)\} + 1. \quad (5.12)$$

For the evolution given by Eq. (5.9) (without measurements) Eq. (5.12) implies that

$$S_0(x, 2t) = \min\{x, t\}. \quad (5.13)$$

Therefore, in the absence of measurements,  $S_0$  grows linearly with time until it saturates to a volume law  $S_0(x, t = \infty) = x$  [31].

Consider the state obtained by application of some quantum circuit composed of random two-site unitaries to an initial product-state  $|\psi\rangle = \prod_{k=1}^N U_{i_k, i_k+1}^{(k)} |\psi_0\rangle$ . A bound on any Rényi entropy  $S_n(x)$  with respect to the state  $|\psi\rangle$  can be obtained by the following procedure. Consider a cut starting from bond  $x$  at the top of the circuit and traversing down to the bottom of the circuit without passing through any two-site unitary (this is made clearer by Fig. 5.1a). The “cost” of a given cut  $S_{\text{cut}}$  is calculated by the number of “legs” (the vertical black lines in Fig. 5.1a) which



the cut passes through on its way to the bottom of the circuit. The claim is that  $S_{\text{cut}}$ , computed for an arbitrary cut, provides an upper bound on the Rényi entropy  $S_n(x) \leq S_{\text{cut}}$ . The tightest bound is provided by the cut with the minimal cost  $S_{\text{min-cut}}$ , also known as the minimal-cut. For the dynamics we consider in this section  $S_0$  saturates the minimal-cut bound [31].

The fact that  $S_n(x) \geq S_{\text{cut}}$  can be seen by observing that the cut defines a representation of the state in terms of two tensors  $L, R$  (see Fig. 5.1b)

$$|\psi\rangle = \sum_{i, \sigma} L_{i_1, \dots, i_{S_{\text{cut}}}}^{\sigma_1, \dots, \sigma_x} R_{i_1, \dots, i_{S_{\text{cut}}}}^{\sigma_{x+1}, \dots, \sigma_L} |\sigma_1 \dots \sigma_x\rangle |\sigma_{x+1} \dots \sigma_L\rangle \quad (5.14)$$

The Schmidt-rank of  $|\psi\rangle$  at bond  $x$ , and hence the bond-dimension, is then bounded by  $\dim(i_1, \dots, i_{S_{\text{cut}}}) = 2^{S_{\text{cut}}}$ , which in turn means that  $S_0(x) \leq S_{\text{cut}}$ . Since for all  $n > 0$  we have  $S_n(x) \leq S_0(x)$ , this shows the general bound.

In Ref. [34] it was shown how the minimal-cut picture can be extended to the case where projective measurements are performed with probability  $p$  after application of each unitary. The effect of performing a projective measurement at time  $t$  on site  $j$  is to fix the value of the spin at point  $(j, t)$ . Consider a cut going through the quantum-circuit as in Fig. 5.1, passing through a “leg” at point  $(j, t)$ . This means that in the tensor-network representation Eq. (5.14) there is no summation on the index  $i_j$  corresponding to  $(j, t)$ , hence the maximal bond-dimension in this case is at most  $S_{\text{cut}} - 1$ . In general, projective measurements lead to broken bonds, which are not counted in the calculation of  $S_{\text{cut}}$ .

For small  $p$ , measurements will lead only to a sparse set of broken bonds meaning that a cut traversing from top to bottom of the circuit will still have to cross  $\sim \min\{x, t\}$  of unbroken bonds, hence  $S_0(x, t)$  is still described by linear growth saturating in a volume-law. On the other hand, in the case of large measurement probability, most bonds will be broken, hence we can find a cut which traverses the quantum-circuit from top to bottom cutting only a small non-extensive number of unbroken bonds. This means that in this case  $S_0(x, t)$  will quickly saturate to a constant independent of  $x, t$ , hence an area-law for entanglement. Hence a transition between an area-law behavior and a volume-law behavior is expected at some critical value of the measurement rate  $p_c$ .

## CRITICAL BEHAVIOR

To understand the expected critical behavior at  $p_c$ , let us consider the minimal-cut picture in the thermodynamic limit  $L = \infty$  at finite  $t$ . The problem of finding the minimal-cut in the presence of measurements can be mapped to what is known as “first passage percolation” problem in 2D. First passage percolation deals with finding the path of minimal cost through a disordered medium. At the critical point the minimal-cut, starting at the top of the circuit, traverses down to the bottom passing through a sequence of zero cost regions, where all bonds are broken (see Fig. 5.2). In the context of first passage percolation, it was shown that the sequence of zero cost regions is of increasingly larger size and their distance is  $O(1)$  [250]. Hence, after traversing  $\log(t)$  regions the cut enters a broken-bond region of scale  $t$  and can reach the bottom of the circuit with no further cost [34, 250]. This leads to the scaling

$$S_0(t; p_c) \sim A \log(t). \quad (5.15)$$



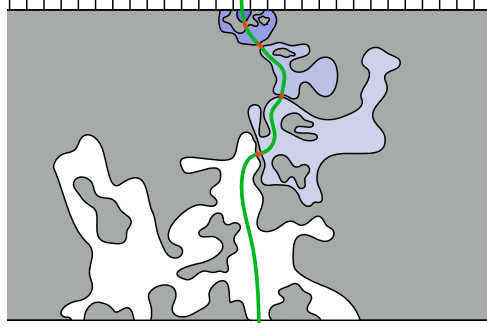


Figure 5.2: A schematic picture of the minimal-cut traversing the quantum circuit at the critical measurement rate  $p_c$ . The gray region represents a space-time area where most bonds are unbroken, while the blue and white regions represent a space-time region where most bonds are broken and hence traversing this regions does not increase  $S_{\text{cut}}$ . Figure taken from Ref. [34].

where in the thermodynamic limit,  $L \rightarrow \infty$ ,  $S_0$  does not depend on the bond  $x$ .

Away from the critical point the size of the broken-bond regions is finite, hence we can assign a finite length-scale with it  $\xi$ . This correlation length diverges at the critical point  $\xi(p) = |p - p_c|^{-\nu}$ , where for  $S_0$  the critical exponent  $\nu$  is expected to be that of 2D percolation transition  $\nu = 4/3$ . From the mapping to the percolation picture the following scaling form can be derived for  $S_0$

$$S_0(t; p) = A \log \xi + F(t/\xi) \quad (L \rightarrow \infty). \quad (5.16)$$

For a finite system, we can obtain the dependence on  $L$  from the above scaling form, by using  $t = 4L$ . We obtain  $S_0(t = 4L) = A \log L + G(L/\xi)$ , which leads to the following scaling form in the long time limit

$$S_0(x = L/2; p) - S_0(x = L/2; p_c) = \tilde{G}((p - p_c)L^{1/\nu}) \quad (t \rightarrow \infty). \quad (5.17)$$

Here  $S_0$  is evaluated for a bipartition at the middle bond of the system. Similar scaling form should hold as long as the subsystem for which  $S_0$  is computed is of extensive size, i.e.  $\sim \alpha L$ .

Numerical simulations of the circuit dynamics using MPS confirm the scaling form, Eq. (5.17), obtained from the minimal-cut picture both for  $S_0$  and for Rényi entropies with  $n > 0$ . In Ref. [34], using simulation for system sizes up to  $L = 24$ , it was found that  $\nu \approx 4/3$  for  $S_0$  but  $\nu \approx 2.03$  for the von-Neumann entanglement-entropy. In Ref. [35] the entanglement growth was studied for much larger system sizes (up to  $L = 512$ ) for the more restricted case of random Clifford circuits (which is efficiently classically simulatable) and an exponent of  $\nu \approx 1.85$  was found (see Fig. 5.3). A later study in Ref. [37] used the tri-partite mutual-information

$$\begin{aligned} \mathcal{I}_{3,n}(A, B, C) = & S_n(A) + S_n(B) + S_n(C) + S_n(A \cup B \cup C) \\ & - S_n(A \cap B) - S_n(A \cap C) - S_n(B \cap C), \end{aligned} \quad (5.18)$$

## 5 Trajectory dependent entanglement transition in a free fermion chain – from extended criticality to area law

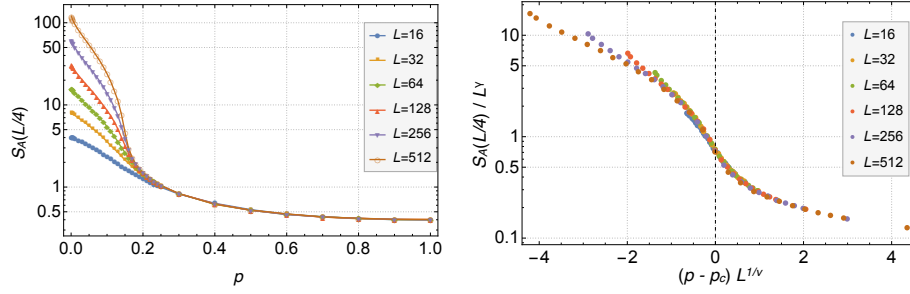


Figure 5.3: Finite-size scaling performed in Ref. [35] for the case of random circuits taken from the Clifford group together with projective measurements.  $S_A(L/4)$  is the entanglement-entropy of a subsystem of length  $L/4$ , computed in the long time limit. Here the best data collapse was obtained with  $\nu = 1.85$  and  $\gamma = 0.3$ . (Figures taken from [35])

A quantity which is expected to be less sensitive to finite-size effects. Performing finite-size scaling analysis for  $\mathcal{I}_{3,1}$  Ref. [37] found  $\nu \approx 4/3$  both for the Clifford evolution case and evolution with random-unitaries sampled from the Haar measure. The findings of [37] suggests  $\nu$  to be consistent with the percolation transition picture also for Rényi entropies with  $n > 0$ , unlike the previous studies in [34, 35].

### CONNECTION TO INFORMATION SCRAMBLING

Choi et al. pointed out a connection between scrambling dynamics and the entanglement phase transition [215]. First, consider that from a naive perspective the stability of the volume-law phase at any finite measurement rate might seem surprising. This is due to the observation that only unitaries which act across the boundary between two subsystems  $A$  and  $B$  can increase the bipartite entanglement-entropy between them. On the other hand, local measurements of any qubit in subsystem  $A$  can disentangle it from qubits in  $B$ . At any time-step of the hybrid circuit evolution an extensive amount of measurements is performed  $\sim pL_A$ , while only  $O(1)$  unitaries act across the boundary between  $A$  and  $B$ . Therefore, one might naively conclude that the effect of measurements will always prevail and the system will never develop an extensive amount of entanglement, in contrast to the numerical observations.

The main observation of Ref. [215] is that the stability of the volume-law phase at weak measurement rate is due to the chaotic nature of the unitary time-evolution which leads to spreading of correlations over many qubits. Although there could be an extensive number of local measurements, correlations between two subsystems are hidden in highly non-local degrees of freedom and cannot be accessed by local measurements.

In order to substantiate this claim, first an analytical argument based on the quantum-decoupling theorem [251, 252] from the field of quantum-communication is given. Consider two entangled subsystems  $A$  and  $B$  of size  $N$ , whose entanglement is  $S_A \sim \gamma N$ . Let us denote by  $\tilde{B}$  the set all qubits in  $B$  which are initially entangled with some parts of  $A$ . Now, imagine the situation where a random-unitary  $U_A$  is applied to subsystem  $A$ , and afterwards a fraction  $p$  of the qubits

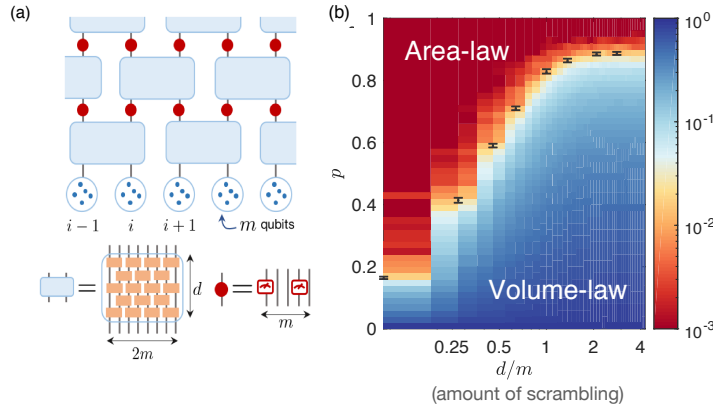


Figure 5.4: Numerical study of a model with tunable scrambling strength by Choi et al. [215]. By increasing the depth  $d$  of unitary circuits which act on  $2m$  qubits between measurements, the system can be driven from the area-law phase to the volume-law phase.

in  $A$  are measured. If we denote by  $A_m$  the set of measured qubits, then the quantum-decoupling theorem can be used to show that

$$\mathbb{E}_{U_A} \|\rho_{A_m \tilde{B}} - \rho_{A_m}^{\max} \otimes \rho_{\tilde{B}}\|_1 \leq 2^{-(1-2p-\gamma)N/2} \quad (5.19)$$

where  $\rho_{A_m}^{\max}$  is the maximally mixed state on  $A_m$ . Eq. (5.19) means that for large  $N$ , the state of  $A_m$  and  $\tilde{B}$  becomes approximately separable after the application of  $U_A$ , as long as the number of measured qubits in  $A$  obeys  $1 - p > \gamma + p$ . In this case measurements on  $A_m$  contain no information on  $\tilde{B}$  and hence cannot reduce the entanglement between  $\tilde{B}$  and  $A$ .

To further exemplify the fact that the entanglement transition in RUC dynamics is a result of a competition between scrambling rate and measurement rate, Choi et al. consider a  $1d$  model with  $L$  blocks of  $m$  qubits, where random projective measurements occur between evolution with two-block unitaries. The block unitaries themselves are composed of circuits of 2-qubit gates acting on the qubits inside the blocks. The depth of the circuit is  $d$  (see Fig. 5.4a). This model allows to control the amount of scrambling between measurements, by varying the depth  $d$ . Via numerical simulations of this model, they show that indeed, varying  $d/m$  at a fixed measurement rate can drive a transition between area-law regime and a volume-law regime (Fig. 5.4b).

### 5.2.3 QUANTUM TRAJECTORY UNRAVELLING OF THE QME

In the works described in previous sections, the entanglement transition was explored in a setting where a pure state is evolved under discrete unitary dynamics, interspersed with strong projective measurements occurring at discrete time steps with a constant rate. In each realization of this evolution, the wave function follows a trajectory in Hilbert-space  $|\psi(t)\rangle$ , which is conditioned on the specific sample of random unitaries and measurement results.

On the other hand, so far in this thesis we have been concerned with open quantum systems, which are described by a mixed-state, and whose dynamics are governed by the QME which contains a unitary part and a dissipative part. In the QME, the dissipative part arises due to a coupling

of the system to some bath whose state is not tracked. In this section we explain how the QME evolution of a mixed-state can be connected to pure state evolution in the presence of measurements, by keeping track of the information transferred from the system to the bath (either theoretically or even in an experiment).

Given a QME with a set of Lindblad operators  $L_i$ ,  $\dot{\rho} = -i[H, \rho] + \sum_i \gamma_i \mathcal{D}_{L_i}[\rho]$ , we define a trajectory unravelling of the quantum master, as a stochastic evolution equation describing pure state evolution

$$d|\psi(t; \xi)\rangle = \left( -i\tilde{H}[\psi(t)]dt + \sum_i \hat{F}_i[\psi(t), \xi_{i,t}] \right) |\psi(t)\rangle, \quad (5.20)$$

with  $\xi_{i,t}$  a set of random variables. At any time  $t$ , expectation values of linear operators with respect to the state  $\rho(t)$  can be obtained from averaging over all realizations of  $|\psi(t; \xi)\rangle$

$$\text{tr}(\hat{O}\rho(t)) = \mathbb{E}_{\xi}[\langle\psi(t; \xi)|\hat{O}|\psi(t; \xi)\rangle]. \quad (5.21)$$

Here we denoted  $\xi \equiv \{\xi_{i,t}\}$ , and  $|\psi(t; \xi)\rangle$  denotes an evolution trajectory with specific noise realization. We emphasize that the operator  $\hat{F}_i$  depends on a random variable  $\xi_{i,t}$  at each infinitesimal time-step. Both  $\tilde{H}$ ,  $\hat{F}_i$  may depend on expectation values with respect to the state itself  $|\psi(t)\rangle$  and hence they are non-linear operators. We will see that the noise  $\xi$  can be related to continuous measurements performed by the bath on the system, a specific trajectory is related to a specific set of measurement outcomes and averaging over the noise is related to “integrating out” the bath.

We note that for a given QME, the trajectory unravelling is not unique. Here we will present two type of unravellings, the quantum-jump (QJ) evolution and the quantum-state diffusion (QSD). While the idea of a stochastic unravelling was first introduced as a theoretical tool to numerically simulate the evolution of an open system, the QJ and QSD evolutions can be related to different physical measurement schemes and the dynamics of individual quantum-trajectories can be observed in experiment in some cases.

## QUANTUM-JUMP TRAJECTORIES

The quantum-jump method was introduced as a way to simulate the time-evolution of quantum-optical systems with dissipative processes by Dalibard et al. [241], and in parallel by Dum et al. [253] in the context of studying a quantum optical system under continuous monitoring. Here we will follow the description provided in the review article [13], which also provides further details about the usage of the method for simulations of open many-body systems.

First let us describe the procedure for evolving a trajectory using the quantum-jump approach<sup>1</sup>. Given the trajectory state  $|\psi(t)\rangle$  the state  $|\psi(t + \delta t)\rangle$  is obtained in the following way. First compute<sup>2</sup>

$$|\tilde{\psi}(t + \delta t)\rangle = (1 - i\delta t H_{\text{eff}})|\psi(t)\rangle, \quad H_{\text{eff}} = H - i \sum_i L_i^\dagger L_i. \quad (5.22)$$

where we absorbed the dissipation rates  $\gamma_i$  into the definition of the Lindblad operators. Then define the probability  $\delta p$  via

$$\delta p = \delta t \sum_i \langle \psi(t) | L_i^\dagger L_i | \psi(t) \rangle \equiv \sum_i \delta p_i, \quad 1 - \delta p = \langle \tilde{\psi}(t + \delta t) | \tilde{\psi}(t + \delta t) \rangle. \quad (5.23)$$

$\delta p$  is the probability that a measurement of the system occurred, as we will justify later. Then, the state  $|\psi(t + \delta t)\rangle$  is chosen probabilistically

$$|\psi(t + \delta t)\rangle = \begin{cases} \frac{|\tilde{\psi}(t + \delta t)\rangle}{\sqrt{1 - \delta p}}, & \text{probability } 1 - \delta p \\ \frac{L_i |\psi(t)\rangle}{\sqrt{\delta p_i / \delta t}}, & \text{probability } \delta p \end{cases}. \quad (5.24)$$

The evolution in the second case is referred to as a *quantum-jump*, and the jump operator is chosen according to the probability distribution  $\Pi_i = \delta p_i / \delta p$ .

To see how the procedure described above reproduces the QME evolution, consider the density operator  $\rho(t) = |\psi(t)\rangle\langle\psi(t)|$ , the propagation of  $\rho(t)$  can be obtained by averaging the probabilistic evolution step

$$\bar{\rho}(t + \delta t) = (1 - \delta p) \frac{|\tilde{\psi}(t + \delta t)\rangle\langle\tilde{\psi}(t + \delta t)|}{1 - \delta p} + \delta p \sum_i \Pi_i \frac{L_i |\psi(t)\rangle\langle\psi(t)| L_i^\dagger}{\delta p_i / \delta t}, \quad (5.25)$$

which after re-organization becomes nothing but the familiar QME

$$\bar{\rho}(t + \delta t) - \bar{\rho}(t) = -i\delta t (H_{\text{eff}} \bar{\rho}(t) - \bar{\rho}(t) H_{\text{eff}}^\dagger) + \delta t \sum_i L_i \bar{\rho}(t) L_i^\dagger. \quad (5.26)$$

Let us note that the QJ evolution can be re-casted to the stochastic form in Eq. (5.20) [11]

$$d|\psi(t; \xi)\rangle = \left[ -i\tilde{H}[|\psi\rangle] dt + \sum_i \xi_{i,t} \left( \langle L_i^\dagger L_i \rangle_t^{-1/2} L_i - 1 \right) \right] |\psi(t; \xi)\rangle. \quad (5.27)$$

where  $\tilde{H}[|\psi\rangle] = H_{\text{eff}} + i \sum_i \langle L_i^\dagger L_i \rangle_t$  and  $\xi_{i,t}$  are random Poisson variables satisfying  $\mathbb{E}[\xi_{i,t}^2] = \langle L_i^\dagger L_i \rangle_t dt$  and  $\xi_{i,t} \xi_{j,t} = \delta_{ij} \xi_{i,t}$ .

<sup>1</sup>The numerical implementation used in practice is slightly different than the procedure outlined here, as we explain later in this chapter. However, the evolution procedure we describe here is more appealing in terms of physical interpretation.

<sup>2</sup>Note that this is just the application of the first order expansion of  $\exp(-i\delta t H_{\text{eff}})$ .

We now turn to the physical interpretation of the quantum-jump evolution, which is easiest to understand with a specific simple example of a two-level system. Due to the coupling to the vacuum electromagnetic field, the system can decay incoherently from the excited state  $|e\rangle$  to the ground state  $|g\rangle$  which results in a photon emission. If we don't keep track of emitted photons the system will evolve under a QME with  $L = \sigma^-$  representing the decay process. Assume that we know the state of the system at time  $t$ ,  $|\psi(t)\rangle = \alpha|g\rangle + \beta|e\rangle$ .

Now, assume that we have a perfect photon detector which measures the photons coming out of the system in a time window  $\delta t$ . At each  $\delta t$  there could be two options: (1) A click has occurred in the photon counter. In this case we know that a quantum-jump has occurred and the state of the system must be  $|\psi(t + \delta t)\rangle = |g\rangle \sim \sigma^-|\psi(t)\rangle$ . (2) A click has not occurred. In this case we also gain some information about the system, namely that it is a bit less probable to find it in the excited-state. This is represented by the evolution with  $H_{\text{eff}}$  which leads to decay of the probability amplitude for finding the system in  $|e\rangle$ :  $|\psi(t + \delta t)\rangle \propto \exp(-iH_{\text{eff}}\delta t)|\psi(t)\rangle = \alpha|g\rangle + \beta e^{-\Gamma\delta/2}|e\rangle$ .

We have thus seen that the quantum-jump trajectory evolution can be interpreted by relating the quantum jump events to photon counting measurements in a quantum-optical system. A more rigorous relation between quantum-jump trajectories and photon counting, beyond the toy example provided here, can be found in [13, 254].

#### QUANTUM STATE DIFFUSION

In the quantum-jump trajectory approach, the effect of the coupling to the bath is modeled by a series of discrete jump events and a deterministic non-unitary evolution in between the jumps. A different unravelling of the QME can be obtained by considering the setup of heterodyne measurement [240, 254, 255]. In this setup the weak photo-current exiting the system, is continuously monitored by interfering it with a second strong coherent light source. In the resulting unravelling, called quantum state diffusion (QSD), the noise is continuous, and it can be viewed as the limit where there are infinite quantum-jumps but each jump has an infinitesimally small effect on the system.

The evolution of a QSD trajectory is governed by the equation

$$d|\psi\rangle = [-idtH_{\text{eff}} + dt \sum_i (2\langle L_i \rangle L_i - \langle L_i^\dagger \rangle \langle L_i \rangle) + \sum_i (L_i - \langle L_i \rangle) d\xi_{i,t}] |\psi\rangle \quad (5.28)$$

where  $H_{\text{eff}}$  was defined in Eq. (5.22), and  $d\xi_{i,t}$  is a Wiener process, that is it is a Gaussian random variable with  $\mathbb{E}[d\xi_{i,t}] = 0$ ,  $\mathbb{E}[d\xi_{i,t} d\xi_{j,t'}] = \delta_{ij} \delta_{tt'} dt$ .

#### 5.2.4 ENTANGLEMENT IN CONFORMAL FIELD-THEORY

One of the main results of this chapter, is the emergence of an extensive regime where the entanglement and correlation properties of the system under consideration show behavior which is expected from a system described by a  $(1+1)d$  conformal field-theory (CFT). In this section we provide a (very) brief introduction to CFTs and their expected entanglement properties.

A CFT is a field theory whose action is invariant under conformal transformations, where a map is called conformal if it locally preserves the angle between two curves. For example, in  $2d$  the

group of conformal transformations is given by all holomorphic functions defined on the complex plane. Hence, conformal invariance of a  $(1+1)d$  field theory enforces a lot of constraints on the theory, which in turn makes it a useful property. CFTs are important in statistical mechanics and condensed-matter theory because many-body systems undergoing (quantum or classical) second-order phase transitions are often conformally invariant at the critical point [142, 256, 257].

Here we briefly introduce several facts about  $(1+1)d$  CFTs which will be important for our work later on in this chapter. For more details refer to the review in Ref. [258]. In the  $2d$  case it is convenient and customary to work with complex representation of the  $2d$  plane  $z = x + iy$ ,  $\bar{z} = x - iy$ . In  $2d$  CFTs there is a class of fields, called *primary-fields*, which, in the case of scalar fields, transform under a conformal map  $z \mapsto w$  as

$$\Phi(z, \bar{z}) \rightarrow \left| \frac{\partial w}{\partial z} \right|^\Delta \Phi(w, \bar{w}), \quad (5.29)$$

where  $\Delta$  is known as the scaling weight of the fields. Using this transformation rule with an infinitesimal transformation  $z \mapsto z + \epsilon(z)$  one can show that this leads to a constraint on the two-point correlation function of primary-fields (here we consider first the infinite-plane geometry)

$$\langle \Phi(z_1, \bar{z}_1) \Phi(z_2, \bar{z}_2) \rangle \sim |z_{12}|^{-2\Delta}, \quad z_{12} \equiv z_1 - z_2. \quad (5.30)$$

To obtain the form of the correlation function in a finite system with periodic boundary conditions at zero temperature, we can use Eq. (5.29) together with a conformal transformation which maps the infinite-plane to the infinite cylinder, namely  $w = L/(2\pi) \log(z)$  (where we assume  $w = \tau + ix$  so the system is periodic in the space direction). Doing so we obtain that the two-point correlation function obeys Eq. (5.30) but with  $z_{12} \equiv \sin(\pi/L(x_1 - x_2))$ .

An important quantity which characterizes a given CFT is the *central-charge*  $c$ . The central-charge can be related to the leading singular short-range behavior of the 2-point correlation function of the stress-energy tensor  $\langle T(z)T(w) \rangle \sim c/2(z-w)^{-4} + \dots$ , where  $T(z) \equiv T_{zz}(z) = 1/4(T_{00} - 2iT_{10} - T_{11})$  [258]. Note that the fact that  $c \neq 0$  implies that  $T(z)$  is not a primary-field, since for primary-fields  $\langle T(z)\phi(w) \rangle \sim \Delta(z-w)^{-2} + \dots$ <sup>3</sup>. The reason we introduced the central-charge here is that in a CFT the entanglement growth with the subsystem size is proportional to  $c$ , as we will shortly see.

Calabrese and Cardy [259] introduced a method to compute the entanglement-entropy of a given CFT in  $(1+1)d$ , by connecting it to correlation functions of certain type of fields. The main idea is a replica trick where one considers the object  $Z_n = \text{tr} \rho_A^n$ , with  $\rho_A$  the reduced density matrix on some sub-interval and  $n \in \mathbb{Z}_+$ . If we can compute  $Z_n$  we can obtain the Rényi entropy  $S_n(A)$ , and by analytic continuation also the von-Neumann entropy.

The quantity  $Z_n(A)$  can be computed, e.g. in the case  $n = 2$ , by first considering a system with two replicas of the full density-matrix  $\rho_{AB}$ . In this replica system,  $Z_2(A)$  is given by the expectation value

$$\text{tr} \rho_A^2 = \text{tr}(V_2(A) \otimes \mathbb{1}_{\rho_{AB}} \otimes \rho_{AB}) = \langle V_2(A) \otimes \mathbb{1} \rangle, \quad (5.31)$$

<sup>3</sup>This is a consequence of the fact that the action of infinitesimal conformal transformations is generated by the charge  $Q$  which is given by a certain contour-integral over  $T$ , together with the infinitesimal version of Eq. (5.29). See [258] for details.

where  $V_2(A) = \sum_{\mathbf{i}_A, \mathbf{i}'_A} |\mathbf{i}_A\rangle \otimes |\mathbf{i}'_A\rangle \langle \mathbf{i}'_A| \otimes \langle \mathbf{i}_A|$  is the SWAP operator which swaps the states of sites in subsystem  $A$  between the two replicas<sup>4</sup>. In a path-integral formulation the replicated system is described by an action with the Lagrangian density  $\mathcal{L}_n = \sum_{i=1}^n \mathcal{L}[\phi_i]$ . The expectation value of the SWAP operator is given by a correlation function of two twist-fields whose operation enforces a constraint on the path-integral such that  $\phi_i(x, 0^-) = \phi_{i+1}(x, 0^+)$  for  $x \in A$ ,

$$Z_n(A) = \langle \mathcal{T}_n(x_1) \tilde{\mathcal{T}}_n(x_2) \rangle. \quad (5.32)$$

The main result of Cardy and Calabrese is that the twist fields are primary-fields with scaling dimension  $\Delta = c/12(n - 1/n)$  [259]. This is a very powerful result, as it allows us to easily compute the scaling behavior of Rényi entropies of CFTs in a variety of geometries. Specifically in an infinite plane geometry one obtains

$$\text{tr} \rho_A^n \propto \langle \mathcal{T}_n(x_1) \tilde{\mathcal{T}}_n(x_2) \rangle \sim |x_2 - x_1|^{-c(n-1/n)/6}, \quad (5.33)$$

which leads to the following results for the entanglement-entropy of a sub-interval of length  $\ell$  in an infinite system

$$S_n(\ell) = \frac{c}{6} \left( 1 + \frac{1}{n} \right) \log \left( \frac{\ell}{a} \right) + c'_n, \quad S_{\text{vN}}(\ell) = \frac{c}{3} \log \left( \frac{\ell}{a} \right) + c'_1. \quad (5.34)$$

Here  $c'_n$  is a non-universal model-dependent constant, and  $a$  is the short range cutoff (i.e. lattice constant) which is needed in order to obtain a dimensionless ratio.

Applying the same conformal-mapping we used for the two-point correlation function above, we can obtain the entanglement-entropy for the geometry of a finite interval in a finite-system with periodic boundary conditions

$$S_{\text{vN}}(\ell; L) = \frac{c}{3} \log \left[ \frac{L}{\pi a} \sin \left( \frac{\pi \ell}{L} \right) \right] + c'_1. \quad (5.35)$$

### 5.3 MODEL AND METHOD

We consider free fermions on a half-filled periodic chain of length  $L$ , which is described by a nearest-neighbor hopping Hamiltonian. Due to weak measurements of the fermion density by the environment the fermions experience dephasing noise, which results in a QME evolution with Lindblad operators  $L_i = n_i$ . The dynamics of the density-matrix is thus described by

$$\dot{\rho} = -i[H, \rho] + \gamma \sum_i \left( n_i \rho n_i - \frac{1}{2} \{n_i, \rho\} \right), \quad H = \sum_l c_{l+1}^\dagger c_l + c_l^\dagger c_{l+1}, \quad (5.36)$$

with fermionic creation and annihilation operators  $c_l^\dagger, c_l$  and we used the fact that for fermions  $n_i^2 = n_i$ . Since  $[H, n_i] = 0$  the total number of particles is conserved during time evolution. Note that since the dynamics are described by a QME with an hermitian Lindblad operator, the

<sup>4</sup>Note that this replica representation is the same that was discussed in Sec. 5.2.1 and was implemented in [247] for an experimental measurement of  $S_2$ .



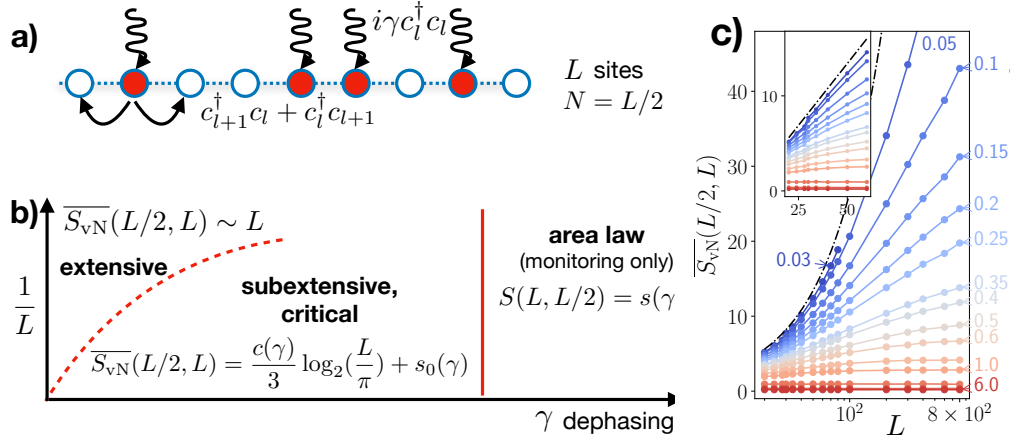


Figure 5.5: (a) The model we consider: free-fermions hopping on a chain of length  $L$  subject to continuous monitoring with dimensionless rate  $\gamma$ . (b) Schematic “phase diagram” showing the different regimes of scaling with the system size  $L$  of the entanglement-entropy of an equal bipartition  $\overline{S}_{\text{vN}}(L/2, L)$ . (c) At weak dephasing, we find an extensive region of the phase-diagram where the entanglement-entropy shows scaling behavior similar to this expected in conformal-field theories. At a critical value of dephasing  $\gamma_c$  a phase-transition occurs between the CFT behavior and an area-law behavior. For small  $\gamma$ ,  $L$ , extensive growth  $\sim L$  is observed (inset), approaching a volume law as  $\gamma \rightarrow 0$ .

steady-state is expected to be a featureless infinite temperature state  $\rho_\infty = \mathbb{1}_N$ . Hence we don’t expect to find any interesting physics in the static properties of the steady-state.

As we explained in Sec. 5.2.3, the QME dynamics can be alternatively described by means of stochastic evolution of pure-states, which we refer to as *quantum-trajectories*. The time-evolution of a fermion pure state  $|\psi(\{\xi\})\rangle$  follows a stochastic trajectory, determined by a specific realization of noise increments  $\xi \equiv \{\xi_{l,t}\}$ , which physically can be thought of as a specific set of measurement outcomes. They encode the effect of interactions of the local fermion density with a (monitored) environment  $\sim i\xi_{l,t}n_l$ . As noted in the introduction and similar to the works done on the entanglement transition under random unitary dynamics with projective measurements (see Sec. 5.2.2) the main quantity of interest in this chapter is the trajectory averaged entanglement entropy, defined as

$$\bar{S}_{\text{vN}}(\ell, t) = \mathbb{E}_\xi[-\text{tr} \rho_\ell(t; \xi) \log \rho_\ell(t; \xi)], \quad \rho_\ell(t; \xi) = \text{tr}_{x \in [\ell, L]} |\psi(t; \xi)\rangle \langle \psi(t; \xi)|, \quad (5.37)$$

with  $|\psi(t; \xi)\rangle$  is the trajectory state at time  $t$  (i.e. the state of the system conditioned on a specific set of measurement outcomes).

We consider three types of trajectory dynamics:

1. *Quantum state diffusion (QSD)* describes fermions interacting with a bath of photons, which are continuously monitored via homodyne detection [240, 242]. In this case the evolution of a trajectory is given by

$$d|\psi\{\xi\}\rangle = \left[ -iHdt + \sum_l \left( \xi_{l,t} \hat{M}_{l,t} - \frac{\gamma}{2} \hat{M}_{l,t}^2 dt \right) \right] |\psi\{\xi\}\rangle, \quad (5.38)$$

$$\hat{M}_{l,t} = n_l - \langle n_l \rangle_t, \quad \mathbb{E}[\xi_{l,t}] = 0, \quad \mathbb{E}[\xi_{l,t} \xi_{m,t'}] = \gamma dt \delta_{l,m} \delta(t - t').$$

Here a specific set of noise values  $\xi$  can be interpreted as the measurement noise observed in a heterodyne measurement of a quadrature of the fluorescent light going out of the system [233, 260].

2. *Quantum jump evolution (QJ)* corresponding to the same bath but where photons scattering off fermions are counted directly [13, 233, 234]. In the quantum jump trajectories, the evolution equation is

$$d|\psi\{\xi\}\rangle = \left[ -iHdt + \sum_l \xi_{l,t} \left( \frac{n_l}{\sqrt{\langle n_l \rangle_t}} - 1 \right) \right] |\psi\{\xi\}\rangle, \quad (5.39)$$

$$\xi_{l,t}^2 = \xi_{l,t}, \quad \mathbb{E}[\xi_{l,t}] = \gamma dt \langle n_l \rangle_t \quad (5.40)$$

for a state with conserved total particle number<sup>5</sup>. Note that the noise is a binary-variable distributed according to  $P(\xi_{l,t}) = \delta_{\xi_{l,t},1} \overline{\xi_{l,t}} + \delta_{\xi_{l,t},0} (1 - \overline{\xi_{l,t}})$ . Here the physical interpretation of a specific noise realization is a series of photon detector clicks occurring at all the times where  $\xi_{l,t} \neq 0$ .

3. A so-called "raw" quantum state diffusion [232, 242, 261], given by

$$d|\psi\{\xi\}\rangle = \left[ -iHdt + \sum_l \xi_{l,t} n_l \right] |\psi\{\xi\}\rangle, \quad (5.41)$$

where the noise  $\xi$  is the same as in Eq. (5.38). Note that this equation is similar to the QSD evolution Eq. (5.38), but lacks the nonlinear "feedback" term  $\langle n_l \rangle_t$ . While Eq. (5.41) constitutes an unravelling of the QME, its main drawback is that it does not conserve normalization of the state and hence lacks a clear physical interpretation. However, if we do normalize the wave-function after each time step, Eq. (5.41) is a continuous version a non-unitary circuit evolution (QSDc) similar to the one recently explored in Ref. [226] in the context of the entanglement transition.

<sup>5</sup>Here we used the fact that the total density is conserved hence the effect of the non-unitary part of the effective Hamiltonian  $\sim i \sum_i n_i = iN$  leads to an overall state-independent factor of  $\exp(-\gamma N dt/2)$  which is then canceled due to the normalization.

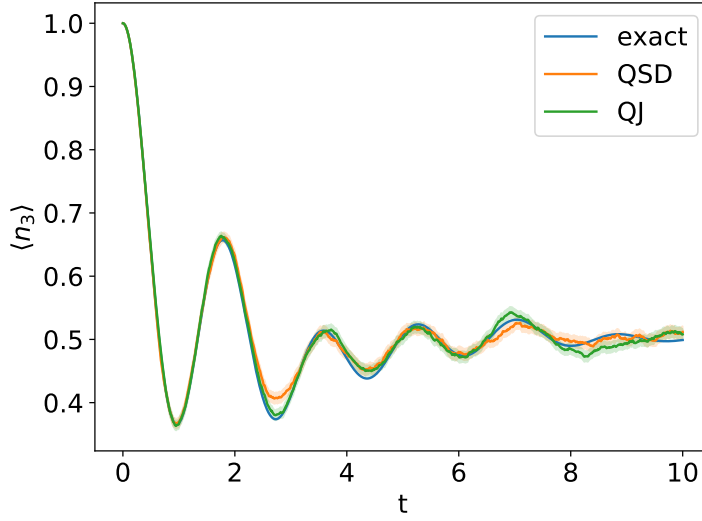


Figure 5.6: Dynamics of the expectation value  $\langle n_3(t) \rangle$  computed for a chain with 3 fermions and 6 sites, evolving under Eq. (5.38) (QSD), Eq. (5.39) (QJ) and Eq. (5.36) (“exact”). As expected the results obtained by averaging over trajectories using either QSD or QJ agree results obtained from an exact time-evolution of the density-matrix according to the QME (“exact”).

For each trajectory evolution, the statistical average over the noise distribution  $P(\xi)$  defines the density matrix

$$|\psi(t; \xi)\rangle\langle\psi(t; \xi)| \equiv \int \mathcal{D}\xi P(\xi) |\psi(t; \xi)\rangle\langle\psi(t; \xi)| = \rho_t.$$

For QSD and QJ trajectories, the density matrix evolution is given by the deterministic QME with Markovian dephasing given in Eq. (5.36) (see Fig. 5.6). The QSDc trajectories reproduce the QME only if we do not normalize the state after each infinitesimal time-step.

In what follows we initialize the system in a short range correlated Néel state

$$|\psi_0\rangle = |010101\dots 01\rangle. \quad (5.42)$$

We evolve multiple trajectories starting from  $|\psi_0\rangle$  according to the different types of trajectory evolutions Eqs. (5.38)- (5.41).

The entanglement entropy, mutual information and correlation functions are computed for each individual trajectory. We denote the statistical average of an observable  $O$  by  $\overline{O}$ . The trajectories are propagated to long enough times such that averaged observables have reached a steady state. See example of the convergence of the trajectory averaged entanglement entropy in Fig. 5.7. For nonlinear functions  $f(|\psi\rangle\langle\psi|)$  of the state,  $\overline{f(|\psi\rangle\langle\psi|)} \neq f(\overline{|\psi\rangle\langle\psi|})$  in general and therefore  $\overline{S_{vN}}(l, L)$  cannot be obtained from the trajectory averaged state  $\rho = \overline{|\psi\rangle\langle\psi|}$  or from the QME (5.36). Hence, different trajectory evolutions may yield different results when the entanglement entropy or other objects which are non-linear in  $|\psi\rangle$  are considered.

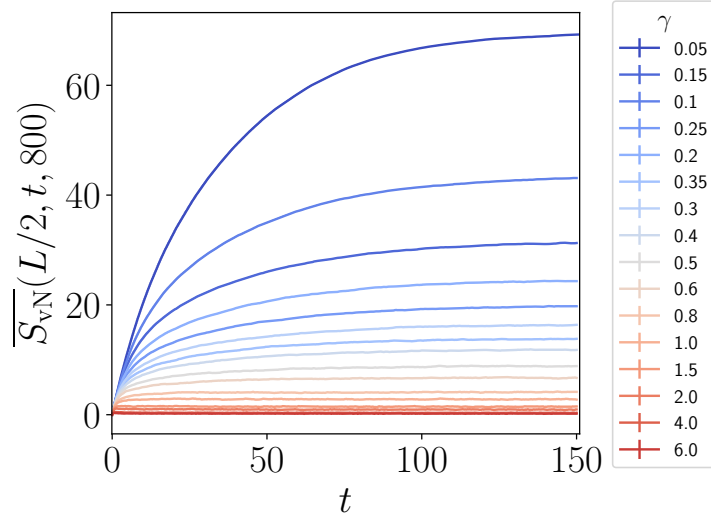


Figure 5.7: Time dependence obtained for the trajectory averaged entanglement entropy  $\bar{S}_{\text{vN}}(L/2, L)$  for  $L = 800$  showing convergence to the steady-state values.

### 5.3.1 FERMIONIC GAUSSIAN STATES

An important feature of the evolution equations Eqs. (5.38)-(5.41) which allows for efficient numerical computation, is that they are quadratic in the fermion operators. This means that if the initial state of the system  $|\psi_0\rangle$  is Gaussian it will remain Gaussian at later times under the trajectory evolution. A Gaussian state is a state whose correlations are completely determined by its covariance-matrix, which, in the number conserving case, is given by

$$D_{lk} = \text{tr}(\rho c_l^\dagger c_k). \quad (5.43)$$

Any higher order correlation functions of a Gaussian state can be obtained from  $D_{lk}$  by the use of Wick's theorem [262]. For example, the 4-point correlation function is given by

$$\langle c_i^\dagger c_j c_k^\dagger c_l \rangle = D_{ij} D_{kl} + D_{il} (\delta_{jk} - D_{kj}). \quad (5.44)$$

In our case we assume that the initial state is pure, and hence the state at later times remains pure under the trajectory evolution. A pure fermionic Gaussian-state  $|\psi(t)\rangle$  of  $N$  particles is parametrized by an  $L \times N$  matrix  $U(t)$  via

$$|\psi_t\rangle = \prod_{l=1}^N \left( \sum_{j=1}^L U_{j,l}(t) c_j^\dagger \right) |0\rangle, \quad (5.45)$$

where  $U^\dagger U = \mathbb{1}$  since we explicitly normalize the state after each time step. In other words, the state  $|\psi_t\rangle$  is a Slater-determinant state of  $N$  fermions where the single-particle wave-functions are given by the columns of  $U$ . The  $l$ -th occupied single-particle state is given by  $|\phi_l(t)\rangle =$

$\sum_j U_{j,l}(t)|j\rangle$ , where  $|j\rangle$  is the wave-function localized on lattice site  $j$ . For a state represented by Eq. (5.45) the correlation matrix can be computed from  $U$  via

$$D_{l,j}(t) = [U(t)U(t)^\dagger]_{j,l}. \quad (5.46)$$

The initial Néel state is represented by the following matrix

$$U_{\text{Néel}} = \text{diag}(0, 1, 0, 1, \dots). \quad (5.47)$$

We can generalize the relation in Eq. (5.46) in order to compute the correlation function between creation and annihilation operators at different times

$$D_{l,j}(t+\tau, t) \equiv \langle c_l^\dagger(t+\tau)c_j(t) \rangle = [U(t)U^\dagger(t+\tau)]_{j,l}. \quad (5.48)$$

Note that the operational meaning  $\langle c_l^\dagger(t+\tau)c_j(t) \rangle$  in the context of a non-unitary trajectory evolution is: (i) evolve the initial state to time  $t$  and apply  $c_j$ , resulting in  $|\chi\rangle = c_j|\psi(t)\rangle$  (ii) evolve  $|\chi\rangle$  to time  $\tau$  and apply  $c_l^\dagger$ , resulting in  $|\tilde{\chi}\rangle = c_l^\dagger|\chi(\tau)\rangle$  (iii) measure overlap with the initial state evolved to time  $t+\tau$ , hence  $\langle c_l^\dagger(t+\tau)c_j(t) \rangle = \langle \psi(t+\tau) | \tilde{\chi} \rangle$ . In the case of unitary evolution this coincides with the expectation values of the operators in the Heisenberg picture  $c_j(t) = e^{iHt}c_j e^{-iHt}$ .

To see explicitly that Eq. (5.48) holds, we plug-in the parameterization in Eq. (5.45) at different times:

$$c_m|\psi(t)\rangle = \sum_k U_{mk}(t) \prod_{l=1, l \neq k}^N \left( \sum_{j=1}^L U_{jl}(t) c_j^\dagger \right) |0\rangle \equiv \sum_k U_{mk}(t) |\phi_k(t)\rangle, \quad (5.49)$$

$$\langle \psi(t+\tau) | c_n^\dagger = \sum_k U_{nk}^*(t+\tau) \langle 0 | \prod_{l=1, l \neq k}^N \left( \sum_{j=1}^L U_{jl}^*(t+\tau) c_j \right) \equiv \sum_k U_{nk}^*(t+\tau) \langle \phi_k(t+\tau) |.$$

Note that  $\langle \phi_{k'}(t') | \phi_k(t') \rangle = \delta_{kk'}$ , and evolving  $c_m|\psi(t)\rangle$  to time  $t+\tau$  results in

$$|\chi(\tau)\rangle = \sum_k U_{mk}(t) |\phi_k(t+\tau)\rangle, \quad (5.50)$$

due to the fact that each  $|\phi_k\rangle$  a Slater determinant state of single-particle modes which evolve independently from each other under the quadratic dynamics. Taking the inner product of  $|\chi(\tau)\rangle$  with  $\langle \psi(t+\tau) | c_n^\dagger$  results in Eq. (5.48).

Using the correlation matrix we can also obtain the entanglement entropy of a subinterval  $A = [m_1, m_2]$ , as first shown in [263]. Without loss of generality assume  $m_1 = 1, m_2 = l$ .

The reduced density matrix  $\rho_A = \text{tr}_{x \notin A} |\psi\rangle\langle\psi|$  with respect to a Gaussian state is completely characterized by the correlation-matrix  $D_A$  given by

$$D_A \equiv \begin{pmatrix} D_{11} & \cdots & D_{1l} \\ \vdots & \ddots & \vdots \\ D_{l1} & \cdots & D_{ll} \end{pmatrix}. \quad (5.51)$$

Consider the unitary transformation which diagonalizes  $D_A$

$$V^\dagger D_A V = \text{diag}(\lambda_1, \dots, \lambda_l). \quad (5.52)$$

Eq. (5.52) implies that the correlation functions of the fermionic operators defined by  $A_j = \sum_k V_{kj} c_k$  obey

$$\text{tr}(\rho_A A_i^\dagger A_j) = \sum_{kk'} V_{ki}^* \langle c_k^\dagger c_{k'} \rangle V_{k'j} = [V^\dagger D V]_{ij} = \lambda_i \delta_{ij}. \quad (5.53)$$

This in turn implies that  $\rho_A$  is a product state in terms of the modes defined by  $\{A_j\}$

$$\rho_A = \rho_1 \otimes \cdots \otimes \rho_l, \quad (5.54)$$

with  $\rho_i = \text{diag}(\lambda_i, 1 - \lambda_i)$  the mixed-state of mode  $A_i$ . The entropy of this state is given by the sum of entropies of the individual modes

$$S_{\text{vN}}(l, L) = - \sum_{j=1}^l \lambda_j \log_2 \lambda_j + (1 - \lambda_j) \log_2 (1 - \lambda_j). \quad (5.55)$$

Given expression (5.55) we can also easily compute the mutual information  $\mathcal{I}(l_A, l_B)$  between two disjoint subsystems  $A = [m_1, m_2]$ ,  $B = [m_3, m_4]$  of length  $l_A, l_B$  (Eq. (5.5)), which is a useful indicator for the location of the entanglement transition [220]. It is obtained via  $\mathcal{I}(l_A, l_B) = S_{\text{vN}}(l_A, L) + S_{\text{vN}}(l_B, L) - S_{\text{vN}}(A \cup B, L)$ . In addition, we will also consider the square of the correlation functions

$$C(l, \tau) \equiv |D_{l+j,j}(t + \tau, t)|^2 = \langle n_{l+j,t+\tau} \rangle \langle n_{j,t} \rangle - \langle n_{l+j,t+\tau} n_{j,t} \rangle,$$

which is the Fock (exchange) contribution to the density-density correlation in a Gaussian state (we emphasize that the last equality is a result of Wick's theorem and is only true for a Gaussian state).

### 5.3.2 NUMERICAL EVOLUTION OF GAUSSIAN STATE TRAJECTORIES

Here, we provide details of the numerical implementation of the trajectory evolution described in Eqs. (5.38), (5.39). As we explained earlier, for each individual trajectory, the state at time  $t$  is a Gaussian state, which is parametrized by an  $L \times N$  matrix  $U(t)$  as in Eq. (5.45). Let us denote a state parametrized by a specific matrix  $U$  as  $|U\rangle$ .

First let us understand how to perform coherent time-evolution of such a state. Consider the state  $e^{-iHt}|U\rangle$ , where  $H = \sum_{ij} h_{ij} c_i^\dagger c_j$  is a general quadratic Hamiltonian and the hopping matrix  $h$  is hermitian. Denote the modes diagonalizing  $H$  by  $a_i = \sum_l V_{il} c_l$  with single-particle energies  $\epsilon_i$ . Since  $H$  is hermitian,  $V$  is unitary and  $VhV^\dagger$  is diagonal. With the matrix  $V$  at hand we can compute that evolution of a single creation operator

$$\begin{aligned} e^{-iHt} c_j^\dagger e^{iHt} &= \sum_i V_{ij} e^{-iHt} a_i^\dagger e^{iHt} = \sum_i e^{-i\epsilon_i t} V_{ij} a_i^\dagger \\ &= \sum_{ik} V_{ik}^* e^{-i\epsilon_i t} V_{ij} c_k^\dagger = \sum_k c_k^\dagger [e^{-iht}]_{kj}. \end{aligned} \quad (5.56)$$

Using  $e^{-iHt}|0\rangle = |0\rangle$  we can thus write

$$e^{-iHt}|U\rangle = \prod_{l=1}^N \left( \sum_{j,k=1}^L [e^{-iht}]_{kj} U_{jl} c_k^\dagger \right) |0\rangle = |e^{-iht}U\rangle. \quad (5.57)$$

We see that the evolution in Eq. (5.57) describes the physical situation where the single-particle wavefunctions, encoded in the columns of  $U$ , evolve independently from each other, as expected from a non-interacting system. Note that Eq. (5.57) also explicitly shows that a Gaussian pure-state remains Gaussian under time evolution with a quadratic Hamiltonian.

#### SIMULATION OF QSD

To simulate the quantum state diffusion evolution we follow the Trotterization approach used in Ref. [228]. The simplest scheme to integrate Eq. (5.38) is using the Euler method, using a finite time-step  $\delta t$

$$|\psi(t + \delta t)\rangle \approx |\psi(t)\rangle - iH\delta t|\psi(t)\rangle + \sum_l \left( \xi_{l,t} \hat{M}_{l,t} - \frac{\gamma}{2} \hat{M}_{l,t}^2 \delta t \right) |\psi(t)\rangle. \quad (5.58)$$

In order to maintain the Gaussian structure we want to express Eq. (5.58) as matrix exponentials operating on  $|\psi(t)\rangle$ . To this end we note that according to Itô's lemma, for a Wiener process  $\xi_t$  and some operator  $\hat{M}$ , the differential of the exponential function obeys<sup>6</sup>:

$$de^{d\xi_t \hat{M}} = 1 + \hat{M}d\xi_t + \frac{1}{2} \langle d\xi_t^2 \rangle \hat{M}^2 + O(dt^2), \quad (5.59)$$

hence we have

$$|\psi(t + \delta t)\rangle \approx e^{\sum_l (\xi_{l,t} \hat{M}_{l,t} - \gamma \hat{M}_{l,t}^2 \delta t)} e^{-iH\delta t} |\psi(t)\rangle. \quad (5.60)$$

Importantly notice the lack of  $1/2$  factor in the  $\gamma$  term.

<sup>6</sup>This can be understood intuitively from the fact that  $\langle d\xi_t^2 \rangle = O(dt)$  for a Wiener process so it needs to be taken into account when computing the differential.

In terms of the matrix  $U$  we obtain, up to normalization,

$$U(t + \delta t) = M e^{-ih\delta t} U, \quad M \equiv \text{diag}(e^{\xi_{1,t} + \gamma(2\langle n_1 \rangle_t - 1)\delta t}, \dots, e^{\xi_{N,t} + \gamma(2\langle n_N \rangle_t - 1)\delta t}), \quad (5.61)$$

where  $h$  is the hopping matrix, and the densities  $\langle n_l \rangle_t$  are computed from the correlation matrix  $D_{l,l}(t, t)$ . We then ensure that the columns of  $U$  are orthonormal by performing a QR decomposition  $U = QR$  and redefining  $U = Q$ . The applied step size is  $\delta t = 0.05$ .

#### SIMULATION OF QJ EVOLUTION

To simulate the quantum-jump evolution Eq. (5.39), we exploit that particle number conservation enforces a constant jump rate  $\gamma N$  and apply the common jump evolution procedure described in [13]:

1. Determine the jump time  $\tau = -\log(r)/(\gamma N)$  by drawing a random number  $r$  uniformly from  $[0, 1]$ . The time  $\tau$  corresponds to the time at which the norm of the state decayed to  $r$ , that is  $||\psi(t + \tau)\rangle||^2 = r$ .
2. Evolve the state at time step  $t$  to  $t + \tau$  via  $U(t + \tau) = e^{-ih\tau} U(t)$ .
3. Choose a jump operator  $n_j$  according to the probability distribution  $p_j = \langle n_j \rangle_{t+\tau}/N$ .
4. Apply the jump operator to the correlation matrix  $D = U(t + \tau)U^\dagger(t + \tau)$ , according to

$$D_{lm} \rightarrow \begin{cases} 1, & l = m = j \\ 0, & l \neq m \text{ and } (l = j \text{ or } m = j) \\ D_{lm} - \frac{D_{jm}D_{lj}}{\langle n_j \rangle_t}, & \text{otherwise} \end{cases}$$

5. Obtain the new  $U$  matrix by performing an SVD decomposition which, for an hermitian matrix, results in  $D = USU^\dagger$  (note  $S_{11} = \dots = S_{NN} = 1, S_{N+1,N+1} = \dots = S_{LL} = 0$ ).

#### 5.4 ENTANGLEMENT ENTROPY AND PHASE DIAGRAM

For a bipartition of the chain into two equal subsystems, the steady-state entanglement entropy  $\bar{S}_{\text{vN}}(L/2)$  shows three different dependencies on the chain length  $L$  and the monitoring rate  $\gamma$ . This is illustrated in Fig. 5.5(c) for the case of QSD evolution. For the coherent time evolution at  $\gamma = 0$ , an initial Néel state develops an extensive entanglement entropy converging to a volume law [264]. This behavior transcends to weak but non-zero dephasing, where one still observes an extensive entanglement growth  $\bar{S}_{\text{vN}}(L/2) \sim L$  for  $L < L_c(\gamma)$  smaller than a  $\gamma$ -dependent cutoff length.

Around  $L \sim L_c(\gamma)$ , the entanglement entropy smoothly crosses over from an extensive to a subextensive growth  $\bar{S}_{\text{vN}}(L/2) \sim \log L$ . For  $0 < \gamma \leq 0.25$ , this crossover is observed for any sufficiently large system with size  $L > L_c(\gamma)$ . For  $\gamma \rightarrow 0$ ,  $L_c(\gamma) \rightarrow \infty$  diverges, following



roughly a stretched exponential  $L_c(\gamma) \sim \exp[-(\gamma_0/\gamma)^\alpha]$  with  $\alpha \approx 0.6$ <sup>7</sup>. The asymptotic behavior of the entanglement entropy  $\bar{S}_{\text{vN}}(L/2)$  in the limit  $L \rightarrow \infty$  is thus always logarithmic for small  $\gamma$ . In any finite-size system, however, an extensive entanglement entropy is observed once  $L_c(\gamma)$  exceeds the system size, e.g., for  $\gamma < 0.15$  system sizes  $L < L_c(0.15) \approx 35$  appear as if they exhibit volume-law scaling, see the inset of Fig. 5.5(c).

Logarithmic growth of the entanglement entropy is characteristic for  $(1+1)$ -dimensional conformal field theories (CFTs) [265, 266], as we explained in Sec. 5.2.4. In order to better understand the CFT scaling regime we explore the scaling of the trajectory-averaged entanglement-entropy  $\bar{S}_{\text{vN}}(l, L)$  as a function of the subsystem size  $l$  at fixed system size  $L$ . This quantity shows several regimes, as seen for QSD in Fig. 5.8(a) and for QJ in Fig. 5.9.

We find a regime where  $\bar{S}_{\text{vN}}(l, L)$  exhibits a logarithmic dependence similar to a CFT with periodic boundaries

$$\bar{S}_{\text{vN}}(l, L) = \frac{c(\gamma)}{3} \log_2 \left[ \frac{L}{\pi} \sin \left( \frac{\pi l}{L} \right) \right] + s_0(\gamma), \quad (5.62)$$

but with a  $\gamma$ -dependent "central charge"  $c(\gamma)$  and residual entropy  $s_0(\gamma)$ , see Fig. 5.8 (b,c). In thermal equilibrium irrational central charges are unconventional but are found, e.g., in disordered systems [267–269]. However, irrational central charges appear to be characteristic for the critical point of nonequilibrium transitions, including percolation [34, 270] and entanglement transitions both in random circuits and Hamiltonian dynamics [34, 220, 225, 226, 243].

In the case of QSDc evolution the conformal scaling (5.62) is observed for any non-zero monitoring and sufficiently large system sizes  $L > L_c(\gamma)$ , as can be seen from Fig. 5.8(b). The central charge approaches itself a scaling form  $c \sim \gamma^{-\theta}$  with  $\theta \approx 0.7$ , see Fig. 5.5(d). This is comparable to an extended conformal invariance in a non-unitary circuit dynamics with disordered free fermions [224], where it was attributed to the spatio-temporal randomness in the combined unitary and non-unitary dynamics. Here, however, we show that the same phenomenon appears when the unitary evolution is disorder free.

A main finding of our work is that this behavior changes qualitatively in the case of QSD and QJ evolution. For stronger monitoring, e.g.,  $\gamma \approx 0.4$  for  $L = 800$  in Fig. 5.8(b), the central charge experiences a sudden, strong suppression as a function of  $\gamma$ . For finite system sizes it approaches zero exponentially fast in  $\gamma$  and vanishes above a critical value  $\gamma_c(L)$ . The transition is evidenced clearly by several different observations:

1. A qualitative change in the entanglement entropy  $\bar{S}_{\text{vN}}(l, L)$ , showing no subsystem-dependence for  $\gamma \geq 0.6$  in Fig. 5.8(a).
2. The scaling of the effective central charge with  $\gamma$  in Fig. 5.8(b), as well as with the system size  $L$  in Fig. 5.10, which drops to zero for  $\gamma > 0.8$  and  $L \rightarrow \infty$ .
3. The zero-crossing of the residual entropy  $s_0(\gamma)$  at  $\gamma \approx 0.5$  in Fig. 5.8(c).
4. Qualitative changes of the mutual information and the correlation function for  $\gamma \geq 0.5$  shown in Figs. 5.12, 5.14, which we further discuss in Sec. 5.6.

<sup>7</sup>This dependence was estimated by solving  $\frac{c(\gamma)}{3} \log_2(L_c(\gamma)/\pi) + s(\gamma) = 0$  with the scaling behavior for  $s(\gamma)$ ,  $c(\gamma)$  from the simulations.

5 Trajectory dependent entanglement transition in a free fermion chain – from extended criticality to area law

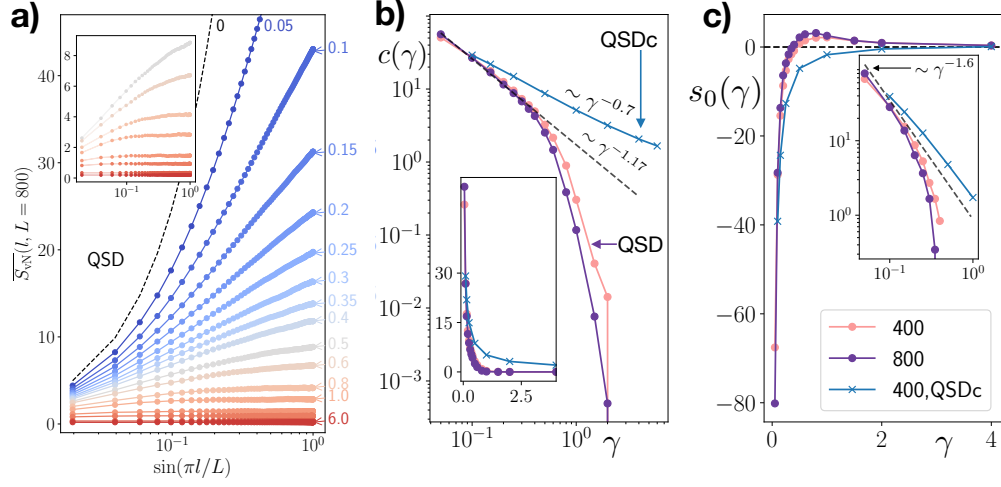


Figure 5.8: (a) The steady-state entanglement entropy as a function of the bipartition size  $l$  in the QSD case. We observe a clear, asymptotic logarithmic growth for slow monitoring and a transition to an area-law for faster monitoring  $\gamma \geq \gamma_c$  (inset). (b,c) The effective central charge and residual entropy obtained by fitting the data to Eq. (5.62). Depending on the trajectory evolution, the logarithmic growth is either cut off at a critical monitoring rate and passes into an area-law regime, or persists up to arbitrarily large  $\gamma$ . The insets show the same data on a linear (d) and logarithmic (e). Results are obtained from averages over 500 trajectories for  $L \geq 600$  and 300 trajectories for  $L = 800$ .

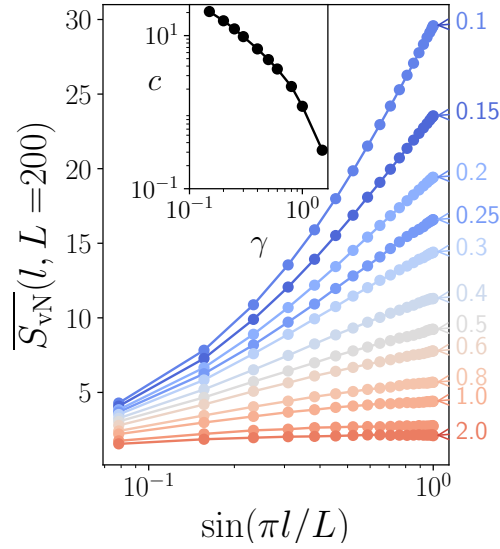


Figure 5.9: The steady-state entanglement entropy as a function of bipartition size  $l$  in the QJ case, for a system of size  $L = 200$ . The inset shows the central charge obtained from a fit to Eq. (5.62). We observe similar behavior to that observed for QSD trajectory evolution.

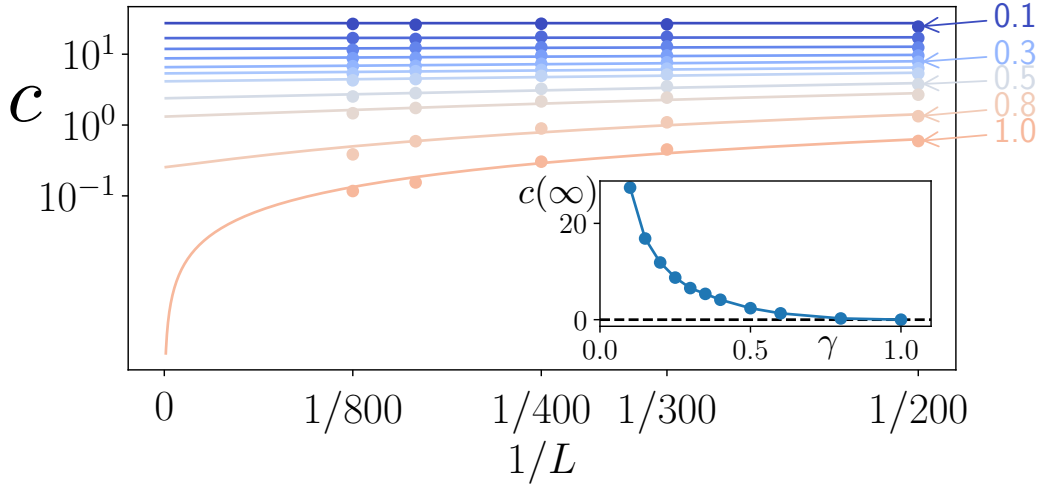


Figure 5.10: Finite size scaling behavior of the effective central-charge obtained from fitting  $\bar{S}_{\text{vN}}(l, L)$  to Eq. (5.62), in the QSD case. Different colors correspond to different values of  $\gamma$  (marked). The curves and the value of  $c(L = \infty)$  (inset) are obtained by minimizing the least-square difference fit between the data and the scaling hypothesis  $c(L) - c(L = \infty) \sim 1/L^{1/\nu}$ , finding a scaling exponent  $\nu = 0.89$ . This confirms a non-zero asymptotic charge  $c > 0$  for  $\gamma \leq 0.8$  and a transition to area law for stronger monitoring.

The precise location of the transition in the thermodynamic limit, however, is hard to determine. We estimate  $\gamma_c(\infty) \approx 0.8$  from the finite size behavior in Fig. 5.10. For stronger monitoring  $\gamma \geq \gamma_c$ , the entanglement entropy follows an area law  $\bar{S}_{\text{vN}}(l, L) = s_0(\gamma)$ , as shown in Fig. 5.8(a, inset) for  $L = 800$ . In the area-law regime the residual entropy  $s_0$  approaches the asymptotic value  $s_0(\gamma \rightarrow \infty) = 0$ . This shows a transition from an extended, supposedly conformally invariant regime to an area law phase for continuously monitored free fermions. Our finding does not contradict earlier work on free fermions, which ruled out a volume law phase at any non-zero monitoring rate but not a subextensive scaling regime [228].

## 5.5 DEVIATING TRAJECTORY ENSEMBLES

All three trajectory evolutions, Eqs. (5.38), (5.39) yield qualitatively similar results for small  $\gamma \leq \gamma_c$ . This includes a subextensive entanglement entropy  $\sim \log L$  for large enough system size and an extensive growth for sufficiently small systems. Only the QSD and QJ evolution exhibit, however, a transition towards an area law phase at larger monitoring rates  $\gamma \geq \gamma_c$ . The QSDc shows no indication of an area law transition and the conformal invariance is extended to arbitrary  $\gamma > 0$ . We conjecture that this is because for  $\gamma \geq \gamma_c$  the nonlinear moments of the correlation matrix start depending significantly on the trajectory evolution and the QSD and QJ evolutions deviate from the QSDc evolution.

This deviation is well illustrated, e.g., by considering the  $m$ -th moment of the norm  $\mathcal{N}(m) \equiv \langle \psi | \psi \rangle^m$ . According to Eqs. (5.38), (5.39) one finds (i)  $\partial_t \mathcal{N}(m) = 0$  for arbitrary  $m$  for the QSD

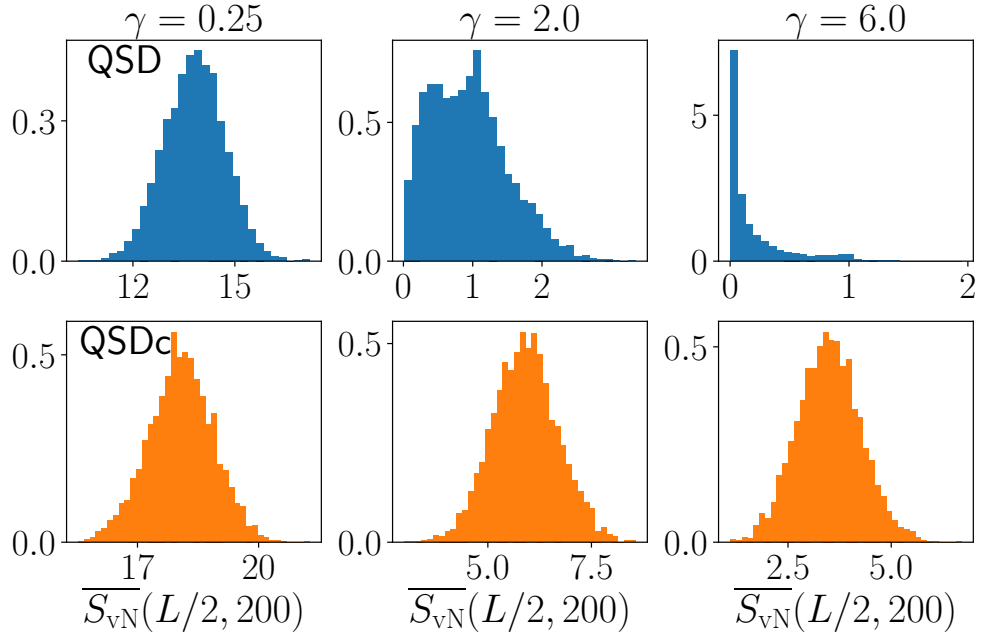


Figure 5.11: The trajectory statistics of the entropy reveal a structural difference between the circuit evolution and QSD when the latter is in the area law regime ( $L = 200$ , 5000 trajectories per histogram)

and QJ evolution but (ii)  $\partial_t \mathcal{N}(m) \sim \gamma m(m-1) L \mathcal{N}(m)$  for the QSDc evolution (see App. 5.A for details). The conservation of all moments  $\mathcal{N}(m)$  reveals the exact probability conservation intrinsic to the QSD and QJ evolutions. It is enforced by a stochastic evolution, which evolves the state orthogonally to its Hilbert space location [240, 242]. The QSDc evolution, however, adds a stochastic component parallel to the state, which leads to a different type of trajectories in Hilbert space. This conserves probability only on average, i.e., it conserves exclusively  $\mathcal{N}(m=1)$ .

We illustrate the difference between QSD and QSDc explicitly by comparing the entanglement entropy distribution for both evolutions in Fig. 5.11. The bins in the histograms reflect the probability for a given entanglement entropy. For weak monitoring, when both types of evolutions predict conformal invariance, both histograms show a distribution with similar mean and variance and which is symmetric around its peak, i.e., both evolutions sample a comparable set of trajectories.

The distribution for the QSDc trajectories remains of similar shape for arbitrarily large monitoring rate and only acquires a smaller mean and variance as  $\gamma$  is increased. The distribution of the QSD trajectories, however, undergoes a structural change when it enters the area law phase. It approaches a strongly asymmetric, bimodal distribution with its main peak approaching zero. A second peak emerges and stays pinned at  $S_{\text{vN}} = 1$ , indicating a pronounced probability for a single non-zero eigenvalue  $\lambda = 0.5$  in Eq. (5.62). In this regime, both distributions deviate structurally from each other, confirming again that QSD and QSDc yield significantly different dynamics for objects with a nonlinear state dependence.

## 5.6 MUTUAL INFORMATION AND CORRELATION FUNCTIONS

In order to verify the extended regime of conformal invariance and an area law transition at non-zero monitoring rate, we investigate several additional indicators, (i) the behavior of the mutual information  $\mathcal{I}(l_A, l_B)$  between two disjoint intervals A, B, (ii) the equal-time correlation function  $\overline{C}(l, 0)$  between two sites at distance  $l$  and (iii) the local auto-correlation function  $\overline{C}(0, \tau)$ .

The mutual information for two disjoint intervals  $l_A = l_B = L/8$ , with centers at a distance  $r_{AB} = L/2$ , is expected to show a sharp peak at the critical point separating the area and the volume law phase [220]. Inspecting  $\mathcal{I}(l_A = l_B = L/8, r_{AB} = L/2)$  for different system sizes in Fig. 5.12(a) shows that it is significantly larger than zero in the entire critical regime and approaches zero rapidly in the area law phase, reflecting extended criticality. A similar peak is observed for the QJ evolution in Fig. 5.12(b). On the other hand in the QSDc case we observe finite value of  $\mathcal{I}$  even at strong  $\gamma$ , where  $\mathcal{I}$  shows slow power-law like decay as a function of  $\gamma$ , as can be seen in Fig. 5.12(c)

To further confirm the CFT behavior, it is useful to consider the mutual-information for variable subinterval sizes and locations. Consider the mutual-information of two subintervals  $A = [m_1, m_2]$ ,  $B = [m_3, m_4]$  which we define  $\mathcal{I}(m_1, m_2, m_3, m_4)$ . This quantity can be connected to a four-point correlation function of the “twist-fields” in the Cardy-Calabrese formalism [226, 259]. In a CFT the four-point function of primary-fields is expected to depend only on the cross ratio  $\eta = \frac{m_{12}m_{34}}{m_{13}m_{24}}$ , where for a periodic-boundary condition geometry we have  $m_{\alpha\beta} = \sin(\pi|m_\alpha - m_\beta|/L)$  [258]. Hence, in the CFT regime we expect  $\mathcal{I}(m_1, m_2, m_3, m_4) = \mathcal{I}(\eta)$  [220].

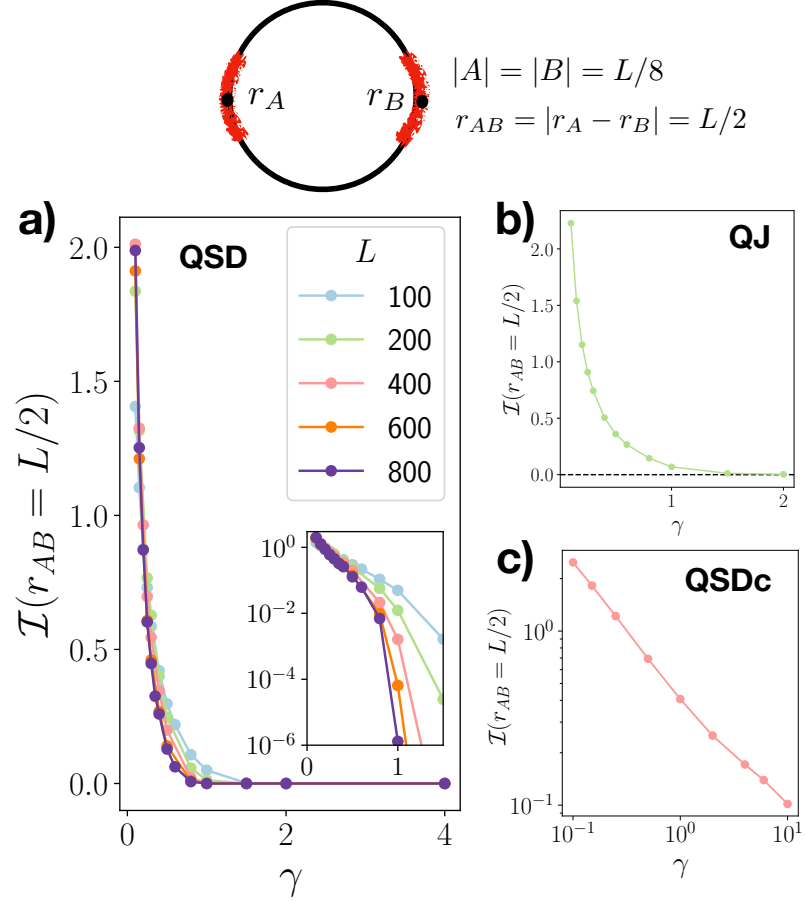


Figure 5.12: Signature of the conformal invariance at weak monitoring in the mutual-information between two subintervals of length  $|A| = |B| = L/8$  whose centers are distance  $r_{AB} = L/2$  from each other. For small  $\gamma$  we observe a non-vanishing value of  $\mathcal{I}(r_{AB} = L/2)$ . In the case of (a) QSD and (b) QJ evolution the mutual-information rapidly decays to zero for  $\gamma > \gamma_c$ , while it always remains with a finite value in the case of QSDc (c) evolution, exhibiting slow power-law decay with  $\gamma$ .

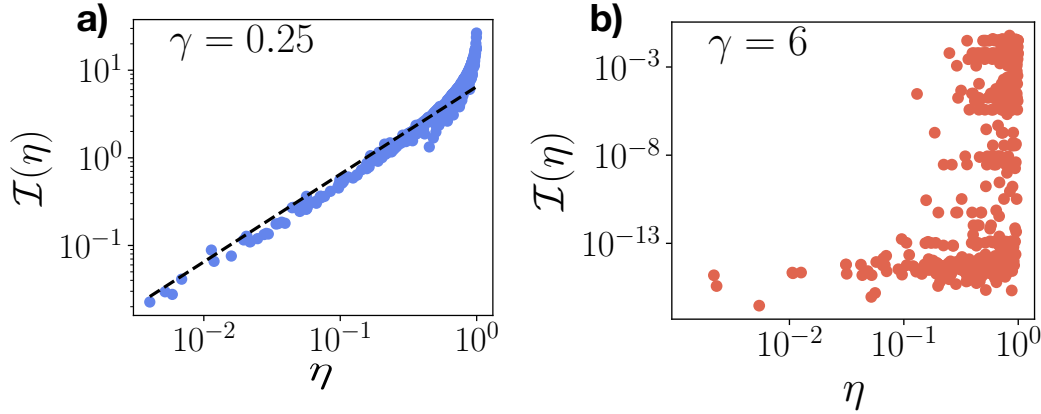


Figure 5.13: CFT signature in the dependence of the mutual-information between  $A = [m_1, m_2]$ ,  $B = [m_3, m_4]$  on the ratio  $\eta = (m_{12}m_{34})/(m_{13}m_{24})$ , where  $m_{\alpha\beta} = \sin(\pi|m_\alpha - m_\beta|/L)$ . Computed for the QSD case with  $L = 400$ . (a) For weak dephasing a scaling collapse of the mutual information as a function of the cross ratio  $\eta$  is observed, indicating the scaling behavior expected for a CFT  $\mathcal{I}(\eta) \sim \eta$ . (b) In the area law regime no collapse is observed.

The expected CFT scaling behavior of  $\mathcal{I}$  is confirmed in Fig. 5.13(a). For weak dephasing in the conformally invariant regime, the mutual information  $\mathcal{I}(\eta)$  collapses onto a single line for all  $\eta$ , with a linear increase  $\sim \eta$  for small cross ratios. The linear dependence in  $\eta$  also implies a power-law decay of the mutual-information  $\mathcal{I} \sim r_{AB}^{-2}$  for small subsystems with large separation [220]. This collapse is a strong indication of conformal invariance and can be observed throughout the entire logarithmic regime. It can be contrasted with the behavior in the area law phase, shown in Fig. 5.13(b), where no collapse is observed.

As we have seen in Sec. 5.2.4, in a CFT two-point correlation functions are expected to exhibit power-law behavior. Hence, we examine the trajectory average of the equal-time correlation functions  $\overline{C}(l, 0) = \mathbb{E}_i[\langle |c_{i+l}^\dagger c_i|^2 \rangle]$  (in addition to trajectory averaging, we also average over position  $i$  to reduce statistical noise). The behavior of  $\overline{C}(l, 0)$ , shown in Fig. 5.14 for different values of  $\gamma$ , quantitatively reflect the phase diagram in Fig. 5.5(b). In the conformally invariant regime, i.e., for  $0 < \gamma \leq \gamma_c$ , two distinct scaling forms are observed depending on whether  $l$  is larger or smaller than  $L_c(\gamma)$ . For  $l > L_c(\gamma)$ , where the entanglement entropy grows logarithmically, an algebraic decay of the correlation function with the square of the distance  $\sim [\sin(\pi l/L)]^{-2}$  is observed. The collapse of the correlation functions for variable system sizes in the inset of Fig. 5.14 demonstrates that this  $\sim [\sin(\pi l/L)]^{-2}$  scaling is observed in the thermodynamic limit  $L \rightarrow \infty$ . On distances  $l < L_c(\gamma)$  the correlations decay significantly slower, well approximated by a  $\sim l^{-1}$  decay. This can be rationalized with the assumption that the extensive growth reflects an evolution in which sites are entangled up to distances  $l \sim L_c(\gamma)$ .

When crossing the transition to the area law regime, the correlations start to decay more rapidly with the distance  $l$  between different sites. In this regime, a heuristic fit  $\overline{C}(l, 0) \sim l^{-5} \exp(-l/l_0)$  yields an increased algebraic decay on short distances compared to the conformally invariant scenario. At larger distances  $l > l_0$ , the correlations drop to zero exponentially, reflecting short-ranged correlations.

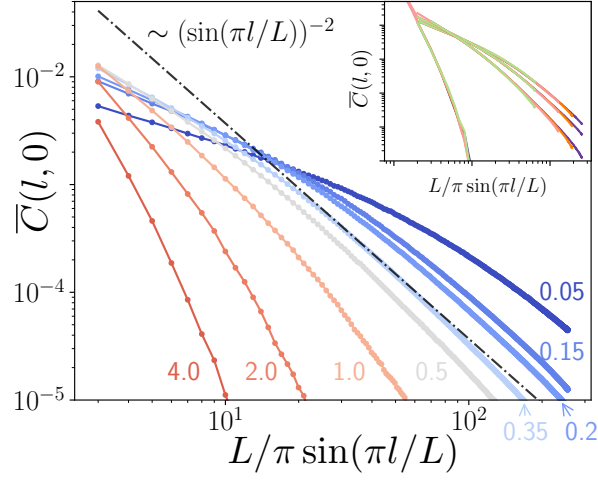


Figure 5.14: Trajectory and position averaged equal-time correlations  $\bar{C}(l, 0) \equiv \mathbb{E}_i[\overline{|\langle c_{i+l}^\dagger c_i \rangle|^2}]$ , computed for  $L=800$  for QSD evolution. The different curves correspond to different values of  $\gamma$  (marked).  $\bar{C}(l, 0)$  decays algebraically  $\sim \sin(\pi l/L)^{-2}$  with the distance  $l$  in the conformally invariant regime, while a rapid exponential decay is observed in the area-law regime. The inset shows a data collapse for different system sizes  $L = 200, 400, 600, 800$  (axes range identical to main plot)

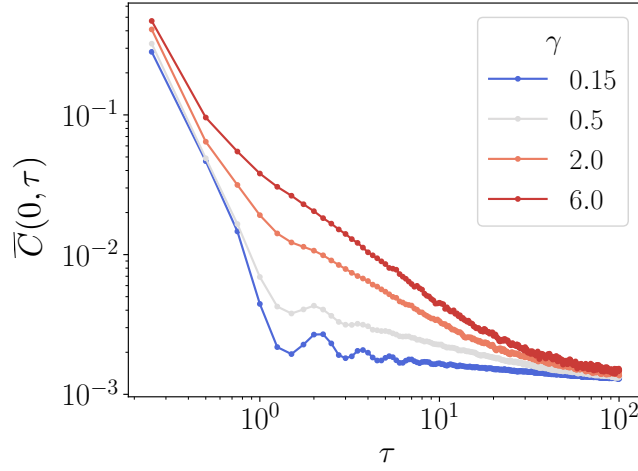


Figure 5.15: Autocorrelation function  $\bar{C}(0, \tau) \equiv \mathbb{E}_i[\overline{|\langle c_i^\dagger(t+\tau)c_i(t) \rangle|^2}]$ , computed in the steady-state regime with  $L = 600$ . In the area-law regime with strong dephasing we observe a quantum-Zeno like regime with slow-relaxation of  $\bar{C}(0, \tau)$ .



Further information on the dynamics can be inferred from the autocorrelation function  $\overline{C}(0, \tau) \equiv \mathbb{E}_i[|\langle c_i^\dagger(t + \tau)c_i(t) \rangle|^2]$  computed in the steady-state regime. For unitary, free fermions it can be shown that they are given by the Bessel function  $\overline{C}(0, \tau) \sim J_0^2(\tau)$ , describing damped oscillations with an envelope decaying as  $\tau^{-1}$ . While damping of the oscillations increases with  $\gamma$ , the overall decay of the auto-correlations slows down. When entering the area law regime, the oscillations become over-damped and the auto-correlation time is enhanced significantly, indicating a slowly evolving, quantum-Zeno regime, see Fig. 5.15.

## 5.7 DISCUSSION

Let us now turn to a summary of the results obtained in this chapter, and provide some outlook. We considered a model of free-fermions hopping on a 1d chain in the presence of continuous dephasing noise, and studied the dynamics of the trajectory averaged entanglement as a function of the dephasing strength for several types of trajectory evolution. We find that at weak enough dephasing the steady-state value of  $\bar{S}_{\text{vN}}$  exhibits logarithmic scaling with the subsystem size, similar to the behavior of  $(1+1)$ -dimensional CFTs. In all three protocols we considered, we observe that the effective central-charge is continuously decreasing with the dephasing strength. The CFT behavior is also exhibited in the algebraic decay of the trajectory averaged connected density-density correlation function, and in the behavior of the bipartite mutual-information.

In the case of QSD and QJ evolution we also find a transition to an area-law regime at a critical dephasing rate, where the effective central-charge vanishes. This is not the case with the QSDc evolution where the system seems to always remain in the CFT regime. A main difference between the QSDc protocol and the QSD and QJ unravellings is that under QSDc evolution probability is not exactly conserved. We conjecture that this is a possible reason for the absence of phase transition to an area-law phase in the QSDc evolution. We also observe a difference in the full distribution of entanglement entropies, where in the QSDc case the distribution is always Gaussian, as opposed to a bi-modal distribution which is observed in the QSD case in the area-law phase. In the future, it would be interesting to further explore the connection between the entanglement transition observed here and the properties of the full distribution of trajectory-states induced by the specific measurement protocol. In any case, our results emphasize that, when considering trajectory entanglement transitions, different measurement protocols may lead to qualitatively different results.

Let us comment on the relation of our work to an earlier work by Cao et al. [228] which investigated the same model we considered here. There, the authors used the generalized-hydrodynamics formalism, developed for closed integrable systems, in order to derive an analytic formula for  $\bar{S}_{\text{vN}}(\ell, L)$ , under certain approximations and using a certain ansatz. From their analysis, Cao et al. reach the conclusion that for free integrable systems an area-law is expected for any non-vanishing dephasing rate. However, we claim that our result is not in contradiction. First, the analytical result obtained in [228] is only valid when  $\ell \ll L$ , while we examine all possible values of  $\ell$  and are interested in the case  $\ell = L/2$ . Second, the numerical results in [228] exclude volume-law behavior but do not exclude sub-linear scaling.

As we explained in Sec. 5.2.2, it was pointed out in [215] that the scrambling property of generic random-unitaries is a key ingredient for the stability of the volume-law phase observed in studies of

RUC dynamics. In this respect it is maybe not surprising that we did not find a volume-law in our nearest-neighbor free-fermion model, since the unitary free-fermion dynamics are integrable. Our work shows however that critical behavior of  $\bar{S}_{vN}$  can be obtained also in non chaotic dynamics. This observation is further substantiated by two works which appeared in parallel to ours, which considered different types of *free* random-unitary circuit evolution and observed CFT like behavior of  $\bar{S}_{vN}$  [226, 243]. This brings the question: what is the alternative mechanism protecting the entanglement in the critical CFT phase against the effect of measurements?

Let us also further comment that it is not yet completely clear that a transition from volume-law to area-law phase is impossible to realize in free-fermion systems. Indeed, our initial explorations indicate that by considering long range hoppings with long enough range, it is possible to obtain a volume-law phase also in the case of free-fermion evolution. So far, we did not find a setting where a volume- to area-law transition could be observed, but we believe it might be possible and definitely merits further investigation. In general it will be interesting to investigate what are the different trajectory entanglement phases which could be observed in general free-fermion models with different symmetries. For example one could consider the case where charge is not conserved, in which case we can still describe the system by a Gaussian state using the basis of Majorana fermions.

Another question which could be explored in future work regards the critical properties of the transition from the area-law phase to the CFT phase. We note that the scenario we observe here is similar to the Kosterlitz-Thouless (KT) scenario of an extensive critical regime, which might provide some hints when trying to build a simplified phenomenological theory of the trajectory entanglement transition. The KT transition is notoriously difficult to study numerically, due to the exponential divergence of the correlation length. Here recent suggestions for studying free-fermion Gaussian states using tensor-networks [271, 272] might be of help, as they allow studying systems of considerably larger sizes than those reachable with the numerical approach we used in this chapter.

Finally it will be interesting to explore the fate of the CFT phase in the presence of weak interactions. One possibility of doing so numerically is using MPS techniques for simulating the trajectory evolution, this should allow describing states with logarithmic entanglement up to a reasonable system size. However, here we have to caution that in the free case we observed volume-law scaling of  $\bar{S}_{vN}$  at system sizes up to  $L \approx 50$  for weak dephasing, and the asymptotic CFT regime appeared only for larger system sizes. A different possible route would be to use a mean-field like approach projecting the state of the interacting system onto a Gaussian state which evolves under an effective non-linear Hamiltonian. Finding such an effective non-linear model which can capture some properties of the volume- to area-law trajectory entanglement transition is an interesting direction for future work.

## APPENDICES TO CHAPTER 5

## 5.A HIGHER MOMENT EVOLUTION

Observables, which depend on higher moments of the state  $|\psi_t\rangle\langle\psi_t|$  may strongly depend on the specific trajectory evolution. An example is the entanglement entropy in the main text. In this appendix we illustrate this with a simple analytical example, the  $m$ -th moment of the norm  $\langle\psi_t|\psi_t\rangle^m$ . We start with the QSD evolution (5.38) and, for simplicity, a single, hermitian Lindblad operator  $\hat{M}$ . The scaling  $\xi_t \sim \sqrt{dt}$  requires that infinitesimal changes are taken into account up to order  $dt^2$ . Up to this order, the infinitesimal change is

$$\begin{aligned} d\langle\psi_t|\psi_t\rangle^m &= m\langle\psi_t|\psi_t\rangle^{m-1}(\langle\psi_t|d\psi_t\rangle + \langle d\psi_t|\psi_t\rangle + \langle d\psi_t|d\psi_t\rangle) \\ &\quad + m(m-1)\langle\psi_t|\psi_t\rangle^{m-2}(\langle d\psi_t|\psi_t\rangle + \langle\psi_t|d\psi_t\rangle)^2. \end{aligned} \quad (5.63)$$

The Hamiltonian evolution cancels out and expanding again up to order  $dt$  one finds

$$\begin{aligned} d\langle\psi_t|\psi_t\rangle^m &= m\langle\psi_t|\psi_t\rangle^{m-1}\left[(\xi^2 - \gamma dt)\langle\psi_t|\hat{M}^2|\psi_t\rangle + \xi\langle\psi_t|\hat{M}|\psi_t\rangle\right] \\ &\quad + 2m(m-1)\langle\psi_t|\psi_t\rangle^{m-2}\xi^2\langle\psi_t|\hat{M}|\psi_t\rangle^2. \end{aligned} \quad (5.64)$$

The trajectory average thus yields

$$\overline{d\langle\psi_t|\psi_t\rangle^m} = 2\gamma m(m-1)\overline{\langle\psi_t|\psi_t\rangle^m\langle\hat{M}\rangle_t^2}dt, \quad (5.65)$$

where  $\langle\hat{M}\rangle_t = \langle\psi_t|\hat{M}|\psi_t\rangle/\langle\psi_t|\psi_t\rangle$ . For the first moment,  $m = 1$ , the term on the right always vanishes, enforcing that the trajectory averaged norm is constant. Higher moments, however, generally do not vanish and their evolution depends on the operator  $\hat{M}$ . For QSDc,  $\hat{M} = n$  is the particle number operator, and one observes in general an exponential growth of the higher moments with an approximate rate  $2\gamma m(m-1)\langle n\rangle^2$ . For QSD, however,  $\hat{M} = n - \langle n\rangle_t$  such that  $\langle\hat{M}\rangle_t = 0$  for any state and thus any moment  $m$  of the norm remains constant over time.

The norms in the QJ evolution are more involved because here  $\xi^2 = \xi \sim dt$  and thus arbitrarily high powers in  $\xi$  contribute to the evolution of  $\langle\psi_t|\psi_t\rangle^m$ . We restrict ourselves to  $m = 1, 2$  and denote  $\hat{M} = \left(\frac{n}{\sqrt{\langle n\rangle}} - 1\right)$ . This yields

$$d\langle\psi_t|\psi_t\rangle = \xi\langle\psi_t|\hat{M}^2 + 2\hat{M}|\psi_t\rangle = 0, \quad (5.66)$$

$$d\langle\psi_t|\psi_t\rangle^2 = \xi\langle\psi_t|\psi_t\rangle\left[\langle\hat{M}\rangle^2 + 4\langle\hat{M}\rangle\langle\hat{M}^2\rangle + \langle\hat{M}^2\rangle^2\right] = 0. \quad (5.67)$$

Here, only the property  $\xi^2 = \xi$  was exploited and no trajectory average was required to show that the evolution is constant for this type of jump operator.

This example can be easily generalized to multiple jump operators  $\hat{M}$  and demonstrates that in QSD and QJ trajectories all higher moments of the norm remain constant over time up to order  $dt^2$  and an initially normalized state remains normalized. For QSDc on the other hand, higher

### *5 Trajectory dependent entanglement transition in a free fermion chain – from extended criticality to area law*

moments  $m > 1$  grow roughly exponentially in time, demonstrating that only the average norm of the state is conserved while its variance is blowing up.

We emphasize that the difference between the different trajectory evolutions is not just a matter of normalization: the additional parallel evolution in QSDc yields trajectories, which explore a different Hilbert space than the trajectories from QSD and QJ. This difference is not resolved by an adhoc normalization of the state after each numerical time step [240].

# 6 CONCLUSIONS AND OUTLOOK

In this thesis we investigated a variety of different phenomena occurring in open many-body quantum systems, whose dynamics are described by a Markovian Lindblad quantum master equation. This is an exciting and emergent interdisciplinary field combining ideas and theoretical tools from both AMO and condensed-matter. It is becoming increasingly more relevant with the advent of synthetic quantum matter systems which are being used in labs around the world as quantum-simulators and for development of quantum computers.

In chapter 3 we explored the many-body physics of coherently pumped bosons in the vicinity of a scattering resonance, a setup which might be of relevance to the experimental platform of Rydberg-polaritons, among others. We have uncovered a rich phase diagram including a molecule condensate and an atom condensate phase, and provided an initial exploration of the phase transition between those different condensates. This work can serve as a basis of more detailed explorations using semi-classical stochastic Gross-Pitaevskii equations or 2PI formalism to study the dynamical behavior, or RG techniques to study the phase transition. In addition it will be interesting to study the regime of weak pumping and losses where interactions might lead to thermalization, allowing an effective Gibbs state description.

In chapter 4 we explored the fate of the many-body localization transition in a driven-open system. As opposed to the common belief that a coupling to an external bath destroys any MBL signatures, we have shown that it is possible to extract a sharp signature of the transition, by studying the response of local temperature fluctuations to a weak coupling to non-equilibrium baths. Using this scheme, we were able to observe the divergence of the dynamical exponent when approaching the transition from the ergodic side, providing further evidence to the existence of a Griffith regime. Our work suggests a new numerical scalable approach for studying the MBL transition. As a future direction it will be very exciting to use our method in order to study the MBL transition in two-dimensions.

In chapter 5 we studied the dynamics of the entanglement-entropy in a model of free-fermions in the presence of dephasing noise. This study was motivated by recent works which found a phase transition between a volume-law entanglement phase and an area-law entanglement phase, in systems evolving under random-unitary circuits in the presence of measurements. In the free-fermion model we find a phase transition of a new type between an area-law phase and a phase with logarithmic entanglement scaling, exhibiting behavior similar to conformal field theories in  $1 + 1$  dimensions. This work suggests many future directions, such as a classification of all possible entanglement phases of different free-fermion models in the presence of measurements, or studying the stability of the CFT phase to weak integrability breaking terms.

Now, we have finally reached the end of our journey in the land of open quantum many-body systems. Hopefully it was an enjoyable one for you, or at the very least provided something useful to think about. Of course, this is not the end but really only the beginning. We hope that the

work presented in this thesis can provide the starting point for several other journeys into the non-equilibrium quantum physics frontier.

## BIBLIOGRAPHY

- [1] Immanuel Bloch, Jean Dalibard, and Wilhelm Zwerger. Many-body physics with ultracold gases. *Reviews of Modern Physics*, 80(3):885–964, 2008.
- [2] R. Blatt and C. F. Roos. Quantum simulations with trapped ions. *Nature Physics*, 8(4):277–284, apr 2012.
- [3] Helmut Ritsch, Peter Domokos, Ferdinand Brennecke, and Tilman Esslinger. Cold atoms in cavity-generated dynamical optical potentials. *Reviews of Modern Physics*, 85(2):553–601, apr 2013.
- [4] Iacopo Carusotto, Andrew A Houck, Alicia J Kollár, Pedram Roushan, David I Schuster, and Jonathan Simon. Photonic materials in circuit quantum electrodynamics, 2020.
- [5] Hannes Bernien, Sylvain Schwartz, Alexander Keesling, Harry Levine, Ahmed Omran, Hannes Pichler, Soonwon Choi, Alexander S. Zibrov, Manuel Endres, Markus Greiner, Vladan Vuletić, and Mikhail D. Lukin. Probing many-body dynamics on a 51-atom quantum simulator. *Nature*, jul 2017.
- [6] J. Zhang, G. Pagano, P. W. Hess, A. Kyprianidis, P. Becker, H. Kaplan, A. V. Gorshkov, Z.-X. Gong, and C. Monroe. Observation of a many-body dynamical phase transition with a 53-qubit quantum simulator. *Nature*, 551(7682):601–604, nov 2017.
- [7] Frank Arute, Kunal Arya, Ryan Babbush, Dave Bacon, Joseph C. Bardin, Rami Barends, Rupak Biswas, Sergio Boixo, Fernando G. S. L. Brandao, David A. Buell, Brian Burkett, Yu Chen, Zijun Chen, Ben Chiaro, Roberto Collins, William Courtney, Andrew Dunsworth, Edward Farhi, Brooks Foxen, Austin Fowler, Craig Gidney, Marissa Giustina, Rob Graff, Keith Guerin, Steve Habegger, Matthew P. Harrigan, Michael J. Hartmann, Alan Ho, Markus Hoffmann, Trent Huang, Travis S. Humble, Sergei V. Isakov, Evan Jeffrey, Zhang Jiang, Dvir Kafri, Kostyantyn Kechedzhi, Julian Kelly, Paul V. Klimov, Sergey Knysh, Alexander Korotkov, Fedor Kostritsa, David Landhuis, Mike Lindmark, Erik Lucero, Dmitry Lyakh, Salvatore Mandrà, Jarrod R. McClean, Matthew McEwen, Anthony Megrant, Xiao Mi, Kristel Michielsen, Masoud Mohseni, Josh Mutus, Ofer Naaman, Matthew Neeley, Charles Neill, Murphy Yuezhen Niu, Eric Ostby, Andre Petukhov, John C. Platt, Chris Quintana, Eleanor G. Rieffel, Pedram Roushan, Nicholas C. Rubin, Daniel Sank, Kevin J. Satzinger, Vadim Smelyanskiy, Kevin J. Sung, Matthew D. Trevithick, Amit Vainsencher, Benjamin Villalonga, Theodore White, Z. Jamie Yao, Ping Yeh, Adam Zalcman, Hartmut Neven, and John M. Martinis. Quantum supremacy using a programmable superconducting processor. *Nature*, 574(7779):505–510, oct 2019.

- [8] Petar Jurcevic, Ali Javadi-Abhari, Lev S. Bishop, Isaac Lauer, Daniela F. Bogorin, Markus Brink, Lauren Capelluto, Oktay Günlük, Toshinaro Itoko, Naoki Kanazawa, Abhinav Kandala, George A. Keefe, Kevin Kruslich, William Landers, Eric P. Lewandowski, Douglas T. McClure, Giacomo Nannicini, Adinath Narasgond, Hasan M. Nayfeh, Emily Pritchett, Mary Beth Rothwell, Srikanth Srinivasan, Neereja Sundaresan, Cindy Wang, Ken X. Wei, Christopher J. Wood, Jeng-Bang Yau, Eric J. Zhang, Oliver E. Dial, Jerry M. Chow, and Jay M. Gambetta. Demonstration of quantum volume 64 on a superconducting quantum computing system. *64*:1–7, 2020.
- [9] Google AI Quantum and Collaborators. Hartree-Fock on a superconducting qubit quantum computer. *Science (New York, N.Y.)*, 369(6507):1084–1089, 2020.
- [10] S. Debnath, N. M. Linke, C. Figgatt, K. A. Landsman, K. Wright, and C. Monroe. Demonstration of a small programmable quantum computer with atomic qubits. *Nature*, 536(7614):63–66, aug 2016.
- [11] Heinz Peter Breuer and Francesco Petruccione. *The Theory of Open Quantum Systems*. 2007.
- [12] Crispin Gardiner and Peter Zoller. *Quantum noise: a handbook of Markovian and non-Markovian quantum stochastic methods with applications to quantum optics*, volume 56. Springer Science & Business Media, 2004.
- [13] Andrew J. Daley. Quantum trajectories and open many-body quantum systems. *Advances in Physics*, 63(2):77–149, Mar 2014.
- [14] S. Diehl, A. Micheli, A. Kantian, B. Kraus, H. P. Büchler, and P. Zoller. Quantum states and phases in driven open quantum systems with cold atoms. *Nature Physics*, 2008.
- [15] Frank Verstraete, Michael M. Wolf, and J. Ignacio Cirac. Quantum computation and quantum-state engineering driven by dissipation. *Nature Physics*, 2009.
- [16] Markus Müller, Sebastian Diehl, Guido Pupillo, and Peter Zoller. Engineered open systems and quantum simulations with atoms and ions. In *Advances in Atomic, Molecular, and Optical Physics*, volume 61, pages 1–80. Elsevier, 2012.
- [17] L M Sieberer, M Buchhold, and S Diehl. Keldysh field theory for driven open quantum systems. *Reports on Progress in Physics*, 79(9):096001, 2016.
- [18] L M Sieberer, S D Huber, E Altman, and S Diehl. Non-equilibrium Functional Renormalization for Driven-Dissipative Bose-Einstein Condensation. *Physical Review B*, 2014.
- [19] Jamir Marino and Sebastian Diehl. Quantum dynamical field theory for nonequilibrium phase transitions in driven open systems. *Physical Review B*, 94(8):085150, aug 2016.
- [20] Jeremy T. Young, Alexey V. Gorshkov, Michael Foss-Feig, and Mohammad F. Maghrebi. Non-equilibrium fixed points of coupled Ising models. pages 1–33, 2019.



- [21] Wim Casteels, Rosario Fazio, and Christiano Ciuti. Critical dynamical properties of a first-order dissipative phase transition. *Physical Review A*, 95(1):012128, 2017.
- [22] Thomas Fink, Anne Schade, Sven Höfling, Christian Schneider, and Ataç Imamoglu. Signatures of a dissipative phase transition in photon correlation measurements. *Nature Physics*, 14(4):365–369, 2018.
- [23] Fabrizio Minganti, Alberto Biella, Nicola Bartolo, and Cristiano Ciuti. Spectral theory of liouvillians for dissipative phase transitions. *Physical Review A*, 98(4):042118, 2018.
- [24] Luca D’Alessio, Yariv Kafri, Anatoli Polkovnikov, and Marcos Rigol. From quantum chaos and eigenstate thermalization to statistical mechanics and thermodynamics, 2016.
- [25] D. M. Basko, I. L. Aleiner, and B. L. Altshuler. Metal-insulator transition in a weakly interacting many-electron system with localized single-particle states. *Annals of Physics*, 321(2006):900–904, jun 2005.
- [26] Dmitry A. Abanin, Ehud Altman, Immanuel Bloch, and Maksym Serbyn. Colloquium: Many-body localization, thermalization, and entanglement. *Rev. Mod. Phys.*, 91:021001, May 2019.
- [27] Arijeet Pal and David A. Huse. Many-body localization phase transition. *Physical Review B*, 82(17):174411, nov 2010.
- [28] Ronen Vosk, David A. Huse, and Ehud Altman. Theory of the many-body localization transition in one-dimensional systems. *Phys. Rev. X*, 5:031032, Sep 2015.
- [29] Pasquale Calabrese and John Cardy. Evolution of entanglement entropy in one-dimensional systems. *Journal of Statistical Mechanics: Theory and Experiment*, (4):15–38, 2005.
- [30] Hyungwon Kim and David A Huse. Ballistic spreading of entanglement in a diffusive nonintegrable system. *Physical Review Letters*, 111(12):1–5, 2013.
- [31] Adam Nahum, Jonathan Ruhman, Sagar Vijay, and Jeongwan Haah. Quantum entanglement growth under random unitary dynamics. *Phys. Rev. X*, 7:031016, Jul 2017.
- [32] Guifré Vidal. Efficient Simulation of One-Dimensional Quantum Many-Body Systems. *Physical Review Letters*, 93(4):040502, jul 2004.
- [33] Ulrich Schollwoeck. The density-matrix renormalization group in the age of matrix product states. *Annals of Physics*, 326:96–192, aug 2010.
- [34] Brian Skinner, Jonathan Ruhman, and Adam Nahum. Measurement-induced phase transitions in the dynamics of entanglement. *Phys. Rev. X*, 9:031009, Jul 2019.
- [35] Yaodong Li, Xiao Chen, and Matthew P. A. Fisher. Quantum zeno effect and the many-body entanglement transition. *Phys. Rev. B*, 98:205136, Nov 2018.

- [36] Yimu Bao, Soonwon Choi, and Ehud Altman. Theory of the phase transition in random unitary circuits with measurements. *Physical Review B*, 101(10), Mar 2020.
- [37] Aidan Zabalo, Michael J. Gullans, Justin H. Wilson, Sarang Gopalakrishnan, David A. Huse, and J. H. Pixley. Critical properties of the measurement-induced transition in random quantum circuits. *Phys. Rev. B*, 101:060301, Feb 2020.
- [38] Ofer Firstenberg, Thibault Peyronel, Qi-Yu Liang, Alexey V. Gorshkov, Mikhail D. Lukin, and Vladan Vuletić. Attractive photons in a quantum nonlinear medium. *Nature*, 502(7469):71–75, sep 2013.
- [39] P. Bienias, S. Choi, O. Firstenberg, M. F. Maghrebi, M. Gullans, M. D. Lukin, A. V. Gorshkov, and H. P. Büchler. Scattering resonances and bound states for strongly interacting Rydberg polaritons. *Physical Review A - Atomic, Molecular, and Optical Physics*, 2014.
- [40] M J Gullans, S Diehl, S T Rittenhouse, B P Ruzic, J. P. D’Incao, P Julienne, A V Gorshkov, and J M Taylor. Efimov States of Strongly Interacting Photons. *Physical Review Letters*, 119(23), 2017.
- [41] Leo Radzihovsky, Jae Park, and Peter B. Weichman. Superfluid transitions in bosonic atom molecules mixture near a Feshbach Resonance. *Physical Review Letters*, 92:160402, 2004.
- [42] M W J Romans, R A Duine, Subir Sachdev, and H T C Stoof. Quantum Phase Transition in an Atomic Bose Gas with a Feshbach Resonance. *Physical Review Letters*, 93(2):020405, 2004.
- [43] Claude Cohen-Tannoudji, Jacques Dupont-Roc, and Gilbert Grynberg. *Atom-photon interactions: basic processes and applications*. 1998.
- [44] Alex Kamenev. *Field theory of non-equilibrium systems*. Cambridge University Press, 2011.
- [45] Michael E. Peskin and Daniel V. Schroeder. *An Introduction to quantum field theory*. Addison-Wesley, Reading, USA, 1995.
- [46] Alexander Altland and Ben D Simons. *Condensed matter field theory*. Cambridge university press, 2010.
- [47] Emanuele G. Dalla Torre, Sebastian Diehl, Mikhail D. Lukin, Subir Sachdev, and Philipp Strack. Keldysh approach for nonequilibrium phase transitions in quantum optics: Beyond the Dicke model in optical cavities. *Physical Review A - Atomic, Molecular, and Optical Physics*, 87(2), feb 2013.
- [48] Mehrtash Babadi, Eugene Demler, and Michael Knap. Far-from-equilibrium field theory of many-body quantum spin systems: Prethermalization and relaxation of spin spiral states in three dimensions. *Phys. Rev. X*, 5:041005, Oct 2015.
- [49] Steven Weinberg. *The quantum theory of fields*, volume 2. Cambridge university press, 1995.

- [50] Esteban Calzetta and Bei-Lok Hu. Nonequilibrium quantum fields: Closed-time-path effective action, wigner function, and boltzmann equation. *Physical Review D*, 37(10):2878, 1988.
- [51] John Negele and Henry Orland. *Quantum Many-particle Systems*. CRC Press, 1998.
- [52] Cheng Chin, Rudolf Grimm, Paul Julienne, and Eite Tiesinga. Feshbach resonances in ultracold gases. *Reviews of Modern Physics*, 82(2):1225–1286, 2010.
- [53] Christian Gross and Immanuel Bloch. Quantum simulations with ultracold atoms in optical lattices. 1001(September):995–1001, 2017.
- [54] Markus Greiner, Olaf Mandel, Tilman Esslinger, Theodor W. Hänsch, and Immanuel Bloch. Quantum phase transition from a superfluid to a mott insulator in a gas of ultracold atoms. *Nature*, 2002.
- [55] Lawrence W. Cheuk, Matthew A. Nichols, Katherine R. Lawrence, Melih Okan, Hao Zhang, Ehsan Khatami, Nandini Trivedi, Thereza Paiva, Marcos Rigol, and Martin W. Zwierlein. Observation of spatial charge and spin correlations in the 2D Fermi-Hubbard model. *Science*, 2016.
- [56] Martin Boll, Timon A. Hilker, Guillaume Salomon, Ahmed Omran, Jacopo Nespolo, Lode Pollet, Immanuel Bloch, and Christian Gross. Spin- and density-resolved microscopy of antiferromagnetic correlations in Fermi-Hubbard chains. *Science*, 2016.
- [57] Matthew A. Nichols, Lawrence W. Cheuk, Melih Okan, Thomas R. Hartke, Enrique Mendez, T. Senthil, Ehsan Khatami, Hao Zhang, and Martin W. Zwierlein. Quantum simulation: Spin transport in a Mott insulator of ultracold fermions. *Science*, 2019.
- [58] Michael Schreiber, Sean S. Hodgman, Pranjal Bordia, Henrik P. Lüschen, Mark H. Fischer, Ronen Vosk, Ehud Altman, Ulrich Schneider, and Immanuel Bloch. Observation of many-body localization of interacting fermions in a quasirandom optical lattice. *Science*, 349(6250):842–845, 2015.
- [59] H. Pichler, A. J. Daley, and P. Zoller. Nonequilibrium dynamics of bosonic atoms in optical lattices: Decoherence of many-body states due to spontaneous emission. *Physical Review A - Atomic, Molecular, and Optical Physics*, 82(6):1–15, 2010.
- [60] Christof Weitenberg, Manuel Endres, Jacob F. Sherson, Marc Cheneau, Peter Schau, Takeshi Fukuhara, Immanuel Bloch, and Stefan Kuhr. Single-spin addressing in an atomic Mott insulator. *Nature*, 2011.
- [61] Henrik P. Lüschen, Pranjal Bordia, Sean S. Hodgman, Michael Schreiber, Saubhik Sarkar, Andrew J. Daley, Mark H. Fischer, Ehud Altman, Immanuel Bloch, and Ulrich Schneider. Signatures of many-body localization in a controlled open quantum system. *Phys. Rev. X*, 7:011034, Mar 2017.

- [62] A. Griessner, A J Daley, S. R. Clark, D. Jaksch, and P. Zoller. Dissipative dynamics of atomic Hubbard models coupled to a phonon bath: Dark state cooling of atoms within a Bloch band of an optical lattice. *New Journal of Physics*, 9, 2007.
- [63] Kristian Baumann, Christine Guerlin, Ferdinand Brennecke, and Tilman Esslinger. Dicke quantum phase transition with a superfluid gas in an optical cavity. *Nature*, 464(April), 2010.
- [64] M Landini, N Dogra, K Kroeger, L Hruby, T Donner, and T Esslinger. Formation of a Spin Texture in a Quantum Gas Coupled to a Cavity. *Physical Review Letters*, 120(22):223602, 2018.
- [65] Ronen M Kroeze, Yudan Guo, Varun D Vaidya, Jonathan Keeling, and Benjamin L Lev. Spinor Self-Ordering of a Quantum Gas in a Cavity. *Physical Review Letters*, 121(16):163601, 2019.
- [66] Logan W Clark, Nathan Schine, Claire Baum, Ningyuan Jia, and Jonathan Simon. Observation of Laughlin states made of light. *Nature*, 582(June), 2020.
- [67] Julian Léonard, Andrea Morales, Philip Zupancic, Tilman Esslinger, and Tobias Donner. Supersolid formation in a quantum gas breaking a continuous translational symmetry. *Nature*, 543(7643):87–90, 2017.
- [68] Juan A Muniz, Diego Barberena, Robert J Lewis-swan, Dylan J Young, Julia R K Cline, Ana Maria Rey, and James K Thompson. Exploring dynamical phase transitions with cold atoms in an optical cavity. *Nature*, 580(April), 2020.
- [69] Peter Kirton, Mor M. Roses, Jonathan Keeling, and Emanuele G. Dalla Torre. Introduction to the Dicke model: from equilibrium to nonequilibrium, and vice versa. pages 1–21, 2018.
- [70] Frank Arute, Kunal Arya, Ryan Babbush, Dave Bacon, Joseph C Bardin, Rami Barends, Rupak Biswas, Sergio Boixo, Fernando GSL Brandao, David A Buell, et al. Quantum supremacy using a programmable superconducting processor. *Nature*, 574(7779):505–510, 2019.
- [71] Eliot Kapit, Mohammad Hafezi, and Steven H Simon. Induced self-stabilization in fractional quantum Hall states of light. *Physical Review X*, 4(3):1–9, 2014.
- [72] José Lebreuilly, Alberto Biella, Florent Storme, Davide Rossini, Rosario Fazio, Cristiano Ciuti, and Iacopo Carusotto. Stabilizing strongly correlated photon fluids with non-Markovian reservoirs. *Physical Review A*, 96(3):1–15, 2017.
- [73] Ruichao Ma, Brendan Saxberg, Clai Owens, Nelson Leung, Yao Lu, Jonathan Simon, and David I Schuster. A dissipatively stabilized Mott insulator of photons. *Nature*, 566(7742):51–57, 2019.

- [74] M W Zwierlein, C A Stan, C H Schunck, S M F Raupach, A J Kerman, and W Ketterle. Condensation of pairs of fermionic atoms near a Feshbach resonance. *Physical Review Letters*, 92(12):120403, 2004.
- [75] C A Regal, M Greiner, and D S Jin. Observation of Resonance Condensation of Fermionic Atom Pairs. *Phys. Rev. Lett.*, 92(4):40403, jan 2004.
- [76] Wilhelm Zwerger. *The BCS-BEC crossover and the unitary Fermi gas*, volume 836. Springer Science & Business Media, 2011.
- [77] Stefano Giorgini, Lev P Pitaevskii, and Sandro Stringari. Theory of ultracold atomic fermi gases. *Reviews of Modern Physics*, 80(4):1215, 2008.
- [78] P. Nozieres and D. Saint James. Particle vs. pair condensation in attractive Bose liquids. *Journal de Physique*, 43(7):1133–1148, 1982.
- [79] Leo Radzihovsky, Peter B Weichman, and Jae I Park. Superfluidity and phase transitions in a resonant Bose gas. *Annals of Physics*, 323(10):2376–2451, 2008.
- [80] Tino Weber, Jens Herbig, Michael Mark, Hanns-Christoph Nägerl, and Rudolf Grimm. Three-Body Recombination at Large Scattering Lengths in an Ultracold Atomic Gas. *Phys. Rev. Lett.*, 91(12):123201, sep 2003.
- [81] Richard J Fletcher, Alexander L Gaunt, Nir Navon, Robert P Smith, and Zoran Hadzibabic. Stability of a Unitary Bose Gas. *Physical Review Letters*, 111(12), 2013.
- [82] P Makotyn, C E Klauss, D L Goldberger, E A Cornell, and D S Jin. Universal dynamics of a degenerate unitary Bose gas. *Nature Physics*, 10:12, 2014.
- [83] Christoph Eigen, Jake A. P. Glidden, Raphael Lopes, Eric A. Cornell, Robert P. Smith, and Zoran Hadzibabic. Universal prethermal dynamics of Bose gases quenched to unitarity. *Nature*, 563(7730):221–224, nov 2018.
- [84] Sourish Basu and Erich J Mueller. Stability of bosonic atomic and molecular condensates near a Feshbach resonance. *Physical Review A - Atomic, Molecular, and Optical Physics*, 78(5), 2008.
- [85] Johannes Otterbach, Matthias Moos, Dominik Muth, and Michael Fleischhauer. Wigner crystallization of single photons in cold rydberg ensembles. *Physical Review Letters*, 2013.
- [86] P. C. Hohenberg and B. I. Halperin. Theory of dynamic critical phenomena. *Reviews of Modern Physics*, 49(3):435–479, jul 1977.
- [87] Jun John Sakurai and Eugene D Commins. Modern quantum mechanics, revised edition, 1995.
- [88] Dmitry S. Petrov. The few-atom problem. In *Many-Body Physics with Ultracold Gases: Lecture Notes of the Les Houches Summer School*. 2013.

- [89] Eric Braaten and H. W. Hammer. Universality in few-body systems with large scattering length. *Physics Reports*, 428(5-6):259–390, oct 2006.
- [90] S Diehl and C Wetterich. Functional Integral for Ultracold Fermionic Atoms. 2007.
- [91] S. Moroz, S. Floerchinger, R. Schmidt, and C. Wetterich. Efimov effect from functional renormalization. *Physical Review A*, 79(4):042705, apr 2009.
- [92] Eddy Timmermans. Feshbach resonances in atomic Bose–Einstein condensates. *Physics Reports*, 315(1-3):199–230, 1999.
- [93] Michael Fleischhauer, Atac Imamoglu, and Jonathan P Marangos. Electromagnetically induced transparency: Optics in coherent media. 2005.
- [94] Alexey V. Gorshkov, Johannes Otterbach, Michael Fleischhauer, Thomas Pohl, and Mikhail D. Lukin. Photon-photon interactions via Rydberg blockade. *Physical Review Letters*, 107(13):1–5, 2011.
- [95] David Petrosyan, Johannes Otterbach, and Michael Fleischhauer. Electromagnetically induced transparency with Rydberg atoms. *Physical Review Letters*, 107(21):1–5, 2011.
- [96] S. Sevinçli, N. Henkel, C. Ates, and T. Pohl. Nonlocal nonlinear optics in cold Rydberg gases. *Physical Review Letters*, 107(15):1–5, 2011.
- [97] J. D. Pritchard, D. Maxwell, A. Gauguet, K. J. Weatherill, M. P.A. Jones, and C. S. Adams. Cooperative atom-light interaction in a blockaded Rydberg ensemble. *Physical Review Letters*, 105(19):1–4, 2010.
- [98] Thibault Peyronel, Ofer Firstenberg, Qi-Yu Liang, Sebastian Hofferberth, Alexey V Gorshkov, Thomas Pohl, Mikhail D Lukin, and Vladan Vuletić. Quantum nonlinear optics with single photons enabled by strongly interacting atoms. *Nature*, 488(7409):57–60, 2012.
- [99] Qi-Yu Liang, Aditya V Venkatramani, Sergio H Cantu, Travis L Nicholson, Michael J Gullans, Alexey V Gorshkov, Jeff D Thompson, Cheng Chin, Mikhail D Lukin, and Vladan Vuletić. Observation of three-photon bound states in a quantum nonlinear medium Downloaded from. Technical report, 2018.
- [100] Jia Ningyuan, Alexandros Georgakopoulos, Albert Ryou, Nathan Schine, Ariel Sommer, and Jonathan Simon. Observation and characterization of cavity Rydberg polaritons. *Physical Review A*, 93(4), 2016.
- [101] D. Maxwell, D. J. Szwer, D. Paredes-Barato, H. Busche, J. D. Pritchard, A. Gauguet, K. J. Weatherill, M. P. A. Jones, and C. S. Adams. Storage and control of optical photons using rydberg polaritons. *Phys. Rev. Lett.*, 110:103001, Mar 2013.
- [102] Y. O. Dudin and A. Kuzmich. Strongly interacting Rydberg excitations of a cold atomic gas. *Science*, 336(6083):887–889, may 2012.

- [103] M Fleischhauer and M D Lukin. Dark-state polaritons in electromagnetically induced transparency. *Phys. Rev. Lett.*, 84(22):5094–5097, 2000.
- [104] J L Roberts, N R Claussen, S L Cornish, E A Donley, E A Cornell, and C E Wieman. Controlled collapse of a Bose-Einstein condensate. *Physical Review Letters*, 86(19):4211–4214, 2001.
- [105] M. J. Gullans, J. D. Thompson, Y. Wang, Q.-Y. Liang, V. Vuletić, M. D. Lukin, and A. V. Gorshkov. Effective Field Theory for Rydberg Polaritons. *Physical Review Letters*, 117(11):113601, sep 2016.
- [106] P D Drummond and D F Walls. Quantum theory of optical bistability. I. Nonlinear polarisability model. *Journal of Physics A: Mathematical and General*, 13(2):725–741, 1980.
- [107] M Foss-Feig, P Niroula, J T Young, M Hafezi, A V Gorshkov, R M Wilson, and M F Maghrebi. Emergent equilibrium in many-body optical bistability. *Physical Review A*, 95(4), 2017.
- [108] Allan Griffin, David W Snoke, and Sandro Stringari. *Bose-einstein condensation*. Cambridge University Press, 1996.
- [109] Yu Li Lee and Yu Wen Lee. Universality and stability for a dilute Bose gas with a Feshbach resonance. *Physical Review A - Atomic, Molecular, and Optical Physics*, 81(6), 2010.
- [110] Christof Wetterich. Exact evolution equation for the effective potential. *Physics Letters B*, 301(1):90–94, 1993.
- [111] Paul Breiding and Sascha Timme. Homotopycontinuation.jl: A package for homotopy continuation in julia. In James H. Davenport, Manuel Kauers, George Labahn, and Josef Urban, editors, *Mathematical Software – ICMS 2018*, pages 458–465, Cham, 2018. Springer International Publishing.
- [112] Alexandre Le Boité, Giuliano Orso, and Cristiano Ciuti. Steady-state phases and tunneling-induced instabilities in the driven dissipative bose-hubbard model. *Physical Review Letters*, 110(23), 2013.
- [113] Jiasen Jin, Davide Rossini, Rosario Fazio, Martin Leib, and Michael J. Hartmann. Photon solid phases in driven arrays of nonlinearly coupled cavities. *Physical Review Letters*, 110(16):1–5, 2013.
- [114] Matteo Biondi, Gianni Blatter, Hakan E. Türeci, and Sebastian Schmidt. Nonequilibrium gas-liquid transition in the driven-dissipative photonic lattice. *Physical Review A*, 96(4):1–7, 2017.
- [115] Matteo Marcuzzi, Emanuele Levi, Sebastian Diehl, Juan P. Garrahan, and Igor Lesanovsky. Universal nonequilibrium properties of dissipative rydberg gases. *Physical Review Letters*, 113(21):1–6, 2014.

- [116] Tony E. Lee, H. Häffner, and M. C. Cross. Antiferromagnetic phase transition in a nonequilibrium lattice of Rydberg atoms. *Physical Review A - Atomic, Molecular, and Optical Physics*, 84(3):1–4, 2011.
- [117] Tony E. Lee, H. Häffner, and M. C. Cross. Collective quantum jumps of rydberg atoms. *Physical Review Letters*, 108(2):1–5, 2012.
- [118] Ryan M. Wilson, Khan W. Mahmud, Anzi Hu, Alexey V. Gorshkov, Mohammad Hafezi, and Michael Foss-Feig. Collective phases of strongly interacting cavity photons. *Physical Review A*, 94(3):1–9, 2016.
- [119] J. J. Mendoza-Arenas, S. R. Clark, S. Felicetti, G. Romero, E. Solano, D. G. Angelakis, and D. Jaksch. Beyond mean-field bistability in driven-dissipative lattices: Bunching-antibunching transition and quantum simulation. *Physical Review A*, 93(2):1–11, 2016.
- [120] Haggai Landa, Marco Schiró, and Grégoire Misguich. Multistability of Driven-Dissipative Quantum Spins. pages 1–10, may 2019.
- [121] Filippo Vicentini, Fabrizio Minganti, Riccardo Rota, Giuliano Orso, and Cristiano Ciuti. Critical slowing down in driven-dissipative Bose-Hubbard lattices. *Physical Review A*, 97(1), 2018.
- [122] Uwe C. Tauber. *Critical Dynamics*. Cambridge University Press, Cambridge, 2013.
- [123] Mohammad F Maghrebi and Alexey V Gorshkov. Nonequilibrium many-body steady states via Keldysh formalism. *Physical Review B*, 93(1):1–17, 2016.
- [124] Ana Maria Rey, B L Hu, Esteban Calzetta, Albert Roua, and Charles W Clark. Nonequilibrium dynamics of optical-lattice-loaded Bose-Einstein-condensate atoms: Beyond the Hartree-Fock-Bogoliubov approximation. *Physical Review A - Atomic, Molecular, and Optical Physics*, 69(3), 2004.
- [125] Thomas Gasenzer, Jürgen Berges, Michael G Schmidt, and Marcos Seco. Nonperturbative dynamical many-body theory of a Bose-Einstein condensate. *Physical Review A - Atomic, Molecular, and Optical Physics*, 72(6), 2005.
- [126] Marin Bukov, Sarang Gopalakrishnan, Michael Knap, and Eugene Demler. Prethermal Floquet Steady States and Instabilities in the Periodically Driven, Weakly Interacting Bose-Hubbard Model. Technical report, 2015.
- [127] Florian Lange, Zala Lenarčič, and Achim Rosch. Pumping approximately integrable systems. *Nature Communications*, 8(1):1–8, 2017.
- [128] Zala Lenarčič, Florian Lange, and Achim Rosch. Perturbative approach to weakly driven many-particle systems in the presence of approximate conservation laws. 2017.
- [129] Michael Schreiber, Sean S. Hodgman, Pranjal Bordia, Henrik P. Lüschen, Mark H. Fischer, Ronen Vosk, Ehud Altman, Ulrich Schneider, and Immanuel Bloch. Observation of



- many-body localization of interacting fermions in a quasirandom optical lattice. *Science*, 349(6250):842–845, 2015.
- [130] Henrik P. Lüschen, Pranjal Bordia, Sebastian Scherg, Fabien Alet, Ehud Altman, Ulrich Schneider, and Immanuel Bloch. Observation of slow dynamics near the many-body localization transition in one-dimensional quasiperiodic systems. *Phys. Rev. Lett.*, 119:260401, Dec 2017.
  - [131] Alexander Lukin, Matthew Rispoli, Robert Schittko, M Eric Tai, Adam M Kaufman, Soonwon Choi, Vedika Khemani, Julian Léonard, and Markus Greiner. Probing entanglement in a many-body-localized system. *Science*, 364(6437):256–260, 2019.
  - [132] J. Smith, A. Lee, P. Richerme, B. Neyenhuis, P. W. Hess, P. Hauke, M. Heyl, D. A. Huse, and C. Monroe. Many-body localization in a quantum simulator with programmable random disorder. *Nat. Phys.*, 12(10):907–911, 10 2016.
  - [133] David J. Luitz, Nicolas Laflorencie, and Fabien Alet. Many-body localization edge in the random-field heisenberg chain. *Phys. Rev. B*, 91:081103, Feb 2015.
  - [134] Vadim Oganesyan and David A. Huse. Localization of interacting fermions at high temperature. *Physical Review B*, 75(15):155111, apr 2007.
  - [135] Jonas A. Kjäll, Jens H. Bardarson, and Frank Pollmann. Many-body localization in a disordered quantum ising chain. *Physical Review Letters*, 113(10):1–5, 2014.
  - [136] Vedika Khemani, S. P. Lim, D. N. Sheng, and David A. Huse. Critical properties of the many-body localization transition. *Physical Review X*, 7(2):1–11, 2017.
  - [137] Maksym Serbyn and Joel E. Moore. Spectral statistics across the many-body localization transition. *Physical Review B*, 93(4):1–5, 2016.
  - [138] R. Vasseur, S. A. Parameswaran, and J. E. Moore. Quantum revivals and many-body localization. *Physical Review B - Condensed Matter and Materials Physics*, 91(14):1–5, 2015.
  - [139] Jan Šuntajs, J Bonča, Tomaz Prosen, and Lev Vidmar. Quantum chaos challenges many-body localization. *arXiv preprint arXiv:1905.06345*, 2019.
  - [140] D. A. Abanin, J. H. Bardarson, G. De Tomasi, S. Gopalakrishnan, V. Khemani, S. A. Parameswaran, F. Pollmann, A. C. Potter, M. Serbyn, and R. Vasseur. Distinguishing localization from chaos: challenges in finite-size systems. pages 1–11, 2019.
  - [141] Zala Lenarčič, Ehud Altman, and Achim Rosch. Activating many-body localization in solids by driving with light. *Phys. Rev. Lett.*, 121:267603, Dec 2018.
  - [142] Subir Sachdev. *Quantum Phase Transitions*. 2011.
  - [143] Marko Žnidarič. Dephasing-induced diffusive transport in the anisotropic heisenberg model. *New Journal of Physics*, 12(4):043001, 2010.

- [144] Rahul Nandkishore, Sarang Gopalakrishnan, and David A. Huse. Spectral features of a many-body-localized system weakly coupled to a bath. *Phys. Rev. B*, 90:064203, Aug 2014.
- [145] Kartiek Agarwal, Sarang Gopalakrishnan, Michael Knap, Markus Müller, and Eugene Demler. Anomalous diffusion and griffiths effects near the many-body localization transition. *Phys. Rev. Lett.*, 114:160401, Apr 2015.
- [146] Sonika Johri, Rahul Nandkishore, and R. N. Bhatt. Many-body localization in imperfectly isolated quantum systems. *Phys. Rev. Lett.*, 114:117401, Mar 2015.
- [147] Mark H Fischer, Mykola Maksymenko, and Ehud Altman. Dynamics of a many-body-localized system coupled to a bath. *Phys. Rev. Lett.*, 116:160401, Apr 2016.
- [148] Mariya V. Medvedyeva, Tomaž Prosen, and Marko Žnidarič. Influence of dephasing on many-body localization. *Phys. Rev. B*, 93:094205, Mar 2016.
- [149] Pranjal Bordia, Henrik P. Lüschen, Sean S. Hodgman, Michael Schreiber, Immanuel Bloch, and Ulrich Schneider. Coupling identical one-dimensional many-body localized systems. *Phys. Rev. Lett.*, 116:140401, Apr 2016.
- [150] Peter Prelovšek. Decay of density waves in coupled one-dimensional many-body-localized systems. *Phys. Rev. B*, 94:144204, Oct 2016.
- [151] Emanuele Levi, Markus Heyl, Igor Lesanovsky, and Juan P. Garrahan. Robustness of many-body localization in the presence of dissipation. *Phys. Rev. Lett.*, 116:237203, Jun 2016.
- [152] David J. Luitz, François Huveneers, and Wojciech De Roeck. How a small quantum bath can thermalize long localized chains. *Phys. Rev. Lett.*, 119:150602, Oct 2017.
- [153] Rahul Nandkishore and Sarang Gopalakrishnan. Many body localized systems weakly coupled to baths. *Annalen der Physik*, 529(7), 2017.
- [154] Benjamin Everest, Igor Lesanovsky, Juan P. Garrahan, and Emanuele Levi. Role of interactions in a dissipative many-body localized system. *Phys. Rev. B*, 95:024310, Jan 2017.
- [155] J. Marino and R. M. Nandkishore. Many-body localization proximity effects in platforms of coupled spins and bosons. *Phys. Rev. B*, 97:054201, Feb 2018.
- [156] Antonio Rubio-Abadal, Jae-yoon Choi, Johannes Zeiher, Simon Hollerith, Jun Rui, Immanuel Bloch, and Christian Gross. Probing many-body localization in the presence of a quantum bath. *arXiv:1805.00056*, 2018.
- [157] Felix Weiner, Ferdinand Evers, and Soumya Bera. Slow dynamics and strong finite-size effects in many-body localization with random and quasiperiodic potentials. *Phys. Rev. B*, 100:104204, Sep 2019.
- [158] Maximilian Schulz, Scott Taylor, Antonello Scardicchio, and Marko Znidaric. Phenomenology of anomalous transport in disordered one-dimensional systems. *arXiv preprint arXiv:1909.09507*, 2019.

- [159] Marko Žnidarič, Antonello Scardicchio, and Vipin Kerala Varma. Diffusive and subdiffusive spin transport in the ergodic phase of a many-body localizable system. *Phys. Rev. Lett.*, 117:040601, Jul 2016.
- [160] A Brooks Harris. Effect of random defects on the critical behaviour of ising models. *Journal of Physics C: Solid State Physics*, 7(9):1671, 1974.
- [161] Andrew C. Potter, Romain Vasseur, and S. A. Parameswaran. Universal properties of many-body delocalization transitions. *Phys. Rev. X*, 5:031033, Sep 2015.
- [162] J. M. Deutsch. Quantum statistical mechanics in a closed system. *Physical Review A*, 1991.
- [163] Mark Srednicki. Chaos and quantum thermalization. *Physical Review E*, 1994.
- [164] P W Anderson. Absence of diffusion in certain random lattices. *Physical Review*, 109(5):1492–1505, 1958.
- [165] E. Abrahams, P. W. Anderson, D. C. Licciardello, and T. V. Ramakrishnan. Scaling theory of localization: Absence of quantum diffusion in two dimensions. *Physical Review Letters*, 42(10):673–676, 1979.
- [166] Antonello Scardicchio and Thimothée Thiery. Perturbation theory approaches to anderson and many-body localization: some lecture notes. *arXiv preprint arXiv:1710.01234*, 2017.
- [167] Ragi Abou-Chakra, DJ Thouless, and PW Anderson. A selfconsistent theory of localization. *Journal of Physics C: Solid State Physics*, 6(10):1734, 1973.
- [168] Wojciech De Roeck and François Huveneers. Stability and instability towards delocalization in many-body localization systems. *Phys. Rev. B*, 95:155129, Apr 2017.
- [169] John Z Imbrie. On many-body localization for quantum spin chains. *Journal of Statistical Physics*, 163(5):998–1048, 2016.
- [170] Bela Bauer and Chetan Nayak. Area laws in a many-body localized state and its implications for topological order. *Journal of Statistical Mechanics: Theory and Experiment*, 2013(09):P09005, 2013.
- [171] Maksym Serbyn, Z. Papić, and Dmitry A. Abanin. Local conservation laws and the structure of the many-body localized states. *Physical Review Letters*, 111(12):127201, sep 2013.
- [172] David A. Huse, Rahul Nandkishore, and Vadim Oganesyan. Phenomenology of fully many-body-localized systems. *Phys. Rev. B*, 90:174202, Nov 2014.
- [173] Jens H. Bardarson, Frank Pollmann, and Joel E. Moore. Unbounded growth of entanglement in models of many-body localization. *Phys. Rev. Lett.*, 109:017202, Jul 2012.
- [174] Marko Žnidarič, Tomaž Prosen, and Peter Prelovšek. Many-body localization in the heisenberg  $x \times z$  magnet in a random field. *Physical Review B*, 77(6):064426, 2008.

- [175] Maksym Serbyn, Z. Papić, and Dmitry A. Abanin. Universal Slow Growth of Entanglement in Interacting Strongly Disordered Systems. *Physical Review Letters*, 110(26):260601, jun 2013.
- [176] Jae-yoon Choi, Sebastian Hild, Johannes Zeiher, Peter Schauß, Antonio Rubio-Abadal, Tarik Yefsah, Vedika Khemani, David A. Huse, Immanuel Bloch, and Christian Gross. Exploring the many-body localization transition in two dimensions. *Science*, 352(6293):1547–1552, 2016.
- [177] J Smith, A Lee, P Richerme, B Neyenhuis, P W Hess, P Hauke, M Heyl, D A Huse, and C Monroe. Many-body localization in a quantum simulator with programmable random disorder. 12(June):907–911, 2016.
- [178] P. Roushan, C. Neill, J. Tangpanitanon, V. M. Bastidas, A. Megrant, R. Barends, Y. Chen, Z Chen, B Chiaro, A Dunsworth, A Fowler, B Foxen, M Giustina, E Jeffrey, J Kelly, E Lucero, J Mutus, M Neeley, C Quintana, D Sank, A Vainsencher, J Wenner, T White, H Neven, D G Angelakis, and J Martinis. Spectroscopic signatures of localization with interacting photons in superconducting qubits. *Science*, 358(6367):1175–1179, 2017.
- [179] Serge Aubry and Gilles André. Analyticity breaking and anderson localization in incommensurate lattices. *Ann. Israel Phys. Soc*, 3(133):18, 1980.
- [180] David J. Luitz, Nicolas Laflorencie, and Fabien Alet. Many-body localization edge in the random-field Heisenberg chain. *Physical Review B - Condensed Matter and Materials Physics*, 91(8):1–5, 2015.
- [181] JT Chayes, L Chayes, Daniel S Fisher, and T Spencer. Correlation length bounds for disordered ising ferromagnets. *Communications in mathematical physics*, 120(3):501–523, 1989.
- [182] Anushya Chandran, Chris R Laumann, and Vadim Oganesyan. Finite size scaling bounds on many-body localized phase transitions. *arXiv preprint arXiv:1509.04285*, 2015.
- [183] Robert B Griffiths. Nonanalytic behavior above the critical point in a random ising ferromagnet. *Physical Review Letters*, 23(1):17, 1969.
- [184] Barry M McCoy. Incompleteness of the critical exponent description for ferromagnetic systems containing random impurities. *Physical Review Letters*, 23(7):383, 1969.
- [185] Yevgeny Bar Lev, Guy Cohen, and David R. Reichman. Absence of diffusion in an interacting system of spinless fermions on a one-dimensional disordered lattice. *Phys. Rev. Lett.*, 114:100601, Mar 2015.
- [186] Michael Zwolak and Guifré Vidal. Mixed-state dynamics in one-dimensional quantum lattice systems: A time-dependent superoperator renormalization algorithm. *Physical Review Letters*, 93(20), 2004.

- [187] Johannes Hauschild and Frank Pollmann. Efficient numerical simulations with Tensor Networks: Tensor Network Python (TeNPy). *SciPost Physics Lecture Notes*, page 5, oct 2018.
- [188] Sebastian Paeckel, Thomas Köhler, Andreas Swoboda, Salvatore R. Manmana, Ulrich Schollwöck, and Claudius Hubig. Time-evolution methods for matrix-product states. 2019.
- [189] Man-Duen Choi. Completely positive linear maps on complex matrices. *Linear Algebra and its Applications*, 10(3):285–290, jun 1975.
- [190] Matthew B Hastings. An area law for one-dimensional quantum systems. *Journal of Statistical Mechanics: Theory and Experiment*, 2007(08):P08024, 2007.
- [191] Selçuk Ş Bayın. Definition of the riesz derivative and its application to space fractional quantum mechanics. *Journal of Mathematical Physics*, 57(12):123501, 2016.
- [192] A Anatolii Aleksandrovich Kilbas, Hari Mohan Srivastava, and Juan J Trujillo. *Theory and applications of fractional differential equations*, volume 204. Elsevier Science Limited, 2006.
- [193] JP Hulin, JP Bouchaud, and A Georges. Strongly disordered chain of impedances: theoretical analysis and numerical results. *Journal of Physics A: Mathematical and General*, 23(7):1085, 1990.
- [194] S D Geraedts, N Regnault, and R M Nandkishore. Characterizing the many-body localization transition using the entanglement spectrum. *New Journal of Physics*, 19(11):113021, 2017.
- [195] F. Verstraete, J. J. García-Ripoll, and J. I. Cirac. Matrix Product Density Operators: Simulation of Finite-Temperature and Dissipative Systems. *Physical Review Letters*, 93(20):207204, nov 2004.
- [196] M. C. Bañuls, J. I. Cirac, and M. B. Hastings. Strong and weak thermalization of infinite nonintegrable quantum systems. *Phys. Rev. Lett.*, 106:050405, Feb 2011.
- [197] A. B. Harris. Upper bounds for the transition temperatures of generalized ising models. *Journal of Physics C: Solid State Physics*, 7(17):3082, 1974.
- [198] J. T. Chayes, L. Chayes, Daniel S. Fisher, and T. Spencer. Finite-size scaling and correlation lengths for disordered systems. *Phys. Rev. Lett.*, 57:2999–3002, Dec 1986.
- [199] Anna Goremykina, Romain Vasseur, and Maksym Serbyn. Analytically solvable renormalization group for the many-body localization transition. *Phys. Rev. Lett.*, 122:040601, Jan 2019.
- [200] Philipp T. Dumitrescu, Anna Goremykina, Siddharth A. Parameswaran, Maksym Serbyn, and Romain Vasseur. Kosterlitz-thouless scaling at many-body localization phase transitions. *Phys. Rev. B*, 99:094205, Mar 2019.

- [201] Mark S Anderson. Locally enhanced raman spectroscopy with an atomic force microscope. *Applied Physics Letters*, 76(21):3130–3132, 2000.
- [202] Aaron Sternbach, James Hinton, Tetiana Slusar, Alexander Swinton McLeod, Mengkun Liu, Alex Frenzel, Martin Wagner, Ruben Iraheta, Fritz Keilmann, Alfred Leitenstorfer, Michael Fogler, Hyun-Tak Kim, Richard Averitt, and Dimitri Basov. Artifact free transient near-field nanoscopy. *arXiv:1706.08478*, 2017.
- [203] Wojciech De Roeck and François Huveneers. Stability and instability towards delocalization in many-body localization systems. *Phys. Rev. B*, 95:155129, Apr 2017.
- [204] Ionut-Dragos Potirniche, Sumilan Banerjee, and Ehud Altman. Exploration of the stability of many-body localization in *dgt*; 1. *Phys. Rev. B*, 99:205149, May 2019.
- [205] Alexandra Nagy and Vincenzo Savona. Variational Quantum Monte Carlo Method with a Neural-Network Ansatz for Open Quantum Systems. *Physical Review Letters*, 122(25):250501, jun 2019.
- [206] Filippo Vicentini, Alberto Biella, Nicolas Regnault, and Cristiano Ciuti. Variational Neural-Network Ansatz for Steady States in Open Quantum Systems. *Physical Review Letters*, 122(25):250503, jun 2019.
- [207] Michael J. Hartmann and Giuseppe Carleo. Neural-Network Approach to Dissipative Quantum Many-Body Dynamics. *Physical Review Letters*, 122(25):250502, jun 2019.
- [208] Nobuyuki Yoshioka and Ryusuke Hamazaki. Constructing neural stationary states for open quantum many-body systems. *Physical Review B*, feb 2019.
- [209] B. R. Mollow. Pure-state analysis of resonant light scattering: Radiative damping, saturation, and multiphoton effects. *Phys. Rev. A*, 12:1919–1943, Nov 1975.
- [210] R. H. Dicke. Interaction-free quantum measurements: A paradox? *American Journal of Physics*, 49(10):925–930, 1981.
- [211] D. Leibfried, R. Blatt, C. Monroe, and D. Wineland. Quantum dynamics of single trapped ions. *Rev. Mod. Phys.*, 75:281–324, Mar 2003.
- [212] Vitaly N. Golovach, Alexander Khaetskii, and Daniel Loss. Phonon-induced decay of the electron spin in quantum dots. *Phys. Rev. Lett.*, 93:016601, Jun 2004.
- [213] D. D. Sukachev, A. Sipahigil, C. T. Nguyen, M. K. Bhaskar, R. E. Evans, F. Jelezko, and M. D. Lukin. Silicon-vacancy spin qubit in diamond: A quantum memory exceeding 10 ms with single-shot state readout. *Phys. Rev. Lett.*, 119:223602, Nov 2017.
- [214] Amos Chan, Rahul M. Nandkishore, Michael Pretko, and Graeme Smith. Unitary-projective entanglement dynamics. *Phys. Rev. B*, 99:224307, Jun 2019.
- [215] Soonwon Choi, Yimu Bao, Xiao-Liang Qi, and Ehud Altman. Quantum error correction in scrambling dynamics and measurement induced phase transition, 2019.

- [216] Chao-Ming Jian, Yi-Zhuang You, Romain Vasseur, and Andreas W. W. Ludwig. Measurement-induced criticality in random quantum circuits. *Phys. Rev. B*, 101:104302, Mar 2020.
- [217] Michael J. Gullans and David A. Huse. Dynamical purification phase transitions induced by quantum measurements, 2019.
- [218] Lei Zhang, Justin A. Reyes, Stefanos Kourtis, Claudio Chamon, Eduardo R. Mucciolo, and Andrei E. Ruckenstein. Nonuniversal entanglement level statistics in projection-driven quantum circuits, 2020.
- [219] Qicheng Tang and W. Zhu. Measurement-induced phase transition: A case study in the nonintegrable model by density-matrix renormalization group calculations. *Phys. Rev. Research*, 2:013022, Jan 2020.
- [220] Yaodong Li, Xiao Chen, and Matthew P. A. Fisher. Measurement-driven entanglement transition in hybrid quantum circuits. *Physical Review B*, 100(13):134306, 2019.
- [221] Michael J. Gullans and David A. Huse. Scalable probes of measurement-induced criticality, 2019.
- [222] M. Szytniszewski, A. Romito, and H. Schomerus. Entanglement transition from variable-strength weak measurements. *Phys. Rev. B*, 100:064204, Aug 2019.
- [223] Shimpei Goto and Ippei Danshita. Measurement-induced transitions of the entanglement scaling law in ultracold gases with controllable dissipation, 2020.
- [224] Yaodong Li, Xiao Chen, Andreas W. W. Ludwig, and Matthew P. A. Fisher. Conformal invariance and quantum non-locality in hybrid quantum circuits, 2020.
- [225] Yohei Fuji and Yuto Ashida. Measurement-induced quantum criticality under continuous monitoring, 2020.
- [226] Xiao Chen, Yaodong Li, Matthew P. A. Fisher, and Andrew Lucas. Emergent conformal symmetry in non-unitary random dynamics of free fermions, 2020.
- [227] Hannes Pichler, Johannes Schachenmayer, Andrew J. Daley, and Peter Zoller. Heating dynamics of bosonic atoms in a noisy optical lattice. *Physical Review A*, 87(3), Mar 2013.
- [228] Xiangyu Cao, Antoine Tilloy, and Andrea De Luca. Entanglement in a fermion chain under continuous monitoring. *SciPost Physics*, 7(2), Aug 2019.
- [229] Dario Poletti, Jean-Sébastien Bernier, Antoine Georges, and Corinna Kollath. Interaction-induced impeding of decoherence and anomalous diffusion. *Phys. Rev. Lett.*, 109:045302, Jul 2012.
- [230] Michael Knap. Entanglement production and information scrambling in a noisy spin system. *Phys. Rev. B*, 98:184416, Nov 2018.

- [231] D. Yang, C. Laflamme, D. V. Vasilyev, M. A. Baranov, and P. Zoller. Theory of a quantum scanning microscope for cold atoms. *Phys. Rev. Lett.*, 120:133601, Mar 2018.
- [232] Inés de Vega and Daniel Alonso. Dynamics of non-markovian open quantum systems. *Rev. Mod. Phys.*, 89:015001, Jan 2017.
- [233] H. M. Wiseman and G. J. Milburn. Interpretation of quantum jump and diffusion processes illustrated on the bloch sphere. *Phys. Rev. A*, 47:1652–1666, Mar 1993.
- [234] Jean Dalibard, Yvan Castin, and Klaus Mølmer. Wave-function approach to dissipative processes in quantum optics. *Phys. Rev. Lett.*, 68:580–583, Feb 1992.
- [235] Scott Aaronson and Daniel Gottesman. Improved simulation of stabilizer circuits. *Physical Review A*, 70(5):052328, nov 2004.
- [236] S. Sarkar, S. Langer, J. Schachenmayer, and A. J. Daley. Light scattering and dissipative dynamics of many fermionic atoms in an optical lattice. *Physical Review A*, 90(2), Aug 2014.
- [237] Sylvain de Léséleuc, Daniel Barredo, Vincent Lienhard, Antoine Browaeys, and Thierry Lahaye. Analysis of imperfections in the coherent optical excitation of single atoms to rydberg states. *Phys. Rev. A*, 97:053803, May 2018.
- [238] S. Helmrich, A. Arias, and S. Whitlock. Uncovering the nonequilibrium phase structure of an open quantum spin system. *Phys. Rev. A*, 98:022109, Aug 2018.
- [239] Bruno Bertini, Pavel Kos, and Tomaž Prosen. Entanglement Spreading in a Minimal Model of Maximal Many-Body Quantum Chaos. *Physical Review X*, 9(2):1–27, 2019.
- [240] N Gisin and I C Percival. The quantum-state diffusion model applied to open systems. *Journal of Physics A: Mathematical and General*, 25(21):5677–5691, nov 1992.
- [241] Jean Dalibard, Yvan Castin, and Klaus Mølmer. Wave-function approach to dissipative processes in quantum optics. *Physical Review Letters*, 68(5):580–583, feb 1992.
- [242] L. Diósi, N. Gisin, and W. T. Strunz. Non-markovian quantum state diffusion. *Phys. Rev. A*, 58:1699–1712, Sep 1998.
- [243] Matteo Ippoliti, Michael J. Gullans, Sarang Gopalakrishnan, David A. Huse, and Vedika Khemani. Entanglement phase transitions in measurement-only dynamics, 2020.
- [244] Charles H Bennett, Herbert J Bernstein, Sandu Popescu, and Benjamin Schumacher. Concentrating partial entanglement by local operations. *Physical Review A*, 53(4):2046, 1996.
- [245] Michael M. Wolf, Frank Verstraete, Matthew B. Hastings, and J. Ignacio Cirac. Area laws in quantum systems: Mutual information and correlations. *Physical Review Letters*, 100(7):1–4, 2008.



- [246] John Preskill. Lecture notes for physics 219: Quantum computation, 2018.
- [247] Rajibul Islam, Ruichao Ma, Philipp M. Preiss, M. Eric Tai, Alexander Lukin, Matthew Rispoli, and Markus Greiner. Measuring entanglement entropy in a quantum many-body system. *Nature*, 528(7580):77–83, 2015.
- [248] A Elben, B Vermersch, M Dalmonte, J I Cirac, and P Zoller. Rényi Entropies from Random Quenches in Atomic Hubbard and Spin Models. *Physical Review Letters*, 120(5):50406, 2018.
- [249] Tiff Brydges, Andreas Elben, Petar Jurcevic, Benoît Vermersch, Christine Maier, Ben P. Lanyon, Peter Zoller, Rainer Blatt, and Christian F. Roos. Probing Rényi entanglement entropy via randomized measurements. *Science*, 364(6437):260–263, 2019.
- [250] J. T. Chayes, L. Chayes, and R. Durrett. Critical behavior of the two-dimensional first passage time. *Journal of Statistical Physics*, 45(5-6):933–951, dec 1986.
- [251] Michał Horodecki, Jonathan Oppenheim, and Andreas Winter. Quantum state merging and negative information. *Communications in Mathematical Physics*, 269(1):107–136, 2007.
- [252] Frédéric Dupuis, Mario Berta, Jürg Wullschleger, and Renato Renner. One-shot decoupling. *Communications in Mathematical Physics*, 328(1):251–284, 2014.
- [253] R. Dum, P. Zoller, and H. Ritsch. Monte Carlo simulation of the atomic master equation for spontaneous emission. *Physical Review A*, 45(7):4879–4887, apr 1992.
- [254] H. M. Wiseman and G. J. Milburn. Quantum theory of field-quadrature measurements. *Physical Review A*, 1993.
- [255] M. B. Plenio and P. L. Knight. The quantum-jump approach to dissipative dynamics in quantum optics. *Reviews of Modern Physics*, 70(1):101–144, 1998.
- [256] John Cardy. *Scaling and Renormalization in Statistical Physics*. Cambridge University Press, apr 1996.
- [257] John L Cardy. Conformal invariance and universality in finite-size scaling. *Journal of Physics A: Mathematical and General*, 17(7):L385, 1984.
- [258] Paul Ginsparg. Applied Conformal Field Theory. 88, 1988.
- [259] Pasquale Calabrese and John Cardy. Entanglement entropy and conformal field theory. *Journal of Physics A: Mathematical and Theoretical*, 42(50), 2009.
- [260] P. Campagne-Ibarcq, P. Six, L. Bretheau, A. Sarlette, M. Mirrahimi, P. Rouchon, and B. Huard. Observing quantum state diffusion by heterodyne detection of fluorescence. *Physical Review X*, 6(1):1–7, 2016.
- [261] See supplementary material appended to this manuscript.

- [262] G. C. Wick. The evaluation of the collision matrix. *Physical Review*, 1950.
- [263] G Vidal, J I Latorre, E Rico, and A Kitaev. Entanglement in Quantum Critical Phenomena. *Physical Review Letters*, 90(22):4, 2003.
- [264] Vincenzo Alba and Pasquale Calabrese. Entanglement dynamics after quantum quenches in generic integrable systems. *SciPost Phys.*, 4:17, 2018.
- [265] Pasquale Calabrese and John Cardy. Entanglement entropy and quantum field theory. *Journal of Statistical Mechanics: Theory and Experiment*, 2004(06):P06002, jun 2004.
- [266] Pasquale Calabrese and John Cardy. Entanglement entropy and conformal field theory. *Journal of Physics A: Mathematical and Theoretical*, 42(50):504005, dec 2009.
- [267] John Cardy and Jesper Lykke Jacobsen. Critical behavior of random-bond potts models. *Phys. Rev. Lett.*, 79:4063–4066, Nov 1997.
- [268] G. Refael and J. E. Moore. Entanglement entropy of random quantum critical points in one dimension. *Physical Review Letters*, 93(26), Dec 2004.
- [269] Nicolas Laflorencie. Scaling of entanglement entropy in the random singlet phase. *Phys. Rev. B*, 72:140408, Oct 2005.
- [270] John Cardy. Linking numbers for self-avoiding loops and percolation: Application to the spin quantum hall transition. *Phys. Rev. Lett.*, 84:3507–3510, Apr 2000.
- [271] Matthew T. Fishman and Steven R. White. Compression of correlation matrices and an efficient method for forming matrix product states of fermionic Gaussian states. *Physical Review B - Condensed Matter and Materials Physics*, 2015.
- [272] Norbert Schuch and Bela Bauer. Matrix product state algorithms for Gaussian fermionic states. *Physical Review B*, jun 2019.

# STATEMENT OF AUTHORSHIP

Hiermit versichere ich an Eides statt, dass ich die vorliegende Dissertation selbstständig und ohne die Benutzung anderer als der angegebenen Hilfsmittel und Literatur angefertigt habe. Alle Stellen, die wörtlich oder sinngemäß aus veröffentlichten und nicht veröffentlichten Werken dem Wortlaut oder dem Sinn nach entnommen wurden, sind als solche kenntlich gemacht. Ich versichere an Eides statt, dass diese Dissertation noch keiner anderen Fakultät oder Universität zur Prüfung vorgelegen hat; dass sie - abgesehen von unten angegebenen Teilpublikationen und eingebundenen Artikeln und Manuskripten - noch nicht veröffentlicht worden ist sowie, dass ich eine Veröffentlichung der Dissertation vor Abschluss der Promotion nicht ohne Genehmigung des Promotionsausschusses vornehmen werde. Die Bestimmungen dieser Ordnung sind mir bekannt. Darüber hinaus erkläre ich hiermit, dass ich die Ordnung zur Sicherung guter wissenschaftlicher Praxis und zum Umgang mit wissenschaftlichem Fehlverhalten der Universität zu Köln gelesen und sie bei der Durchführung der Dissertation zugrundeliegenden Arbeiten und der schriftlich verfassten Dissertation beachtet habe und verpflichte mich hiermit, die dort genannten Vorgaben bei allen wissenschaftlichen Tätigkeiten zu beachten und umzusetzen. Ich versichere, dass die eingereichte elektronische Fassung der eingereichten Druckfassung vollständig entspricht.

Ori Alberton, 12.02.2021

## TEILPUBLIKATIONEN

- Lenarčič, Z.\*, Alberton, O.\*, Rosch, A., Altman, E. (2020). *Critical Behavior near the Many-Body Localization Transition in Driven Open Systems*. [Physical Review Letters](#), 125(11), 116601. (\*equal contribution)
- Alberton, O., Buchhold, M., Diehl, S. (2020). *Trajectory dependent entanglement transition in a free fermion chain – from extended criticality to area law*. (preprint, currently under peer-review) [arXiv/2005.09722](#).